Synthesis of silver nanoparticles using a plasma-liquid process

Mine Er

UNIVERSITÉ PARIS 13
ÉCOLE DOCTORALE GALILÉE

THÈSE

présentée par

Mine ER

pour obtenir le grade de
DOCTEUR D'UNIVERSITÉ
Spécialité : Génie des Procédés

Synthèse de nanoparticules d'argent à l'aide d'un procédé plasma-liquide

soutenue publiquement le 16 mai 2019 devant le jury composé de

Stéphanie OGNIER	Rapporteur
Christophe COLBEAU-JUSTIN	Rapporteur
Franck CLEMENT	Examinateur
Dominique VREL	Examinateur
Arlette VEGA GONZÁLEZ	Co-encadrante
Xavier DUTEN	Directeur de thèse

Thèse préparée au sein du Laboratoire des Sciences des Procédés et des Matériaux

LSPM-CNRS, UPR 3407, Villetaneuse

Acknowledgements

First of all, I want to thank my director of thesis Prof. Xavier DUTEN and co-supervisor Arlette VEGA-GONZALEZ for giving me the opportunity to work with them on this PhD project. It has been an educative experience in which I have gained much scientific knowledge in multidisciplinary research fields. Furthermore, it has been an experience, which allowed me to develop myself on a personal level.

I also want to thank Cathy ROND for her valuable advices and discussions on the project.

It would not be possible to perform experiments without technical assistance of Nicolas FAGNON, Pascal BOUTIN, and Noël GIRONDON-BOULANDET. Therefore, I want to thank them for their effort in helping me with designing and developing the experimental set-up as a part of this PhD work.

I want to thank Samir FARHAT for his advice and also for allowing me to perform particle characterization using the DLS.

I want to thank Ovidiu BRINZA for his advice and help during the particle characterization process.

I also want to thank the members of the PhD committee, Christophe COLBEAU-JUSTIN, Stephanie OGNIER, Franck CLEMENT, and Dominique VREL, for their time and valuable comments on my PhD work.

Lastly, I would like to thank the administration, permanents, students, and technicians at LSPM for their kindness and personal support.

Abstract

The main objectives of this thesis are to develop a plasma liquid immersion (PLI) method for the synthesis of silver nanoparticles.

Synthesis of silver nanoparticles is first investigated with respect to chemical parameters (concentration of precursor and of stabilizing agent, and initial pH of the precursor solution) in the aim of optimizing PLI process and silver nanoparticles in order to synthesize spherical, small-sized, and uniformly-distributed silver nanoparticles. This investigation is performed using a MARX pulse generator. Secondly, synthesis of silver nanoparticles is investigated with respect to physical parameters (pulse duration, applied voltage, and applied voltage over the inter-electrode distance for a constant ratio). For this investigation, a solid-state BEHLKE switch is used in the generation of plasma pulses.

The study showed that the synthesis and morphology of silver nanoparticles are process dependent. Differences in the generation of plasma discharges are observed, when using two types of pulse generators, and are further explained. Optimized silver nanoparticles, synthesized using the MARX pulse generator, are spherical and uniformly distributed with an average hydrodynamic diameter of 10nm. These silver nanoparticles were produced by injecting only 40mJ energy into pulsed plasma discharges of the PLI process with 2W in power consumption. Synthesis of silver nanoparticles at similar synthesis conditions using the BEHLKE pulse generator resulted in the production of larger-sized polyhedral-shaped silver nanoparticles.

Résumé

Le principal objectif de cette thèse sont de développer un procédé plasma / liquide (PLI) pour la synthèse de nanoparticules d'argent.

La synthèse de nanoparticules d'argent est d'abord étudiée en fonction de paramètres chimiques (concentration du précurseur et d'agent stabilisant, pH initial de la solution) dans le but d'optimiser le procédé de PLI et de synthétiser des particules sphériques de petite taille et uniformément réparties. Cette étude est réalisée à l'aide d'un générateur d'impulsions MARX. Dans la suite, la synthèse de nanoparticules d'argent est étudiée en fonction de paramètres physiques (durée d'impulsion, tension appliquée et tension appliquée sur la distance inter-électrodes pour un rapport constant). Pour cette étude, un commutateur BEHLKE à semi-conducteurs est utilisé pour la génération d'impulsions haute tension.

L'étude a montré que la synthèse et la morphologie des nanoparticules d'argent sont dépendantes de paramètres de processus chimiques et physiques. Des différences dans la génération de décharges de plasma sont observées lors de l'utilisation de deux types de générateurs d'impulsions et sont expliquées plus en détail. Les nanoparticules d'argent synthétisées à l'aide du générateur d'impulsions MARX sont sphériques et uniformément réparties avec un diamètre hydrodynamique moyen de 10 nm. Ces nanoparticules d'argent ont été préparées par des décharges pulsées ayant une énergie de 40 mJ/impulsion et une puissance de 2 W. La synthèse de nanoparticules d'argent dans des conditions de synthèse similaires à l'aide du générateur BEHLKE a abouti à la production de nanoparticules d'argent de taille plus grande et polyhédriques.

Chapter I - Introduction

For more than a century, catalysis has played a key role in many industrial applications. From the Berger lamp in 1898[1] to enzymes, catalysis is currently used in more than 80% of industrial applications. In general, catalysis refers to the acceleration or reorientation of reaction kinetics by means of a catalyst, and in some cases selectivity to direct a reaction in a preferred direction.

The catalysts do not appear generally in the reaction balance and are often used in smaller amounts than the reactive products, especially when they are used in the form of nano-catalysts. Indeed, the smaller a particle, the greater the ratio between the number of atoms of its surface and those present in its volume. At the scale of the nanoparticles, the physical properties of the materials that constitute them vary according to the inverse of their radius, and are often very different from those of the massive materials. For example, in the case of gold, particle size has a remarkable effect on their reactivity. Indeed, if it is inert in the massive state, the gold can become extremely reactive in the form of nanometric particles. Particle size also has an effect on the physical properties of the metal. For example, while solid gold melts at 1063 °C, a gold nanoparticle measuring 2.5 nm in diameter melts at 300 C.

During the thesis of Zixian Jia[2], the 3PE team (*Polyphasic plasma processes & Environment)* developed, in collaboration with the NINO team (*Nanomatériaux INOrganiques)* of the LSPM, a two-phase process coupling an electric discharge at atmospheric pressure and a nano-catalyst based on mixed oxide (from type TiO_2 / Ag or TiO_2 / Au) for the degradation of pollutant present in low concentration in a gas flow. In this context, the work of Z. Jia had shown that it was possible to degrade more than 90% of a model molecule (CH_3CHO - 10/500 ppm) at atmospheric pressure and ambient temperature, with very low energy consumption. The initial idea of the first studies of two phase plasma/catalysis process was to combine the advantages of the operation of non-thermal plasmas at room temperature, their low energy consumption (0.1-5 W) coupled with their high chemical reactivity in the gas phase[3] (via the energy electron

[1] https://www.maison-berger.fr/
[2] Jia Z., Elaboration des matériaux composites nanostructures à base de TiO2 pour la dépollution des effluents gazeux avec une activation par plasma, (2013), Université Paris 13
[3] Kim.H.H, Plasma Processing and Polymers, (2004), 1:91-100.

production, reactive species such as O, O_3, OH, N_2 *, ...) and an additional catalytic effect (mainly via the reduction of by-products), by immersing a catalyst in a plasma[1, 3, 4]

As part of the work of this thesis, **the objectives of the 3PE team were to develop a process coupling an electric discharge produced in a liquid containing a metal precursor, in order to synthesize particles of controlled size and morphology**.

Synthesis of nanoparticles in liquid phase has many advantages in nanoparticle synthesis. The main advantage is to control nanoparticle surface properties and to prepare nanoparticles for use in specific applications. One of the noble metallic nanoparticles that are highly demanded in nanoparticle synthesis and application is silver nanoparticles[5]. This relies on the low-cost and broad application field of silver nanoparticles[5].

Conventional methods in nanoparticle synthesis do not always meet the requirements of a green nanoparticle synthesis, which are at the same time economic and time-saving. In this regard, alternative synthesis processes are taken into use in this work, which respects thus following process criteria:

- ***One-step process*** – A simple process, which requires few synthesis steps as possible
- ***Time-saving*** – A process of short reaction time in which particles are produced
- ***"Green"*** – A process, which avoids the use of harmful and hazardous reactants, generation of reduced by-products and waste
- ***Cost-effective*** – A process operating with low energy consumption. This being at ambient reaction temperatures under atmospheric pressure.

In addition, following requirements will be met in this work for synthesis of silver nanoparticles:

- ***High purity*** – A process, which does not result in nanoparticle contamination from the electrode material, or nanoparticles being exposed towards oxidation
- ***Reproducible*** – A process, which yields in a reproducible nanoparticle synthesis
- ***Fine-tuning of particle morphology*** – A process, which gives the freedom to control particle size, shape, and particle dispersion

[4] Holzer.F, Roland.U, Kopinke.F-D, Applied Catalysis B: Environmental, (2002), 38:163.
[5] Dong X-Y, Gao Z-W, Yang K-F, Zhang W-Q, Xu L-W, Catal. Sci. Technol., (2015),5, 2554-2574

Since it is a start-up project for plasma-synthesized nanoparticles, the initial aim of this work is to develop a PLI (Plasma Liquid Immersion) experimental set-up, which provides synthesis of pure and metallic nanoparticles. Generation of stable plasma discharges reaching up to 16kV in a liquid phase is a quite challenging task in comparison to plasma generation in the gaseous phase. The realization of nanoparticle synthesis through plasma liquid immersion technique is generation of plasma discharges in an aqueous metal salt solution containing dissolved silver ions. Usually, in solution chemistry, metal ions are exposed to an energy source in the form of heat or UV-light exposure in the presence of a reducing agent in order to reduce metal ions into metal nanoparticles. In plasma synthesis of nanoparticles, highly energetic electrons are generated from plasma discharges to dissociate water molecules into radicals (O, H, OH) and ions (H_2O^+, O_2^-). These plasma-created reactive species participate thus in the reduction of metal ions into metal nanoparticles.

The goal of this study is to investigate synthesis of silver nanoparticle through a parametrical study in the use of a PLI synthesis technique.

The first part focuses on optimization of the PLI process for synthesis of small-sized and uniformly distributed silver nanoparticles. A parametric study has been performed to investigate the influence of chemical parameters on silver nanoparticle synthesis.
In the second part of this thesis synthesis of silver nanoparticles has been realized in order to study the influence of physical process parameters on silver nanoparticle synthesis.

This thesis is structured in the following procedure:

In the first chapter, a short introduction to the thesis is given in terms of objectives and the structure of thesis.

The second chapter is devoted to a literature review on the state of the art, pointing out the technological and scientific challenges as well as fundamental aspects on metal nanoparticle synthesis, non-thermal plasma generation, and plasma-liquid interaction and reaction pathways.

In the third chapter, description of commonly applied nanoparticle characterization methods has been included. Particle characterization techniques that provided further information about nanoparticles produced in this work are: Determination of particle nature and state of oxidation,

as well as particle purity performed by X-ray Diffraction (XRD), Electron Dispersive X-ray Spectroscopy (EDS), and X-ray Photon Spectroscopy (XPS). Characterization of as-synthesized nanoparticles was performed by UV-visible absorption spectroscopy and Dynamic Light Scattering (DLS). Later, particles were characterized by Scanning Electron Microscopy (SEM) and particles below 20nm were characterized by Transmission Electron Microscopy (TEM). In the continuation of chapter 3, a description of the laboratory-developed PLI system has been performed in the application of plasma pulses generated by MARX and BEHLKE pulse generator. In the following, a parametrical study on silver nanoparticle synthesis applying MARX and BEHLKE was performed.

The fourth chapter concerns the first parametrical study on silver nanoparticles synthesized in the use of the PLI process with plasma pulses generated by the MARX generator. This parametrical study is performed with focus on chemical parameters related to silver nanoparticle synthesis. Parameters of main interest are: Concentration of silver precursor (i.e. $AgNO_3$), concentration of stabilizing agent (i.e. PVP), and initial pH of precursor solution. The PLI process has been optimized to produce spherical, small-sized and uniformly distributed silver nanoparticles.

The fifth chapter concerns the second parametrical study performed by the PLI process with plasma pulses generated by BEHLKE generator. This parametrical study is performed with focus on physical parameters related to the PLI process. Parameters of main interest are: Pulse duration, applied voltage, and applied voltage over the inter-electrode distance for a constant ratio. By investigating these parameters, particle growth mechanism and nanoparticle morphology has been studied.

In the sixth chapter, a final conclusion of this work on the parametrical study on silver nanoparticle synthesis has been delivered.

Table of Contents

Chapter II - Bibliographic study and state of the art

2.1 Introduction to metallic nanomaterials

The definition of **nanomaterial** according to International Organization for Standardization (ISO) is clusters of atoms or molecules measured in the **nanoscale** size range, approximately between 1nm and 100nm *(ISO 2015a)*. In the lower limit (<1nm) of the nanoscale, atoms and individual molecules exist, and are not considered as nano-objects. In the upper limits, objects exceeding the nanoscale measured between 100nm and 1µm are classified as sub-micro-particles *(ISO 2015a)*. Nano-objects are in possession of at least one external dimension (this is to say, height, length, and depth), which are all measured *within* the nanoscale (<100nm). Under these conditions nano-objects are enabled to exist in different sizes and shapes.

2.1.1 Classification of nanomaterials

Fundamental shapes of nano-objects constitute of **nanoplate** (one external dimension), **nanofibre** (two external dimensions), and **nanoparticle** (three external dimensions) *(ISO 2015b)*. Classification of nanomaterials based on dimensioning was first developed by *(Gleiter 2000)*. Since the dimensioning of nanomaterials did not account for structures such as fullerenes, nanotubes, and nano-flowers, the dimensioning of nanomaterials was later extended to 0D, 1D, 2D, and 3D nanostructures by *(Pokropivny and Skorokhod 2007)*. Nanomaterials are classified based on their dimensionality, which contains following nanoparticle structures:

- **0D nanostructures** are quantum dots (uniformly arrayed particles), heterogeneous nanoparticles, core-shell *(Trinh et al. 2015)*, hollow spheres *(J.-M. Lee et al. 2007)*, and fullerenes.
- **1D nanostructures** are nano-wires, -rods, -tubes *(Eatemadi et al. 2014)*, -belts, and -ribbons.
- **2D nanostructures** are nano-plates, -sheets, -walls, and -disks. These nanostructures have only one dimension in the nanoscale.
- **3D nanostructures** are nano-balls, -coils, -cones, -pillar, and -flowers. Increased surface area in comparison to 0D, 1D, and 2D nanomaterials, due to highly porous particles *(Tiwari, Tiwari, and Kim 2012)*.

A selection of nanomaterials for each dimension is presented below in figure 1.

0D nanomaterials (three external dimensions in the nanoscale)

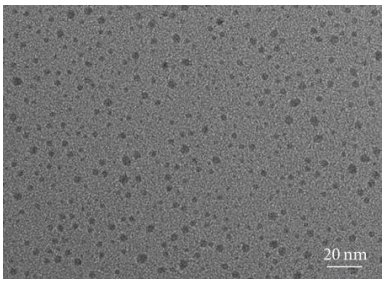

Quantum dots

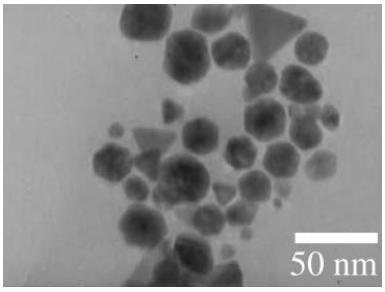

Nanoparticles

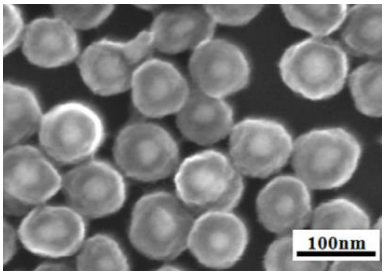

Core-shell

1D nanomaterials (two external dimensions in the nanoscale)

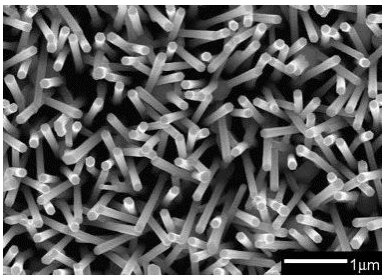

Nanorods

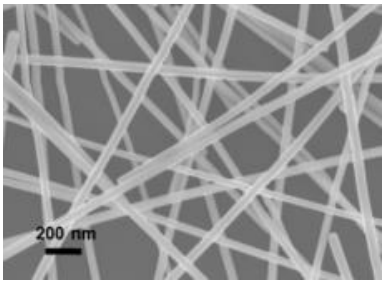

Nanofibre

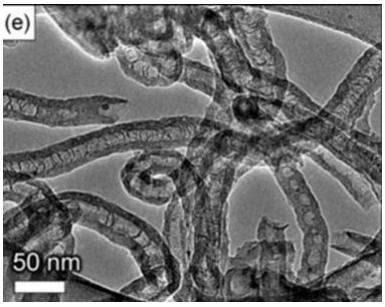

Nanotubes

2D nanomaterials (one external dimension in the nanoscale)

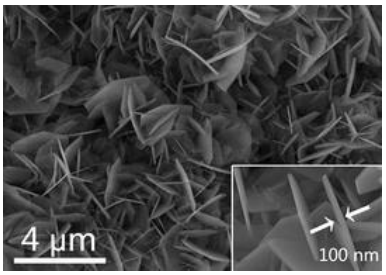

Nanoplates

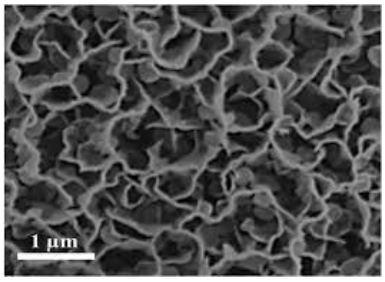

Nanowalls

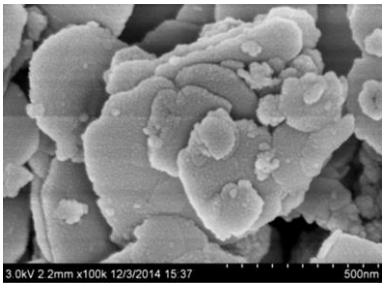

Nanosheets

3D nanomaterials

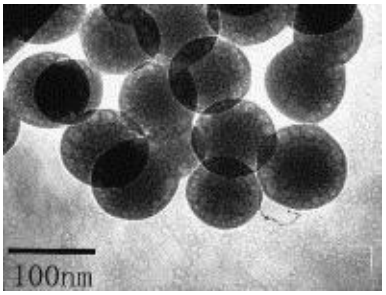

Nanoballs

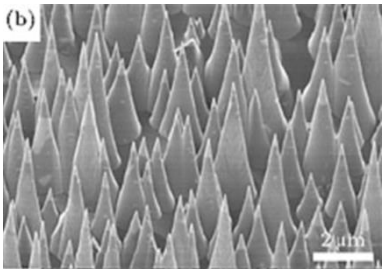

Nanocones

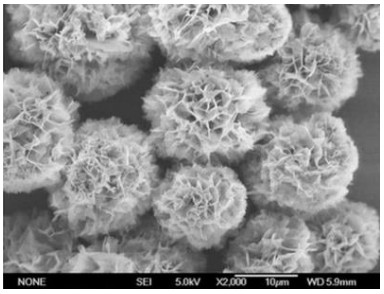

Nanoflowers

Figure 1: Nanomaterial classification based on dimensions. 0D: Quantum dots *(J.-Y. Wu et al. 2014)*, nanoparticles *(Hieda, Saito, and Takai 2008)*, core-shell *(Park, Im, and Park 2011)*. 1D : Nanorods (L. Zhu et al. 2008)**, nanofibre *(Langley et al. 2013)*, nanotubes *(Fang et al. 2014)*. 2D : Nanoplates *(Jia Liu et al. 2011)*, nanowalls *(Prasad et al. 2017)*, nanosheets *(Feng et al. 2015)*. 3D: Nanoballs *(Teng, Wang, and Zhu 2008)*, nanocones *(Z.-C. Wu et al. 2017)*, nanoflowers *(Z.-F. Wu et al. 2016)*.**

Properties of nanomaterials are size-dependent. An increment in **surface-to-volume ratio**, exposes atoms on the surface, leading to higher reactivity, and thus improvement in material properties *(Roduner 2006)*. This is also what makes nanomaterials unique as compared to their bulk counterparts. Improvements are mainly observed in properties regarding magnetic *(Mørup, Frandsen, and Hansen 2017)*, optical (K. L. Kelly et al. 2003), catalytic *(Cuenya 2010)*, and electrical properties *(Radoń et al. 2018)*.

In the following, optical properties of metallic nanoparticles will be discussed.

2.1.2 Optical properties in nanomaterials

In quantum mechanics, size-dependent properties of nanomaterials are explained by the **quantum confinement effect**. This effect is observed in what corresponds to quantum dots, quantum wires, and quantum wells, which is the intermediate of bulk semiconductor materials and single molecules or atoms. Electrons of quantum wells, quantum wires, and quantum dots are confined in one-, two, or three-dimensions, respectively *(Brazis 2017)*. An increase in electron energy increases the strength of electron confinement, and agrees to 1D > 2D > 3D, for electron confinement of quantum wells being the weakest *(Ashrafi 2011)*. Electron energy levels in quantum dots are discrete and not continuous as in bulk semiconductor materials. As it is shown on figure 2, a transition from continuous to discrete electron confinement increases the electron band gap, and restricts thus the movement of electrons. Therefore, as nano-crystal size decreases, the band gap energy increases, and emits thus a greater energy resulting from electron-hole recombination *(Ashrafi 2011)*.

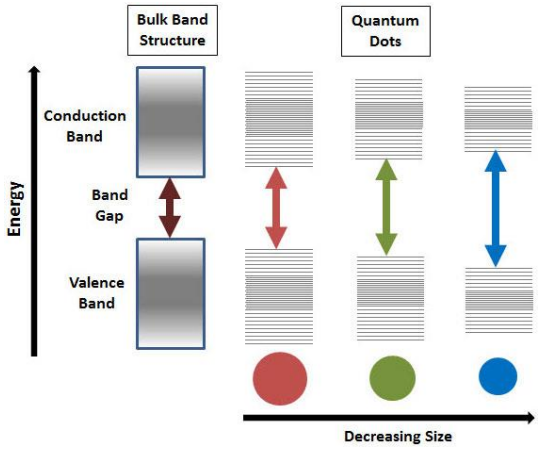

Figure 2: Quantum confinement effect. The transition from continuous energy levels in bulk semiconductor materials towards discrete energy levels in quantum dots by a decrease in particle size *(Sigma-Aldrich 2018)*.

Optical effect is also observed in metallic nanoparticles, and is known as the **Surface Plasmon Resonance** (SPR). This phenomenon occurs, when an external electric field (e.g. photons) is applied, thus giving rise to collective oscillations of free valence electrons. As electrons are charged elementary particles, vibrations from valence electrons generate an electric field. Hence, the resonance of electric field (e.g. electro-magnetic field) from the light source and valence electrons causes the so-called SPR on metallic nanoparticle surface (Satoshi Horikoshi and Serpone 2013). Irradiation of nanoparticles, which are smaller in size than the wavelength of the incident light beam deviates the electric field causing surface polarization of metallic nanoparticles. This is the so-called **L**ocalized **S**urface **P**lasmon **R**esonance (LSPR) effect, which is illustrated on figure 3.

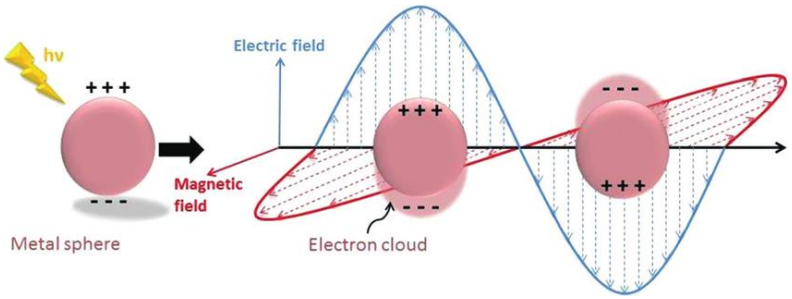

Figure 3: LSPR of metallic nanoparticles. Reproduced from *(Peiris, McMurtrie, and Zhu 2016).*

SPR depends on dielectric properties of the metal, the dispersing media, extent of particle agglomeration, and on particle size and shape *(Rivera, Ferri, and Marega 2012)*. SPR in metallic nanoparticles occur mainly in the ultraviolet (UV) region of the electromagnetic spectrum, while in few metals (i.e. gold (Au), silver (Ag), and copper (Cu)), the SPR shifts towards the visible region *(Singh 2016)*. In case of spherical gold nanoparticles SPR appears around 520-550nm, which corresponds to a red color at visible light. For spherical silver nanoparticles SPR appears at around 400nm, corresponding thus to a yellow color at visible light (Satoshi Horikoshi and Serpone 2013). Absorption spectra of gold- and silver colloidal solutions are presented in figure 4, which shows the SPR peak of small-sized and spherical nanoparticles.

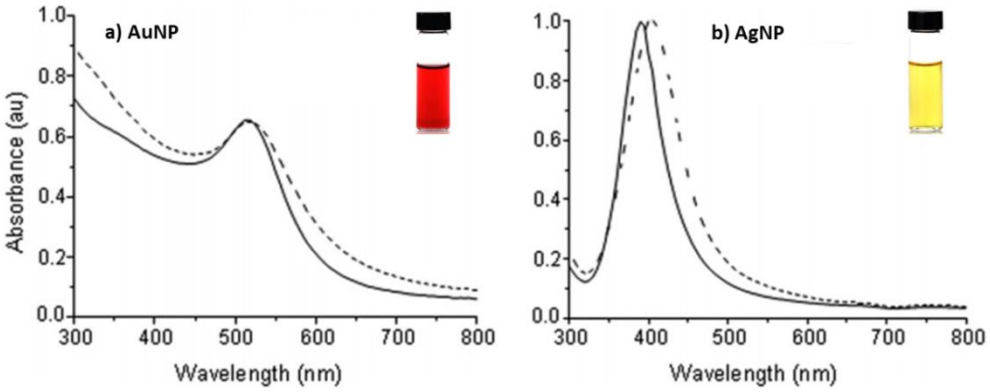

Figure 4: Absorption spectra of small-sized and spherical metallic nanoparticles of a) AuNP and b) AgNP with SPR around 520nm and 400nm, respectively. Modified and reproduced from *(Brown et al. 2012)*. Insets images show representative colloidal solution of AuNP and AgNP at the given SPR wavelengths. Modified and reproduced from *(nanoComposix 2018)*.

2.1.3 Application of silver nanoparticles

An advantage of nanoscience and -technology is the possibility to engineer nanoparticles by fine-tuning of their surface parameters (e.g. size, shape, composition, and structure) through application of various synthesis routes. Since nanoparticle properties are determined by surface parameters of nanoparticles, it is through fine-tuning of these parameters possible to modify nanoparticle properties *(Xia et al. 2009)*. Due to the unique and improved properties of nanoparticles, it is therefore of great interest to incorporate nanoparticles in different application fields. Silver nanoparticles are in particular promising for application in diagnostics *(Cordeiro et al. 2016)*, sensing *(Doria et al. 2012)*, energy storage *(C. Liu et al. 2010)*, catalysis *(Haruta 2004)*, medicine *(Odularu 2018)*, daily life products *(Pulit-Prociak and Banach 2016)*, and in many other fields.

Some examples of silver nanoparticle application in research and industrial applications are mentioned in the following:

Application of silver nanoparticles as an antibacterial agent is common in many fields. The agent is most efficient, when the specific surface area of silver nanoparticles is increased *(Helmlinger et al. 2016)*. Improved antimicrobial properties of silver nanoparticles was also reported by *(Agnihotri, Mukherji, and Mukherji 2014)*, when the size of nanoparticle was reduced to 5nm. *(Kujda et al. 2015)* demonstrated the antimicrobial properties of silver

nanoparticles by its interaction with bacteria. They demonstrated that silver nanoparticles attached to bacteria culture and caused disintegration of the cell membrane. The antimicrobial properties of silver nanoparticles have also been proved to be effective by combining silver nanoparticles with other materials. As an example, *(Yamada et al. 2017)* demonstrated that application of zirconia coated with silver nanoparticles is possible in dentistry as antimicrobial agent.

Silver nanoparticles are further applied in water disinfection, due to its toxicity towards microorganisms (e.g. viruses, bacteria, and fungi) that may exist in water and wastewater *(Lu et al. 2016)*. Several techniques in water disinfection were proposed. One of them includes the technique reported by Kujda *et al.*, in which microorganism disintegrates through direct contact with silver nanoparticles. There is a tendency for silver nanoparticles to aggregate in aqueous media due to limited stability, and this is a problem in application, since aggregation of silver nanoparticles will reduce its reactivity and hence efficiency as an antimicrobial agent *(Shrivastava et al. 2007)*, *(Kvítek et al. 2008)*. Therefore, other techniques have been proposed. Instead of direct application of silver nanoparticles in the aqueous medium, nanoparticles are attached to filter materials (e.g. cellulose fibers) via in-situ reduction of silver ions *(Dankovich and Gray 2011)*.

Quantum dots are applied in electronics as in photovoltaic devices, sensors, and light-emitting diodes (LED) *(Kang et al. 2017)*. Due to blinking of their luminescence and their toxicity, their application has been restricted in health science *(H. Zhang, Yee, and Wang 2008)*. Silver nanoparticles has been presented as a better alternative in overcoming these issues, since silver nanoparticles has lower toxicity, good reproducibility, and are stable in solutions. *(Maretti et al. 2009)* prepared highly-stable fluorescent silver nano-clusters, which are smaller than 3nm. Silver nano-clusters are applicable in bio-imaging *(Kundu et al. 2017)*, chemical sensing *(Xiong et al. 2016)*, and fluorescence labeling *(Jian Zhang et al. 2008)*.

Another common application field of silver nanoparticles is its use as supported catalyst in various chemical processes, due to increased efficiency and selectivity. In catalysis, application of silver nanoparticles is also preferred over other noble elements such as gold, platinum, and palladium nanoparticles, due to being a low-cost element *(Dong et al. 2015)*.

Chemical processes include among others the catalytic decomposition of H_2O_2 in the presence of colloidal silver *(Weiss 1935)*. In another study performed by *(Chimentao et al. 2007)* silver nanoparticles were prepared by different techniques and deposited onto α-Al_2O_3 in order to study the epoxidation of styrene to styrene oxide in the presence of silver nanoparticles. Silver nanowires were obtained via polyol reduction technique, and silver polyhedral nanoparticles obtained via the wetness impregnation reduction technique. With this study, Chimentao *et al*. showed that catalysis preparation and reaction conditions would have an influence on catalytic activity and selectivity on resulting products. Furthermore, it was in this study determined that morphology of silver nanoparticles does have an influence on selective oxidation of oleofins. In this case silver nanowires showed improved catalytic activity over polyhedral nanoparticles.

(Jiang, Liu, and Sun 2005) did also introduce the catalytic application of silver nanoparticle in reduction of dyes such as methylene blue. In this study, the silver nano-catalyst was immobilized onto SiO_2 support in order to avoid agglomeration of silver nanoparticles during the catalytic reduction process of dyes. They determined that the catalytic activity of silver nanoparticles is influenced by the presence of stabilizing agents and addition of electrolytes.

Silver nanoparticles have a large variation of applications with the above-mentioned being some of them. In the following section, different nanoparticle synthesis methods, based on conventional chemical and physical methods, will be presented.

2.2 Synthesis methods

Metallic nanoparticles are either prepared by bottom-up or top-down approaches, as illustrated on figure 5. In **top-down** approaches, bulk materials are reduced down to nano-scale particles by destructive methods, such as mechanical milling *(Koch 2003)*, nano-lithography *(Venugopal and Kim 2013)*, laser ablation *(M. Kim et al. 2017)*, sputtering *(Terashima et al. 2013)*, and thermal decomposition *(Odularu 2018)*. The bulk material is mechanically transformed into metal powder, before achieving the final product. Most of these techniques (e.g. laser ablation) are expensive, and energy-intensive in nanoparticle production, but result in small-sized nanoparticles. Mechanical techniques (e.g. milling) are not an option if small-sized, pure and uniform nanoparticles containing no defects are of importance.

In **bottom-up** approaches, atoms or molecules condenses in gas or liquid phase, and coalesces into nanoparticles by chemical or physical forces. Examples of synthesis techniques in the bottom-up approach are chemical vapor deposition (CVD) *(Manawi et al. 2018)* and chemical reduction technique *(Jun Liu et al. 2013)*. This approach is initiated by atomic-scaled components, which nucleates into nano-clusters, followed by the growth and production of nanoparticles.

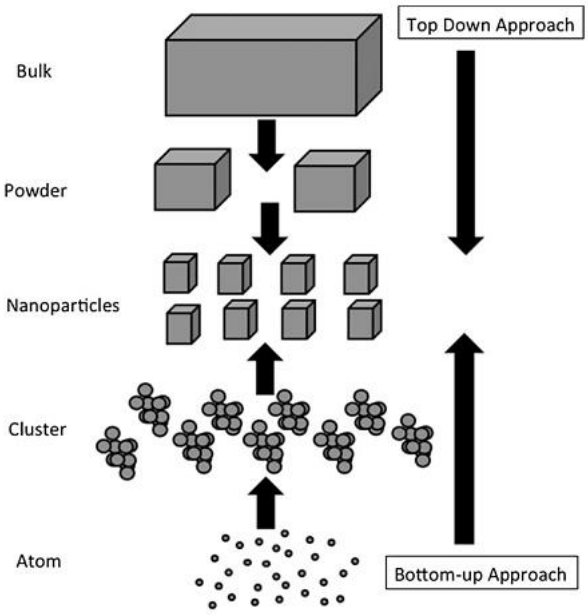

Figure 5: Top-down and bottom-up approaches in nanoparticle production. Reproduced from *(Su and Chang 2018)*.

Advantages in bottom-up approaches for nanoparticle production are plenty. In bottom-up approach it is possible to control particle properties and fine-tune surface parameters of nanoparticles (e.g. size, shape, structure, and composition). This is possible since, metallic component exists in the dispersing media initially in the atomic scale range. Nanoparticle synthesis in liquids is energy efficient, when the synthesis is carried out under atmospheric pressure (P_{atm}), and when the reaction temperature is close to ambient temperature (T_{amb}). In comparison to vapor phase, working in liquid phase enables size and shape selective recovery of nanoparticles by taking into use advanced techniques such as ultra-centrifugation or filtration *(Meireles et al. 2010)*, *(Robertson et al. 2016)*. Challenges in liquid phase of nanoparticle synthesis include up-scaling of the process for commercialization, since changes of process

parameters and an increase of batch volume results in lack of nanoparticle reproducibility *(Tsuzuki 2009)*, *(Paliwal, Babu, and Palakurthi 2014)*. Disadvantages in chemical reduction techniques performed in liquid phase, is the use of chemical reactants that are in most cases toxic and hazardous to human health and environment *(Dahl, Maddux, and Hutchison 2007)*. And the resulting product may not be as pure as nanoparticles produced from the gas phase, due to contamination from chemical reactants and by-products.

Nanoparticle synthesis techniques applying bottom-up approaches are in possession of advantages and qualities over synthesis techniques applying the top-down approach. These techniques are especially promising in optimization of nanoparticle synthesis towards a time-saving, cost-effective, and environmental-friendly process. **Based on these point-of-views, it is decided to continue this work in the direction towards nanoparticles synthesis techniques applying the bottom-up approach in liquid phases.**

In the following, examples of chemical and physical conventional nanoparticle synthesis techniques applying the bottom-up approach will be presented.

2.2.1 Chemical methods

Chemical reduction of metal salts

In chemical nanoparticles synthesis processes three main components are generally employed, these include metal precursors (usually metal salts as source of metal ions), reducing agents (e.g. $NaBH_4$), and stabilizing or capping agents. In order to control nanoparticle surface parameters, presence of stabilizing or capping agents may be required in some cases. Chemical reduction techniques involve two stages, nucleation and subsequent growth, which are important in controlling the size and shape of nanoparticles. Nucleation and subsequent growth stages are usually controlled by adjusting several process parameters such as reaction temperature, pH, concentration of precursors, reducing agents, and stabilizing agents *(Saleh and Gupta 2016)*. The most well-known chemical reduction synthesis technique is the Turkevich method developed by *(Turkevich, Stevenson, and Hillier 1951)*. In this method, synthesis of gold nanoparticles proceeds in the reduction of $AuCl_4^-$ by sodium citrate in aqueous solution under heating for an accelerated reaction rate. This technique has later been employed on the synthesis of silver nanoparticles by *(P. C. Lee and Meisel 1982)*. Citrate served both as reducing and stabilizing

agent in the process and had also a significant role in the growth of nanoparticles. In another chemical reduction method gold nanoparticles are synthesized in an organic solution, and $AuCl_4^-$ is reduced by $NaBH_4$. This method is known as the Brust-Schiffrin method and was developed by *(Brust et al. 1994)*.

Electrochemical nanoparticle synthesis

Electrochemistry is applied in processes such as treatment of water and electroplating of metal surfaces. Another very common process in which electrochemistry is applied is the production of nanoparticles. In this technique, the synthesis of nanoparticles occurs mainly due to electrochemical reactions. Transport of charges in such processes is provided by applying low voltage electrical discharges to a pair of electrodes (via electrons), which are immersed in an electrolyte solution (via ions). The electrolyte solution serves to enhance conduction of the electric current during nanoparticle synthesis. Electrochemical reactions that occur on the interface between the electrode surface and the electrolyte include red-ox reactions. Due to oxidation of the counter electrode (known as the anode), dissolution of the anode yields in the generation of metal ions *(Bagotsky 2005)*. In this case metal ions that exist in the electrolyte solution are source to nanoparticle synthesis. Metal ions become reduced on the surface of the working electrode (known as the cathode) into metal atoms, and grow into clusters. This corresponds to the electrochemical process performed by *(Yu et al. 1997)*. In this study gold nano-rods were prepared in the application of 3mA current to the electrodes during 30min. The nanoparticle synthesis was prepared under ultra-sonication at elevated temperatures at around 40°C. In another study *(Yang et al. 2003)* prepared copper nano-rods in the application of current densities between 0.14-0.3mA·cm^{-2} to the electrolytic cell during 30min. It occurs also that the electrochemical synthesis of nanoparticles is prepared, in which metal ions already exist in the electrolyte as dissolved metal salts, and are reduced into metal atoms using two inert electrodes *(J.-J. Zhu et al. 2001)*. In this case silver nano-rods were prepared in the application of 10mA to the electrodes during 25min. The nanoparticle synthesis was like-wise prepared under ultra-sonication at 20°C. The frequently occurring disadvantages in electrochemical synthesis of nanoparticles are that the process is time consuming, and that the resulting product is oxidized, and can result in agglomerated particles. Furthermore, the use of hazardous chemicals is involved in the electrochemical synthesis of nanoparticles.

2.2.2 Physical methods

Chemical vapor deposition (CVD)

CVD is the most applied thin-film deposition technique for nanomaterial synthesis. It is also a preferred technique for mass production of CNT *(Andrews et al. 1999)*. It is possible to produce CNT by different variations of the CVD technique. Some of these CVD variations are hot-wire CVD *(Lehman et al. 2006)*, hot-filament CVD *(Dikonimos Makris et al. 2004)*, and microwave plasma-enhanced CVD *(Y. C. Choi et al. 2000)*. CNT are produced in a closed reaction chamber in the presence of a precursor and a catalyst (preferred catalyst for CNT is iron) with a process time between minutes up to hours. Furthermore, the technique operates at process temperatures between 500-1000°C under vacuum. Advantages of CNT production with CVD technique is that it is possible to obtain the desired structure by controlling deposition parameters as in alignment, length, wall number and diameter *(Manawi et al. 2018)*.

Pulsed laser ablation

In laser ablation techniques a high energy laser source is applied for etching of surface atoms by breaking of chemical bonds, when focusing on a solid surface target. As a result, atoms vaporize into the surrounding media (gas or liquid phase). The pulsed laser ablation technique is schematically illustrated on figure 6, which shows the nanoparticle formation mechanism. Due to collision between reactive species and surrounding molecules, a laser-induced plasma plume is generated on the target surface *(M. Kim et al. 2017)*. Production of nanoparticles is controlled by process parameters such as laser properties (e.g. laser power and laser source), target material, pressure, and the surrounding media. These process parameters have an impact on nanoparticle surface parameters. As an example, laser-ablation in low-pressure gas phase is preferred for generation of small-sized nanoparticles, since a larger plume is obtained under these conditions. Laser ablation in gas phase does results in production of nanoparticles of high-purity, since particle purity depends in this case only on purity of metal source and surrounding media. Drawbacks in laser ablation techniques are difficulties in controlling particle size distribution and particle agglomeration *(M. Kim et al. 2017)*.

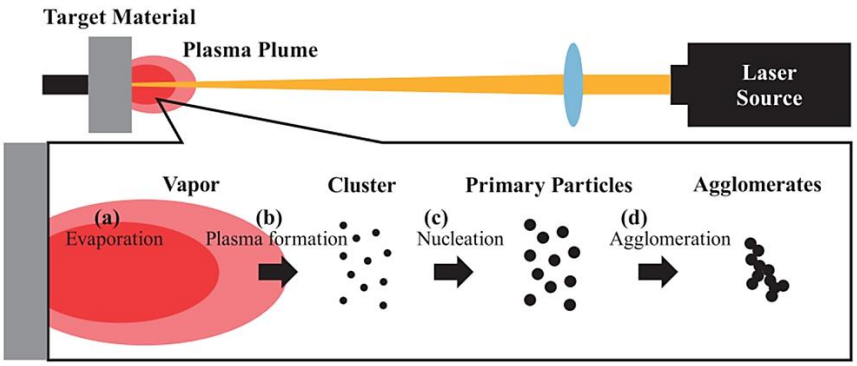

Figure 6: Nanoparticle production in laser ablation technique, and a schematic presentation of nucleation and growth of nanoparticle formation. Reproduced from *(M. Kim et al. 2017).*

Laser ablation permits generation of different types of nanoparticles including quantum dots *(Horoz et al. 2012)*, oxide nanoparticles *(P. Liu et al. 2011)*, and CNT *(Chrzanowska et al. 2015)*. Gold nanostructures was also produced on a substrate under P_{atm} *(Nikov et al. 2017)*. In their study, it was reported that morphology of nanostructures strongly depended on the deposition geometry (i.e. deposition angle between substrate and plasma plume).

Conventional nanoparticle synthesis techniques applying the bottom-up approach was presented in the production of metallic nanoparticles in a liquid phase. In the following, common synthesis techniques and methods applied for the production of silver nanoparticles will be covered.

2.2.3 Silver nanoparticle synthesis

The demand of silver nanoparticles has increased, due to its applicability in multiple fields. Over the years, various synthesis techniques have been developed and techniques have been optimized in order to prepare small-sized and uniform silver nanoparticles.

Silver nanoparticles were prepared by *(P. C. Lee and Meisel 1982)* using the chemical reduction technique. In this synthesis silver ions are reduced by sodium citrate. Further investigation on the role of citrate revealed that besides acting as a reducing agent, citrate anions also has a stabilizing effect on silver nanoparticles. At this point the LaMer nucleation and growth mechanism was used to describe the nucleation and growth of nanoparticles. However, studies of *(Van Hyning and Zukoski 1998)* revealed that the LaMer nucleation and growth

mechanism does not relate to their observations. Therefore, Van Hyning *et al*. studied the nucleation and growth mechanism, which is applicable to their results. They prepared silver nanoparticles via the chemical reduction technique in which silver perchlorate ions are reduced by sodium borohydride. In their study it was determined that an increase of the sodium borohydride concentration would result in the instability of silver nanoparticles.

In the study performed by *(Zielińska et al. 2009)* the stability of silver nanoparticles were of main focus. Silver nanoparticles were prepared using the chemical reduction method. Zielińska *et al*. showed that the type of precursor has an effect on particle stability. According to their research, stable and spherical silver nanoparticles were synthesized using silver citrate as the precursor in the presence of $NaBH_4$, as both reducing agent and stabilizing agent. These results were compared to silver nanoparticles prepared in the use of silver nitrate or silver acetate as the precursor. In this case silver nanoparticles were unstable and precipitated shortly after the synthesis. Alternatively, *(Malina et al. 2012)* presented in their study that it is also possible to synthesize stable and uniform spherical silver nanoparticles via the chemical reduction technique using $AgNO_3$ as precursor and $NaBH_4$ as reducing agent and polymer as the stabilizing agent.

In a study performed by *(Hsu and Wu 2011)* crystalline silver nanoparticles between 3-15nm were prepared in the reduction of silver ions ($AgNO_3$) by formaldehyde using three stabilizing agents. Reduction by formaldehyde is rather slow and requires thus catalysts or a reaction promoter in order to speed up the reaction process. Furthermore, synthesis at high pH favors the reducing efficiency in the presence of poly-(N-vinyl-2-pyrrolidone) (PVP) yielding average particle size of 15nm spherical silver nanoparticles. Thiosalicylic acid as the stabilizing agent in this case would yield 8nm spherical silver nanoparticles. Finally, triethylamine (TEA) would yield the smallest particles of 3nm spherical silver nanoparticles. It has been observed that without addition of stabilizing agent, particles would agglomerate, which were prevented through Ag-N bonding by TEA. Concentration of the stabilizing agent has a determining role, as an increased TEA concentration would lead to an increase in particle agglomeration.

(Rodríguez-Sánchez, Blanco, and López-Quintela 2000) produced silver nanoparticles in the application of 20V to silver electrodes. Another observation is that the complete coverage of the cathode limits nanoparticle formation and favors thus the particle deposition process. To avoid

cathode deposition and limiting nanoparticle production *(Khaydarov et al. 2009)* used two metallic silver plates as an electrode pair for the synthesis of colloidal silver nanoparticles.

In another study performed by *(Dikovska et al. 2013)* the effect of laser wavelength on particle morphology was investigated. They showed that deposition of metallic silver nanoparticles on silica substrate by laser ablation under vacuum resulted in the decrease of particle size as the laser wavelength was decreased.

Conventional synthesis techniques in metal nanoparticle synthesis have been covered. Furthermore, the disadvantages in these techniques have been discussed, which include the following: Use of chemicals, which are hazardous towards the environment. Some of them are time-consuming, and are energy-intensive. Difficulties in synthesis of size- and shape controlled nanoparticle have been observed as well. For this reason an increased interest in ”green” nanoparticle synthesis techniques are developed.
Metal nanoparticle synthesis techniques that is promising and that may be a solution to the above-mentioned problematics is the combination of physical and chemical techniques, namely plasma-liquid synthesis of metal nanoparticles

2.3 Nanoparticle nucleation and growth mechanisms

Formation of nanoparticles is explained in terms of nucleation and growth mechanisms under different nanoparticle synthesis processes. The first theory in nucleation and growth mechanism was formulated by *(LaMer and Dinegar 1950)*, and other theories were proposed eventually.

2.3.1 Nucleation

The classical nanoparticle growth theory was transposed to nanoparticle synthesis by *(LaMer and Dinegar 1950)*, which is based on the classical nucleation theory. They introduce the burst-nucleation concept, where nuclei are formed simultaneously, and will grow afterwards without further nucleation, due to **homogeneous nucleation**. Nanoparticle synthesis processes (e.g. seed mediated growth) are usually resulting in synthesis of monodisperse nanoparticles. This is valid, when nucleation and growth mechanism are in agreement with homogeneous nucleation, and thus the classical LaMer theorem.

LaMer mechanism of nanoparticle nucleation and growth is divided in three main steps, as shown in figure 7, where monomer concentration is presented as a function of time. In the first step of the LaMer diagram "generation of atoms" a rapid increase in concentration of free monomers occurs (reduction: $M^+ + e^- \rightarrow M^0$). In the second step "self-nucleation", the monomers undergo burst-nucleation, and reduction in concentration of free monomers in the solution occurs (dimerization: $M^0 + M^0 \rightarrow M_2$). Towards the end of stage two, concentration of monomers are below the minimum nucleation concentration (C_{min}), and almost no nucleation occurs. In the last step "growth", nanoparticle clusters grows upon collision with neighboring clusters, which results in aggregation and coalescence.

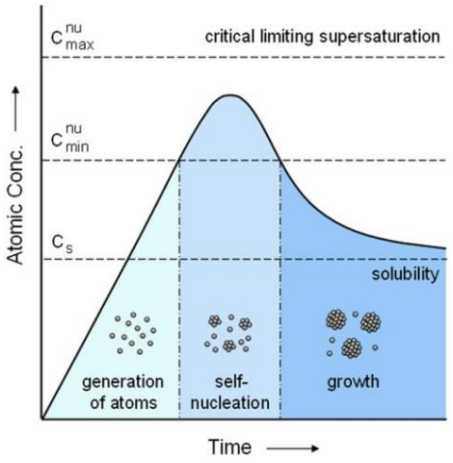

Figure 7: The classical LaMer model on nucleation and growth mechanism of nanoparticle synthesis. Reproduced from *(Xia et al. 2009)*.

It was up to debate, whether the LaMer model (based on the classical nucleation theory) is able to describe particle growth and predict size of nanoparticles. This was determined based on studies performed by *(Van Hyning and Zukoski 1998)*, which showed the inconsistency in results, when compared to the LaMer model. For this reason, alternative nucleation and growth models for describing nanoparticle nucleation and growth mechanism was proposed by *(J. Polte et al. 2012)*. This model was adapted to the work of Van Hyning and Zukosi, which is based on the reduction of silver perchlorate ($AgClO_4$) with $NaBH_4$. Nanoparticle nucleation and growth mechanisms are usually confirmed by time-resolved in-situ experimental techniques such as small-angle X-ray scattering (SAXS) *(J. Polte et al. 2012)*, *(Wuithschick et al. 2013)* and in-situ

UV-vis spectroscopy measurements combined with ex-situ transmission electron microscopy (TEM) characterization of nanoparticles.

The nucleation and growth mechanism that describes silver nanoparticle synthesis by reduction with $NaBH_4$ consists of four steps, as illustrated on figure 8.

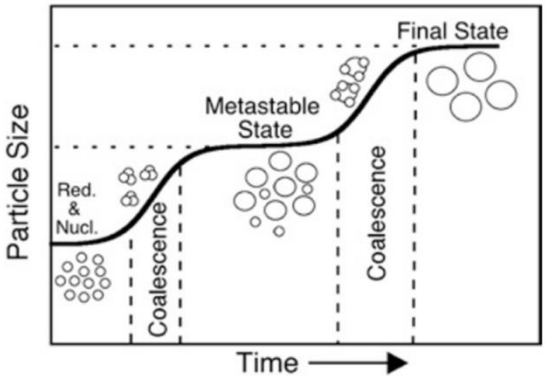

Figure 8: A four-step nucleation and growth model on nanoparticle synthesis proposed by *(J. Polte et al. 2012).* Reproduced from *(Pacioni et al. 2015).*

In the first step of the nucleation and growth model, rapid reduction of silver ions into silver atoms occurs during the first 200ms of the synthesis. In the second step, reduced metal atoms form dimers, trimers etc. These clusters coalesce until the particles have certain stability. These two steps occurs within the first 5s into nanoparticle synthesis, which results in a particle size of around 2-3nm. This step is followed by a metastable state (third step), which is also described as an intermediate phase of stability, in which particles larger than 1nm remain at a constant size for about 5-10min. In the final step, the stability of nanoparticles decreases, which induces a further growth due to coalescence within 30-60s. This produces stable nanoparticles of around 5-8nm *(J. Polte et al. 2012).*

2.3.2 Growth

Several theories for describing growth processes of nanoparticles from their nuclei state were later developed. *(Reiss 1951)* developed a growth model known as "growth by diffusion", which was developed with focus on the LaMer nucleation and growth model. In this case, the growth rate of spherical particles depends on the monomer flux supplied to the particles. Reiss deduced that if diffusional growth is only depending on monomer flux, small nanoparticles will grow faster in the presence of large particles to result a narrow size distribution. Since this growth

mechanism does not consider other growth effects such as aggregation, coalescence, or dissolution (Ostwald ripening), Reiss's model was later extended by *(Sugimoto 1987)*.

The **Ostwald ripening** mechanism of growth is caused by the change in solubility of nanoparticles dependent on their size which is described by the Gibbs-Thomson relation. Due to the high solubility and the surface energy of smaller particles within solution, these re-dissolve and in turn allow larger particles to grow even more, as shown in figure 9a *(Thanh, Maclean, and Mahiddine 2014)*. However, the Ostwald ripening is, according to *(Jörg Polte 2015)* unlikely to occur, due to metallic nanoparticles being thermodynamically stable at the common reaction temperature ranges (<200°C).

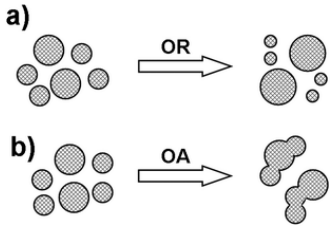

Figure 9: Nanoparticle growth mechanisms. a) Ostwald ripening, and b) Oriented attachment. Reproduced from *(Jing Zhang, Huang, and Lin 2010)*.

Therefore, the coalescence growth mechanism of nanoparticles is more likely to occur instead as a result of insufficient nanoparticle surface stabilization. These growth mechanisms are similar, and both result in decreased particle concentration with increasing particle size.

Coalescence and **oriented attachment** are two other very similar examples of growth mechanisms that nanoparticles are able to undergo during the nanoparticle growth phase. The main difference lies on the attachment between particles at the grain boundaries. In coalescence there is no particular preference for the attachment, thus the lattice planes are randomly oriented. On the other hand, in oriented attachment there is a common crystallographic alignment, which allows for continuous crystallographic planes *(Thanh, Maclean, and Mahiddine 2014)*. The two former growth mechanisms are illustrated without showing details in figure 9b.

2.3.3 Stabilization of metallic nanoparticles

Stabilization of metallic nanoparticles is necessary in controlling their size and shape during the growth phase. Without colloidal stabilization of clusters, unstable colloidal particles would grow continuously, thus forming aggregates, and precipitation of metallic particles would occur in the dispersing media *(Cosgrove 2010)*. To some extent, it is possible to reverse the interaction of weakly bonded particles (agglomerations) in the application of external forces such as stirring or mixing. Agglomerates are a group of particles, which are influenced by weak forces (e.g. Van der Waals forces). However, this is not the case, if attractive forces holding particles together are stronger than applied external forces (e.g. covalent bonds). In this case, particles are irreversibly aggregated, which is also known as particle coagulation. To obtain a system of well dispersed particles sufficiently strong repulsive forces, that are at least stronger than attractive forces, are required. Stabilization mechanisms that provide colloidal stability include electrostatic and steric stabilization. Example of a stable and unstable colloidal solution is illustrated on figure 10.

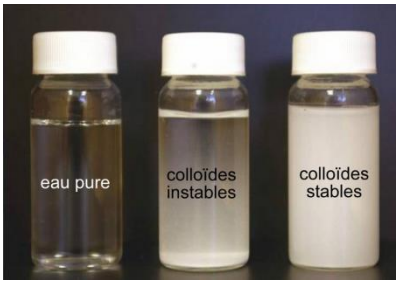

Figure 10: Difference between stable and unstable colloidal solution. Reproduced from *(Medix 2016).*

A theory in **electrostatic stabilization** of colloidal solutions was developed by *(Verwey 1947),* which is also known as the DLVO theory. Nanoparticles are electrostatically stabilized, when Van der Waals attraction forces between two negatively charged particles are counterbalanced by Coulomb repulsive forces, as shown in figure 11. It states that the total interaction energy of particles (W_{total}) is the sum of interaction energy of attractive Van der Waals forces (W_A) and interaction energy of repulsive Coulomb forces (W_R), as expressed in **equation 1**:

$$W_{total}(D) = W_A(D) + W_R(D) \qquad \textbf{Equation 1}$$

In terms of spherical particle stabilization, the interaction energy of particles exposed to Van der Waals attractive forces are expressed as in **equation 2**:

$$W_A(D) = -\frac{Ar}{12D}$$ **Equation 2**

Where, **A**: Hamaker constant; **r**: Particle radius; and **D**: Distance between two particle surfaces

The interaction energy of particles exposed to Coulomb repulsive forces is expressed as in equation 3:

$$W_R(D) = 2\pi\varepsilon\varepsilon_0 r\zeta^2 e^{-\kappa D}$$ **Equation 3**

Where, **ε**: dielectric constant of the solvent; **ε_0** : vacuum permittivity; **ζ** : zeta potential; **κ** : thickness of electrical double layer (EDL).

The electrostatic stability of nanoparticles is affected by parameters such as the ionic strength, nanoparticle surface potential, and particle size. The ion concentration is directly proportional to **κ**, and thus to the exponential decrease in the surface potential. This means that the higher the ion concentration, the smaller is the EDL *(Jörg Polte 2015)*.

Electrostatically stabilized nanoparticles are described to have at least one electrical double layer due to surface charges. The resulting Coulomb repulsion forces between particles decay exponentially with the particle-particle interaction distance. Hence, if the electrostatic repulsion is sufficiently high, it prevents the particles from coagulation. When particles are farther than approx. 10nm (corresponding to thickness of EDL) no overlap of EDL occurs, and electrostatic repulsion between particles is zero. However, an overlap in EDL leads towards development in repulsive forces between particles *(G. Cao 2004)*.

As a simple and economic stabilizing method, the disadvantage of stabilizing colloidal solution electrostatically is the stabilization mechanism being sensitive towards ionic strength of the liquid media *(Shi 2002)*.

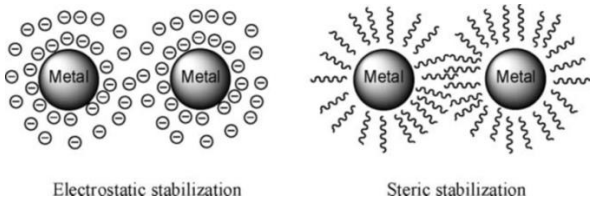

Figure 11: Electrostatic- and steric stabilization mechanisms of metallic nanoparticles. Reproduced from *(Gual et al. 2010)*.

Steric stabilization of nanoparticles is provided by adsorption of long-chained macro-molecular structures, such as polymers or surfactants, onto particle surface, as shown on figure

11. This protective layer of long-chained molecules creates a repulsive force, which counterbalances Van der Waals forces preventing thus nanoparticle aggregation. Steric stability does not depend on the size of nanoparticles, since particle stabilization depends on parameters such as concentration of stabilizing agent, process temperature, chain length and solubility of the stabilizing agent *(Shi 2002)*. The steric stabilization of nanoparticles is explained by adding a term to the DLVO theory, which describes the repulsive forces, due to the repulsive interactive energy (W_{steric}), as expressed in equation 4:

$$W_{total}(D) = W_A(D) + W_R(D) + W_{steric} \qquad \textbf{Equation 4}$$

In steric stabilization of metallic nanoparticles, the surface of particles is modified, when interacting with compounds, such as polymers *(Surudzic et al. 2013)*, complex ligands *(H. Liu et al. 2012)*, or surfactants *(Kora, Manjusha, and Arunachalam 2009)*. Stabilizing agents interacts with metal nanoparticles by surrounding the particle surface, which limits the surface accessibility of particles. This reduces thus the reactivity of metal nanoparticles and modifies their properties *(Jiang, Liu, and Sun 2005).*

In a study performed by *(Surudzic et al. 2013)*, it was shown that the concentration of surfactants has an impact on the concentration of nanoparticles. Thus, increasing capping agent (i.e. PVA) concentration would accordingly increase nanoparticle concentration, due to the stabilizing effect of PVA.

2.3.4 Size- and shape controlled synthesis of metal nanoparticles

Surface characteristics or morphology (i.e. size, shape, composition, and structure) of metal nanoparticles are controlled during nanoparticle synthesis in the liquid phase. Nanoparticle morphology is usually controlled, since nanoparticle properties are determined by surface characteristics of metal nanoparticles. In order to tailor the morphology of metal nanoparticles, several nanoparticle synthesis techniques have been developed.

Nanoparticle synthesis control initiates once clusters have grown past a critical size, and exist as seeds. Seeds may exist as single crystals (c.f. figure 12a) or single- or multiple-twinned crystal structure (c.f. figure 12b). It is even possible that these co-exist in a synthesis.

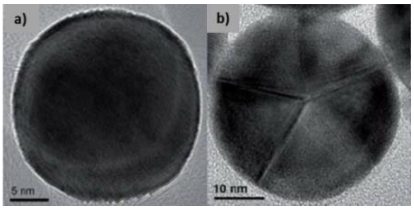

Figure 12: Nanocrystals as a) Single crystal or b) multiple-twinned crystal. Recreated and reproduced from *(Q. Zhang et al. 2010)*.

Seeds of single-crystal structure can develop into octahedron, cuboctahedron, cube, or octagonal rod, while seeds of multiple-twinned crystal structure can develop into decahedron, icosahedron, or five-fold twinned rod *(K. W. Choi et al. 2014)*. Shape control of nanoparticles occurs by controlling the distribution of these seeds via kinetic- and thermodynamic depending factors. Under **thermodynamic synthesis control**, formation of single-crystal seeds is developed in the attempt to minimize the total surface free energy of the system. In terms of a FCC structured crystal, the surface energies of the crystallographic facets are estimated as $\gamma_{\{111\}} < \gamma_{\{100\}} < \gamma_{\{110\}}$. In shape-controlled growth the nanocrystals grows in the presence of both {111} and {100} facets, or in the presence of {111} or {100} in order to minimize the total surface energy, and other facets of higher energy disappears *(K. W. Choi et al. 2014)*. Under **kinetic synthesis control**, formation of multiple twinned seeds is developed when keeping the reduction rate of metal ions slow. Thus, the population of seeds may be controlled, and seeds take form into kinetically controlled shapes. This is achieved by slowing the reduction rate of the metal precursor in order to prevent nuclei growing auto-catalytically into polyhedral structures *(K. W. Choi et al. 2014)*. Crystal structures, which are in thermodynamic equilibrium and shape of structures in the decrease in thermodynamic equilibrium, are shown in figure 13.

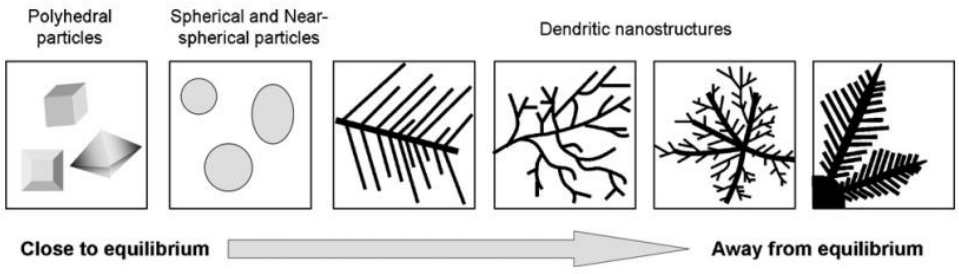

Figure 13: The distance of nanocrystals away from thermodynamic equilibrium. Reproduced from *(Tang et al. 2009)*.

Oxidative etching is another method to control crystal growth, in which zero-valent metal atoms are oxidized back into metal ions. Presence of a ligand in combination with O_2 in the solution results in a strong etchant to seeds. The oxidative etching is susceptible to occur in multiple-twinned crystal seeds rather than single-crystal seeds, due to the fact the defect zones having a higher energy. Therefore, single-crystal seeds are more resistant towards oxidative etching. *(K. W. Choi et al. 2014)*. As a result of shape- and size control of metal nanoparticles, properties of metal nanoparticles are modified. In terms of optical properties, modification in shape and size affects the SPR of metal nanoparticles. The influence of shape control of metal nanoparticles is observed on extinction, absorbance, and scattering spectra of silver nanoparticles as presented on figure 14.

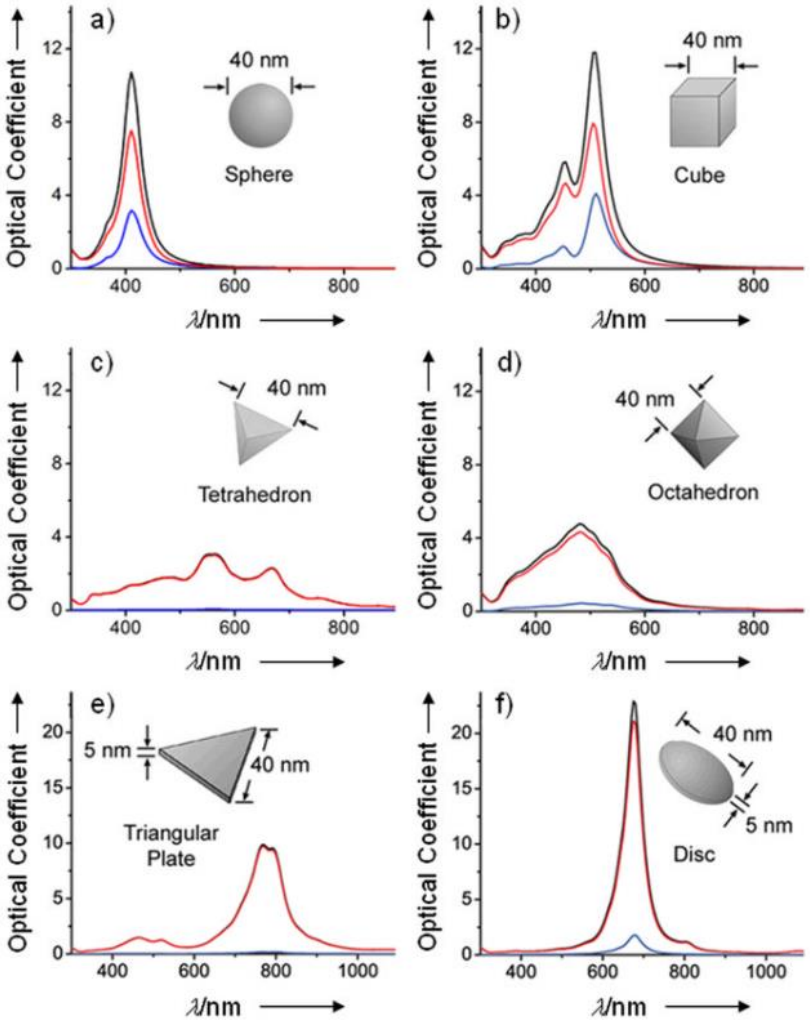

Figure 14: Calculated UV-vis extinction (black), absorption (red), and scattering (blue) spectra of silver nanostructures. Modified by *(Xia et al. 2009)* from original by *(Wiley et al. 2006)*.

2.4 Plasma-liquid interaction in nanoparticle synthesis

Plasma is the fourth state of matter, which is defined by an ionized gas that is made up of a collection of freely moving charged particles, electrons, ions, and neutral particles, which in average becomes electrically neutral. Also, the density of electrons and ions are nearly equal, thus making plasma quasi-neutral. Naturally occurring plasmas can only exist in the atmosphere if the conditions are adequate and is observed in most cases as lightning and northern lights in the atmosphere, but makes up 99% of matter in the universe. On the other hand, engineered plasmas are found as glow *(Xuechen Li et al. 2017)*, arcs *(Hrabovský 2002)*, or corona discharges *(Veldhuizen and Rutgers 2001)*. Engineered plasmas has a broad field of application such as in water treatment *(Foster 2017)*, plasma medicine *(Haertel et al. 2014)*, *(von Woedtke et al. 2013)*, nanoparticle synthesis *(Kondeti et al. 2017)*, and many other fields *(Nijdam et al. 2012)*. They exist in various forms and shapes, and are thus characterized based on electron temperature (T_e) and electron density (n_e). Other examples of engineered and naturally occurring plasmas are shown in figure 15 in correlation to T_e and n_e.

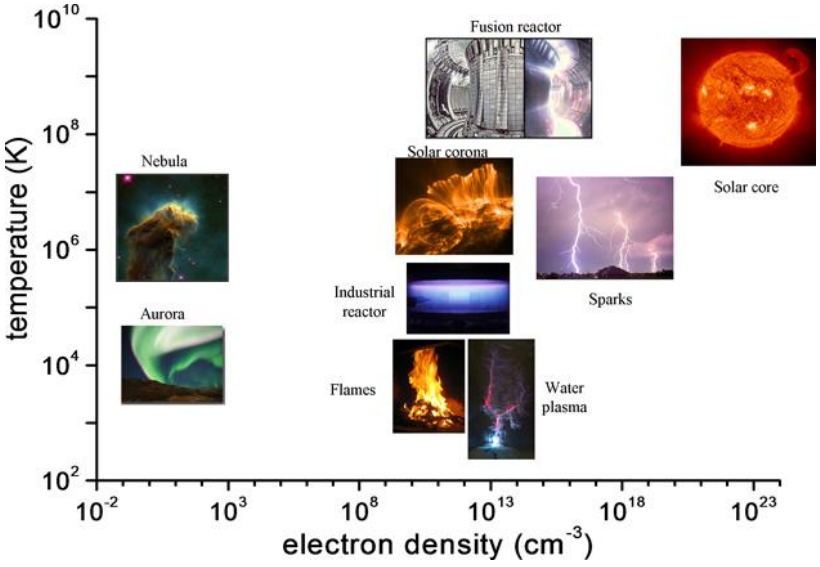

Figure 15: Classification of engineered and natural plasmas based on their T and n_e. Reproduced from *(LPP 2018)*.

2.4.1 Classification of plasma

Plasma discharges are commonly classified based on its electron temperature (T_e). In this case plasmas are classified as thermal plasmas (T_e > 100eV) and non-thermal plasmas (NTP) (T_e < 10eV) *(Dorelon, Lombardi, and Maan 1982)*.

Thermal plasmas are in thermal equilibrium, which is established by frequent elastic collisions between electrons and heavy particles as shown in figure 16. This is explained by loss of kinetic energy (KE) in electrons (T_e), whereas heavy particles (T_h) gain energy and becomes thermal *(Serway and Jewett 2003)*. Thermal plasmas usually exist as arcs or radio frequency (RF) discharges and are often associated with Joule heating and thermal ionization. Application possibilities of thermal plasmas are plenty as in waste decomposition *(Van Oost 2017)*, but are limited in energy efficient applications, due to low excitation selectivity, high gas temperature and, electrode related problems *(Fridman, Gutsol, and Cho 2007)*.

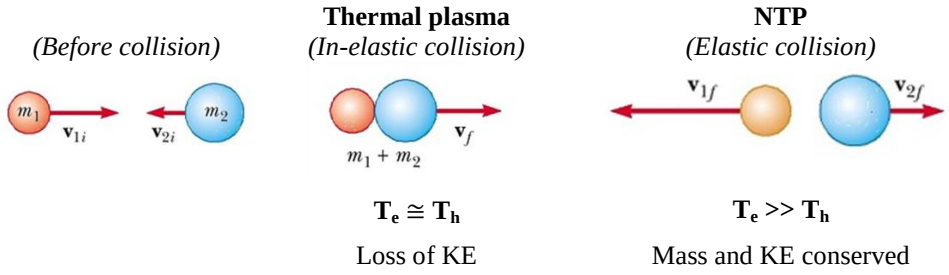

Figure 16: Particle collisions in thermal plasmas and NTP. Reproduced and recreated from *(Serway and Jewett 2003)*.

NTP are in thermal non-equilibrium, due to a non-uniform temperature distribution between electrons and heavy particles. Unlike thermal plasmas, only electrons in NTP get thermal, whereas heavy particles remain close to T_{amb}, due to few elastic collisions as shown in figure 16. These energetic electrons produce reactive species (e.g. free radicals and ions), which are essential in plasma chemistry, providing high selectivity and high energy efficiency in plasma chemical reactions *(Fridman, Gutsol, and Cho 2007)*. NTP exist as glow, corona, and RF inductively-coupled plasma (ICP). NTP operating under P_{atm} are commonly applied in environmental related industrial applications *(Fridman, Chirokov, and Gutsol 2005)*.

2.4.2 Plasma-liquid interactions

In plasma-liquid interactions (PLI) processes, plasma discharges is either generated to be in direct contact (immersed), or in no direct contact (above liquid) with the liquid phase. This is determined by the configuration of electrodes. Most applied electrode configurations in PLI systems in plasma generation are as follows:

a) Plasma discharges ***in*** liquid phase
b) Plasma discharges ***above*** liquid phase
c) Multi-phase plasma discharges

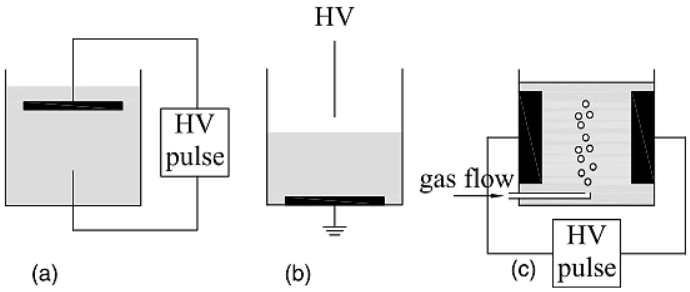

Figure 17: Common electrode configurations in PLI processes: a) Plasma discharge immersed in a liquid phase, b) Plasma discharge generated above a liquid phase, c) Plasma discharges generated in a multi-phasic system. Reproduced from *(P. Bruggeman and Leys 2009)*.

Plasma discharges *in* liquid phase

The electrode configuration of this PLI process is when the discharges are generated being immersed in a liquid phase between the rod and plate electrode pair as shown on figure 17a. The electrode shape and size depends on the goal of the process, and can for this reason vary. It is common to observe this pin-to-plane electrode configuration in PLI processes for characterization of plasma discharges in water *(Kolb et al. 2008)*, (R. P. Joshi et al. 2009), *(P. Bruggeman et al. 2009)*, *(Kocik et al. 2013)*. In nanoparticle synthesis, plasma discharge is generated in a smaller inter-electrode distance of equally shaped electrode rods *(Saito, Hieda, and Takai 2009), (Bratescu et al. 2011), (Pootawang, Saito, and Lee 2013)*, *(H.-J. Kim et al. 2018)*. Generating plasma in complete liquid immersion creates thus two interfaces: plasma/gas and gas/liquid, as shown in figure 18.

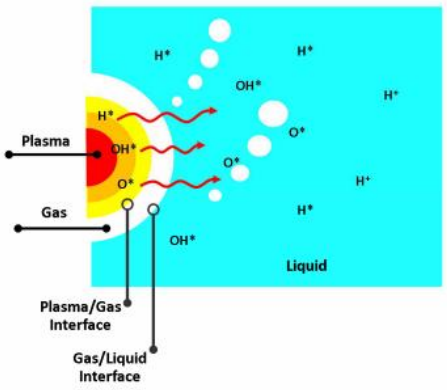

Figure 18: Plasma immersed in liquid phases. Reproduced from *(Pootawang 2011)*

Higher chemical reaction rates are thus expected in these processes, due to the fact that complete immersion of plasma in the liquid phase provides an increased contact of the plasma phase. In this PLI process it is possible to generate plasma discharges of the streamer or spark type depending on plasma parameters, such as voltage or inter-electrode distance *(B. R. Locke et al. 2006).*

Plasma discharges *above* liquid surfaces

The electrode configuration of this PLI process is when the discharge is generated above a liquid surface. In this case the working electrode is placed above the liquid surface, while the counter electrode is placed in the bottom of the reactor to provide conduction of the electrical current through the PLI system. This electrode configuration in plasma processes is shown on figure 17b. Studies which were performed using this particular electrode configuration are *(Richmonds and Sankaran 2008)*, *(Patel et al. 2013), (Gorbanev, O'Connell, and Chechik 2016), (Skiba et al. 2017)*. Since the plasma is generated above the liquid surface, an amount of plasma-generated reactive species are lost in the atmosphere. Therefore a complete use of the plasma phase is not the case in the plasma process. In this PLI process, it is possible to generate plasma discharges of the streamer or glow discharge type.

Plasma discharges in multi-phasic system

Plasma discharges in multi-phasic systems refer to electrical breakdown in gas bubbles inside a dielectric liquid media. This electrode configuration in plasma processes is shown on figure 17c. An example of this type of PLI process was performed by *(Gershman et al. 2007)*. In this work, a single stationary bubble was formed inside a liquid media with a metal needle electrode tip

emerging from the reactor inside the bubble formation. The stationary bubble facilitates plasma characterization in comparison to freely moving bubble formations. A single discharge of 1µs pulse duration applied to the electrode tip resulted in multiple corona discharges inside the bubble. Other studies performed under these conditions are *(Sommers and Foster 2014)*, *(Hayashi et al. 2015)*, *(Levko, Sharma, and Raja 2016)*, *(H.-J. Kim et al. 2018).* Plasma generation in a gas bubble depends on several parameters including the distance between the electrodes, type of gas used for bubble formation, conductivity and pH of the liquid media.

2.4.3 Physical and chemical processes in PLI

Non-thermal plasma discharges in liquid phase is generated by discharging of a capacitor in the means of a sparking gap. An alternative method is to generate plasma discharges in the use of solid-state switches. The type of power sources can either by direct current (DC), pulsed, or alternative current (AC), which depends on the type of plasma to be generated. *(P. Bruggeman and Leys 2009)*

In PLI processes it is common to observe production of reactive species *(Gorbanev, O'Connell, and Chechik 2016)*, strong UV/VUV emission *(Lukes et al. 2008)*, micro bubble *(H. H. Kim et al. 2013)* (c.f. figure 19a) and shock wave generation *(Katsuki et al. 2006)* (c.f. figure 19b), and thermal effects *(Mizuno et al. 2000)* from the plasma phase. Micro bubble and shockwave generation from pulsed plasma discharges in liquid phase are illustrated in figure 19.

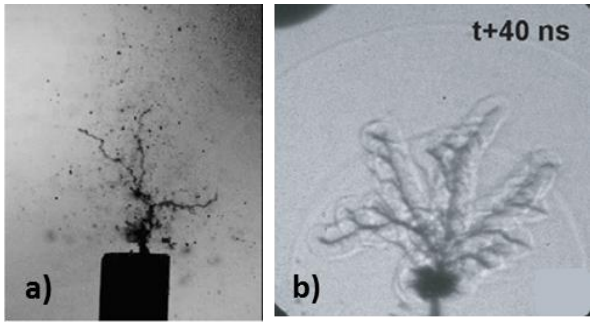

Figure 19: Pulsed filamentary corona discharges generating: a) micro bubbles and b) shock waves in de-ionized water. Recreated and reproduced from a) *(H. H. Kim et al. 2013)*, b) *(Marinov et al. 2013)*.

Plasma discharges are generated as filamentary luminous and conductive structures in direct contact with the liquid phase. These are also known as streamer discharges or partial discharges, since the discharges only appear on one electrode. In the propagation of streamer discharges,

bush-like structures are formed. These are called primary streamers (c.f. figure 20). This is followed by the propagation of tree-like filamentary structures. These are called secondary streamers, which appear longer (c.f. figure 20). Secondary streamers are formed, once the electric field of primary streamer tips is sufficiently high. Primary streamers propagates on a velocity of $100m \cdot s^{-1}$ to a few $km \cdot s^{-1}$, which is slower than the propagation of secondary streamers, which have a propagation velocity in the range of $10\text{-}100km \cdot s^{-1}$. Propagation velocity of streamers depends on the conditions, in which it is generated. *(P. Bruggeman and Leys 2009)*

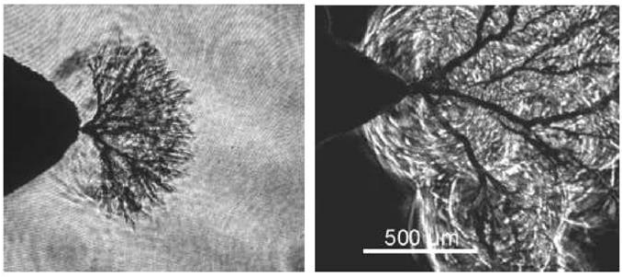

Figure 20: Primary (left) and secondary (right) streamer discharges. Reproduced from *(An, Baumung, and Bluhm 2007)*

The transition from streamer to spark discharges in the form of electrical breakdown in water occurs for an electric field in the order of magnitude of $1MV \cdot cm^{-1}$ (in microsecond pulsed discharges). Electrical breakdown in liquids is reached, when a conductive plasma channel spans the entire inter-electrode distance and connects the metal electrodes. This results in spark/arc generation. Micro bubble generation does have a significant role in triggering the breakdown of electrical discharges.

Several studies have been performed on streamer propagation mechanisms. Streamer propagation mechanism in a pin-to-plane electrode configuration is shown on figure 21, which is based on the results obtained by *(Kocik et al. 2013)*.

In the pre-discharge region, an opaque region on the vicinity of the electrode tip has been observed. Kocik *et al*. determined that it occurs due to modification of the electric field with variation in the permittivity, which thus changes the refractive index of the water. According to *(Fujita et al. 2014)*, the shadow region (or opaque region) occurs due to changes in the electric permittivity induced by strong electric field during voltage application. Due to an electric force

expansion of fluctuations occurred as a result of heat conduction and heat convection. Based on their results, the shadow region occurs due to Joule heating effects.

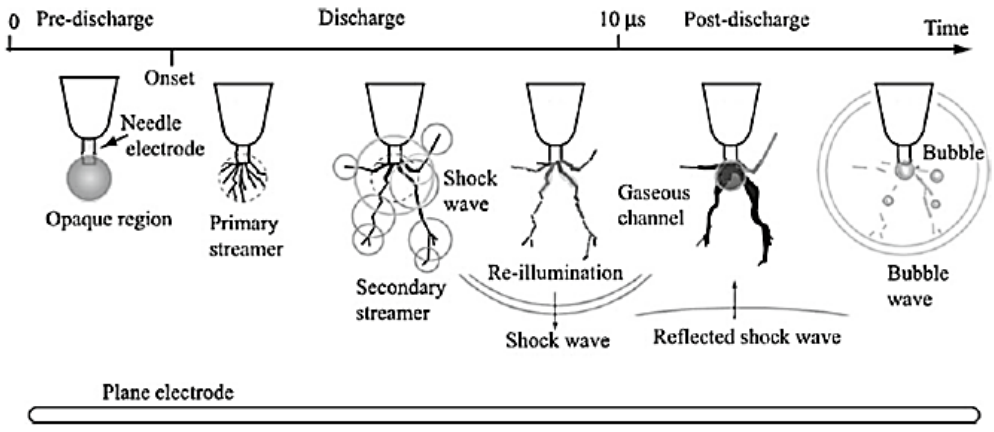

Figure 21: Streamer discharge propagation mechanism as proposed by Kocik *et al*. Reproduced from *(Kocik et al. 2013)*.

Within the spherical opaque region, primary "bush-like" streamers are developed, due to electron avalanche in low density. According to observations made by Fujita *et al*. luminous streamers are developed from protrusions of micro bubble clusters on the electrode tip. From the high electric fields of the primary streamer ends, secondary streamer discharges propagates. Secondary streamers propagate beyond the opaque region and long filamentary channels are created due to the field induced dissociation and ionization at the streamer ends. Kocik *et al*. also reported that strong shockwaves are generated due to large pressures at the electrode boundaries. Re-illumination effects are observed due to charge accumulation in the interface between gas and liquid. In the post-discharge region, wide gaseous channels occur. During streamer discharge propagation internal heating can occur, and result in the generation of gas bubbles. In the end bubble waves are formed as a result of bubble growth and collapse *(Kocik et al. 2013)*.

Reactive species are generated near streamer discharges, in which an increase in the electric field of secondary streamers for above $10 MV \cdot cm^{-1}$ dissociates and ionizes water molecules. Reactive species that are generated depends on the type of plasma, the discharge environment, the input energy, and the gas used in the generation of plasma discharges in the liquid phase *(Bruce R Locke 2012).*

Highly energetic electrons, which are generated in the plasma phase, are injected to the water, which results in the generation of hydrated electrons (e_{aq}^-) (reaction 1):

$$H_2O + e^- \rightarrow e_{aq}^- \qquad \textbf{Reaction 1}$$

Interaction of e_{aq}^- with water molecules result in the formation of short-lived primary reactive species, such as OH•, H•, and O• radicals (reaction 2-4) *(Lukes 2001)*:

Dissociation $H_2O + e_{aq}^{-\bullet} \rightarrow OH^\bullet + H^\bullet + e^-$ **Reaction 2**

Ionization $H_2O + e_{aq}^{-\bullet} \rightarrow H_2O^+ + 2e^-$ **Reaction 3**

Dissociation $H_2O^+ + H_2O \rightarrow H_3O^+ + OH^\bullet$ **Reaction 4**

As primary species are highly reactive, they recombine to form secondary long-lived and stable species, such as H_2, O_2, and H_2O_2, or reform water (reaction 5-7) *(Lukes 2001)*, *(Ruma et al. 2013), (Akolkar and Sankaran 2013):*

$$H^\bullet + H^\bullet \rightarrow H_2 \qquad \textbf{Reaction 5}$$

$$OH^\bullet + OH^\bullet \rightarrow H_2O_2 \qquad \textbf{Reaction 6}$$

$$H^\bullet + OH^\bullet \rightarrow H_2O \qquad \textbf{Reaction 7}$$

Information on plasma-liquid interface interaction and mechanism is limited, due to the highly complex nature of the plasma-liquid interface. However, it has been possible to point out some of the possible plasma-liquid interface reactions, mainly on the plasma-liquid cathode interactions *(P. Bruggeman and Leys 2009)*. An up-to-date plasma-liquid cathode interface interaction mechanism is presented on figure 22.

In the case of plasma-above liquid, plasma-liquid interaction in the gas-liquid interface at P_{atm} also adds other atoms existing in the atmosphere such as N_2. Reactions between N_2 and reactive species result in acidification of the dispersion media, due to formation of acidic compounds, such as HNO_2 and HNO_3, as observed in figure 22 *(P. J. Bruggeman et al. 2016)*.

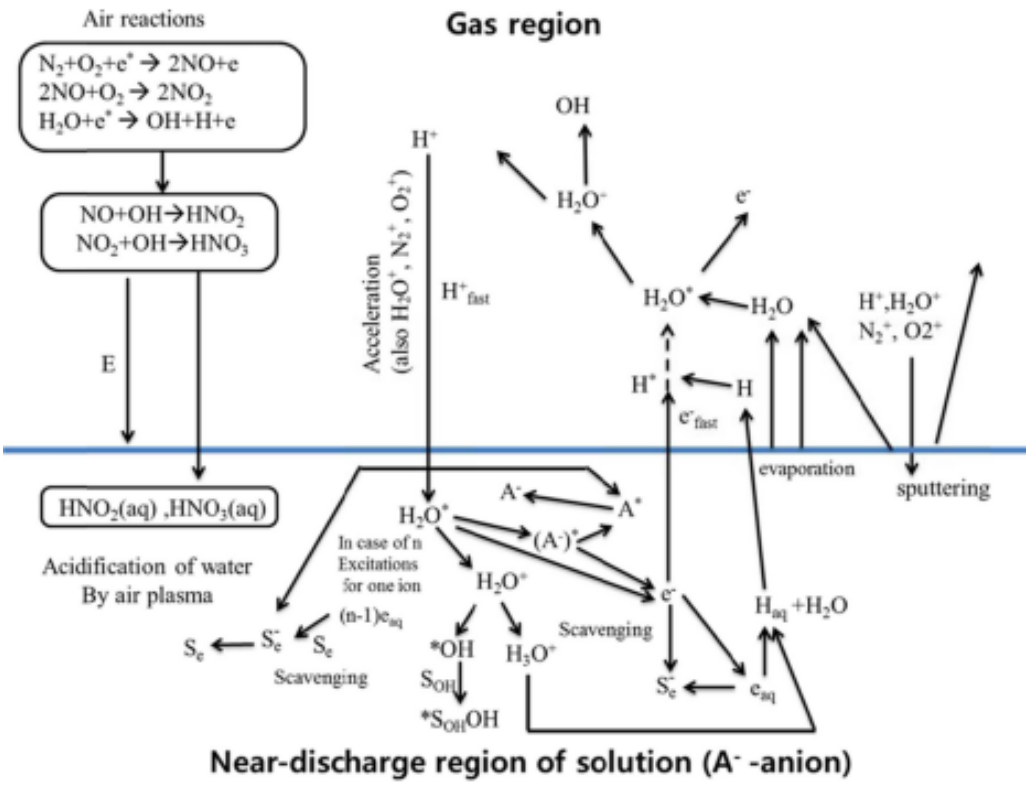

Figure 22: Chemical reaction mechanism in a plasma-liquid interface. Reproduction of a recreated version by *(Mun et al. 2017)*. Original version by *(P. Bruggeman and Leys 2009)*

In contrast to plasma generated above liquid surface, plasma discharges in the liquid phase are operated in gas bubbles or vapor channels. Discharge processes are different, but based on studies performed by *(P. Bruggeman et al. 2009)* *(Graham and Stalder 2011)*, and *(Sunka et al. 1999)*, it is shown that similar reactive species are generated in plasma above the liquid and plasma in gas bubbles. Similar reactive species are detected in streamer discharges in liquids, however due to additional discharge effects (e.g. shockwaves and re-illumination effects) enhancement in reaction mechanisms occur *(Chen, Li, and Li 2015)*.

Species originates mainly from the decomposition of water, which is atomic O, atomic H, and OH radicals. These are similar to those occurring from the plasma above the liquid surface. N_2 related species are negligible in plasma discharges in the liquid phase, due to no interaction with atmosphere *(Chen, Li, and Li 2015)*, *(Mun et al. 2017)*.

2.4.4 Metal nanoparticle synthesis by PLI

Generation of plasma-induced reactive species promotes the synthesis of metal nanoparticles using plasma-liquid processes. Nanoparticle synthesis using plasma-liquid processes is based on the reduction of metal. Several studies shows that metal ions can be reduced by e_{aq}^- *(X. Z. Huang et al. 2013)* or H• *(Saito, Hieda, and Takai 2009)*, *(Cho et al. 2011), (Skiba et al. 2018)*. In some cases H_2O_2 acts as the reducing agent, which has only been observed in synthesis of gold nanoparticles *(Patel et al. 2013)*.

Reduction reaction of metal ions in nanoparticle synthesis in plasma processes with e_{aq}^- and H• as the reducing agent is as follows (M = metal) *(Chen, Li, and Li 2015), (Kondeti et al. 2017)*:

$$M^{n+} + ne_{aq}^- \rightarrow M^0 \qquad \textbf{Reaction 8}$$

$$M^{n+} + H^\bullet \rightarrow M^0 + H^+ \qquad \textbf{Reaction 9}$$

In the following, PLI processes which are most commonly applied in nanomaterial synthesis will be discussed. These concerns, plasma immersed in the liquid and plasma above the liquid surface.

An overview of nanoparticles which have been synthesized using non-thermal plasma process techniques are shown in

table **1**.

Plasma discharges *in* liquid phase

Plasma discharges in direct contact with the liquid phase is a process, which is used for nanomaterial synthesis. This process is most often known as solution plasma processing *(Takai 2008)*, *(Takai 2014)*. Metal nanoparticles are synthesized in which metal ions originates either from the dissociation of a metal salt in the liquid phase, or from anodic dissolution of metal electrodes.

(Saito, Hieda, and Takai 2009) applied this technique for synthesis of about 20nm anisotropic (triangular, pentagonal, hexagonal) gold nanoparticles by applying plasma discharge of 3.2kV during 45min. In another study performed by (Heon Lee et al. 2013) for silver- and (Heon Lee, Park, Seo, et al. 2014) copper nanoparticles, they showed that well-dispersed and small-sized

nanoparticle are obtained in the addition of surfactant (i.e. CTAB), and that the discharge time is an important parameter for the development of the particles. In this study bipolar-pulsed power supply (250V and 30kHz) was applied for the generation of stable plasma for avoiding deposit accumulation onto electrode surfaces. It was also concluded that the use of less inert electrode material (i.e. tungsten) are not optimal in such techniques as they participate in the nanoparticle synthesis.

Plasma discharges *above* liquid surfaces

This is one of the most applied techniques in nanoparticle synthesis as the plasma is easily generated in the gas phase. Microplasma discharges are also preferred in nanoparticle synthesis as they are operated under P_{atm}, which results in a cost-effective process *(Mariotti, Bose, and Ostrikov 2009)*. In a study performed by *(Richmonds and Sankaran 2008)* they showed that it is possible to produce uniform and high-purity gold and silver spherical nanoparticles of 10nm by micro-plasmas operated at P_{atm} applying 2kV and keeping the current constant at 5mA. It was necessary to include additional compounds such as acids to increase solution conductivity, and addition of fructose as a stabilizing agent to prevent uncontrolled growth and agglomeration. From what they mention in their research, microplasma technique has a lot in common with electrochemical reactions which was performed in another complementary study by *(Chiang, Richmonds, and Sankaran 2010)* in an electrochemical cell assisted by a microplasma discharge applying the same experimental conditions. In another study, *(Patel et al. 2013)* have come to the conclusion that H_2O_2 serves as a reducing agent and that gold nanoparticles become electrostatically stable, for which surfactants and stabilizing agents are not required. This was based on the synthesis of gold nanoparticles applying 2kV and keeping a constant current at 5mA. Thus, after a discharge time around 10min it was shown that not only spherical, but also hexagonal- and triangular-shaped gold particles between 7-60nm was formed without adding stabilizing agents. (R. Wang et al. 2015) also obtained spherical, hexagonal, and triangular shaped sodium citrate-stabilized gold nanoparticles of 20nm after 10min of discharge time by microplasma applying 16.77W to the system. They also reported the influence of several parameters on nanoparticle size, and showed that stirring mode, stabilizer concentration, and discharge power can be used in controlling nanoparticle size which will be discussed in section 2.5.1. Furthermore, that the parameters influenced nanoparticle plasmonics *(X. Z. Huang et al. 2013)*, *(X. Huang, Li, and Zhong 2014)*.

Table 1: Metal nanoparticle synthesis by plasma-liquid interaction techniques

Element	Power supply	Precursor	Electrode	Inter-electrode distance	Voltage	Current	Frequency	Pulse length	References
Plasma above liquid									
Ag	DC	$AgNO_3$	Pt	2mm	2kV	3mA			*(X. Z. Huang et al. 2013)*
Ag	DC	$AgNO_3$	Pt	2mm	2kV	5mA			*(Richmonds and Sankaran 2008)*
Au	DC	$HAuCl_4$	Pt	2mm	2kV	5mA			*(Richmonds and Sankaran 2008)*
Au	DC	$HAuCl_4$	C	0.7mm	2kV	5mA			*(Patel et al. 2013)*
Au	DC	$HAuCl_4$	Pt	1mm	-	-			*(R. Wang et al. 2015)*
Plasma in liquid									
Au	Pulsed DC	$HAuCl_4$	W	0.3 mm	1.6-3.2 kV		15 kHz	2µs	*(Saito, Hieda, and Takai 2009)*
Ag	Bi-polar pulsed DC	$AgNO_3$	W	0.2 mm	250V		30kHz	2µs	*(Heon Lee et al. 2013)*
Cu	Bi-polar pulsed DC	$CuCl_2$	W	0.3 mm	250V		30kHz	5µs	*(Heon Lee, Park, Seo, et al. 2014)*
Mn	Bi-polar pulsed DC	$MnCl_2{\cdot}4H2O$	W	0.3 mm	250V		30kHz	5µs	*(H.-G. Kim et al. 2013)*
C	Bi-polar pulsed DC	Benzene or glucose	W	1 mm	1kV		10-25kHz	2µs	*(O. L. Li et al. 2013)*
Cu	Pulsed DC	$CuCl_2\ 2H_2O$	W	0.5mm	900V		20kHz	-	*(Pootawang, Saito, and Lee 2013)*

2.5 Plasma-liquid interactions for silver nanoparticle synthesis

2.5.1 Influence of process parameters on nanoparticle synthesis

Time-saving nanoparticle synthesis processes resulting in small-sized nanoparticles of high product yield is ideal, but this is not always the case in many processes. However, it is possible to control the synthesis process and tailor nanoparticle morphology. This is possible by regulation of synthesis process parameters during nanoparticle synthesis. Some of the chemical and physical process parameters that have been reported to have a significant influence on nanoparticle synthesis and particle morphology will be discussed in the following sections based on previous studies.

2.5.2 Chemical parameters

Metal precursor concentration

The metal precursor concentration in nanoparticle synthesis has been shown to have an influence on the morphology of metal nanoparticles during synthesis using plasma discharges. One of the studies that have reported to observe the influence of precursor concentration on nanoparticle morphology is *(X. Z. Huang et al. 2013).* In this study, Huang *et al*. synthesized silver nanoparticles during 15min using microplasma discharges of 2kV and 3mA. The plasma was ignited by a DC power supply through a 100kΩ ballast resistor and generated between the tip of a stainless steel capillary electrode and the surface of an aqueous $AgNO_3$ precursor solution. A Pt foil was immersed in the precursor solution as the counter-electrode in order to conduct the electrical current. The microplasma was sustained by Helium gas flowing through the capillary at 25sccm.

In this study, Huang *et al*. determined that for an increase in the $AgNO_3$ concentration from 2mM to 8mM resulted in an increase in particle absorbance, which indicated an increase in silver nanoparticle concentration. Silver nanoparticles produced using 4mM $AgNO_3$ resulted in an average diameter between 10-25nm.

Another study on the influence of plasma current on nanoparticle synthesis was performed by *(Patel et al. 2013)*. They performed this study on gold nanoparticles, in which high voltage DC microplasma of 2kV and 5mA in discharge current was generated on the $HAuCl_4$ electrolyte surface during 10min. The plasma was generated between the tip of a stainless steel capillary and

the electrolyte surface, in which a carbon rod was dipped into the electrolyte in order to conduct the electrical current. The plasma was sustained by a helium gas flowing through the capillary at 25sccm.

An increase in the precursor concentration from 2.5µM to 1.0µM resulted in an increase in the average nanoparticle size from 5nm to several 100nm, respectively. Furthermore, it was observed that for an increase in precursor concentration the shape of gold nanoparticles would increase in the proportion of shaped particles (i.e. triangular, pentagonal, and hexagonal). Patel *et al*. propose that an isotropic aggregation of gold atoms occurs for low precursor concentrations (2.5µM) in the bulk of the reaction solution, which results in spherical shaped gold nanoparticles. However, for increased precursor concentrations (0.05µM-1.0µM) the probability of the interaction and reduction of partially reduced $HAuCl_4$ onto existing nanoparticles is higher, which results in the growth and shaping of gold nanoparticles.

Based on these results different observations have been made on the influence of precursor concentration of the morphology and synthesis of metal nanoparticles. This is an indication to that this parameter is highly depending on the synthesis conditions and on the nanoparticle to be synthesized.

Stabilizing agent concentration

The influence of stabilizing agent concentration on the metal nanoparticle morphology was investigated by *(R. Wang et al. 2015)*. In this study, a DC high-voltage negative-polarity power supply was used in the ignition of the atmospheric pressure non-thermal microplasma through a 5kΩ ballast resistor. The microplasma was generated between the tip of a copper needle and the 1.214mM $HAuCl_4$ electrolyte surface, in which a Pt plate was immersed due to conduction of the electrical current. Furthermore, the plasma was pressurized with an argon gas, which was flowing through the needle at a constant flow rate (50sccm). The microplasma was generated during 10min above the reaction solution, which consists of an aqueous $HAuCl_4$ solution at a constant concentration of 1.214mM.

For an increase in the sodium citrate concentration from 3.4mM to 68mM, a decrease in the average gold nanoparticle size was observed from 53.5±15.8nm to 11.5±12.3nm. This decrease in size is reported by Wang *et al*. to be due to the stabilizing effect of sodium citrate.

In studies performed by *(X. Z. Huang et al. 2013)* and *(Heon Lee et al. 2013)*, it was shown that the surfactant/precursor molar ratio is important for an enhanced stabilization effect of as-synthesized nanoparticles for a given process time. On the right conditions, addition of surfactant resulted in uniformly dispersed and small-sized nanoparticles.

Addition of stabilizing agent is important for processes resulting in aggregated nanoparticles. Efficiency of the stabilization effect on nanoparticles depends on surfactant concentration, on the nature of surfactant, or on the compatibility with nanoparticles to be synthesized.

Initial solution pH

Initial solution pH of the precursor solution was shown to have an influence on nanoparticle morphology using the soft chemical synthesis techniques. However, the influence of this parameter is less commonly investigated on nanoparticle morphology using plasma synthesis techniques. Based on information on pH values reported in studies related to plasma synthesis techniques, this can be due to the fact that the pH value is not stable during the process. The pH is controlled by chemical reactions that occur in the reaction solution through generation of reactive species, which thus influences nanoparticle synthesis. The evolution in pH during plasma processes have been reported in *(Rumbach et al. 2013)*. The atmospheric pressure microplasma discharge was generated between the tip of a stainless steel capillary and above the surface of an aqueous NaCl solution. A Pt foil was immersed in the solution as the counter electrode. In this study, the microplasma was ignited by a high voltage DC power supply. The micro plasma was operated at a current of 1.62mA, but the voltage changed depending on the type of gas. For Ar, N_2, O_2, and air the applied voltage were 250V, 1100V, 1350V, and 1100V, respectively. In this study the evolution in pH of the reaction media was demonstrated to depend on the composition of the background gas. An increase in pH was observed during the plasma process using Ar or O_2 as the background gas. This increase in pH is due to reaction between plasma generated electrons and aqueous ions, which results excess in OH^-, and thus a basic reaction solution. On the other hand, a decrease in pH was observed during the plasma process using air and N_2 as the background gas. This decrease in pH is due to reaction between reactive neutral species (formed in the plasma phase) and the solution, which produced HNO_2 and HNO_3, and creates thus an acidic reaction solution.

Similar observations in pH evolution of the reaction solution in terms of nanoparticle synthesis have been reported. *(Mariotti et al. 2012)* reported a decrease in solution pH during gold nanoparticle synthesis using helium sustained plasma discharges above the liquid surface. In another study, *(Pootawang, Saito, and Lee 2013)* reported a decrease in solution pH during copper nanoparticle synthesis under atmospheric pressure plasma discharges immersed in the reaction solution.

In the following study, the influence of pH on gold nanoparticle synthesis was studied by *(Bratescu et al. 2011)*. Gold nanoparticles were synthesized by applying high voltage DC pulsed plasma discharges of 250ns and 10kHz in frequency to a pair of Pt wire electrodes. The Pt wire electrodes were immersed in an aqueous $HAuCl_4$ solution with 130µS·cm^{-1} in conductivity and 3.2 in initial solution pH. The atmospheric pressure plasma was generated in the discharge region of the Pt wires in the inter-electrode distance of 0.2mm and the synthesis of gold nanoparticles lasted for 30min.

In this study, the influence of gold nanoparticle synthesis via plasma discharges in an aqueous $HAuCl_4$ solution with the pH values 3, 6 and 12 on gold nanoparticle morphology were investigated. They showed that for an increase in pH from 3 to 12, the average nanoparticle size would decrease from 10nm to 1-2nm, respectively.

Based on the results presented in this study and other related studies, it is shown that the pH value has an influence on nanoparticle synthesis in plasma processes.

2.5.3 Physical parameters

Applied voltage

Applied voltage is one of the physical plasma parameters, which have been shown to have an influence on nanoparticle morphology. The influence of applied voltage has been studied by *(Hieda, Saito, and Takai 2008)*, *(Saito, Hieda, and Takai 2009)* on the synthesis of gold nanoparticles. Gold nanoparticles were synthesized by applying high voltage DC pulsed plasma discharges of 2µs and 15kHz in frequency to a pair of tungsten electrodes. The tungsten wire electrodes were both immersed in the $HAuCl_4$ electrolyte during synthesis.

In this investigation, Hieda *et al*. and Saito *et al*. did apply 1600V, 2400V, and 3200V to the synthesis of gold nanoparticles. This study showed that an increase in the applied voltage did

influence on the synthesis rate, in which the application of an increased applied voltage would result in the synthesis of gold nanoparticles of smaller sizes. Saito *et al*. explains that this occurs due to an increased dissolution rate of the gold nanoparticles, which results in reduced particle size. From this study, it is shown that the applied voltage does have an influence on the synthesis rate and morphology of gold nanoparticles.

Plasma current

The influence of plasma current on silver nanoparticle synthesis was studied by *(Chiang, Richmonds, and Sankaran 2010)*. In this study, the microplasma was ignited by a high-voltage DC power supply through a 160kΩ ballast resistor. The plasma was generated between the tip of a stainless steel capillary and the surface of the electrolyte solution (diluted acid solution), in which a silver foil has been immersed as a source to nanoparticle synthesis. The microplasma was sustained by an Argon gas flowing through the capillary at 25sccm.

The influence of plasma current on silver nanoparticle synthesis was observed as the plasma current has been increased from 2.5mA to 7.5mA. An increase in plasma current did result in an increase in the silver nanoparticle concentration, which was determined through optical characterization techniques. W-H Chiang *et al*. could therefore relate these observations to an increase in the nanoparticle synthesis rate.

Another study on the influence of plasma current on nanoparticle synthesis was performed by *(Patel et al. 2013)*. They performed this study on gold nanoparticles, in which high voltage DC microplasma of 2kV was generated on the $HAuCl_4$ electrolyte surface. The plasma was generated between the tip of a stainless steel capillary and the electrolyte surface, in which a carbon rod was dipped into the electrolyte in order to conduct the electrical current. The plasma was sustained by a helium gas flowing through the capillary at 25sccm.

Under the above-mentioned synthesis conditions, synthesis of gold nanoparticles in the application of plasma currents from 1mA to 5mA would result in an increased gold nanoparticle concentration. From these results they could make connections to the nanoparticle synthesis rate, and thus conclude that an increase in the plasma current increases the nanoparticle synthesis rate.

Discharge power

Discharge power is another plasma parameter that has been documented to have an influence on nanoparticle morphology. In one study, *(R. Wang et al. 2015)* investigated the influence of plasma power on the synthesis of gold nanoparticles. In this study, a DC high-voltage negative-polarity power supply was used in the ignition of the atmospheric pressure non-thermal microplasma through a 5kΩ ballast resistor. The microplasma was generated between the tip of a copper needle and the $HAuCl_4$ electrolyte surface, in which a Pt plate was immersed due to conduction of the electrical current. Furthermore, the plasma was pressurized with an argon gas, which was flowing through the needle at a constant flow rate (50sccm).

Generation of microplasma discharges with plasma power of 4.19W, 9.78W, and 16.77W resulted in the synthesis of spherical gold nanoparticles with an average diameter of 35.8±9.3nm, 27.1±10.4nm, and 22.3±8.6nm, respectively. From this study, it was confirmed that a decrease in plasma power reduces the average nanoparticle size.

Pulse duration

Pulsing of the electrical plasma discharges are often applied in nanoparticle synthesis, and can be described as that shown in equation 5.

$$t_{OFF} = \frac{1}{f} - t_{ON} \qquad \textbf{\textit{Equation 5}}$$

Here, the plasma period is defined by *1/f*, for which *f* is the plasma repetition frequency. The t_{OFF} is the duration within the plasma period, which corresponds to charging of capacitor. Thus, plasma is not "active". The t_{ON} is the duration within the plasma period, which corresponds to discharging of capacitor. Thus, plasma generation is "active". As the pulse duration increases (t_{ON}), duration of UV-light emission as a result of recombination of plasma-excited atoms would increase systematically for an increase in pulse durations *(Lukes et al. 2008).*

Hence, varying the pulse duration of plasma discharges in nanoparticle synthesis has been confirmed by several researchers to have an influence on the nanoparticle morphology. Some of these observations were made by *(H.-J. Kim et al. 2018)* in the synthesis of silver nanoparticles by the generation of pulsed bi-polar plasma discharges of 3.8kV and 5kHz immersed in pure de-ionized water (80°C). Silver nanoparticles were thus produced using a pair of silver wires as

electrodes and source to silver nanoparticle production. During silver nanoparticle synthesis, pulse duration of 20µs, 40µs, and 60µs were applied, which then resulted in the production of 13-37nm, 36-53nm, and 0.2-0.87µm of silver nanoparticles, respectively. From this study, it has been shown that a decrease in pulse duration reduces the average nanoparticle size.

Several other physico-chemical parameters have been reported to influence the nanoparticle morphology during the synthesis, which have not been mentioned previously. Some other parameters regard stirring mode *(R. Wang et al. 2015)*, reaction temperature, and inter-electrode distance *(Hoonseung Lee, Ueno, and Saito 2015)*.

2.6 Conclusion

Metal nanoparticles are particles in the nano-scale range and are due to an increased surface-to-volume ratio highly reactive in comparison to their bulk counterparts. Their highly reactive nature provides different and improved material properties, in which they become applicable in many different fields, such as catalysis or diagnostics. Particle properties are highly-dependent on their particle surface properties, and if nanoparticle becomes less reactive, due to an increase in size or due to particle agglomeration, material properties decreases. In order to control material properties of nanoparticles, synthesis pathways in nanoparticle synthesis is controlled by regulation of relevant synthesis parameters. Through a controlled synthesis, it is possible to fine-tune the size and shape of nanoparticles, which hence result in specific results. The fine-tuning of nanoparticles is easily performed through liquid-based bottom-up synthesis techniques, and is also in advantage over the top-down synthesis techniques. This is due to bottom-up synthesis techniques being cost-efficient and is low in energy consumption.

Although the advantages, most conventional bottom-up techniques do not imply as “green” synthesis techniques, it is therefore of increasing interest to develop “green” nanoparticle synthesis techniques. These would use less toxic and hazardous reagents and in the end to generate less by-products and waste.

In this regard, PLI process is proposed as an alternative to conventional nanoparticle synthesis techniques. In PLI processes, a range of long- and short-lived reactive species (e.g. e_{aq}^-, H•, OH•, H_2O_2 etc.) is generated in the liquid phase, which reduces metal ions into metal nanoparticles.

PLI processes are suitable for production of shape- and size selective nanoparticles, due to fine-tuning of nanoparticle morphology by regulation of process parameters, which includes applied voltage, pulse duration, precursor concentration.

Chapter III – Materials, silver nanoparticle synthesis, and characterization techniques

In this work, synthesis of silver nanoparticles will be performed using a technique based on the generation of plasma discharges in liquids. With this work, it is the first time at LSPM that synthesis of nanoparticles is performed using a plasma-in-liquid (PLI) synthesis technique, thus there are neither previous results nor experiences. An essential part of this work was therefore to develop an experimental set-up for a plasma in-liquid (PLI) synthesis technique. The complete development of the PLI process, from "scratch", took almost one and a half year.

Development of the nanoparticle synthesis process was managed in order to be able to synthesize nanoparticles using a clean and isolated system. In this regard, a pair of electrodes completely isolated towards the surrounding liquid media was developed. As a result, the generation of stable plasma discharges has been provided, avoiding any parasitic arc discharges. As part of the electrode system development, the shape of the electrode tips has also been taken into consideration, as this would have an influence in generating stable plasma discharges.

In the first part of this chapter, an introduction to a general synthesis of silver nanoparticles using the newly-developed process will be covered. This will include the presentation of the two different techniques used for generating DC-pulsed plasma discharges with MARX- and BEHLKE pulse generators. In the last part, an introduction to the characterization techniques that were applied for nanoparticle size and morphology assessment will be covered.

3.1 Synthesis of silver nanoparticle using a plasma-in-liquid process

In this section, the following items will be presented: the reactor and electrodes system, the data acquisition, and the experimental procedure for the synthesis of silver nanoparticles, , and electrodes cleaning .

3.1.1 Reactor and electrodes

The synthesis of silver nanoparticles is performed in an uncovered borosilicate glass vessel (Ø95×55mm) at P_{atm} and T_{amb}, as the one presented on figure 23.

The electrode system consists of a symmetrical electrode pair of 200µm in diameter platinum (Pt) wires of 99.99% purity, in a pin-to-pin configuration. Only a small part of the Pt wire (0.5mm in length) is in contact with the liquid media. The rest of the metallic electrode components have been completely isolated from the surrounding liquid with electrically non-conductive plastic and capillary tubes (c.f. inset on figure 23)

The inter-electrode distance between the electrodes is set to 3mm, this distance can be changed using a micrometer screw, according to the desired experimental conditions.

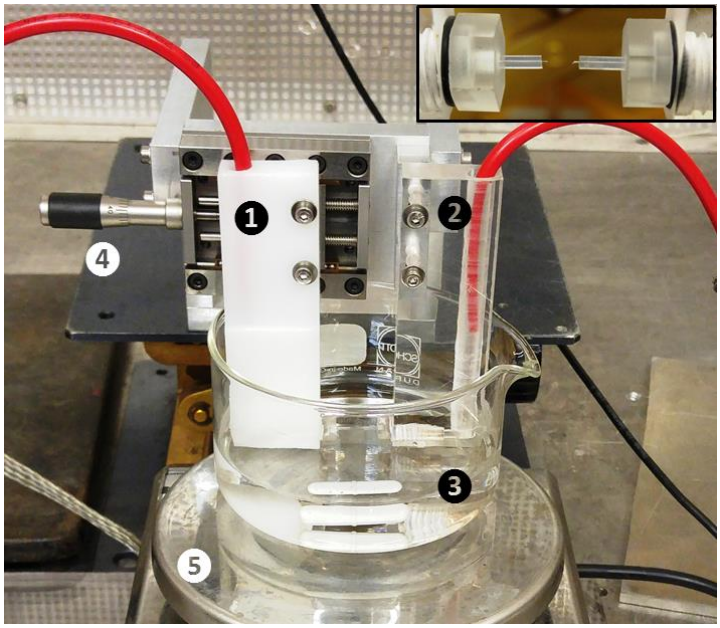

Figure 23: Reactor and electrodes utilized in nanoparticle synthesis. It is composed by: ① Anode electrode connected to a HV probe. ② Cathode electrode connected to a current probe. ③ Electrodes immersed in a PYREX reactor containing liquid media. ④ Height regulation system connected to a micrometer for adjusting the inter-electrode distance of electrodes. ⑤ Magnetic stirrer including a magnetic stirring bar. The inset image shows a close-up of the inter-electrode distance of electrodes

Tests were performed in order to investigate the influence of shaped and non-shaped electrode tips on plasma generation. The procedure for shaping the Pt wires is based on an electrochemical etching technique *(Kupper 2012).* In this procedure, low voltage (DC 17.5V – 1.25A) was applied between two copper electrodes. The anode is immersed in concentrated H_2SO_4 (ICH Chimie, 95-97%); the volume of acid is adjusted to cover the anode plate. A pair of Pt wires of similar external length is fixed onto the Cu cathode plate, which is fixed and positioned in a way that would result in an equal perpendicular length of the Pt wires being in contact with the acid

solution. In order to promote obtaining pointed tips at the end of the etching process, the Pt wires are center-positioned in an electric field, which was created in two symmetrically circular-shaped holes of the Cu anode plate. Once the electrochemical etching starts, the shaping of the Pt wires is controlled regularly. In general, point-tipped electrodes are obtained after 1.5 hours of etching. Figure 24 shows the Pt wires before and after the electrochemical etching.

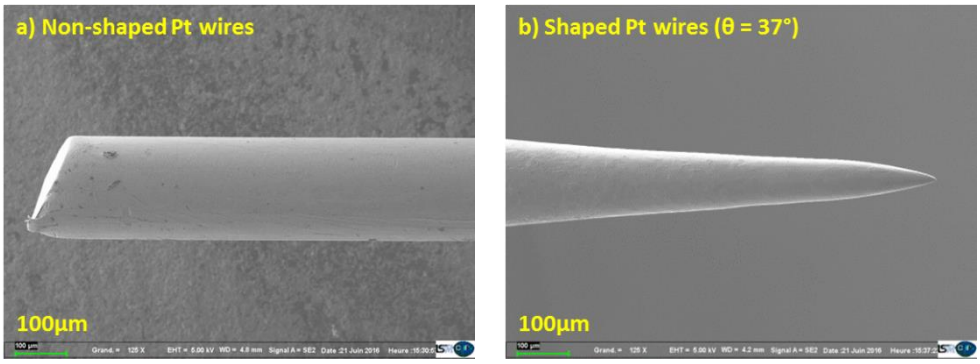

Figure 24: Pt wire electrodes as a) shaped and b) non-shaped

The current and voltage waveforms obtained for plasma discharges with non-shaped and shaped Pt wires are presented in figure 25. These results show that shaping the Pt wire tips does not have any significant effect on plasma generation on when working with wires of diameters as low as 200µm. For this reason, electrodes were used with no further shaping of their tips.

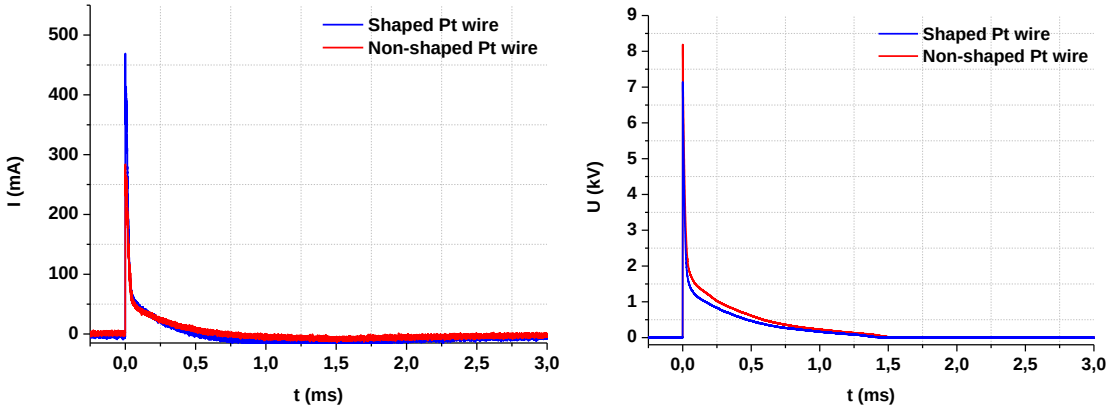

Figure 25: Current and voltage waveforms resulting the silver nanoparticle synthesis using shaped- (blue) and non-shaped (red) Pt wire electrodes

In the plasma-in-liquid process, one electrode is connected to the high voltage power supply, whilst the other is connected to the ground. Regarding their electrical poles during the synthesis, electrodes will be called anode and cathode, respectively.

Agitation of the precursor solution was provided using an agitator (200 rpm, TMA 2071) and a magnetic bar.

The plasma-in-liquid experimental set-up is placed inside of a metal mesh cage, also known as a Faraday cage. This is done to avoid any external influences that can interfere with the plasma and to avoid signal perturbation that causes noises in the electrical waveforms.

3.1.2 Preparation of the metallic precursor solution

Preparation of the metal precursor solution is performed by dissolution of $AgNO_3$ (Acros organics, 99.85%) in 100mL filtrated deionized water (Biotechnofix, 18.2MΩ·cm).

Polyvinyl pyrrolidone (PVP, MW=10000g·mol^{-1}, Sigma Aldrich) can be added to the initial solution as a stabilizing agent. PVP prevents agglomeration through coverage of the nanoparticles surface with long-chained micelles.

The typical $AgNO_3$ and PVP mass and concentration values used in this work are presented below.

	$AgNO_3$	**PVP**
Mass (mg)	34	20
Concentration (mM)	2	0.02

Ex-situ conductivity (SensION+ EC71, HACH) and pH (SensION+ MM340, HACH) measurements of the reaction media were conducted prior to and after nanoparticle synthesis. Under these conditions, the initial pH and conductivity values of the precursor solution (in the presence of PVP) are 4.5 and 300µS/cm, respectively.

In the following chapters, the effect of pH on the characteristics of the synthesized nanoparticles is studied. The pH was changed from 2 to 11, adding a buffer into the initial metallic precursor solution as shown below.

pH	buffer
2-4	HNO_3
7-11	NH_4OH

Chemical compounds were used without further purification.

3.1.3 Experimental procedure

Once the vessel is filled with 100 mL of the metallic precursor solution, the electrodes are adjusted to an inter-electrode distance of 3mm by a micrometric system. Then, the electrodes are immersed into the solution until complete coverage of the Pt wires (c.f. figure 23).

A high voltage, with a pulse repetition frequency of 50Hz, is applied to the immersed electrodes during a process time of 20min. As presented in the next section, two different high voltage generators were used.

Visually, we can observe the generation of bush-like filamentary plasma discharges on the cathode tip and small spot-like discharges on the anode tip.

Gentle agitation (200 rpm) is applied in order to keep a constant Ag^+/AgNP exchange in the small discharge volume region throughout the synthesis. The agitation rate is kept low in order to not perturbate the plasma generation. Agitation is further applied in order to ensure uniform temperature distribution of the solution, due to thermal effects from the plasma phase, which was documented by *(Mizuno, 2000)*.

An increase in the solution temperature at the end of the discharge is observed. This increase does not exceed more than 10°C. When starting with a solution at ambient temperature, the solution will reach a maximum of 30°C after the 20 minutes process.

The physico-chemical characteristics of the solution, before and after exposition to the plasma discharge, were monitored by ex-situ pH and conductivity measurements.

3.1.4 Data acquisition

The anode is connected to a HV probe (LeCroy PMK 14kV, 1000:1, 100MHz), and the cathode is connected to a Rogowski coil current probe (Pearson Electronics, 1:1 divider). The applied high voltage and discharge current were simultaneously recorded by an oscilloscope (HDO9104

- 1GHz, Teledyne LeCroy) with a sampling rate of up to 40GS/s. Current and voltage waveforms were averaged over 100 sweeps by the oscilloscope during the PLI process.

3.1.5 Cleaning of the electrodes

It was observed that metallic silver particles would attach onto the surface of the cathode during the PLI process, as shown on figure 26. Thus, between each synthesis, the electrode system was cleaned in order to remove all the nanoparticles attached to any of the surfaces, avoiding particle transmission from one experiment to the other.

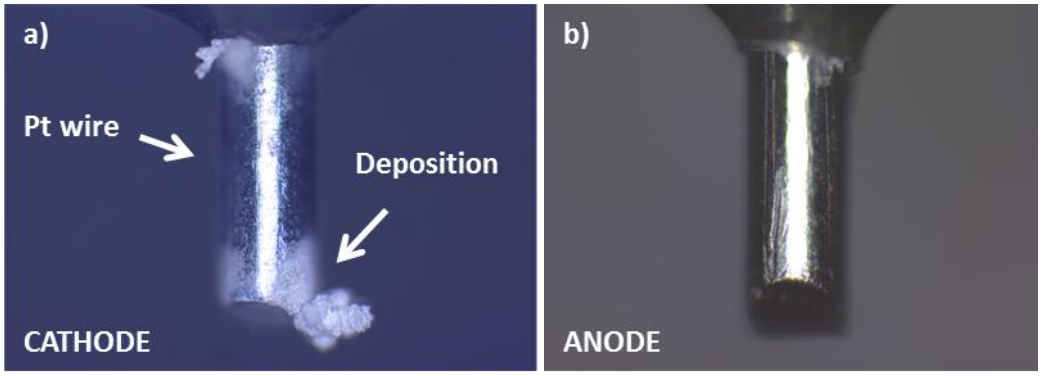

Figure 26: Pt wire electrodes after silver nanoparticle synthesis using the PLI process. a) Cathode and silver deposition on surface and b) anode

A two steps cleaning method is used. First of all, Pt wires that have been in direct contact with the precursor solution are cleaned by applying low voltage using a low voltage DC power supply (M10-DP305E, MCP). For this, the electrodes are immersed in a NaCl solution (σ = 1mS/cm). The anode is connected to the negative polarity channel and the cathode is connected to the positive polarity channel. An electric current (0.25V - 0.01A) is applied during 1 to 5 min (cleaning time depends on particle removal efficiency), resulting in the removal of the particles deposited on the cathode's surface. Then, the electrodes are immersed in pure deionized water (σ = 0.5µS/cm) for 10min, while keeping the solution under agitation, in order to remove any residual ions.

In addition, the different parts composing the electrodes insulation system are cleaned with an ethanol imbibed tissue, in order to remove any remaining particles. These pieces are then immersed in ethanol and placed in an ultrasonic bath for 10min.

3.2 DC-pulse generation techniques in plasma-in-liquid processes

3.2.1 Method 1: Marx high voltage DC-pulse generator

Method 1 concerns nanoparticle synthesis by a PLI process in which the HV DC-pulsed plasma discharges are generated by a Marx pulse generator. The Marx pulse generator was first described by Erwin Otto Marx in 1924 and later developed by J. C. Martin in 1960. It was mainly developed for the purpose of generating short-duration high voltage (HV) pulses from a low voltage (LV) DC power supply. The HV pulses are generated by charging a number of capacitors in parallel, and then discharged in series by a number of switches. The system proved to provide stable and reproducible pulses *(Miller 1982)*.

The switches in Marx generators are usually gas-filled spark gaps of fixed dimensions. Gasses which are commonly used and are suitable for this work are nitrogen and air. In this work, the latter is used.

The idea of synthesizing nanoparticles based on a Marx generator is based on using a simple and low-cost generation of HV pulsed plasma discharges. In addition, in a previous work of our group, a laboratory-crafted MARX pulse generator was developed and dimensioned *(Aggadi 2006)*, and its application for gas phase discharges was further studied *(Redolfi 2007) (Klett 2011)*.

For simplicity, a single stage Marx unit is used in the PLI process. A closed electrical RLC circuit showing each component included in the experimental set-up, and the Marx pulse generator used in this work, are shown in figure 27a-b.

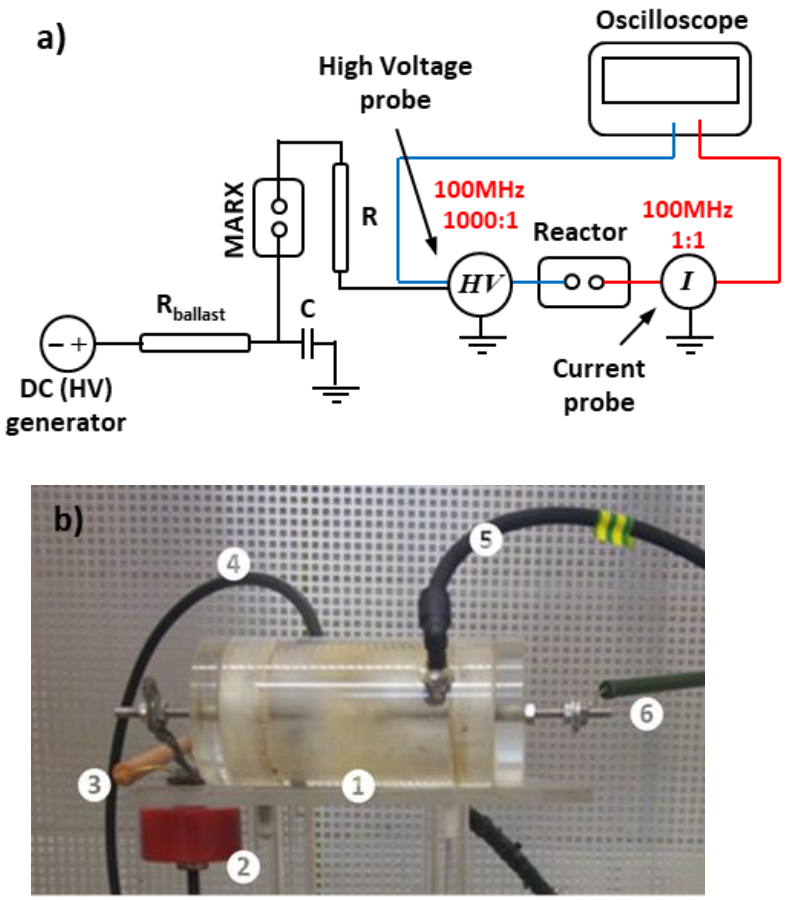

Figure 27: a) Electrical circuit of a Marx-pulsed PLI process for nanoparticle synthesis. b) Single-unit Marx HV pulse generator applied in PLI process for nanoparticle synthesis. It is composed by: ① Gas-filled Marx switch placed inside a plastic insulator. ② A capacitor (1nF) for charging/discharging of HV pulses. ③ Ballast resistor (100kΩ). ④ Inlet air gas-flow (P_{atm}). ⑤ Outlet air gas-flow (P_{atm}). ⑥ HV-cable connection to reactor over a resistor (500Ω).

The process is driven by a 30kV/30mA direct current (DC) positive-polarity high-voltage (HV) power supply (TECHNIX CCR-30P450), used to adjust the high voltage to the desired value, up to 16kV. The current was limited through a 100kΩ ballast resistor ($R_{ballast}$). The MARX generator spark gap allowed a ceramic capacitor (1nF) to discharge into the reactor system at a chosen pulse frequency, in the range of 10Hz to 90Hz. An additional resistor (R=500Ω) was added between the Marx and the reactor in order to control the input energy.

3.2.1.1 Generation of pulsed plasma discharges in liquid media via the Marx pulse generator

In this section, the optimization of the synthesis conditions and parameters for which stable pulsed plasma discharges are generated in a liquid phase, will be discussed. Challenges in using a Marx generator in the PLI process have been encountered:

1) A reduced life-time of the efficiency of the Marx generator has been observed, and estimated to about seven syntheses. Indeed, after seven syntheses, a decrease in the input energy occurs. A closer look into the sparking region of the Marx generator revealed that this decrease occurs as a result of the oxidation of the electrodes, which consist of metallic cap nuts. Therefore, in order to keep the experimental conditions as constant as possible, the cap nuts are changed every seven syntheses.
2) It was observed that the plasma discharges generated in the liquid phase, using the Marx pulse generator with new cap nuts, lead to the formation of very unstable discharges. It was stated that, when using new cap nuts in the Marx generator a stabilization step is required. Indeed, in order to obtain stable pulsed plasma discharges suitable for the nanoparticle synthesis, it is necessary to perform a blank run discharge. This blank run discharge has to be carried out in a similar reaction media to the one used for the nanoparticle synthesis and with the same discharge parameters as well.

In order to determine the plasma parameters and process time to be used in the plasma-in-liquid process for silver nanoparticle synthesis, a three-hour synthesis was performed. During three hours, the evolution over process time of the voltage and input energy (per pulse) has been followed, as shown in figure 28a and figure 28b, respectively. It was determined, that for an inter-electrode distance of 3mm, applying a high voltage below 7kV, plasma discharges were not visible, but production of bubbles would occur. Between 7-8kV, light emission from the discharge is observed, but the discharges were not generated regularly. Between 8-9.5kV, discharges occurred regularly and became steady. Filamentary streamer-like discharges appeared on the cathode. Between 9.5-12kV streamer-like discharge connects the anode and cathode through spark discharges. **Therefore a voltage between 8-9.5kV is suitable for this work for generation of stable plasma discharges**.

During three hours of discharge at 8.5kV, the discharges became visually unstable from 30min. This is explained by a decrease in the efficiency of the MARX pulse generator, since input

energy and voltage decreased with an ongoing process time. A discharge lasting three hours with an initial voltage of 8.5kV and energy at 42mJ/pulse is shown in figure 28a and figure 28b, respectively. It is thus pointed out that the process time should not exceed more than 20min, due to great changes in plasma parameters. **A process time between 10-20min is therefore optimal for nanoparticle synthesis with our actual experimental set-up.**

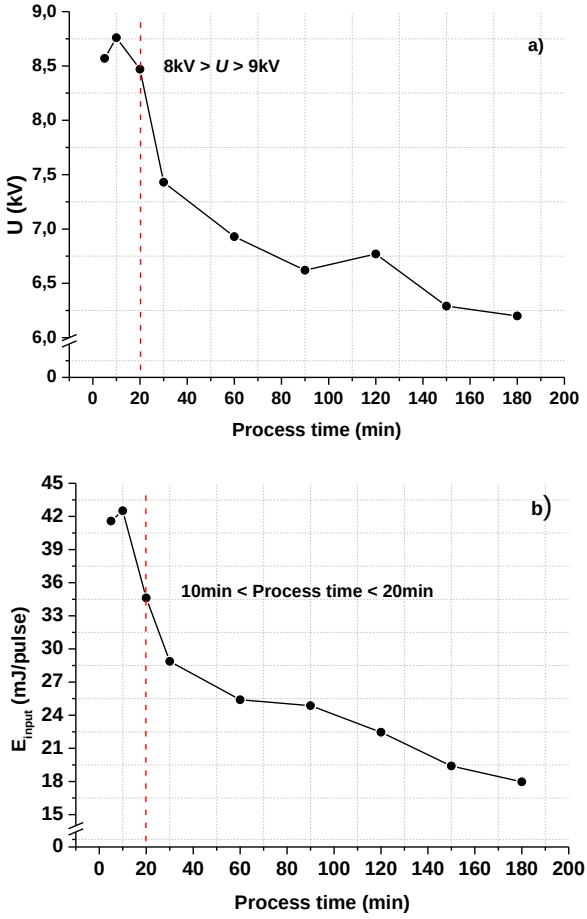

Figure 28: Evolution in a) voltage and b) input energy (per pulse) during a three-hour synthesis of silver-based nanomaterials using a Marx pulse generator

In this work, nanoparticle synthesis using a Marx pulse generator is performed at a high voltage between 8-9.5kV during 20min.

3.2.1.2 Generation of pulsed plasma discharges – *Electrical waveforms*

The resulting electrical waveforms (current, voltage and input energy) that are usually obtained from a DC-pulsed plasma discharge in a plasma-in-liquid process for nanoparticle synthesis are presented in figure 29a-c). The characteristic decrease in the current and voltage signal applies for DC-pulsed discharges in a RCL circuit. The rise time of the voltage was determined to be 35ns. In the first τ = 0.45μs of the current and voltage waveforms, (inset waveforms in figure 29a-b) it is shown that strong oscillations occur and that these oscillation becomes damped until 200ns.

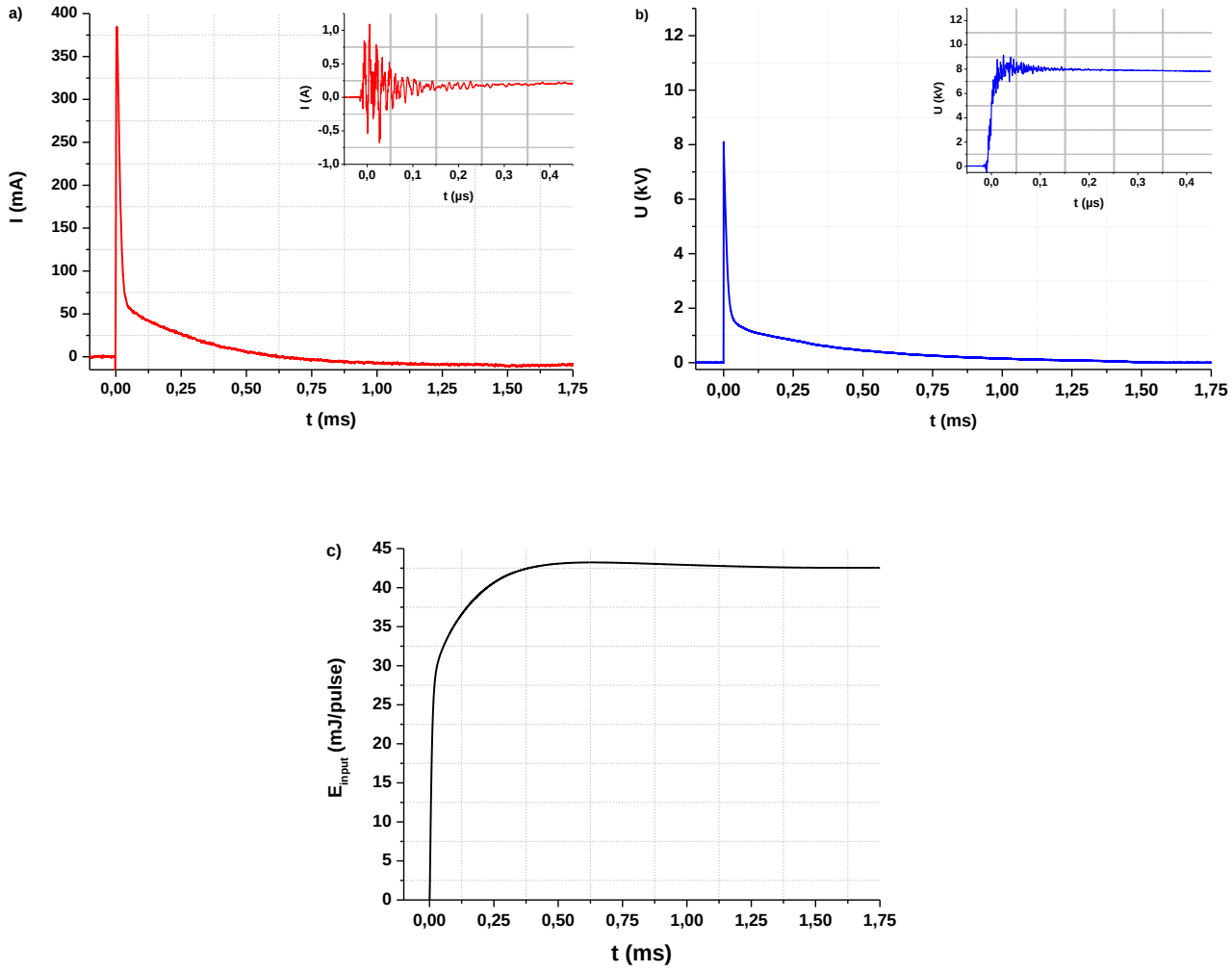

Figure 29: Electrical waveforms of one pulse recorded for 20min plasma discharge in silver nanoparticle synthesis a) Current (τ=1.5ms) and b) voltage (τ=1.5ms) waveforms. Inset current and voltage waveforms shows up to τ=0.45μs. c) Calculated input energy (per pulse) of the plasma-in-liquid process for 20min of plasma discharge.

The input energy of plasma discharges per pulse has been determined using equation 6. This corresponds to the energy that was injected into the discharge occurring in a liquid phase generated in the inter-electrode distance over the duration of a single pulse. The input energy was thus determined by integrating the product of the measured current and voltage values over the pulse duration with an upper integration limit at around 1.5ms. Current and voltage waveforms (τ = 1.5ms) in figure 29a-b have been used for this purpose.

This results in the waveform of a typical input energy (c.f. figure 29c) of DC-pulsed plasma discharges in the plasma-in-liquid process using the Marx pulse generator. The input energy (per pulse) value that is taken into consideration is the one corresponding to a complete pulse profile, around τ = 1.5ms.

$$E_{input} = \int_{t0}^{t} I \cdot U \, dt \qquad \textbf{Equation 6}$$

Furthermore, the injected power of pulsed plasma discharges in a plasma-in-liquid process is likewise determined by applying equation 7:

$$P = E_{input} \cdot f \qquad \textbf{Equation 7}$$

3.2.2 Method 2: Behlke high voltage DC-pulse generator

As an alternative to the Marx pulse generator, a fast solid-state high voltage transistor switch (HTS) has been applied in the generation of high voltage DC-pulsed plasma discharges in the plasma-in-liquid process for silver nanoparticle synthesis.

The device is a HTS 161-06-GSM manufactured by Behlke Electronic GmbH. The electrical characteristics of this device are: max. voltage 2×16kV, max. peak current 2×60A, max. resistance 2×16Ω, and min. pulse duration 150ns (c.f. table 2) *(Behlke Power Electronics GmbH 2018)*.

Table 2: Technical specifications of Behlke HTS 161-06-GSM

Type: HTS 161-06-GSM				
Dimension *(mm)*	**Voltage** *(kV)*	**Peak current** *(A)*	**On resistance** *(Ω)*	**On time** *(ns)*
263×70×35	2×16	2×60	2×16	150 - ∞

This type of device consists of two identical metal oxide semiconductor field effect transistor (MOSFET), which forms a half bridge circuit, also called a push-pull circuit. This circuit does not require large energy storage capacitors, but only current for charging the connected load capacitance. Regardless of pulse width, frequency and duty cycle, the device is precise in the timing of switches. Advantage of applying a Behlke HTS is the fast rise and fall times, and short pulse durations, starting from 150ns. The Behlke pulse generator and its components are shown on figure 30, and the corresponding electrical circuit of the plasma-in-liquid process is shown on figure 31.

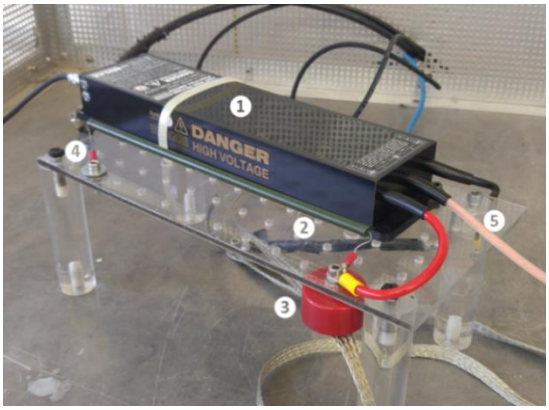

Figure 30: Behlke solid state HV switch applied in PLI process for nanoparticle synthesis. It is composed by: ① Solid power switch from Behlke. ② Ballast resistor (500Ω). ③ A number of capacitors for charging/discharging of HV pulses (1nF). ④ HV DC power generator. ⑤ HV-cable connection to reactor.

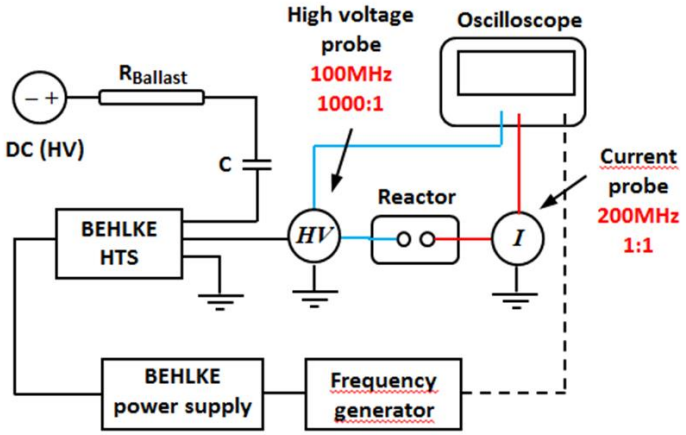

Figure 31: Components of the electrical circuit of the PLI process in method 2 using a Behlke solid-state switch. The solid lines in the circuit are fixed cabling lines. The dashed line is applied in predefining process parameters using the oscilloscope, and is removed during the synthesis.

The process is driven by a 30kV/30mA direct current (DC) positive-polarity HV power supply (TECHNIX CCR-30P450) through a 500Ω ballast resistor ($R_{ballast}$). Pulses are generated by

charging and discharging a 1nF capacitor using a Behlke HV switch (HTS 161-06-GSM, Behlke Electronic GmbH). The Behlke HV switch was powered by a stabilized 5V DC power supply (ALR3003, ELC). Repetition rate of the pulses was adjusted to 50Hz. Discharge parameters (i.e. frequency and pulse duration) are set using a pulse generator (TGP110 10MHz Pulse generator, TT*i*).

3.2.2.1 Generation of HV plasma discharges – *Electrical waveforms*

Current and voltage waveforms that were obtained as a result of the plasma-in-liquid process in silver nanoparticle synthesis using a Behlke pulse generator are presented in figure 32a-c. These waveforms are comparable to those obtained using the Marx pulse generator. The only difference that is observed in Belhke generated pulses is that for a given pulse duration the signal does not reach zero at an equal rate and for this reason a plateau is observed.

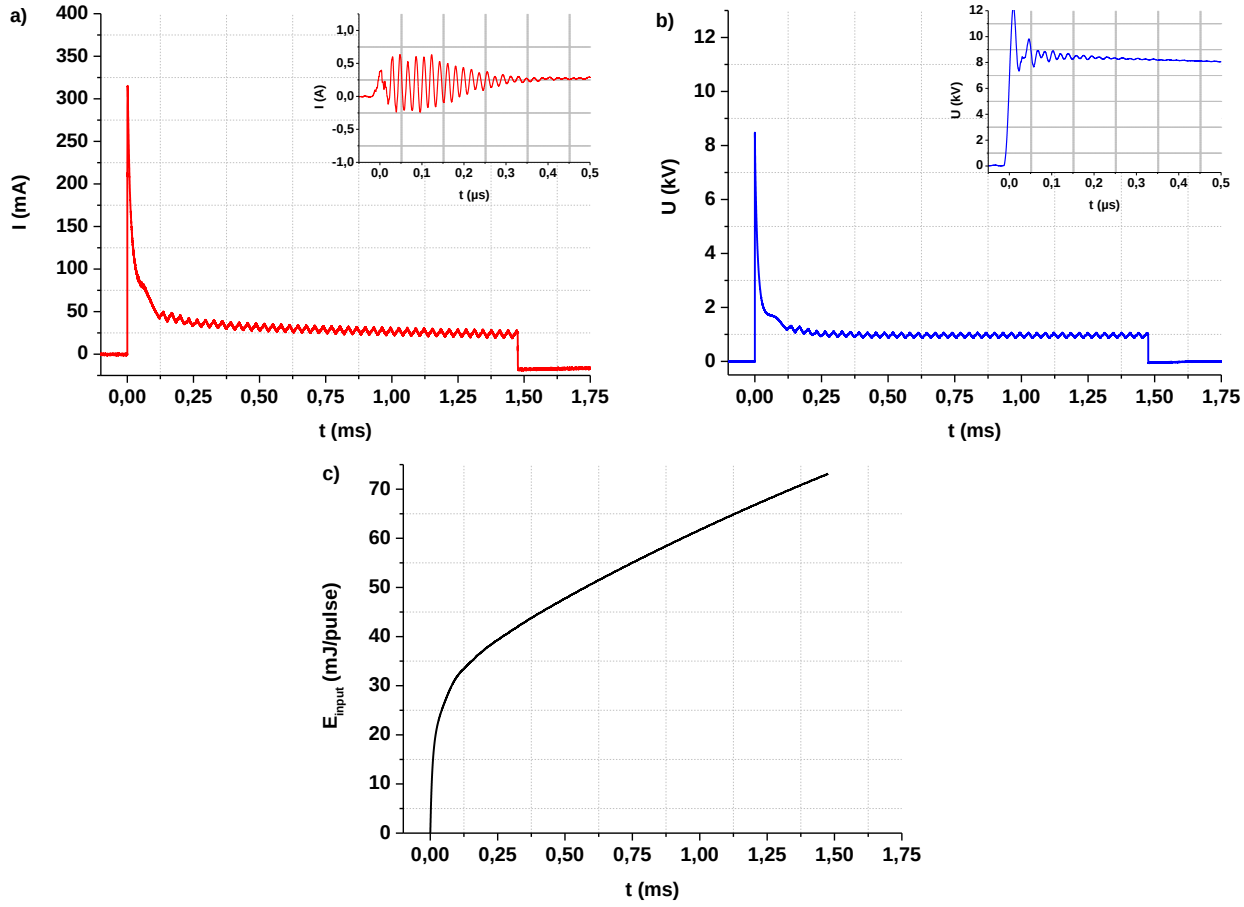

Figure 32: Electrical waveforms of one pulse recorded for 20min plasma discharge in silver nanoparticle synthesis a) Current (τ = 1.5ms) and b) voltage (τ = 1.5ms) waveforms. Inset current and voltage waveforms shows up to τ = 0.50µs. c) Calculated input energy (per pulse) of the plasma-in-liquid process for 20min of plasma discharge.

The input energy of pulsed plasma discharges was likewise determined by applying equation 6 using current and voltage waveforms (τ = 1.75ms) in figure 32a-b. This results in the waveform of a typical input energy (c.f. figure 32c) of DC-pulsed plasma discharges in the plasma-in-liquid process using the Behlke pulse generator. In this case, the input energy (per pulse) value that is taken into consideration is the one corresponding to a pulse duration of τ=1.5ms. Furthermore, the injected power of pulsed plasma discharges is equally determined by applying equation 7.

3.3 Nanoparticle characterization techniques

Up to date, many different kinds of characterization techniques have been developed, and various information about nanoparticle characteristics are readily obtained. In this section, characterization techniques that have been applied in silver nanoparticle characterization will be presented. In addition, preparation of samples for each characterization technique is given. The techniques used for the characterization of the silver nanoparticles concern the following:

Characterization techniques based on laser spectroscopy:

- Ultraviolet-visible spectroscopy (UV-vis)
- Dynamic light scattering (DLS)

Characterization techniques based on electron microscopy:

- Scanning electron microscopy (SEM)
- Transmission electron microscopy (TEM)

Characterization techniques based on particle composition and elemental analysis:

- X-ray diffraction (XRD)
- Electron dispersive X-ray spectroscopy (EDX)
- X-Ray Photo-electron Spectroscopy (XPS)

3.3.1 UV-vis spectroscopy

Ultra**v**iolet-**vis**ible (UV-vis) spectroscopy is a technique that can be used to quantify scattered incident light by a solution containing particles (e.g. colloidal solution). A set-up of UV-vis spectrometer is shown in figure 33. In general, a UV-vis spectroscopy measurement is carried out by irradiating a sample with a light beam. The light beam travels through fiber optics cables and passes through a sample of 1cm light pathway.

The scattered light beam reaches the spectrometer and is collimated by a mirror. A grating diffracts the collimated light, and is passed towards a second focusing mirror, and projects the spectrum onto a linear detector array *(Avantes 2015)*. The collected data are graphically visualized by the software as the amount of light absorbed or transmitted as a function of wavelength. Information about nano-scaled particles obtained by UV-vis spectroscopy depends on factors related to particle characteristics, including size, shape, and composition.

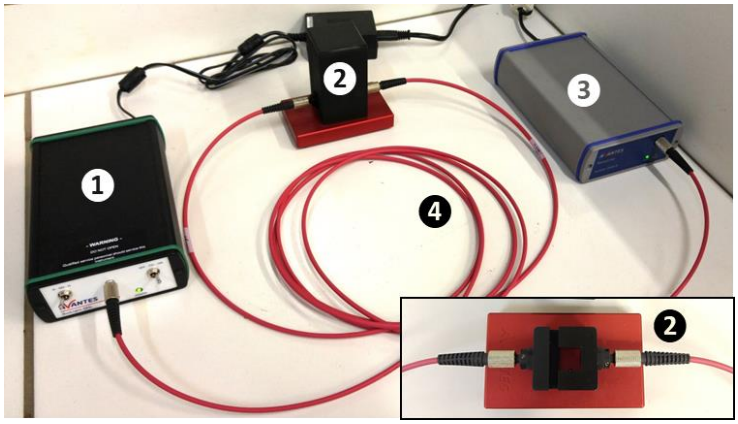

Figure 33: UV-vis spectrometer ① Light source of Deuterium and halogen lamp, ② Sample holder (Inset shows a beam pathway, ③ Spectrometer, and ④ Fiber optics cable connections.

For instance, the wavelength at which a maximum of light is absorbed (λ_{max}) by the particles depends on the compound and its size. Furthermore, the intensity of light absorption depends on the number of particles absorbing light. A majority of elements absorbs light in the ultraviolet region, whereas some elements (e.g. Au, Ag, and Cu) in the nanoscale size range show particular optical properties and absorb light in the visible region of the electromagnetic spectrum *(Creighton and Eadon 1991)*. When an incident light of an appropriate amount of energy irradiates atoms or molecules, electrons get excited and transition to a higher energy level, which results in emission of energy corresponding to a certain wavelength in the electromagnetic spectrum.

The advantage of UV-vis spectroscopy is that it is a non-invasive and non-destructive technique. The disadvantage is that interferences may occur from the sample turbidity *(Pacioni et al. 2015).*

Principle

For quantitative measurements in UV-vis spectroscopy the Beer-Lamberts law is applied for the determination of the element concentration. Beer-Lamberts law states that the concentration (c) of an element is directly proportional to the absorbance (A) of the solution:

$$A = kcL \qquad \textbf{Equation } \boldsymbol{8}$$

Where L is the light pathway, and k is the extinction coefficient, which depends on the interaction between the element and the wavelength of the light source (c.f. figure 34). Absorbance is related to transmittance (%T) and is explained by the following equation:

$$A = \log\left(\frac{I_0}{I}\right) = \log\left(\frac{100}{T}\right) \qquad \textbf{Equation } \boldsymbol{9}$$

This is explained with an incident light source of intensity (I_0) irradiating particles and transmitting light of intensity (I).

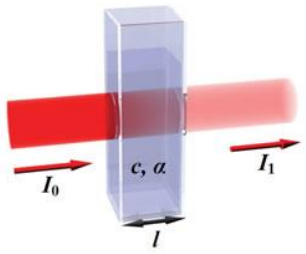

Figure 34: Illustration of a cuvette explaining the Beer-Lamberts law. Reproduced form *(APS Physics 2018)*.

UV-vis spectroscopy was applied as a qualitative characterization technique. This technique is mainly applied for determining the presence of AgNP, which is determined due to a significant color change in which the wavelength of light absorbed by particles corresponds to that of the **S**urface **P**lasmon **R**esonance of AgNP.

In this context, absorbance is determined by UV-vis absorption spectroscopy composed by a spectrometer (AvaSpec-2048 XL, Avantes) combined with a deuterium-halogen light source (AvaLight-DHc). Prior to the analysis, particles are placed in an ultrasound bath during 10min in order to eliminate agglomeration. 2mL of the AgNP solution is transferred into a 10mm×10mm quartz cuvette, and placed in the sample holder. The analysis is performed using an auto-

integration mode (integration time: 13.97ms, average of 36 scans, and 2 smooths) on the Avalight software in the wavelength range 350-800nm.

3.3.2 Dynamic light scattering

Dynamic **L**ight **S**cattering (DLS), also known as **P**hoton **C**orrelation **S**pectroscopy (PCS) is a technique for measuring the size of sub-micron particles in suspension (e.g. colloids). Particle size is determined by the measurement of particles diffusing in a random motion caused by the collision of surrounding molecules in a solvent as a function of time. This random particle movement is known as the **Brownian motion**. When **laser beam** passes through the **sample**, the beam is scattered in every direction by diffusing particles, and results thus in intensity fluctuations in the scattered laser beam around a mean value. The intensity of scattered laser beam is collected by a **detector** at a certain detection angle and particle size is determined based on these information (c.f. figure 35). The detector is very sensitive, and gets easily saturated if too much light is detected *(Malvern 2014)*. Here, particle concentration and size is of charge. High particle concentration or large particles increase the scattering intensity in contrast to low particle concentration or small particles that has a decreased scattering intensity of the laser beam. To prevent saturation of the detector an **attenuator** is used.

The attenuation will decrease to pass reduced amount of light through the sample to the detector as particle concentration is too high or the sample contains larger particles. Scattering intensity signal are then passed to the **correlator** for deriving the rate at which the intensity is varying. Based on this information the **software** derives particle size information. The advantages of DLS are that it is a simple and rapid characterization technique, it is non-invasive and non-destructive, and it requires small sample volumes. The disadvantage is that it has limitations for measuring poly-dispersed particles (in case of 90° detection angle) *(Pacioni et al. 2015)*.

Particle size information differs with respect to particle state all depending on detection angle of the scattered light. The 90˚ of scattered light detection is the classical technique, and is generally applied in determining the size of samples consisting of monodisperse particles. Another possibility is to detect scattered light at 173˚. This technique is known as the backscatter detection, or **N**on-**I**nvasive **B**ack-**S**catter (NIBS). Backscatter detection technique is useful in

order to reduce multiple scattering effects. This is to prevent the scattered light from being re-scattered by other particles.

Reduction of multiple scattering effect, and thus allows higher concentration to be measured (scattered light from one particle is itself scattered by other particles). Effect of dust is greatly reduced, since large particles mainly scatter in forward direction *(Malvern 2014)*.

Table 3: Detection angles in DLS particle size measurement techniques. *(Malvern Instruments Ltd 2018)*.

Detection angle	Method
90˚	90 degrees
173˚	Backscattered detection – NIBS

Furthermore, DLS technique uses the speed of particles in solvent to determine particle size. Speed limiting parameters of particle diffusion as solvent temperature and viscosity are thus of importance, and is taken into consideration for particle size determination, as expressed in Stokes-Einstein relation (c.f. equation 13). In theory, smaller particles move faster as a function of time than larger particles.

The instrument that was used in the characterization of the nanoparticle solutions is a Zetasizer Nano S90 equipped with a red He-Ne gas laser (λ=632.8nm). This DLS model is suitable for measurements of particles in the size range 1nm to 3µm (in hydrodynamic diameter). The particle scattering angle of the laser is detected at an angle of 90˚, and particle sizes are determined by fitting of an autocorrelation function (ACF) that is in agreement for monodisperse particles.

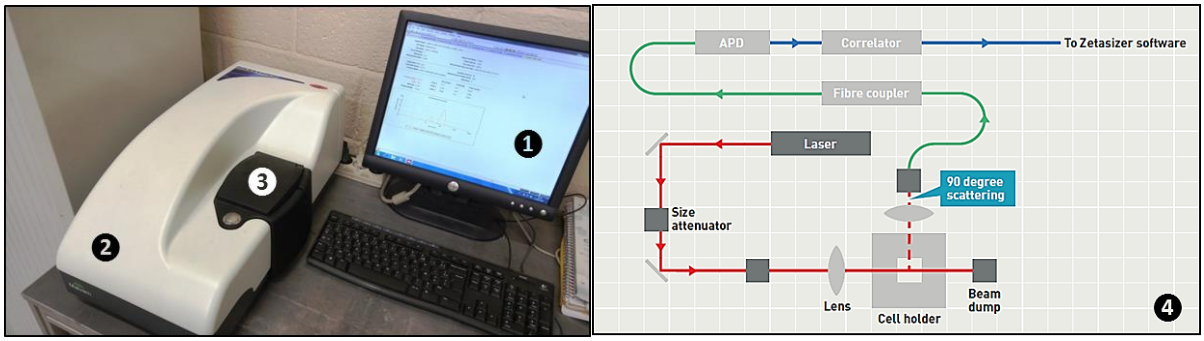

Figure 35: DLS technique illustrated. ① DLS software, ② DLS instrument, ③ Sample chamber, ④ Mechanism of DLS showing the positioning of each component *(Malvern Instruments Ltd 2018)*.

Principle

From the scattered light intensity signals it is possible to gain information about particles by photon correlation spectroscopy (PCS). PCS is based on the analysis of the (ACF) G(τ) calculated from the light intensity fluctuations and is given by:

$$G(\tau) = \langle I(t+\tau) \cdot I(t) \rangle \qquad \textbf{Equation 10}$$

Where I(t) is the scattered intensity light at time t and ⟨...⟩ represents the average over time.

For a monodisperse particle suspension, it has been well established that the ACF is given by a decaying function:

$$G(\tau) = \exp(-\Gamma\tau) \qquad \textbf{Equation 11}$$

With Γ the decay rate given by:

$$\Gamma = Dq^2 \qquad \textbf{Equation 12}$$

Where q is the scattering vector and D is the translational diffusion coefficient.

Then by using Stokes-Einstein relationship, the particle size d can be calculated as:

$$d = \frac{kT}{3\pi\eta D} \qquad \textbf{Equation 13}$$

Where k is the Boltzmann's constant, T is the absolute temperature and η is the viscosity of the solvent. Therefore, by fitting the ACF one can obtain the decay rate Γ and from equation 12 and equation 13 deduce the particle size. This is only valid for very narrow particle size distributions.

In the case of polydisperse particle suspensions, a more complex data evaluation is needed to extract the particle size distribution (PSD) from the raw data. For a polydisperse particle distribution, equation 14 can be written as a Laplace transform:

$$G(\tau) = \int_0^{+\infty} C(\Gamma) \exp(-\Gamma\tau)\, d\Gamma \qquad \textbf{Equation 14}$$

Where C(Γ) represents the distribution of decay rates due to the PSD. Several methods have been developed to solve the inverse problem of equation 14. The most widespread method is

based on the fitting of the ACF by the Non Negative Least Squares technique. *(Mailer, Clegg, and Pusey 2015)*

Prior to the DLS analysis, the colloidal solution is transferred into an ultrasound bath (Branson 1200, 47kHz) during 10min in order to eliminate possible agglomeration of silver nanoparticles. 1mL of the AgNP solution is transferred into a 10mm×10mm quartz cuvette, and placed in the DLS sample chamber. The measurement is performed using an automated mode for which number of runs is adjusted by the DLS software with respect to the amount of scattered light detected.

3.3.3 Scanning electron microscopy

Scanning electron microscopy (SEM) is an electron microscope technique for which high energy electron beam is focused on a surface of a solid sample and scanned over a small surface area (c.f. figure 36). Interaction between electron beam and surface atoms and molecules of a sample generates signals including secondary electrons, back-scattered electrons, and X-ray, which provides information about sample topography, composition, conductivity, etc. It is a requirement in SEM characterization that the sample is conducting the electron beam. Non-conductive samples are usually being coated with a thin layer of conductive material in order to prevent accumulation of static electric charge on the surface *(M. Joshi, Bhattacharyya, and Ali 2008).*

An advantage of SEM is that it is a technique which provides observation of sample morphology at higher magnification, higher resolution and focus in comparison to optical microscopy. Having a lower resolution than TEM, SEM is able to image nanoparticles of bulk surfaces and for direct visualization of nanocrystals in larger assemblies. Disadvantages in SEM are charge effects of semi-conducting materials caused by the accumulation of static electric fields, a destructive technique towards particles, and incompatible with liquids samples. *(Pacioni et al. 2015), (M. Joshi, Bhattacharyya, and Ali 2008).*

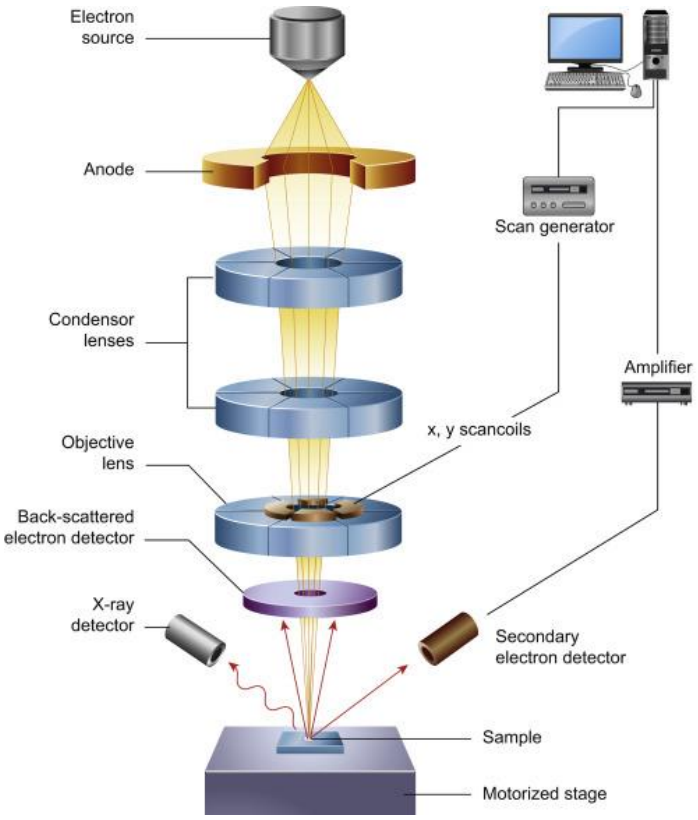

Figure 36: Principles in SEM. Reproduced from *(Inkson 2016)*.

In this work, a field emission gun (FEG)-SEM (Carl Zeiss, Supra VP40 FEG-SEM) was used to characterize the morphology of the silver nanoparticles under vacuum mode. The field emission gun is of the Schottky type with W/ZrO filament being heated at 1800°K.

SEM characterization of silver nanoparticles has been realized by transferring silver nanoparticles from liquid to solid state. In this regard, silver nanoparticles were deposited onto the surface of borosilicate glass plates as support. Prior to the deposition, the glass plates have been treated in concentrated H_2SO_4 (ICH Chimie, 95-97%) by immersion of the plates in acid for 4h at T_{amb}. After 4h of acid treatment, the glass plates are rinsed thoroughly by soaking them in deionized water until a neutral pH value is obtained. Finally, the glass plates are dried overnight at 80°C.

The sample for SEM characterization is prepared by immersion of a surface treated glass plate (10mm×10mm×1.1mm) into a solution of as-synthesized silver nanoparticles for 1h. Then, the

glass plate is rinsed from excessive particles and unreacted ions by immersion in deionized water for 2 minutes. The silver deposited glass plates are then dried in the oven overnight at 80°C.

Prior to SEM characterization, the glass plate is attached onto an aluminum stub by applying a carbon-based adhesive. In order to make sure that the adhesive is dry and organic solvents have been degassed from the adhesive, the sample is dried at 45°C for 30min. In order to avoid charge effects from the sample, the surface of the glass plates is coated with a thin-layered metallic carbon film of 25Å thickness. This was realized by using a precision etching coating system (Model 682, Gatan) for which film thickness was monitored using a film thickness monitor (Model 681-20000, Gatan).

3.3.4 Energy dispersive X-ray spectroscopy

Energy dispersive X-ray spectroscopy (EDS) is a technique used for performing elemental analysis of particles in solid samples. This technique is accomplished by coupling a sensitive X-ray detector with i.e. SEM. The electron beam (10-20keV) causes X-rays emission from the sample. Screening of samples gives rise to variation in emitted X-ray energy, which is due to X-ray energy emissions being distinguished by elements. It is also possible to estimate proportions of detected elements based on intensity of emitted energy. The resulting EDS analysis over a scanned area of a sample is observed as an X-ray spectrum with Y-axis representing number of counts, and X-axis representing energy levels. *(M. Joshi, Bhattacharyya, and Ali 2008),*

Principle

Moseley's law is the basis for elementary analysis by EDS spectroscopy. By measuring the energy of a given K, L, or M line, it is possible to determine the atomic number of a given element. As the characteristic radiation energy within a given series of lines varies with atomic number, Moesley's law is given by the following: *(Hafner 2006)*.

$$E = C_1(Z - C_2)^2 \qquad \textbf{Equation 15}$$

Where E: Energy emission line for a given X-ray series, Z: Atomic number, and C_1 and C_2 are constants.

Composition of nanoparticles was also determined by employing an EDS-equipped SEM instrument (SEM S440, Leica) with a tungsten filament. The resulting nanoparticle product was

separated from the reaction media batch-wise by centrifugation (Eppendorf, Centrifuge 5804) at 10000rpm for 30min. The supernatant solution was decanted and discarded, once it was ensured that silver nanoparticles were not present. The sediment was washed three times with deionized water by following the above-mentioned centrifugation procedure and dried overnight at 80°C. Once particles have been dried, a small amount of the recovered powder was attached onto an aluminum SEM stub using a double-sided adhesive carbon tape.

3.3.5 Transmission electron microscopy

Transmission electron microscopy (TEM) is an electron microscope technique, which transmits a beam of electrons through a thin sample, as observed in figure 37. The sample is prepared as a thin film in order to let the electron beam penetrate the sample. Electron beam is diffracted by crystalline particles. Diffraction intensity depends on the orientation of crystal planes and atoms. At some angles the beam is diffracted strongly or being transmitted completely *(M. Joshi, Bhattacharyya, and Ali 2008)*.

From this interaction, an image of particles is formed, which is then magnified and projected onto a fluorescent screen and captured by a high-speed CCD camera. TEM reveals detailed morphological information about shape and size of microstructural phases.

Furthermore, information about crystallographic structures is obtained by high- resolution electron microscopy (HR-TEM). High resolution imaging can detect the presence of certain crystalline defects, and thus providing a measure of the lattice spacing and crystallographic parameters. The main advantage of the HR-TEM is the direct observations of detailed nanostructures (up to 0.1nm) due to high resolution. One disadvantage of TEM is the time-consuming sample preparation process. The disadvantages in TEM characterization techniques are same as those mentioned for SEM *(Pacioni et al. 2015)*.

As-synthesized particles are kept under dark and cold conditions (4°C). Prior to sample preparation, the silver nanoparticles solution is transferred into an ultrasound bath for 10min in order to eliminate possible agglomeration. A drop of the solution was drop-casted onto a carbon coated cupper TEM grid and dried at ambient pressure and room temperature. Nanoparticle morphology was performed using a TEM JEOL 2010 operated at 200kV with LaB6 filament.

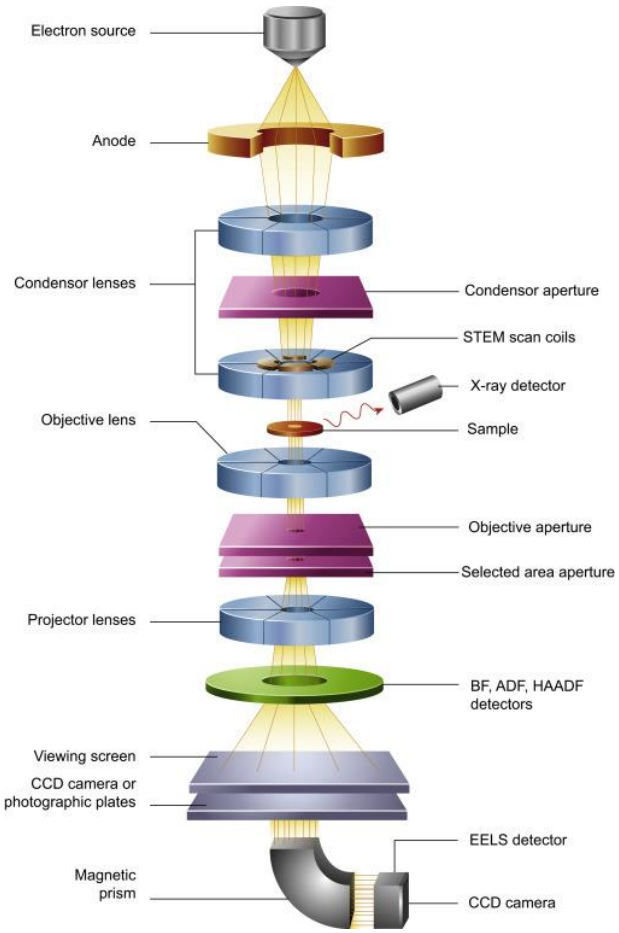

Figure 37: Principles in TEM. Reproduced from *(Inkson 2016)*.

3.3.6 X-ray diffraction

X-ray diffraction (XRD) is a technique which is used for determining crystallinity, crystallite, orientation of crystallites, and phases of particles. This is possible, as each crystalline particle, including metal, metals oxides, semi-crystalline polymers, etc., possesses a characteristic crystallographic structure, and hence a characteristic diffraction pattern. This technique is based on the diffraction of incident X-rays by crystal lattice in different directions. Diffraction occurs in a given direction when the scattered beam from a crystallographic plane is in phase with scattered beam from the adjacent planes of the crystal. This results in constructive interference of the scattered light, which thus gives rise to an enhancement and reinforcement of the X-ray beam. Diffracted X-rays are detected by a detector placed on the opposite direction which is in agreement with the Braggs law. The advantage of XRD is that this technique is non-destructive, and it is possible to apply this technique for a large group of materials *(Das, Ali, and Hamid*

2014). Disadvantages in XRD technique is the low intensity of diffracted X-rays compared to electron diffractions *(X.-F. Zhang et al. 2016)*.

Principle

Different geometries are commonly used for X-ray diffraction. For the reference method, called the θ-2θ geometry, the sample forms an θ angle with the incident beam, and an θ angle with the diffracted beam, so there is a 2θ angle between the incident and diffracted beams (see figure 38). The geometry used for this study is slightly different, using the asymmetric Bragg-Brentano geometry, or ω-2θ geometry, where the incident beam has a constant ω angle with the sample, and a curved detector analyzes the whole diffraction pattern simultaneously.

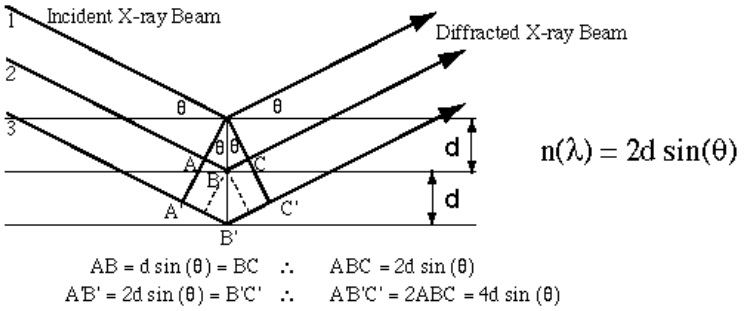

Figure 38: Principles in XRD. Reprinted from *(Iowa State University 2018)*

When X-rays are incident on a crystal, different lattice planes causes simultaneous reflections of the X-ray beam. These simultaneous reflections may cause constructive or destructive interference depending on the angle of incidence of X-rays. This law is called the Bragg's law:

$$n\lambda = 2dsin(\theta) \qquad \textbf{Equation 16}$$

Where d: separation between the planes of the crystal;

θ: the X-ray incident angle (or half the 2θ angle in e.g. the ω-2θ geometry);

λ: X-ray wavelength

Elemental analysis, crystallinity and phase of AgNP were determined by XRD (equinox 1000, INEL) with an X-ray radiation source CoKα_1 (λ=1.789Å). Preparation of samples for XRD analysis was performed following the same procedure as described in the section concerning

SEM-EDS. Particles were dried and collected by re-dispersion in ethanol. For the XRD analysis, particles were drop-casted onto a microscope glass slide. The characterization was performed at ambient temperature and atmospheric pressure.

3.3.7 X-ray photoelectron spectroscopy

X-ray photoelectron spectroscopy (XPS) is a powerful surface characterization technique, which is used for analyzing the surface chemistry of materials. Among other measurements, XPS is used for determination of elemental composition, empirical formula, chemical state and electronic state of elements in a material. An XPS spectrum is obtained by irradiating a solid surface with a beam of X-ray, while simultaneously measuring kinetic energy (KE) and number of emitted electrons 10nm above surface elements of sample being analyzed.

Energies and intensities of the photoelectron peaks enable identification and quantification of all surface elements (except hydrogen and helium) *(Thermo Scientific 2018)*.

Principle

In XPS, sufficient amount of energy is put into the irradiation of atoms and molecules with an X-ray beam for ensuring that electrons are ejected. Kinetic energy depends on photon energy and binding energy of electrons, which is the energy required to remove electrons from surfaces (see figure 39).

It is possible to determine the binding energy of electrons, since the energy of X-ray beam is known, with equation 17:

$$E_{Binding} = E_{Photon} - E_{Kinetic} - \Phi \qquad \textbf{Equation 17}$$

Where:

$E_{binding}$: energy of the electron being emitted from the electron configuration within an atom,

E_{photon}: energy of X-ray photons,

$E_{kinetic}$: energy of emitted electron measured by the instrument,

Φ: work function of the spectrometer

The binding energy depends on the element from which the electron is emitted, the orbital from which the electron is ejected, and the chemical environment of the atom from which the electron was emitted *(Thermo Scientific 2018).*

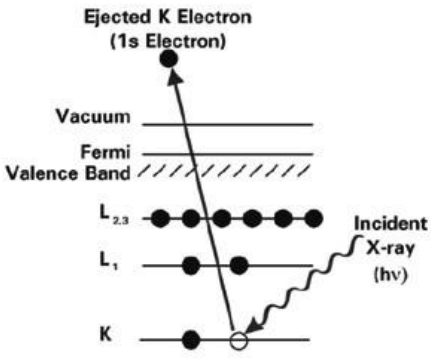

Figure 39: Principles in XPS. Reproduced from *(Thermo Scientific 2018)*

XPS analysis was performed in order to determine whether silver nanoparticles were produced in the form of oxidized silver particles as a result of the plasma-in-liquid process. The analysis was performed by the XPS responsible Philippe Decorse at the laboratory of ITODYS, University of Paris Diderot. Particles were analyzed using an XPS (K-alpha^{+}, ThermoFisher Scientific) with an X-ray radiation source AlKα (1486.6eV) at 200W was obtained. A survey spectrum (0-1000eV) and a high resolution spectrum of Ag3d electron configuration within the atom being observed were obtained. Preparation of samples for XPS analysis was performed following the same procedure as described in the XRD section.

3.4 Conclusion

The experimental set-up presented in this chapter is aimed for the synthesis of silver nanoparticles using a technique based on the generation of plasma discharges in a liquid solution. The synthesis of nanoparticles is realized through the reduction of metal ions without the addition of any reducing agent. In this chapter, two methods for the generation of HV DC-pulsed plasma discharges in the liquid phase are proposed. The first method is to utilize a conventional Marx pulse generator charged and discharged by a ceramic capacitor (1nF). The second method is to utilize a Behlke solid-state HV switch. Challenges in plasma generation in a liquid phase have been encountered, and further discussed. Optimal experimental parameters of the discharge (i.e. voltage and duration of nanoparticle synthesis) were defined from syntheses performed using the Marx pulsed generator. A common experimental procedure for the nanoparticle synthesis has been developed.

The different techniques used for nanoparticle characterization were presented, and the sample preparation procedure explained.

Chapter IV – Synthesis of silver nanoparticles by a pulsed plasma discharge in liquid (PLI): In the use of a MARX pulse generator

The main purpose of chapter IV is to perform a parametrical study on silver nanoparticles production with focus on the physicochemical parameters of the solution. The production is carried out with a newly laboratory-developed PLI process in the application of a Marx pulse generator. The implementation of a Marx pulse generator is due to the fact that it is a low-cost product in comparison to high-cost *solid state switch* pulse generators. **One of the questions that will be answered in this chapter is whether the Marx pulse generator is an efficient alternative to solid state switches.** To answer this question, a parametrical study with main focus on the influence of the solution physicochemical characteristics on the particles synthesis will be performed. From a literature review, physicochemical parameters that are known to influence the nucleation and growth mechanism of silver nanoparticles have been selected.

With this study, it will be the first time that the newly laboratory-developed PLI process will be used to produce silver nanoparticles. It is therefore important to confirm the nature and composition of particles resulting from the PLI process. Research groups *(Burakov et al. 2015)* and (Heon Lee, Park, Kim, et al. 2014) working with plasma-based processes documents the production of oxidized metal particles, which is of no interest in the current work. Prior to the parametrical study, it is therefore important to confirm that this process results in the production of **metallic** silver nanoparticles. The most common techniques to examine the nature and composition of particles are by performing particle characterization and elemental analysis. Particle characterization techniques that are applied in this study comprise of XRD, SEM-EDS and XPS, which are all powerful techniques resulting in important information that are required to proceed this study.

With this parametrical study, it is of question, whether the PLI process can be optimized to produce spherical and small-sized (<20nm in diameter) silver particles of uniform distribution. To be able to answer this question, the parametrical study is initiated by the investigation of the silver precursor concentration (i.e. $AgNO_3$). This study is followed by the investigation of the effect of using a stabilizing agent (i.e. PVP) on the synthesized nanoparticles, and the influence

of its concentration. The final parameter that will be investigated is the influence of the initial pH of the precursor solution.

4.1 Particle characterization and elemental analysis of silver-based nanomaterials

Silver-based nanoparticles are produced from a newly laboratory-developed PLI system using a Marx pulse generator. The Marx pulse generator is the component that allows generating DC-pulsed plasma discharges in a liquid phase. At this point, composition of the resulting product is not known. In order to determine its nature and composition, particle characterization and elemental analysis are performed. Particle characterization techniques that are applied in this study require a given amount of product, in a dry and powdered state. The amount of product obtained from a 3 hours-time plasma discharge process was sufficient in order to perform the characterization of the resulting particles. The particle synthesis and sample preparation are presented below.

In the production of silver particles, a 100mL aqueous silver precursor solution of 2mM $AgNO_3$ is prepared without adding any other chemical compound (pH 5 and σ=300µS/cm). Two platinum wire electrodes (d=200µm) of 3mm in inter-electrode distance are horizontally immersed in the $AgNO_3$ precursor solution, in a pin-to-pin electrode configuration (c.f. figure 40a). Plasma discharges are generated in the precursor solution by applying an 8kV high voltage DC pulsed-plasma discharge (f=50Hz) between the high voltage electrode (anode) and the ground electrode (cathode). The generated pulsed plasma discharges resulted in partial corona discharges appearing at the cathode tip, as shown in the inset image of figure 40b. The applied high voltage is measured on the anode through a high voltage probe, and the current is measured on the cathode, through a current probe. Characteristic *U*- and *I*-waveforms from the pulsed plasma discharge are presented on figure 40b, showing an exponential decrease as a result of capacitive discharge of an RLC circuit.

During 3 hours of plasma discharge, dark-colored particles were produced and did sediment at the bottom of the reactor, as shown in figure 40c. A close observation of the resulting particle sediments is performed through SEM characterization. From the SEM micrograph on figure 40d,

it is revealed that **particle sediments are agglomerates of large-sized particles with particle diameter above 200nm**.

Particle characterization techniques that have been performed to obtain information on particle nature and composition include XRD, SEM-EDS and XPS. As an exception, XPS was performed by XPS responsible Philippe Decorse at the laboratory of ITODYS, University of Paris Diderot. Particles were collected through centrifugation (30min, 10000rpm), and hereafter rinsed in de-ionized water. Prior to characterization, particles were dried and re-dispersed in ethanol. In the case of XRD and XPS techniques, particles were drop-casted on a microscope slide. In the case of SEM-EDS, dry particles were attached onto the sample holder.

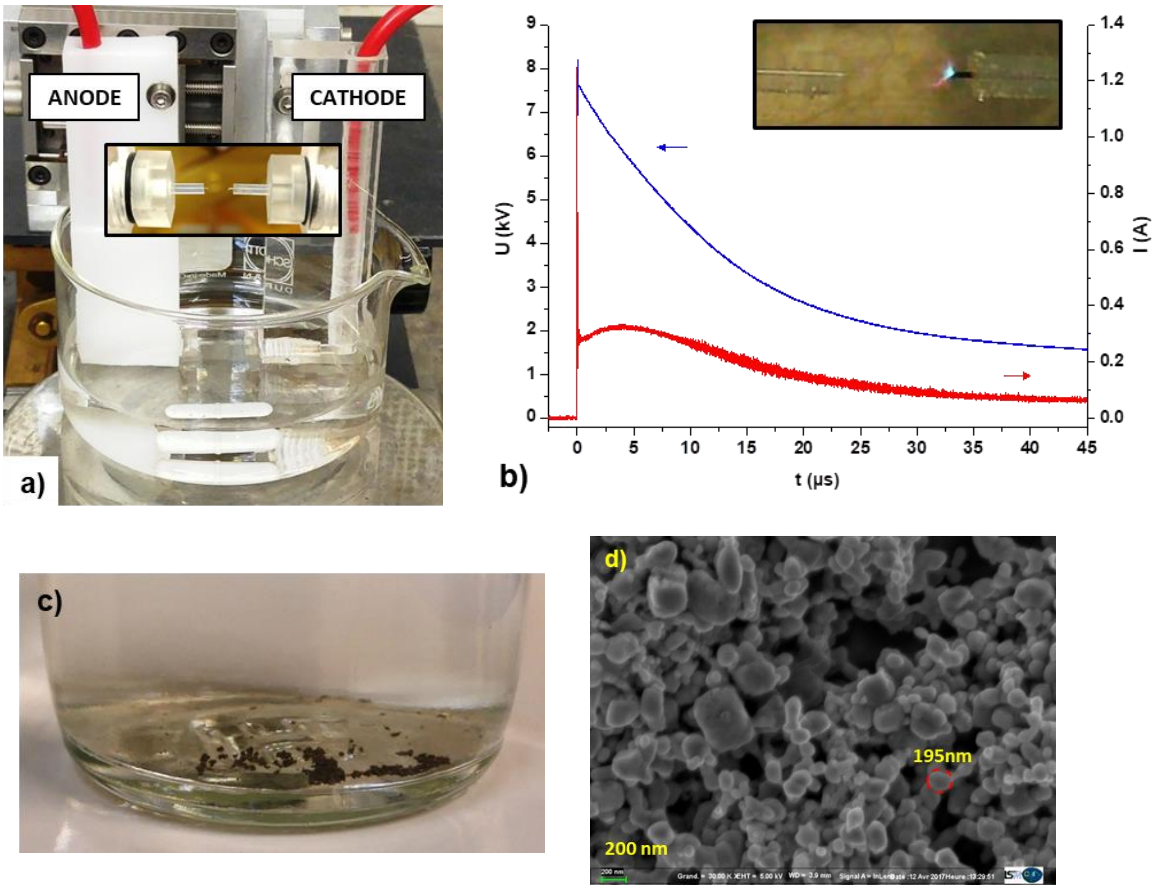

Figure 40: a) Experimental set-up and electrode configuration of the newly-developed laboratory PLI process. b) Characteristic U-I waveforms of pulsed plasma discharge. Inset image shows visibly corona discharges in the liquid phase. c) Dark-colored particle sediments in the aqueous solution as a result of a 3 hour plasma discharge. d) SEM micrograph of dark-colored particle sediments (magnification 30kX)

XRD is performed in order to investigate structural properties of the powdered nanomaterial. This includes determination of phases and the lattice parameter. The resulting XRD pattern was obtained from the reflection of an incident X-ray beam ($CoK\alpha_1$, λ= 1.789 Å) on atomic planes following Bragg's law. In order to determine crystallite structure and lattice parameter, a Rietveld refinement analysis was carried out using the MAUD software *(Lutterotti 2010)*. Rietveld refinement is a tool that is used to obtain a full powder diffraction profile based on crystal structure, sample, and instrument effects. In order to minimize the difference between the calculated and the experimental powder diffraction pattern, parameters are varied using a least-square method. A comparison of the peak locations of the XRD pattern with diffraction peak locations of different silver components found on the **I**nternational **C**enter for **D**iffraction **D**ata (ICDD) was performed using the MATCH software. The diffraction pattern for which the diffraction peaks are in close proximity to the obtained experimental diffraction pattern is ICCD no. 04-016-6676 for metallic silver. The refinement analysis was performed by importing the **C**rystallographic **I**nformation **F**ile (CIF) corresponding to metallic silver (ICDD, no. 04-016-6676) into MAUD. Initially, the background of the diffraction pattern was fitted by a fourth order polynomial function by refinement of the background. Location of peaks was corrected in terms of shifts by successive refinements. Finally, parameters on crystallographic structure were refined. The resulting Rietveld refinement of silver particles is shown on figure 41. Experimental values are represented by blue dots, while refined diffraction pattern of metallic silver is represented by the red line.

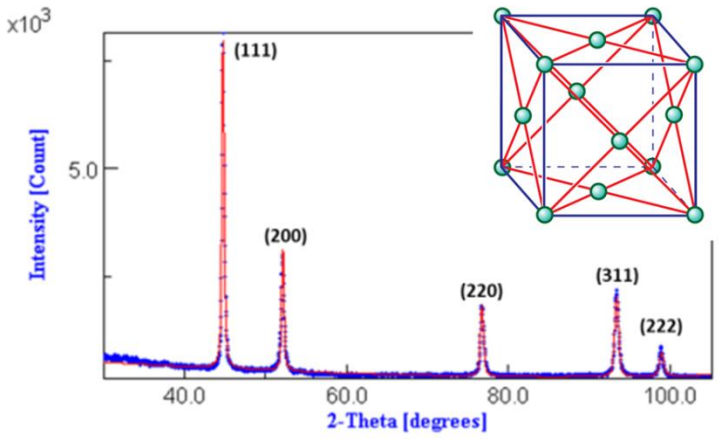

Table 4: Resulting diffraction peaks and corresponding miller indices of silver nanopowder

2θ of peaks ***(deg)***	**Miller indices** ***(hkl)***
44.75	(111)
52.03	(200)
76.70	(220)
93.25	(311)
98.55	(222)

Figure 41: Rietveld refinement of silver-based nanoparticles obtained after 3h PLI process. Red line represent the theoretical diffraction pattern of metallic AgNP from ICDD, no. 04-016-6676, while blue dots represents experimental values. Inset image: FCC crystal structure of silver.

The resulting diffraction peaks at 2θ values of 44.75˚, 52.03˚, 76.70˚, 93.25˚, and 98.55˚ were indexed as (111), (200), (220), (311), and (222) crystallographic planes, respectively, in the **F**ace-**C**entered **C**ubic (FCC) structure of silver (see inset image on figure 41). The lattice constant determined from the refinement is 4.078Å, which is in good agreement with ICDD, no. 04-016-6676 of crystalline silver. The crystallite size have been like-wise determined from the Rietveld refinement. The crystallite size is around 60nm and refers to the size of a single crystallite of a particle.

The resulting diffraction pattern of the powdered silver particles revealed that a monophasic compound **without impurities from other elements was produced**. Furthermore, it is also determined from the diffraction pattern that the PLI process did not result in the production of crystallized silver oxide particles. If silver oxide was produced, diffraction peak of crystalline oxide from the silver oxide would be detected and would have appear in the 2θ range of 35-40°, which corresponds to the (110) lattice plane *(Ananth and Mok 2016)*.

From the above experimental results, it is thus concluded that the resulting powder is in good agreement with XRD diffraction pattern of metallic silver.

SEM-EDS particle characterization technique is also performed on the silver nano-powder to provide further evidence on elemental composition of the resulting product. The peaks that are observed in the SEM-EDS spectrum in figure 42, at around 3keV, correspond to metallic silver (Ag-Lα1). More precisely, the X-ray emission lines (see table 5) that define metallic silver are all present in the spectrum on figure 42, and are located at 2.633keV (Ag-L1), 2.984keV (Ag-Lα1), 3.151keV (Ag-Lβ1), 3.348keV (Ag-Lβ2), and 3.520keV (Ag-Lγ1) *(Bearden 1967)*. The peak appearing at 0.277keV corresponds to the emission line of carbon (C-Kα1) and is significantly lower in intensity in comparison to emission lines of silver. The carbon peak is present as a consequence of the sample preparation, since a conductive double-sided carbon tape was used for the adhesion of the particles onto the aluminum SEM stub. The absence of an oxygen peak at 0.525keV (O Kα1) is an additional confirmation of the absence of metallic oxides in the powder.

Similar EDS results with silver emission lines at around 3keV were obtained by *(Tien et al. 2010)*. In their study, they produced metallic silver nanoparticles using an arc discharges were generated by sending DC-pulsed discharges of low voltage (135 V) and high current (6.4A)

through the electrodes, a pair of silver rods. As a result of erosion of the electrode material, vaporization and condensation of metallic silver takes place in the reaction media resulting in production of metallic silver nanoparticles.

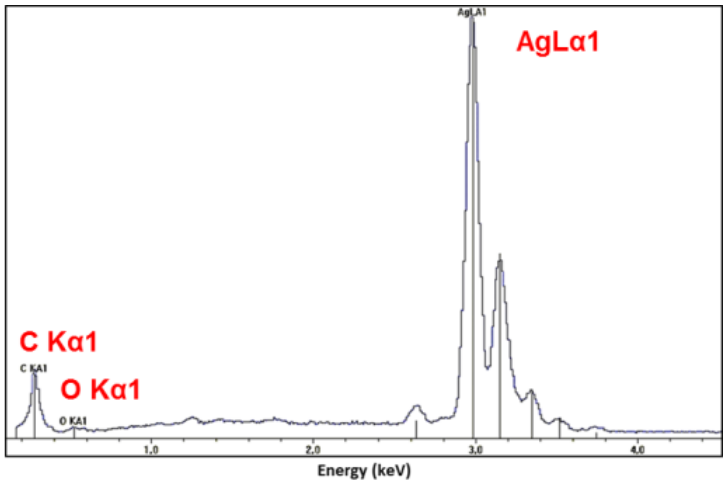

Figure 42: EDS spectrum showing X-ray emission lines of powdered silver particles.

Table 5:Theoretical X-ray emission lines of metallic silver from *(Bearden 1967)*

X-ray emission lines	Energy (keV)
Ag-L1	2.633
Ag-Lα1	**2.984**
Ag-Lβ1	3.151
Ag-Lβ2	3.348
Ag-Lγ1	3.520

From this study, it is thus concluded that the pulsed-plasma liquid immersion technique results in production of high-purity metallic silver particles.

The presence of silver oxides is also assessed through the evaluation of the presence of any possible bonding between silver and oxygen atoms, leading to the formation of a silver oxide structure. For this, high resolution XPS analyses were carried out. Silver-based samples are equivalent to those used in XRD and SEM-EDS characterization that is, obtained by a 3h synthesis using the PLI process. Silver particles were collected by centrifugation (10000rpm, 30min), and later the sample was re-dispersed in ethanol and drop-casted onto a microscope slide. The XPS spectrum presented in figure 43 shows silver peaks in the Ag 3d region. From this spectrum it is observed that two distinctive peaks are located at 374.18eV and 368.18 eV, which are attributed to the Ag $3d_{3/2}$ and Ag $3d_{5/2}$ silver photoelectron lines, respectively. The location of the binding energies (BE) are in agreement with the theoretical BE values of metallic silver, which are 374.2 for Ag $3d_{3/2}$ and 368.2 eV for Ag $3d_{5/2}$ according to *(Moulder et al. 1992)* as presented in table 6.

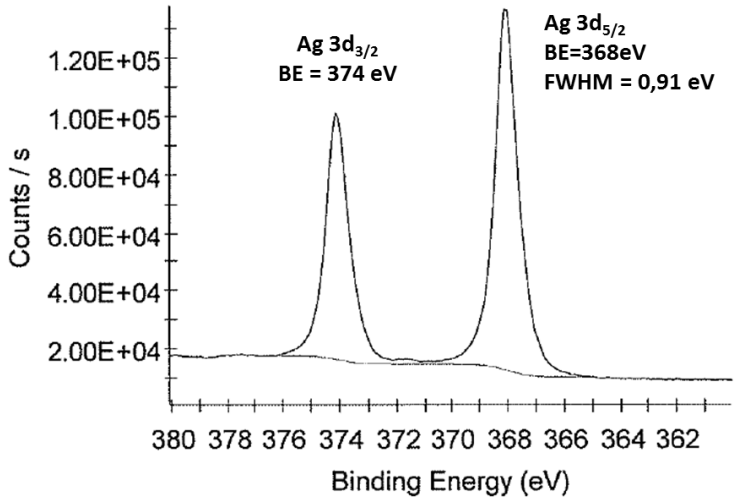

Figure 43: XPS spectrum of powdered silver particles. Analyzed particle were obtained by pulsed plasma-liquid synthesis technique.

Table 6: Theoretical and experimental XPS values for metallic silver and silver oxide particles

Compound	Ag $3d_{3/2}$ *(eV)*	Ag $3d_{5/2}$ *(eV)*	ΔBE *(eV)*	Reference
Ag(0)	**374.18**	**368.18**	**6**	***This study***
Ag(0)	374.2	368.2	6	*(Crist and XPS International LLC 1999)*
Ag_2O	373.42	367.51	6	*(Crist and XPS International LLC 2005)*
AgO	372.77	366.80	6	*(Crist and XPS International LLC 2005)*

Furthermore, the resulting particles are metallic since the difference in the binding energy (ΔBE) of the 3d spin-orbit separation is 6eV. In the case of silver oxides, it is reported that Ag $3d_{5/2}$ peak shifts towards lower BE values. For Ag_2O, Ag $3d_{5/2}$ is located at 367.5 eV. For AgO, Ag $3d_{5/2}$ is located at 367.4 eV *(Kaspar et al. 2010)*.

The results obtained from the XPS surface characterization of the PLI-synthesized silver-based particles confirm the production of metallic silver nanoparticles.

4.1.1 Summary

Silver-based nanoparticles were synthesized by the reduction of an aqueous silver salt ($AgNO_3$) solution to metallic silver, using DC-pulsed plasma discharges. After 3h of plasma discharge, dark-colored silver particles are visible and sediment at the bottom of the reactor. The resulting product was characterized by a range of characterization techniques, including XRD, SEM-EDS, and XPS. Based on the results obtained from the XRD analysis it is concluded that the silver-based sample possesses highly-crystalline structure and is composed of mono-phasic silver. These results were further confirmed by SEM-EDS and high-resolution XPS technique. SEM-EDS results showed that high-intensity X-ray emission lines corresponding to crystalline silver were present. The absence of an oxygen peak in this spectrum confirms the above-mentioned results obtained from XRD. In addition, the XPS analyses show that the obtained binding energy of the silver photoelectron lines of the sample are in accordance with the theoretical values for the binding energy of metallic silver. **It is thus concluded that synthesis of highly-pure and metallic silver nanoparticles is possible with the newly-developed PLI process.**

These results confirm another important aspect of the PLI process and that is, that **as a result of the HV DC-pulsed plasma discharges in the liquid solution, no erosion of the Pt electrodes occurred.**

The only drawback that has been encountered is the production of large-sized agglomerated silver nanoparticles.

4.2 The influence of the metal precursor concentration on the silver nanoparticle synthesis

In the previous section, a newly-developed laboratory PLI process has been used to produce silver particles. From this study, it has been demonstrated that it is possible to produce metallic and non-oxidized silver particles, though agglomerated and large-sized. In the continuation of this chapter, the goal is to optimize the PLI process for synthesis of small-sized and uniformly distributed silver nanoparticles. This optimization will be performed through a parametrical study with focus on chemical synthesis parameters.

The first parameter that has been investigated is the precursor concentration, which has shown to have a significant impact on nanoparticle size during particle synthesis *(Ajitha et al. 2013)*. In this study, silver nitrate ($AgNO_3$), which is a solid metal salt, is used as the precursor to silver nanoparticle production. In plasma-in-liquid processes for nanoparticle synthesis, it is common to work in the mM-concentration unit of the precursor concentration *(Heon Lee et al. 2013);(Saito, Hieda, and Takai 2009)*. **Based on this observation, the selected precursor concentration is in the working range of 2 - 4mM $AgNO_3$.**

Plasma discharges were generated by applying 8kV high voltage DC-pulsed plasma discharges (f=50Hz) to a pair of Pt electrode wire, sub-merged in the aqueous $AgNO_3$ solution. The electrode pair is in the pin-to-pin configuration with a 3mm inter-electrode distance. High voltage DC pulses are generated using a one-stage Marx pulse generator. Millisecond pulsed discharges of short rise time (35ns) are generated in the sparking gap of the Marx pulse generator by means of capacitive discharge. Plasma discharges generated in the aqueous solution are classified as corona discharges. The discharges do not form conducting vapor channels in the discharge zone between the electrode wires to reach breakdown. Therefore, corona discharges generated in the solution are considered as partial corona discharges or streamer-like discharges. The process time in nanoparticle synthesis is 20 minutes. The process time was determined from a previous study with focus on optimal process parameters in activation of plasma discharges using the PLI experimental set-up (see chapter III, section 3.2). Process parameters applied in this study are presented in table 10:

Table 7: PLI process parameters for the parametrical study with focus on $AgNO_3$ concentration

Discharge Physical parameters	**Solution Physicochemical parameters**
Applied voltage ($U_{applied}$): 8kV	Reaction volume (V): 100mL
Pulse repetition frequency (f): 50Hz	**$AgNO_3$ concentration: 2-4mM**
Inter-electrode distance (l_{Pt}): 3mm	pH: 5
Discharge time (t_{plasma}): 20min	Conductivity (σ): 295-580µS/cm

Current (*I*) and voltage (*U*) signals were measured by current and high voltage probes, and recorded towards the end of each synthesis (t_{plasma} = 20min). Characteristic *I*- and *U*- waveforms represent plasma discharges in the on-going synthesis and are presented on figure 44. In the current waveforms, a complete profile of a single pulse is presented, as well as a detailed profile of the first 40μs of the pulse (see inset graphs of I-waveforms on figure 44a-b). Voltage waveforms of a single pulse are presented in a similar approach, but the detailed profile of the pulse concerns the range from the start up to τ = 0.4μs (see inset graphs of U-waveforms on figure 44a-b), in order to confirm the applied voltage. Discharge parameters were determined from the waveforms, which are presented in table 8. It is common to observe oscillations in the electrical waveforms, which occurs due to charge effects during charging and discharging of the capacitor in the RLC electrical circuit *(L. Wang et al. 2018).* For this reason, the measured voltage may be higher than the applied voltage.

Table 8: Plasma parameters corresponding to the silver nanoparticle synthesis with 2mM and 4mM $AgNO_3$ solutions

Precursor concentration	**Voltage**	**Input energy per pulse**	**Injected discharge power**
[$AgNO_3$], *mM*	***U, kV***	***E_{input}, mJ/pulse***	***P_{plasma}, W***
2	8	36.6	1.8
4	8	31.0	1.6

The input energy per pulse (E_{input}) is calculated by integrating the voltage times the discharge current over the pulse duration (t_0 → t), as shown in equation 18. The injected discharge power (P_{plasma}) of the pulsed discharge is calculated by multiplying the input energy per pulse with the pulse repetition frequency, as shown in equation 19.

$$E_{input} = \int_{t0}^{t} I \cdot U_{applied}\, dt \qquad \textbf{Equation 18}$$

$$P = E_{input} \cdot f \qquad \textbf{Equation 19}$$

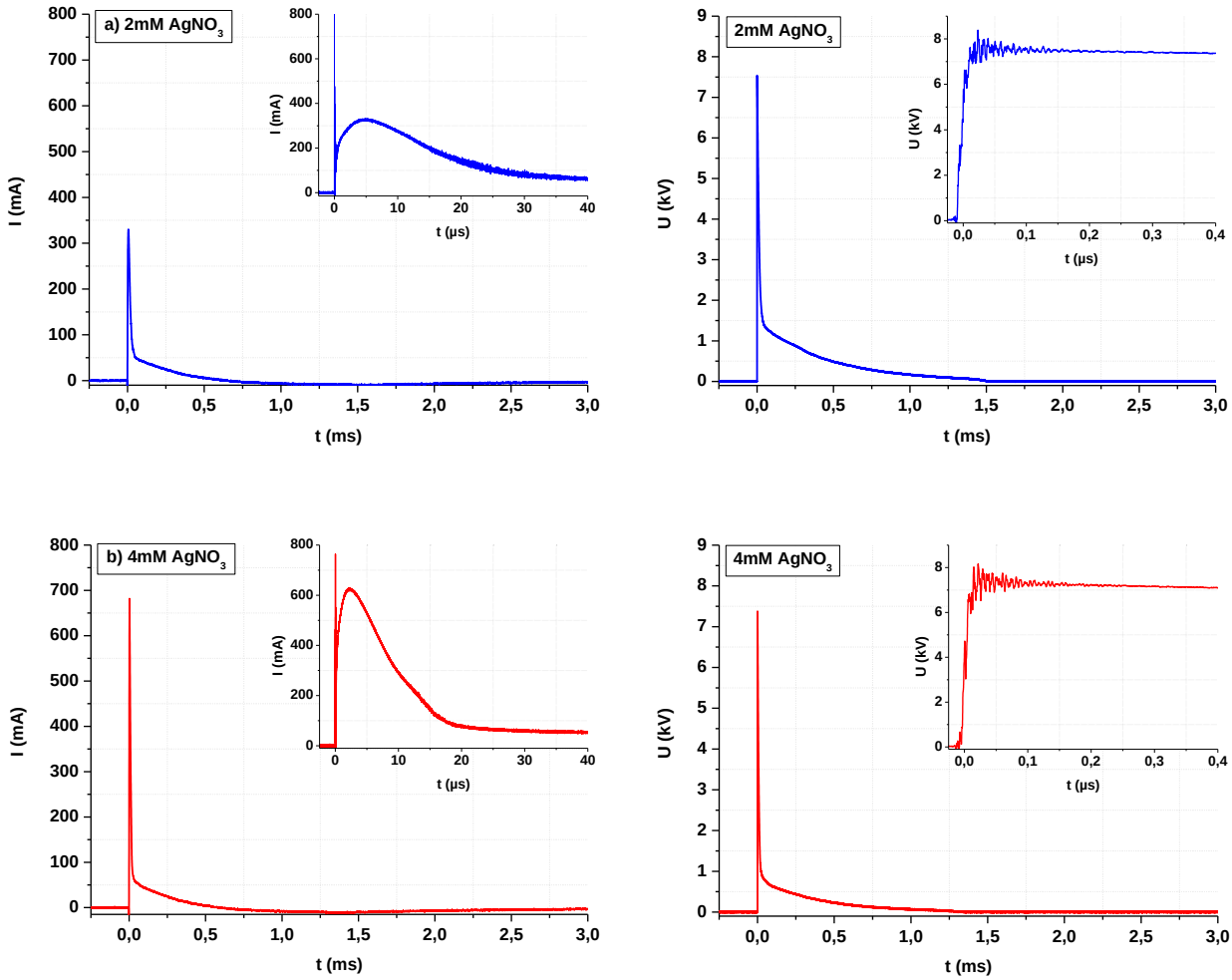

Figure 44: I- and U-waveforms for one pulse (at the end of the process t=20min). Plasma discharges generated in 2mM (blue) and 4mM (red) $AgNO_3$ solutions.

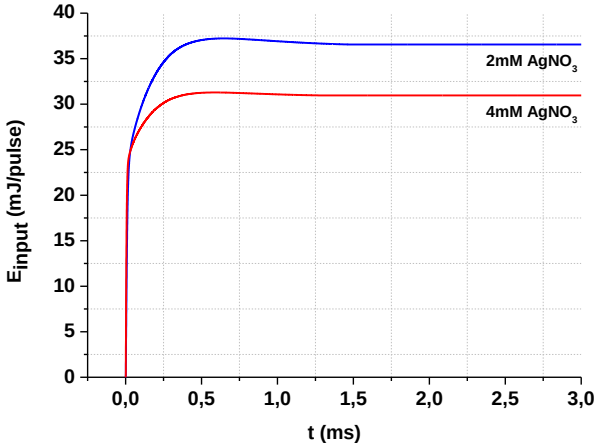

Figure 45: Input energy per pulse of the plasma discharge generated in 2mM (blue) and 4mM (red) $AgNO_3$ solutions

The E_{input} (per pulse) waveforms are calculated from *I*- and *U*-waveforms of a single pulse (c.f. figure 44) and the resulting waveform is presented in figure 45. The E_{input} (per pulse) value is characteristic for each synthesis, and is determined in the steady region starting from τ = 1.25ms. The E_{input} (per pulse) value is then used to calculate the injected power of plasma discharges, representing specific synthesis conditions.

Differences in plasma discharges between the syntheses at 2mM and 4mM [$AgNO_3$] are reflected in the *I*- and *U*-waveforms in figure 44. As shown in the *U*-waveforms on figure 44, an increase in $AgNO_3$ concentration results in the decrease of the pulse duration. This duration decreases from 1.5ms to 1ms when increasing the concentration from 2mM to 4mM, respectively. It is likewise shown from the *I*-waveforms that an increase in $AgNO_3$ concentration results in an increase in the current value, and that a rapid decay of the current pulse occurs. In electrical discharges, the precursor serves as an electrolyte. The solid $AgNO_3$ salt dissociates into ions in the de-ionized water, and provides thus enhanced conduction of the electric current in the liquid media. Therefore, ions present in the reaction media behaves as charge carriers. In this case, when the ion concentration increases, an increase of charge carriers yields in an increase in the electron flow, and thus increases the instantaneous current value. Hence, an increase in E_{input} (per pulse) would be expected. It should be remarked that waveforms were recorded towards the end of the synthesis process. As a matter of fact, E_{input} of the process using 4mM $AgNO_3$ might have been greater than E_{input} of the process using 2mM $AgNO_3$ in the initiation of the synthesis process. The E_{input} per pulse of generated plasma discharges decreases by around 5mJ for an increase in $AgNO_3$ concentration. This decrease in input energy per pulse may occur as an influence of the nanoparticle growth mechanism.

From the electrical waveforms, it is shown that an increase in $AgNO_3$ concentration increases the conduction of electric current, and thus an increase in the E_{input} should be expected. However, a decrease in the E_{input} of the pulsed plasma discharge (t_{plasma} = *20min*) occurred.

During nanoparticle synthesis, it was observed that the uncolored precursor solution (t_{plasma}=*0 min*) started to change color from t_{plasma} = *2min*. This change in color continues until t_{plasma}=*10 mi*, and from then on, color saturation of the reaction media appears. The evolution in the solution color change during 20min of process time is shown in figure 46. The color change

under the synthesis conditions presented in this figure are not very perceivable and appeared light yellow for t_{plasma}=*5 min*. The saturation in the color change appears for t_{plasma}=*20 min*, and the reaction media starts to decrease in transparency.

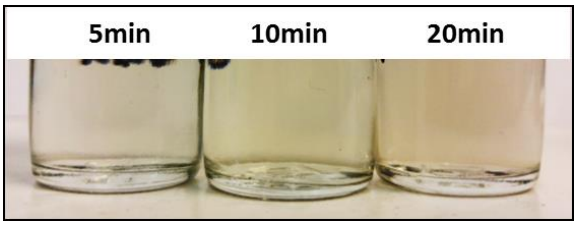

Figure 46: Color change in the silver precursor solution (2mM $AgNO_3$) after 5min, 10min, and 20min of plasma exposure

Generation of plasma discharges in de-ionized water result in the dissociation of water molecules and the production of radicals and reactive species, which react with the compounds existing in the aqueous solution. This process results in changes in the solution chemistry, such as the formation of chemical compounds, that may influence the solution properties *(P. J. Bruggeman et al. 2016).* In order to monitor changes in the physicochemical characteristics of the liquid phase, several techniques were applied. Ex-situ measurements of the pH and the solution conductivity, before and after plasma discharge were carried out. The results are presented in table 9.

Table 9: Initial and final solution parameters obtained from ex-situ pH and conductivity measurements.

Precursor concentration *[$AgNO_3$], mM*	**pH**		**Solution conductivity** *σ, $\mu S.cm^{-1}$*	
	Initial	*Final*	*Initial*	*Final*
2	5.0	3.7	295	336
4	4.7	3.7	580	620

The results show an increase in the initial solution conductivity from 295µS.cm^{-1} to 580µS.cm^{-1} for an increase in $AgNO_3$ concentration. This corresponds to a two-fold increase when the $AgNO_3$ concentration is doubled, and is in agreement with the linear proportionality of ion concentration and solution conductivity of strong electrolytes or salts, like $AgNO_3$ ($\sigma(AgNO_3) = c(AgNO_3) \cdot a$). At a given voltage, a larger conductivity leads to a shortening of the discharge channels and higher amplitudes of the discharge current, resulting in a higher

power density within the discharge, and an increased electron density *(Šunka 2001)*. The results shown in figure 44 are in accordance with this. The generated plasma could thus produce more reductive species, leading to an increase in silver ions reduction and thus, an increase in particles production *(X. Z. Huang et al. 2013)*.

An increase in the solution conductivity of the reaction media (c.f. table 9) was observed during plasma exposure, as well. In this case, the solution conductivity increased by 40µS/cm for both, 2mM and 4mM $AgNO_3$ concentration after 20min of plasma discharge. This increase may be due to an increase in the amount of ions present in the reaction media, which occurs as a result of water dissociation by plasma electrical discharges.

Concerning pH measurements, it is shown that after 20min of plasma discharge a decrease in the pH of the reaction media occurred for all $AgNO_3$ concentrations. A decrease in pH indicates acidification of the reaction media, which occurs during plasma exposure and generation of highly reactive species. For nanoparticle synthesis in a plasma-liquid process with microplasma discharges generated above the liquid surface, a decrease in the solution pH has been observed by *(Sakiyama et al. 2012)* and *(Takamatsu et al. 2014)*. In this plasma-liquid process, the plasma phase comes in direct contact with the atmospheric air. In the presence of N_2 and O_2 in the gas phase, long-lived species such as HNO_2 and HNO_3 are readily created in the plasma phase (see reaction 10-14 *(P. Bruggeman and Leys 2009)*. These acid compounds are thus transferred into the liquid phase in the gas flow direction and results in acidification.

$$N_2 + O_2 + e^{\bullet -} \rightarrow 2NO^{\bullet} + e^-_{aq} \qquad \textbf{Reaction 10}$$

$$2NO^{\bullet} + O_2 \rightarrow 2NO_2 \qquad \textbf{Reaction 11}$$

Water dissociation:

$$H_2O + e^{\bullet -} \rightarrow OH^{\bullet} + H^{\bullet} + e^-_{aq} \qquad \textbf{Reaction 12}$$

Acidification:

$$NO^{\bullet} + OH^{\bullet} \rightarrow HNO_2 \qquad \textbf{Reaction 13}$$

$$NO^{\bullet}_2 + OH^{\bullet} \rightarrow HNO_3 \qquad \textbf{Reaction 14}$$

Since the plasma phase is completely immersed in the liquid phase in our work, plasma discharges are not in direct contact with atmospheric air. Therefore, the above-mentioned acidification reaction mechanism is not an option and does not explain acidification of the reaction media. The acidification must therefore be produced through the reaction of plasma-generated species with compounds already existing in the solution. As the metal precursor used in this work is $AgNO_3$, nitrate ions (NO_3^-) are present in the reaction solution (c.f. reaction 15):

$$AgNO_{3\,(s)} \xrightarrow{H_2O} Ag^+_{(aq)} + \boldsymbol{NO_3^-}_{(aq)} \qquad \textbf{Reaction 15}$$

Thus, reactions of nitrate ions with some of the species generated by the discharge have to be considered (c.f. reaction 16):

$$NO_3^- + H^\bullet \rightarrow HNO_3^- \qquad \textbf{Reaction 16}$$

A decrease in NO_3^- concentration is expected due to the acidification and formation of HNO_3.

Interaction with plasma created reactive species would therefore result in the formation of HNO_3 (pKa = -1.8), which is a strong acid, and thus decrease pH of the reaction media. *(Heon Lee et al. 2013)* used a liquid-phase plasma (LPP) reduction method to prepare silver nanoparticles from a solution of silver nitrate using a high frequency (30kHz) bipolar pulsed electric discharge system. Their results have shown that the solution pH steadily decreased during the treatment. They suggested that the oxygen radicals produced by the LPP process reacted with molecular nitrogen (N_2) dissolved in the solution to produce nitric acid (HNO_3), which contributed to the decrease in pH. A similar scenario could explain the decrease in pH observed in our case.

Sampling of the reaction media was done for 5min, 10min, and 20min of plasma exposure during synthesis of silver nanoparticles, which were characterized by UV-vis absorption spectroscopy. UV-vis absorption spectra obtained from these measurements are shown in figure 47 and data from this measurement are presented in table 7. From these results, it is revealed that the wavelength at which a maximum of light is absorbed by the silver nanoparticles (λ_{max}) is around 400nm. This is in accordance with the typical surface plasmon resonance wavelength (λ_{SPR}) of

spherical colloidal silver nanoparticles *(Creighton and Eadon 1991)*, *(J. M. Kelly, Keegan, and Brennan-Fournet 2012)*. The presence of an absorption peak at around 400nm for a 5min process time indicates that nanoparticle production already occurs within 5min of the process. In theory, the characteristic color change for spherical colloidal silver nanoparticles for surface plasmon absorption at 400nm results typically in a strong yellow color change. This color change is further an indication that particles produced are of small-size (<20nm) and are uniformly distributed. As the process time of nanoparticle synthesis increases, an increase in absorbance of the SPR peak (λ_{max} = 400nm) occurs from 0.089 (t_{plasma} = 5 min) up to 0.290 (t_{plasma} = 20 min). This increase in absorbance at 400nm is explained by an increase in light absorbing particles. Therefore, for an increase in process time, the production of silver nanoparticles and thus particle concentration increases.

(X. Z. Huang et al. 2013) produced silver nanoparticles by microplasma discharges (plasma above liquid). They have performed a similar study, and showed that an increase in $AgNO_3$ concentration (in the absence of stabilizing agent) resulted in an increase in the maximum absorbance value, which corresponds to an increase in nanoparticle concentration. This is true, as an increase in silver ion concentration provides reduction and formation of an increased amount of silver nanoparticles for an increase in electron density. Although, the maximum absorbance depends on the synthesis process, it is common that the maximum absorbance in the absence of a stabilizing agent is lower. As an example, Huang *et al*. obtained an absorbance around 0.15 (λ_{max} = 420nm) from a synthesis using 2mM $AgNO_3$ in the absence of stabilizing agent. The resulting absorption band was described as a broad absorption peak and explained by non-uniform particle distribution.

A slight evolution in the solution color during plasma exposure and an appearance of a pale yellow color has been presented in figure 46 and discussed earlier. The reason to a slight evolution in color change and a pale yellow color of the solution may be due to particle agglomeration, and/or polydisperse particles. It may as well be due to the formation of silver oxide particles, but this is not of an option, since particle characterization confirmed the existence of non-oxidized metallic silver nanoparticles (see chapter IV, section 4.1).

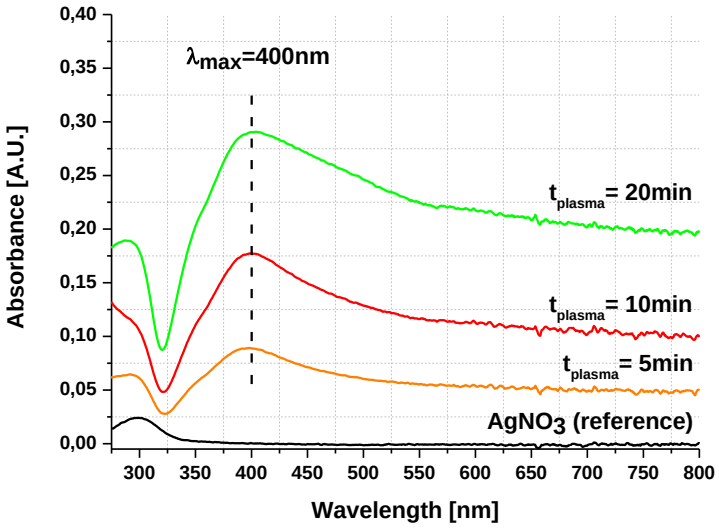

Figure 47: UV-vis absorption spectra of 2mM $AgNO_3$ precursor solution (black line) being exposed to 5min (orange), 10min (red), and 20min (green) of plasma discharge.

Table 10: UV-vis measurements at different discharge times

t_{plasma}	Absorbance	λ_{max}
min	*a.u.*	*nm*
0	0	0
5	0.089	400
10	0.175	400
20	0.290	400

All the absorption spectra on figure 47 are broad (not a Gaussian distribution). A broad absorption band occurs in the presence of agglomerated nanoparticles, as well as for polydisperse nanoparticles (particles of multiple size population) *(Tomaszewska et al. 2013)*, *(Capek 2017b)*. Since the broad absorption peak appears from a process time of 5min, it may be due to agglomeration of nanoparticles at an "early" stage of the process.

The resulting silver nanoparticle solution after 20min of plasma discharge for different initial $AgNO_3$ concentrations are analyzed by DLS for determination of particle size. A small volume (1mL) of the as-synthesized silver colloidal solution is analyzed and the obtained results are presented in figure 48a-b and table 11. Particle size measurement results in figure 48a-b are both presented in intensity and number based **P**article **S**ize **D**istribution (PSD). Presenting PSD in terms of intensity and number weighted percentages is important in order to gain thorough understanding about the synthesized particles in the dispersing liquid media. This is especially necessary to reveal whether or not nanoparticles are monodisperse.

Table 11: Results obtained by DLS size measurements performed on the AgNP solutions from different initial $AgNO_3$ concentrations

Precursor concentration *[$AgNO_3$], mM*	Intensity-based size %I, *nm*	Number-based size %N, *nm*	Count Rate *kcps*
2	280	242	1045
4	450	390	2775

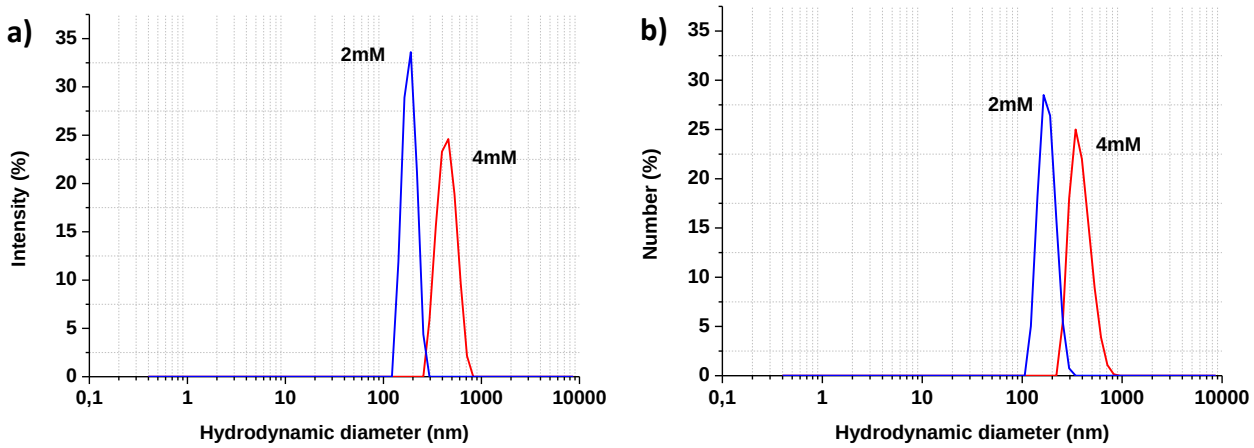

Figure 48: DLS measurements performed on the AgNP solution obtained from an initial $AgNO_3$ concentration of 2mM (blue) and 4mM (red). PSD are presented in terms of a) intensity and b) number.

In intensity based PSD (see figure 48a), particles synthesized by the PLI process for a process time of 20min for 2mM $AgNO_3$ concentration (represented by the blue line) resulted in a single size population at around 280nm. Performing the synthesis with an increased precursor concentration (4mM $AgNO_3$) (represented by the red line) also results in a single size population around 450nm. In the number-based PSD (see figure 48b) similar results to the intensity-based PSD have been obtained. Silver nanoparticles obtained from a 2mM $AgNO_3$ solution result in smaller particles in the PSD (242nm), than silver nanoparticles obtained from a 4mM $AgNO_3$ solution (390nm). These results showed that for an increase in $AgNO_3$ concentration, an increase in nanoparticle size is obtained. According to the results obtained by the DLS technique, large-sized nanoparticles (>100nm) are obtained. An increase in the average nanoparticle diameter for an increase in precursor concentration have been confirmed by *(Mariotti et al. 2012)*. Instead of silver, they produced gold nanoparticles through microplasma discharges (plasma above liquid) using 0.05mM-1mM $HAuCl_4$ as the electrolyte solution. The microplasma was generated using

He/Ar gas flow (25sccm), and was powered by a DC power supply applying up to 2kV to the carbon anode immersed in the electrode. Mariotti *et al*. demonstrated that by increasing the precursor concentration from 0.05mM to 1mM (for 10min of synthesis) a linear increase in average particle diameter was obtained from around 12nm to 180nm, respectively. This was obtained keeping the discharge current constant at 5mA.

From the above-mentioned results regarding UV-vis absorption and particle analysis, it could be considered that agglomerates rather than uniformly distributed particles are obtained.

It is also possible to detect an increase in particle concentration by the DLS method from the **C**ount **R**ate (CR) value presented in table 11. This value represents the intensity of the scattered laser beam (measured in *kcps*) by the particles present in the solution, detected by a sensitive **A**valanche **P**hotodiode **D**etector (APD). From our measurements, an increase in $AgNO_3$ concentration resulted in an increase of the scattered light intensity from 1045kcps (2mM $AgNO_3$) up to 2775kcps (4mM $AgNO_3$). The increase in CR shows thus that an increase in $AgNO_3$ concentration results in an increase in particle concentration.

From the results obtained by the DLS measurements, increasing the $AgNO_3$ concentration (2mM → 4mM) results thus in an increase in average particle size, and also in an increase in particle concentration.

In the following, silver nanoparticles were characterized using electron microscopy techniques of high resolution. Samples characterized by **S**canning **E**lectron **M**icroscopy (SEM) were prepared by deposition of as-synthesized silver nanoparticles onto a piece of microscopy glass plate during 30min. The plate was rinsed carefully with de-ionized water during 2min in order to remove excessive and unreacted ions from the substrate (Ag^+, NO_3^-, etc.). The plate was later dried in the oven overnight at 80°C. Samples characterized by **T**ransmission **E**lectron **M**icroscopy (TEM) were prepared by drop-casting as-synthesized nanoparticles onto a carbon-coated cupper grid. The samples were left to dry under ambient conditions. In these sample preparation conditions, nanoparticles went from a liquid state to a dried state, and may hence accumulate during the drying process.

Results from SEM and TEM characterizations are shown in figure 49a-c. Synthesis of silver nanoparticles using a 2mM $AgNO_3$ solution and 20min of discharge reveals that agglomerates

consisting of large-sized and irregular-shaped particles occur (see figure 49a and figure 49c). SEM characterization also revealed that agglomerates of large-sized and irregular-shaped particles were obtained from nanoparticle synthesis using 4mM $AgNO_3$ concentration (see figure 49b).

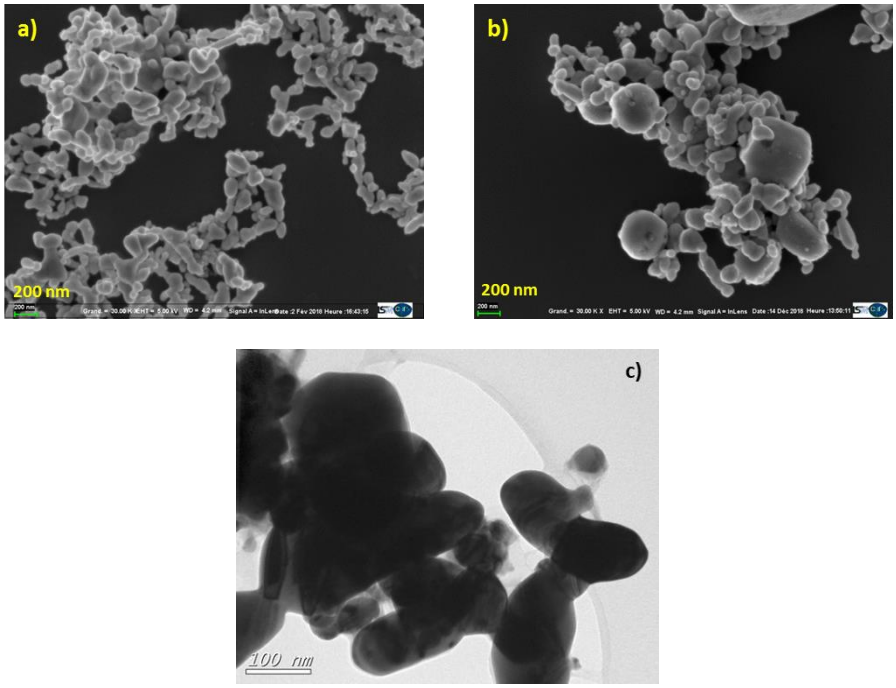

Figure 49: SEM micrographs of the obtained silver nanoparticles from a) 2mM $AgNO_3$ and b) 4mM $AgNO_3$ solutions (Magnification: 30kX). c) TEM micrographs of silver nanoparticles.

On figure 49, an increase in the average size of the silver particles is observed for an increase in $AgNO_3$ concentration. Results obtained from electron microscope techniques are hence in accordance with observations made during the synthesis and results achieved in this study.

From the current results, it is determined that the developed PLI process (under currently applied experimental conditions) produced non-uniform and large-sized silver particle agglomerates of irregular shapes. It is therefore concluded that an increase in $AgNO_3$ concentration in PLI process increases the average size of silver particles.

4.2.1 Plasma-liquid interaction and nanoparticle growth mechanism

The generation of electrical plasma discharges sub-merged in aqueous silver precursor solution creates strong electric fields, UV radiation and shockwaves. Filamentary partial corona discharges appear on the ground electrode. Visually, discharges exhibit a white-blue spot on the

electrode tip, which is surrounded by magenta streamers. According to *(P. Bruggeman and Leys 2009)* and *(Šunka 2001)*, magenta colored streamers occurs due to Hydrogen Balmer lines. In the optical emission spectrum of streamer generation in water, it is usual to detect hydrogen Balmer, atomic oxygen and hydroxyl lines *(Šunka 2001)*. When the electric field becomes high enough at the electrode tip, evaporation of water provokes the formation of vapor channels and the streamers propagation. According to *(Lisitsyn et al. 1999)*, the injected plasma power should be in agreement with the power required to vaporize the liquid within the streamer volume. Highly energetic electrons ($e^{-\bullet}$) interacts with water molecules through avalanche propagation in streamers. Interaction between water molecules and $e^{-\bullet}$ initiates water dissociation and ionization reactions as in reaction 17-19 *(Kozáková 2011), (Pootawang 2011)*.

Water dissociation and ionization

$$H_2O + e^{-\bullet} \rightarrow OH^{\bullet} + H^{\bullet} + e_{aq}^{-} \qquad \textbf{Reaction 17}$$

$$H_2O + e^{-\bullet} \rightarrow H_2O^{+\bullet} + 2e_{aq}^{-} \qquad \textbf{Reaction 18}$$

$$H_2O^{+\bullet} + H_2O \rightarrow H_3O^{+} + OH^{\bullet} \qquad \textbf{Reaction 19}$$

Furthermore, recombination reactions of highly reactive radicals form stable molecules as shown in reaction 20-22 *(Kozáková 2011), (Pootawang 2011)* .

Recombination

$$H^{\bullet} + H^{\bullet} \rightarrow H_2 \qquad \textbf{Reaction 20}$$

$$OH^{\bullet} + OH^{\bullet} \rightarrow H_2O_2 \qquad \textbf{Reaction 21}$$

$$H^{\bullet} + OH^{\bullet} \rightarrow H_2O \qquad \textbf{Reaction 22}$$

From the above-mentioned reactions, it can be seen that highly reductive species, hydrated electrons (e_{aq}^{-}) and H•, are formed during the discharge. Silver ions are known to readily scavenge plasma-generated e_{aq}^{-} and H•, which results in the reduction of the metal ion into zero-valence silver atoms (Ag^0) *(Soroushian et al. 2005)*. The reduction rate, in which silver ions are reduced by e_{aq}^{-} and H•, are shown in reaction 23 and reaction 24, respectively *(NIST 2019a), (NIST 2019b)*:

$$Ag^{+} + e_{aq}^{-} \rightarrow Ag^0 \qquad (k = 3.2 \cdot 10^{10} M^{-1} s^{-1}) \qquad \textbf{Reaction 23}$$

$$Ag^{+} + H^{\bullet} \rightarrow Ag^0 + H^{+} \qquad (k = 2.0 \cdot 10^{10} M^{-1} s^{-1}) \qquad \textbf{Reaction 24}$$

In the study of *(Kondeti et al. 2017)*, it is shown that the reduction of Ag^+ ions by e_{aq}^- is reasonable due to the high rate constant (c.f. reaction 23), however, Kondeti *et al*. showed that the reduction of Ag^+ ions is dominated by H• (c.f. reaction 24) in the synthesis of silver nanoparticles in plasma-liquid processes. The reduction of Ag^+ ions by H• in plasma-liquid processes was also confirmed in studies performed by *(Saito, Hieda, and Takai 2009), (Skiba et al. 2018).*

As stated before (section 4.2), increasing the initial precursor concentration results in a proportional increase in the conductivity, which in turn lead to a higher amplitude of the discharge current and a more dense plasma *(Šunka 2001)*. Thus, a higher amount of reducing agents may be produced by the discharge, which may result in an increase in the reduction rate of Ag^+ ions. Therefore, the formation rate of silver particles increases, and results in fast particle synthesis. Above-mentioned was confirmed by *(Saito, Hieda, and Takai 2009)*, who performed a kinetic study on gold nanoparticles prepared through plasma discharge technique with electrodes immersed in the liquid phase.

In homogeneous nucleation, the rate of nucleation is proportional to the initial concentration. A higher initial concentration favors the formation of a large number of smaller nuclei (G. Cao 2004). Thus, the final average size of the silver nanoparticles, produced in the newly-developed PLI process, might be related to the nucleation process. After the initial nucleation, the concentration of silver ions decreases until reaching a level where no more nuclei will form, and nanoparticle growth will proceed. Therefore, there is a possibility that an increase in the silver ion concentration results in a larger number of nuclei that will coalesce, leading to the formation of larger particles. The proposed nucleation and growth mechanism of silver nanoparticles produced by the PLI process is shown in figure 50. The first step of this mechanism, the "Reduction" step, concerns the reduction of silver ions into silver atoms.

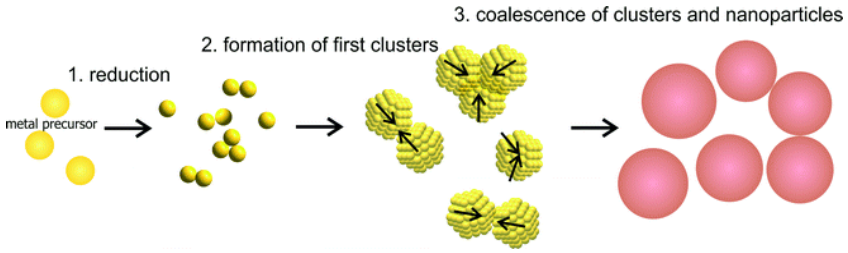

Figure 50: Growth mechanism of silver nanoparticle as a result of coalescence. Reproduced from *(Jörg Polte 2015)*

The second step, "Formation of clusters", concerns the clustered growth of primary silver nanoparticles. The cluster formation occurs since binding energy between two metal atoms is stronger than the atom-solvent bond energy. As silver atoms diffuse in the solvent, due to Brownian motion, an encounter of two silver atoms (Ag_0) lead to dimerization (Ag_2) (see reaction 25). This is followed by an autocatalytic nucleation process resulting in an increase in particle size. In the final step, "Coalescence of clusters and nanoparticles", generation of silver nanoparticles occur by coalescence of clusters (Ag_n) as shown in reaction 26 *(Belloni 2006)*.

Dimerization: $Ag^0 + Ag^0 \rightarrow Ag_2$ **Reaction 25**

Clustered growth: $Ag_m + Ag_p \rightarrow Ag_n$ **Reaction 26**

It is also possible that interaction of metal atoms and charged particles (ions (Ag^+), dimers (Ag_2^+), and clusters (Ag_n^+)), are faster than the production rate of reducing agents. The reduction of metal ions occurs therefore in-situ on already formed clusters. As a consequence, the new atom formed results in the growth of clusters as shown in reaction 27 *(Belloni 2006)*:

$$Ag_n^0 + Ag^+ \rightarrow Ag_{n+1}$$ **Reaction 27**

Apart from an increase in particle size, another observation was made on silver nanoparticle production, which concerns agglomeration of nanoparticles. It was previously observed in section 4.1, that a 3-hour process time would result in highly agglomerated particles. However, decreasing the process duration to 20min did not lead to a reduction of particle agglomeration. It was thus shown that from decreasing the process time, particle agglomeration was not prevented. Also, agglomeration occurred regardless of the initial precursor concentration for 2mM and

4mM. The main reason to nanoparticle agglomeration may be due to repulsive electrostatic forces being dominated by attractive Van der Waals forces.

The production of electrostatic stabilized silver and gold nanoparticles by an arc discharge technique *(Tien et al. 2010)* and by a microplasma (plasma above liquid) discharge technique *(Patel et al. 2013)* have been reported. Nevertheless, the current process parameters used in the PLI process developed in this work did not allow obtaining electrostatically stabilized silver nanoparticles.

4.2.2 Summary

In this study, the effect of the precursor concentration (i.e. $AgNO_3$) on metallic silver nanoparticles formation was studied. The working range of $AgNO_3$ concentration is between 2 - 4mM. Nanoparticles were synthesized by the PLI process in which DC-pulsed high voltage discharges (U=8kV; f=50Hz) were applied to a pair of Pt electrodes. Plasma discharges were generated in the $AgNO_3$ solution during 20min, and the resulting nanoparticles were later characterized in terms of particle morphology and size measurements by techniques such as UV-vis spectroscopy, DLS, SEM and TEM. It was shown that an increase in $AgNO_3$ concentration resulted in an increase of the average nanoparticle size. From the literature review and the obtained results, it is shown that an increase in the precursor concentration did influence the plasma generation, through an increase in the discharge current, which is transferred by ions. By increasing the solution conductivity, the increased discharge current will lead to a higher power density within the discharge which may increase the number of generated reducing agents. An increased concentration of the reducing agents may increase the reduction rate of silver ions into silver nanoparticles. This could result in a faster nucleation rate that could further lead to clusters coalescence and thus an increase in the average nanoparticle diameter. Based on the results obtained from this study, silver nanoparticles of lower average particle size were obtained for an $AgNO_3$ concentration of 2mM. Thus, this concentration will be used for the rest of the study.

4.3 Influence of surfactant concentration on silver nanoparticle synthesis

In the previous section, it was determined that increasing the $AgNO_3$ concentration resulted in an increase in the average particle size. This study was performed on nanoparticles produced

from a PLI process applied for 20min on an aqueous $AgNO_3$ solution. Problems that have been encountered with these particles are that they are irregular-shaped and large-sized. This is a result of aggregation and coalescence of smaller sized particles.

From the previous results it was decided to continue the parametrical study with a 2mM $AgNO_3$ solution concentration. As agglomerated nanoparticles do not favor in increased nanoparticle reactivity and an enhancement of nanoparticle properties, agglomeration will be a problem in their application in specific fields. In order to avoid nanoparticle agglomeration, it is therefore necessary to study the influence of the presence of a stabilizing agent during silver nanoparticle synthesis.

The stabilizing agent that was applied in this work is poly-vinyl pyrrolidone (PVP, MW=10000g·mol^{-1}). PVP is a bio-compatible and non-toxic surfactant that has hydrophilic end-groups *(Koczkur et al. 2015)*. It is possible to find PVP with molecular weights of 10000g·mol^{-1}, 55000g·mol^{-1}, and 1300000g·mol^{-1}. PVP of 10000g·mol^{-1} was used in this work, based on results obtained from *(Shin et al. 2004)*. They showed that molecular weight of PVP has an influence on the average size of stabilized silver nanoparticles, and obtained the smallest average particle size, when using 10000g·mol^{-1} PVP. **The chosen PVP concentration is in the working range of 0 - 0.05mM**. Depending on the component and structure of the stabilizing agent used, the amount required to stabilize nanoparticles may vary. In literature, it is common to apply a low concentration of stabilizing agent. In this study, silver nanoparticles are prepared in the same way as in the previous section. The silver precursor solution consists of an aqueous solution of 2mM $AgNO_3$ with a given concentration of PVP. A pair of Pt wire electrodes of 3mm inter-electrode distance was immersed in the silver precursor solution for which high voltage DC-pulsed plasma discharges of 8kV and a pulse repetition frequency of 50Hz is applied. High voltage pulsed discharges are generated using a one-stage Marx pulse generator. Millisecond-pulsed discharges of short rise time (35ns) are generated in the spark gap of a Marx pulse generator by means of capacitive discharging. The plasma discharges generated under these conditions are in the corona plasma regime and did not reach breakdown. The PLI process parameters applied in this study are presented in table 12.

Table 12: PLI process parameters for the parametrical study with focus on PVP concentration

Discharge Physical parameters	Solution Physicochemical parameters
Applied voltage ($U_{applied}$): 8kV	Reaction volume (V): 100mL
Pulse repetition frequency (f): 50Hz	$AgNO_3$ concentration: 2mM
Inter-electrode distance (l_{Pt}): 3mm	**PVP concentration: 0-0.05mM**
Discharge time (t_{plasma}): 20min	pH: ≈ 4.5
	Conductivity (σ): 330µS/cm

Current and voltage waveforms were recorded towards the end of the nanoparticle synthesis ($t_{plasma}=20min$) and are presented in figure 51. The electrical waveforms were treated in a similar way as done in the previous section. From these waveforms, discharge parameters were determined and are presented in table 13. The input energy per pulse (E_{input}) and the discharge injected power (P_{plasma}) were likewise calculated from equation 18 and equation 19, respectively.

Table 13: Electrical parameters of the discharge for different PVP concentrations

Stabilizing agent concentration	Voltage	Input energy per pulse	Injected discharge power
[PVP], mM	*U, kV*	E_{input}, *mJ/pulse*	P_{plasma}, *W*
0	**7.5**	**36.6**	**1.8**
0.005	8	35.8	1.8
0.02	8	42.5	2.1
0.05	8	42.0	2.1

The influence of the PVP concentration on the generation of plasma discharges in the reaction media is determined through *I*- and *U*-waveforms in figure 51.

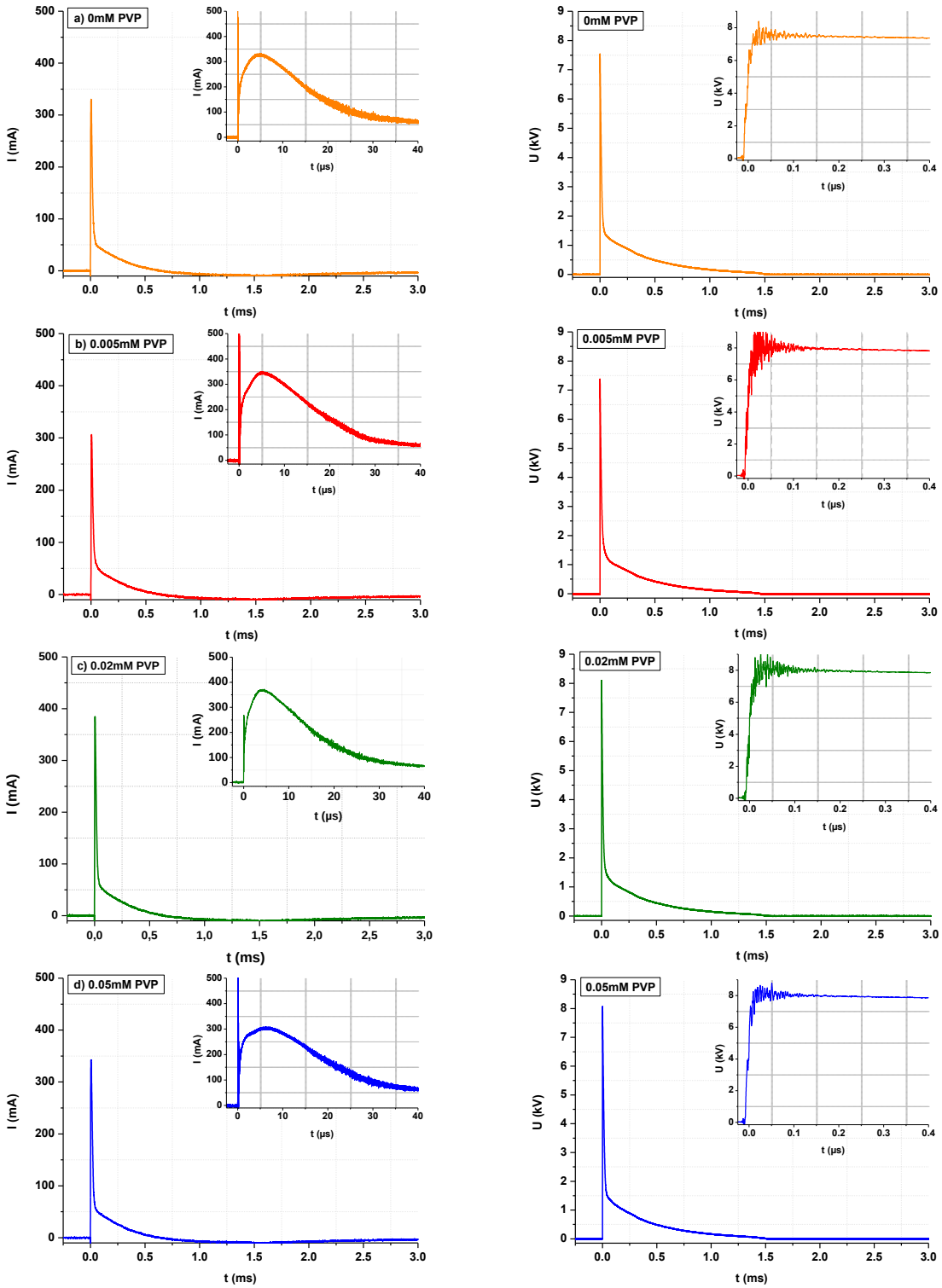

Figure 51: I- and U-waveforms for one pulse (at the end of the process t=20min). Plasma discharges generated in 2mM $AgNO_3$ precursor solution in the presence of a) 0mM PVP, b) 0.005mM PVP, c) 0.02mM PVP, and d) 0.05mM PVP

As it is observed in the *U*-waveforms, the U-value was kept constant throughout the synthesis, but a variation between 7.5kV-8kV among syntheses did occur as shown on the voltage waveforms. It is on the *I*-waveforms shown that an increase in the PVP concentration does not cause major changes in the slope of the decaying current pulses, and that the current values are constant at around 300-350mA among syntheses. These observations are expected, since the $AgNO_3$ concentration was kept constant at 2mM. Due to similarities in current conduction, it is also shown from the voltage waveforms that for an increase in the PVP concentration, the pulse duration remains constant at around 1.5ms. **It is thus shown that an increase in the PVP concentration does not result in significant modifications in the electric waveforms, and hence does not influence the plasma generation.** The reason for this is due to the fact that polymers in general are electrically non-conductive compounds, which does not act as charge carriers to conduct the electrical current.

However, small variations in the E_{input} values for an increase in the PVP concentration are observed in table 13. It is shown that in the absence of PVP and for the lowest PVP concentration (0.005mM), the E_{input} per pulse is around 36mJ. As the PVP concentration is increased to 0.02mM and 0.05mM, an increase in E_{input} up to 42.5mJ takes place, hence an increase of 6mJ/pulse. This increase in the discharge energy may occur due a faster ionic mobility provided by amorphous PVP. According to studies performed by *(Ravi et al. 2013)*, and *(Subba Reddy et al. 2006)* the presence of dipole carbonyl group (C=O) in the side chains of PVP, it forms complexes with inorganic salts and enhances free ions in the solution. This enhancement in the amount of free ions in the solution may thus explain a modification in the discharge current and thus, an increase in E_{input}, for an increment of the PVP concentration.

A significant increase by 6mJ/pulse in E_{input} is observed for an increase in PVP concentration. The increment by may be due to an increased ionic mobility resulting from the C=O group in the side chains of PVP.

Conductivity and pH measurements for each PVP concentration were performed before and after the plasma discharge and the results are presented in table 14. Initial pH values for all precursor solutions containing PVP remained constant at around 4.5. It is further observed, that the pH of the precursor solution decreases slightly as soon as the PVP is added. This is due to the presence of the amide group (R-CO-NH_2-R) in the pyrrolidone ring of PVP, which is slightly

acidic.

Table 14: Physicochemical characteristics of the solution before and after the AgNP synthesis

Stabilizing agent concentration *[PVP], mM*	**pH**		**Solution conductivity** σ, $mS.cm^{-1}$	
	Initial	*Final*	*Initial*	*Final*
0	**5.0**	**3.7**	**295**	**336**
0.005	4.6	3.3	327	375
0.02	4.5	3.6	331	373
0.05	4.3	3.6	328	370

After 20min of discharge, the pH of the reaction media is measured. For all cases, an acidification of the reaction media occurs. This occurs as a result of plasma-induced chemical reactions, resulting in the formation of acidic compounds (i.e. HNO_3).

Addition of PVP results in a slight increase in the initial precursor solution conductivity. After 20min of plasma discharge, the solution conductivity usually increases as a result of the formation of different species due to plasma-liquid interaction.

During the 20 min of plasma discharge, it was observed that the initially transparent and uncolored precursor solution becomes colored from 2 min of discharge. This evolution in color continues and the intensity in the color change increases until the end of the plasma discharge. As it is shown in figure 52a, when no PVP is added, only a slight evolution in the solution color is observed, which can be related to large-sized and aggregated silver particles (section 4.2). When adding PVP, as in figure 52b, the color change appeared as strong yellow, which may be an indication of the presence of small-sized and uniformly distributed silver nanoparticles.

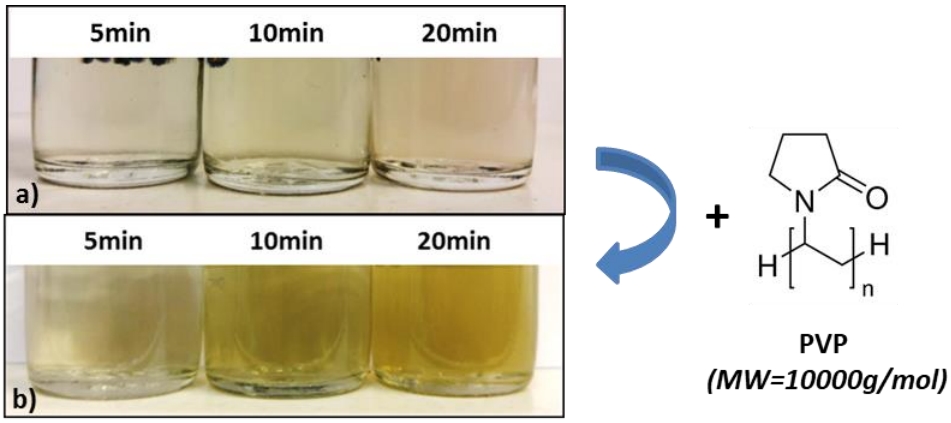

Figure 52: Changes in solution color during 20min of plasma discharge for a) no stabilization, and addition of b) 0.05mM PVP.

At the end of the discharge process, the solutions are characterized by UV-vis absorption spectroscopy, the resulting absorption spectra and the different related parameters are presented in figure 53 and table 15, respectively. The polydispersity of particles is determined by the width of the absorption band, and is thus represented by the full width half maximum (FWHM) value. It was not possible to determine FWHM for highly aggregated and poly-disperse particles produced in the absence of PVP. When adding low amounts of PVP (0.005mM), the stabilizing effect of the PVP on the silver nanoparticles production is immediately observed in the absorption spectra on figure 53. **Addition of PVP results in a two-fold increase in the maximum absorption of the resulting solution, in comparison to the one where no PVP is present**. A decrease in polydispersity and agglomeration of nanoparticles is also observed by a decrease in the FWHM value (c.f. table 15). Addition of 0.005mM PVP is also causing particles to become smaller, hence the slight blue-shift in λ_{SPR} by 4nm. A further increase in PVP concentration from 0.005mM to 0.05mM resulted in a further increase in the maximum absorption value (c.f. figure 53). The maximum absorption reaches around 0.750 in absorbance (for λ_{max}=397nm) when the PVP concentration is higher than or equal to 0.02mM. The similarity in the absorbance values between 0.02mM PVP and 0.05mM PVP may be an indication that particle concentration has reached saturation starting from 0.02mM in PVP concentration. A decrease in polydispersity and agglomeration is also reflected in the FWHM value if compared to the one at 0.005mM PVP, since a decrease of 1.5 times is obtained for both 0.02mM and 0.05mM PVP. Lastly, the average particle size is observed to decrease, as a blue-shift in the λ_{SPR}

between 3-8nm is observed in comparison to no PVP addition.

Table 15: Results obtained by UV-vis absorption spectroscopy performed on AgNP solutions with different PVP concentrations

Stabilizing agent concentration	Absorbance	λ_{max}	FWHM
[PVP], mM	*a.u.*	*nm*	*nm*
0	0.290	400	n/a
0.005	0.635	396	204
0.02	0.750	397	137
0.05	0.757	392	130

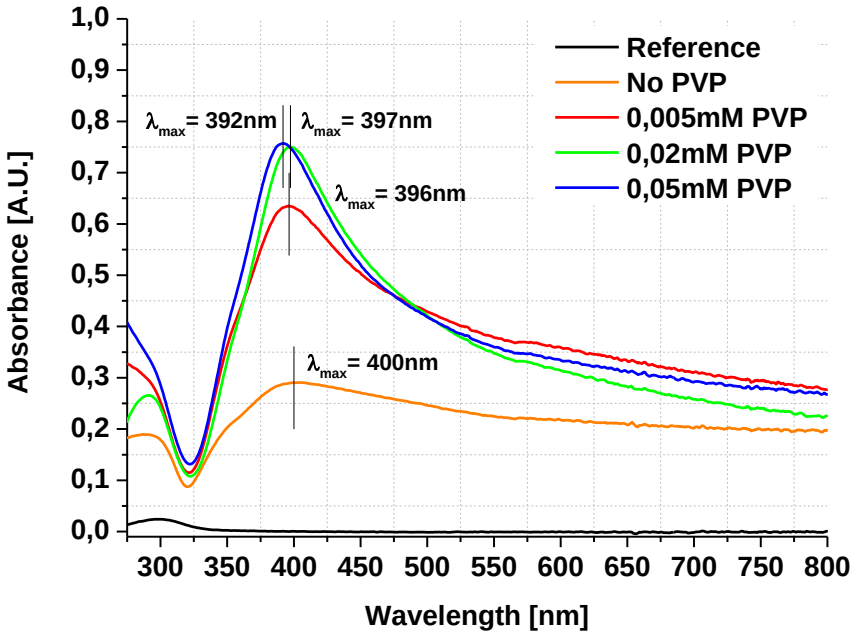

Figure 53: UV-vis absorption spectroscopy of 2mM $AgNO_3$ solutions exposed to 20min of plasma discharge in the presence of stabilizing agent. Reference solution (black line), no stabilization (orange line), 0.005mM PVP (red line), 0.02mM PVP (green line), and 0.05mM PVP (blue line).

(Malina et al. 2012) have investigated the influence of PVP concentration on silver nanoparticles synthesis with focus on a chemical reduction method using $NaBH_4$ as the reducing agent. UV-vis absorption spectroscopy results showed that the polydispersity in particles decreased for an increase in the PVP content in the range of 1-5%. This is thus in agreement to what have been obtained from the results presented in the current study.

Similar observations have been made by *(Roldán, Pellegri, and de Sanctis 2013)* in the application of a polymeric stabilizing agent for silver nanoparticle synthesis. Roldán *et al.* produced silver nanoparticles through an electrochemical synthesis technique in the presence of polyethylene glycol as a stabilizing agent. The synthesis was performed by immersion of two platinum electrodes in a 2.5mM $AgNO_3$ electrolyte solution. They have obtained spherical and non-agglomerated silver nanoparticles in the size range between 10-200nm in diameter. The slow decay in the absorption band was associated to nanoparticle polydispersity.

The silver nanoparticle solutions obtained after 20min of a plasma discharge in a 2mM $AgNO_3$ aqueous solution in the presence of different PVP concentrations were analyzed by DLS for the determination of the PSD. For each concentration, a small volume (1mL) of the as-synthesized silver nanoparticle solution is analyzed by DLS. The results obtained from the DLS analysis are presented in table 16, and the corresponding PSD graphs are presented in both, intensity and number percentages, in figure 54a-b.

Table 16: Results obtained by DLS size measurements performed on AgNP solutions with different PVP concentrations

Stabilizing agent concentration *[PVP], mM*	**Peaks**	**Intensity-based size** *%I, nm*	**Number-based size** *%N, nm*	**Count Rate** *kcps*
0	1	280	242	1045
0.005	1	19.86	15.42	7648
	2	132.4		
0.02	1	9.0	7.99	7300
	2	31.40		
	3	132		
0.05	1	9.110	7.984	8417
	2	36.54		
	3	150.5		

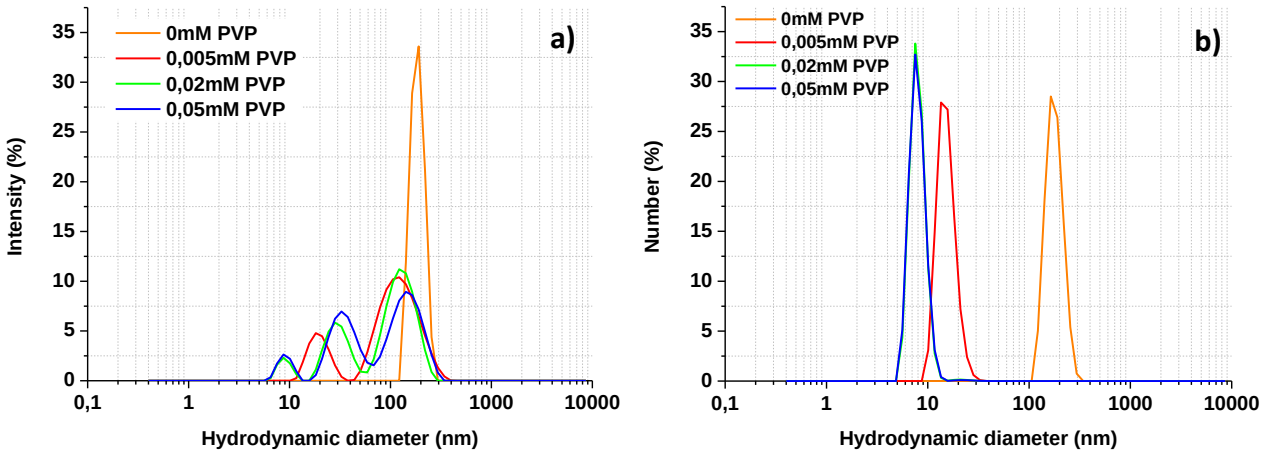

Figure 54: DLS size measurements performed on AgNP solution containing no PVP (orange), 0.005mM PVP (red), 0.02mM PVP (green), and 0.05mM PVP (blue) for 20min of plasma discharge. Results are presented in a) intensity and b) number based PSD as a function

The results obtained from the DLS measurements are in agreement with the results obtained by UV-vis analysis. In the absence of PVP, one particle size population was detected at around 280nm and 242nm, from the intensity and number-based PSD, respectively. In the presence of 0.005mM PVP, a bi-modal (two particle size populations) distribution is detected. Indeed, particles having sizes at around 20nm and 130nm from the intensity based PSD are identified. From the number-based PSD, mainly particles of 15nm are identified. From these results it is shown that the stabilizing effect of PVP appears even at a low PVP concentration of 0.005mM. This resulted in the formation of smaller-sized particles, and in the presence of a reduced amount of agglomerates in the reaction media. Moreover, as can be seen from figure 54b the number of the small-sized particle population is dominating over the number of agglomerates, and only one particle size population is present of around 15nm in hydrodynamic diameter. For an increase in PVP concentration above 0.005mM, it is observed in figure 54a-b that the as-synthesized nanoparticles show multi-modal (multiple particle size populations) PSD of lower scattering intensity. This might indicate that non-agglomerated and well-dispersed silver nanoparticles have been synthesized. Particle size populations for 0.02mM in intensity-based PSD are around 9nm, 31nm, and 132nm in hydrodynamic diameter, corresponding to scattering intensities of 6.5%, 28.1%, and 65.4% respectively. For 0.05mM PVP particle size populations are around 9nm, 36.5nm, and 150,5nm in hydrodynamic diameter, corresponding to scattering intensities of 7.7%,

37.6%, and 54.7%, respectively. With the appearance of a third peak in figure 54a, it is further demonstrated that the presence of agglomerates and larger sized particles have been reduced. This is also valid for number-based PSD in figure 54b as only one particle size population is present at around 8nm.

(Malina et al. 2012) have also performed DLS size measurement on chemically reduced silver nanoparticles stabilized by PVP in the concentration range between 1-5%. Although the results were presented in volume based PSD, an obvious decrease in the average particle size distribution was observed.

It has been determined that the addition of PVP during silver nanoparticle synthesis results in the decrease of the average particle size. Through particle stabilization an increase in particle concentration has been further observed.

The silver nanoparticles synthesized with different PVP concentrations have been characterized by SEM, and the obtained results are shown in figure 55a-d. The synthesis of silver nanoparticles using 2mM $AgNO_3$ in the absence of PVP reveals agglomeration of large-sized and irregular shaped particles (see figure 55a). In the presence of 0.005mM PVP, the particle size becomes smaller, but they are still slightly agglomerated as observed in figure 55b. A further increase of the PVP concentration to 0.02mM and 0.05mM reveals that nanoparticles are no longer agglomerated as shown in figure 55c-d, and are small-sized and uniformly distributed. The evolution of the particles size, when increasing the PVP concentration is similar to that observed from the DLS and UV-vis measurements. Mainly, particles polydispersity decreases, and the particle concentration increases, as a result of less agglomeration of the particles due to the presence of PVP.

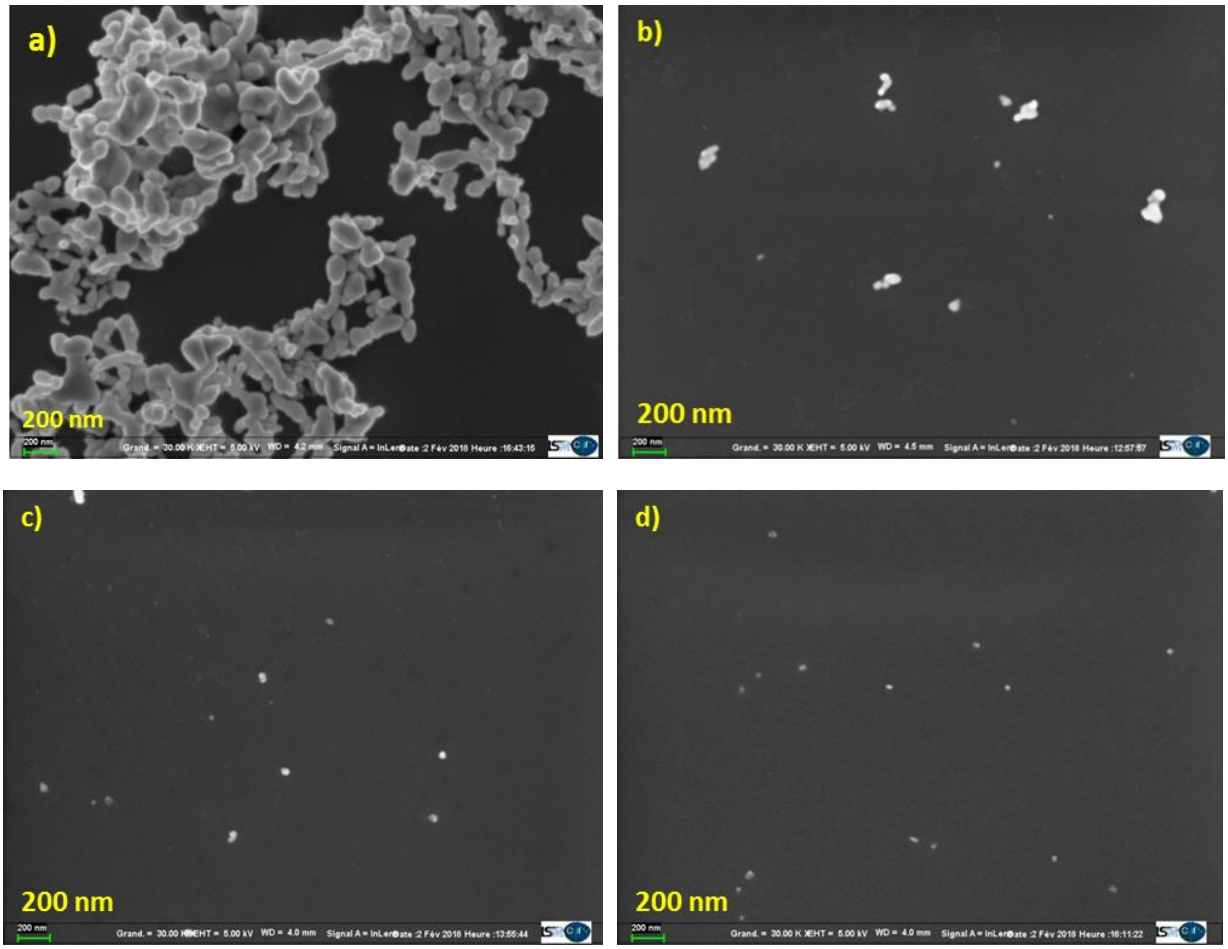

Figure 55: SEM micrographs showing 20min synthesis of AgNP containing a) no PVP, b) 0.005mM PVP, c) 0.02mM PVP, and d) 0.05mM PVP. Magnification 30kX

In order to be able to study the particles morphology, small-sized particles were further characterized by TEM, and the results are shown in figure 56a-d. Observations made in TEM micrographs are similar to those made in SEM micrographs. In the absence of PVP, silver nanoparticles are large-sized and highly agglomerated as shown in the TEM micrograph on figure 56a. In the presence of a low PVP concentration (0.005mM PVP), average particle size of silver nanoparticles decreased and reduction of particle agglomeration occurs, as observed on figure 56b. This showed that stabilization of particles did occur, but for a PVP concentration of 0.005mM particle agglomeration was not prevented completely. When increasing the PVP concentration to 0.02mM, the average particle size further decreases as a result of the stabilizing effect of PVP, as observed on figure 56c. This would result in the production of non-agglomerated spherical, small-sized (nm), and uniformly distributed silver nanoparticles. Similar

observations have been made for 0.05mM PVP, as shown on figure 56d. This might indicate that the stabilizing effect of PVP does apply from a certain concentration. These results are in accordance with results presented in the literature *(Malina et al. 2012), (Dung Dang et al. 2012)* showing that when increasing PVP concentration, the silver nanoparticles size decreases until an optimum is reached. It is therefore important to use a PVP concentration which falls in the concentration range allowing obtaining small-sized silver nanoparticles.

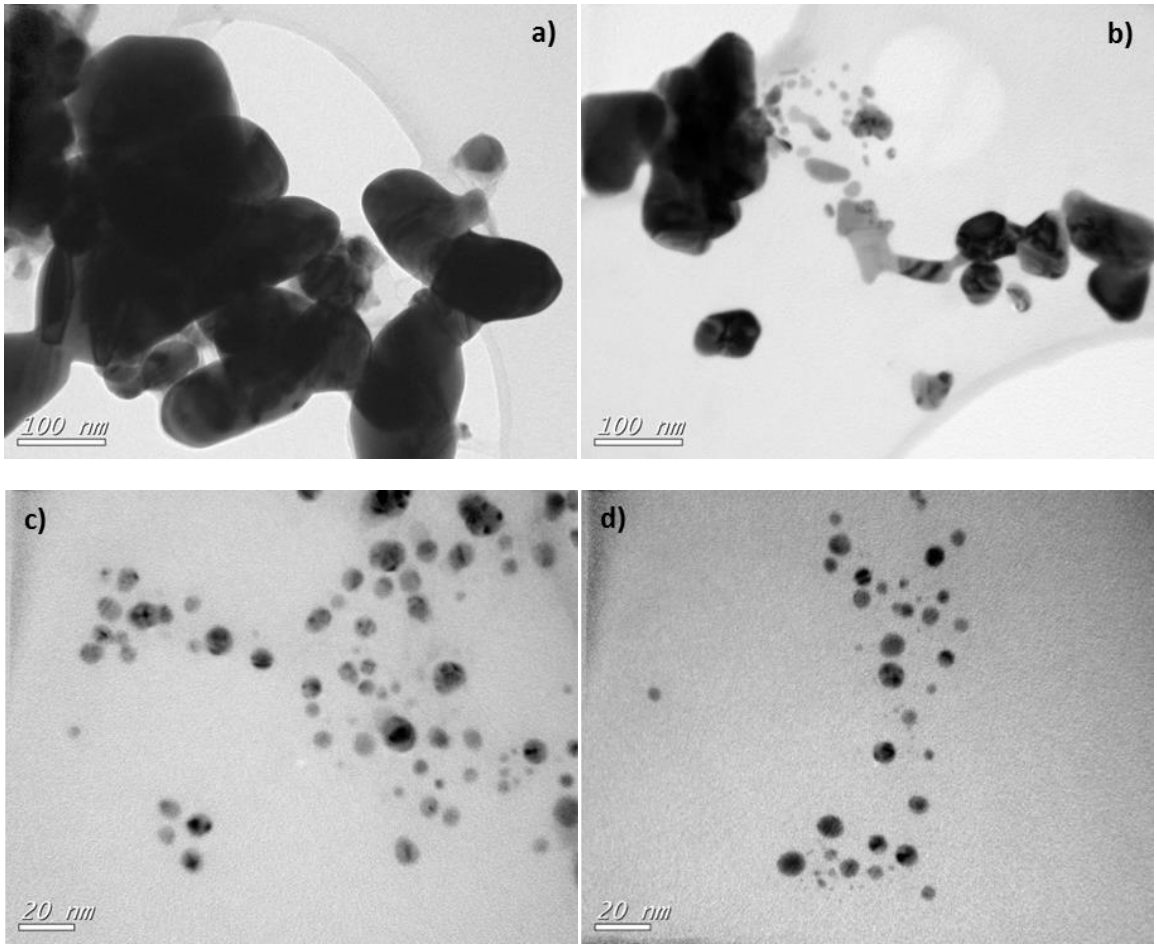

Figure 56: TEM micrographs showing 20min synthesis of AgNP containing a) no PVP, b) 0.005mM PVP, c) 0.02mM PVP, and d) 0.05mM PVP. Magnification 30kX

4.3.1 Silver nanoparticle growth mechanism in the presence of stabilizing agent

In this study, it has been demonstrated that synthesis of silver nanoparticles in the presence of a stabilizing agent did result in significant changes on their morphology. It was shown that an increase in the PVP concentration lead to a decreased average size of silver nanoparticles. In addition, by increasing the PVP concentration, the degree of particle agglomeration decreases significantly, resulting thus in a uniform distribution of the silver nanoparticles. According to *(Belloni 2006)*, coalescence of free clusters may be limited by a polymeric stabilizer. Functional groups with high affinity for the metal ensure the anchoring of the molecule at the cluster surface, while the polymeric chain protects the cluster from coalescing with the neighboring metal atom, and thus inhibits at early stage coalescence through steric hindrance. The final size of metal clusters depends on the metal, and decreases when the initial polymer/ion ratio increases.

From the HR-TEM micrographs on figure 57, it is shown that PVP interacts with silver nanoparticles by forming a thin polymeric coating that surrounds the particles. The thickness of this coating is not homogeneous on the particle surface, and may be up to 5nm in thickness as observed in figure 57.

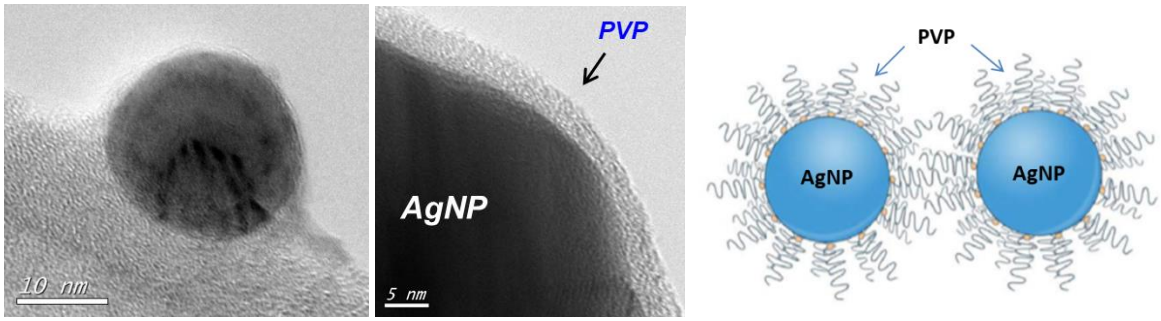

Figure 57: HR-TEM micrograph of silver nanoparticles in the presence of a polymeric stabilizing agent PVP (*this work*). A representation of the steric repulsion effect for AgNPs coated with PVP. Modified and reproduction of *(F. Yu et al. 2017).*

In the presence of a long-chained polymeric stabilizing agent, silver nanoparticles do not have the possibility to interact and result in particle coalescence. As it is shown in a representation of stabilized particles in figure 57, the long chained stabilizing agent prevents further interaction between particles, and provides hence their stabilization.

In the absence of a stabilizing agent, the particles collide and become chemically bonded through coalescence, resulting in aggregation and large-sized particles. From a given amount of PVP concentration, nanoparticles becomes sterically stabilized by a coating of a polymeric layer, as shown in figure 57, covering the entire particle surface. Attractive Van der Waals forces between particles are thus counter-balanced by repulsive inter-particle interactions.

The anchoring of the polymer molecule onto the surface of silver nanoparticles may occur from the coordination of N and O in PVP with silver ions *(Z. Zhang, Zhao, and Hu 1996), (H. Wang et al. 2005)*. This would generate a layer of polymeric coating, which blocks the active sites of the silver nanoparticles. An increase in the reduction rate of silver ions occurs in the presence of PVP. This is due to the fact that the functional groups in PVP (C=O) contributes in an increased electric density to silver ions, in which the Ag^{+}-PVP complex obtains electrons easily *(Z. Zhang, Zhao, and Hu 1996).*

Zhang *et al*. proposed a mechanism in the stabilization of silver nanoparticles. The mechanism initiates by PVP donating lone pair electrons of O and N to silver ions, which thus forms a coordinative complex of PVP and silver ions. In the second step, metallic silver nucleation is promoted by PVP, because silver ions are reduced owing to silver ions receiving electron clouds from the PVP. In the third step, they propose that PVP prohibits aggregation of silver nanoparticles as a result of its steric effect. However, in a more recent study performed by *(H. Wang et al. 2005)*, it has been determined that the coordination between N and silver ions are the main reaction. This makes the reaction of O and silver less important. They determined thus that the stabilization of silver nanoparticles by PVP was due to the coordination of N and silver ions. The reaction mechanism on figure 58 explains the stabilization of metallic silver by PVP.

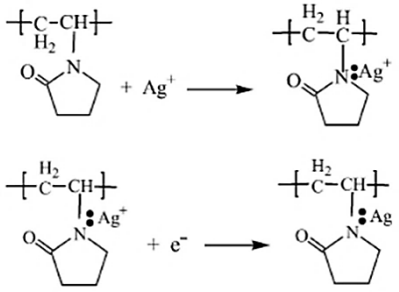

Figure 58: Stabilization mechanism of AgNP by PVP proposed by *(H. Wang et al. 2005)*

In another study performed by *(Shin et al. 2004),* the growth mechanism on PVP-stabilized silver nanoparticles has been proposed. In this study, silver nanoparticles were produced as a result of γ-irradiation of an aqueous solution of $AgNO_3$ in the presence of PVP. From this study, it was shown that an increase in PVP concentration resulted in a decrease in average silver nanoparticle size. Growth mechanism on PVP-stabilized silver nanoparticles proposed by Shin *et al*. is illustrated on figure 59, and consists of a three-step process:

1. Interaction of dissolved Ag^+-ions with polymeric PVP
2. Reduction of Ag^+-ions to Ag atoms by hydrated electrons (e^-_{aq}) formed as a result of γ-irradiation in an aqueous solution. Ag atoms form clusters that correspond to primary particles.
3. Primary particles coalesce and form larger aggregates that correspond to secondary particles

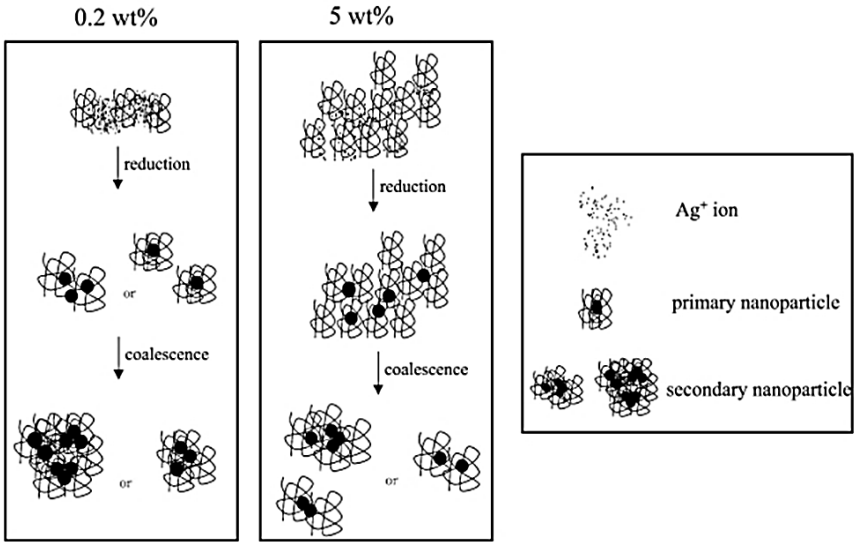

Figure 59: Growth mechanism of silver nanoparticles in the presence of 0.2wt% and 0.5wt% PVP. Growth mechanism proposed by *(Shin et al. 2004)*.

Both of the proposed mechanisms are likely to explain the stabilization of silver nanoparticles by PVP obtained when using a plasma-liquid synthesis process.

4.3.2 Summary

In this section the effect of PVP stabilization and PVP concentration on silver nanoparticles was studied. PVP concentration was applied between 0.005-0.05mM PVP. In previous section it was determined that 2mM $AgNO_3$ provided lowest average particle size of silver nanoparticles, and is

hence applied in this study. We observed that, in the absence of PVP, silver nanoparticles became aggregated and particles of irregular shapes were developed. This is a consequence of attractive Van der Waals forces, which lead towards particle collision, and hence aggregation occurred through coalescence of particles. In order to obtain smaller-sized particles, stabilization of particles was required. In this case, synthesis of silver nanoparticles in the presence of low PVP concentration (0.005mM) resulted in production of reduced average particle size, and reduction in degree of particle agglomeration. Since particle agglomeration was not prevented completely, PVP concentration was further increased to 0.02mM. Results showed that particles are spherical, small-sized and non-agglomerated. Further increase in PVP concentration of 0.05mM did not provide improved results on silver nanoparticle morphology. In this study small-sized and spherically-shaped silver nanoparticle has been stabilized in the presence of 0.02mM PVP, and will be used further in this work.

4.4 The influence of initial pH of the metal precursor solution on silver nanoparticle synthesis

This study is performed based on the information that water chemistry strongly impacts the physical and chemical characteristics of silver nanoparticles. The influence of water chemistry on nanoparticles is observed to cause aggregation, dissolution, or stabilization *(Xuan Li and Lenhart 2012)*. In this study, the influence of the water chemistry on silver nanoparticles will be studied with focus on the initial pH value of the precursor solution, and its influence on particle morphology will be investigated. It is very common to study the influence of pH on nanoparticle morphology using chemical reduction techniques *(Shabbeer et al. 2012)*, but less common in nanoparticle synthesis using plasma processes. This is due to the fact that pH is not a stable parameter and will eventually evolve during plasma discharge with the generation of reactive species and ionic compounds resulting from the plasma-liquid interaction.

The precursor solution has been modified through variation of the initial pH values in the range of pH2-11. This is done by the addition of buffers to a 2mM precursor solution containing 0.02mM PVP.

Silver nanoparticles are prepared in the same way as in the previous sections. The silver precursor solution consists of an aqueous solution of 2mM $AgNO_3$ and 0.02mM PVP. The pH of

the initial precursor solution is adjusted by addition of buffers. In order to prepare acidic and alkaline precursor solutions, different amounts of HNO_3 or NH_4OH are added into the solution, respectively. These buffers were chosen in order to avoid any reaction between the buffer and the metal precursor salt.

A pair of Pt wire electrodes of 3mm inter-electrode distance is immersed in the silver precursor solution for which high voltage DC-pulsed plasma discharges of 8kV and 50Hz are applied. High voltage pulse discharges are generated using a one-stage Marx pulse generator. Millisecond-pulsed discharges of short rise time (35ns) are generated in the spark gap of a Marx pulse generator by means of capacitive discharging. The plasma discharges generated under these conditions are in the corona plasma regime and do not reach breakdown. The PLI process parameters applied in this study are presented in table 17.

Table 17: PLI process parameters of parametrical study with focus on initial pH of the precursor solution

Discharge Physical parameters	Solution Physicochemical parameters
Applied voltage ($U_{applied}$): 8kV	Reaction volume (V): 100mL
Pulse repetition frequency (f): 50Hz	$AgNO_3$ concentration: 2mM
Inter-electrode distance (l_{Pt}): 3mm	PVP concentration: 0.02mM
Discharge time (t_{plasma}): 20min	Conductivity (σ): 298-1278µS/cm
	pH: 2-11

Current and voltage waveforms have been recorded towards the end of the synthesis process (t_{plasma}=20min), and characteristic I- and U- waveforms are presented in figure 60. The electrical waveforms were treated in the similar way as was done in the previous section. From these waveforms, discharge parameters were determined and presented in table 18. The E_{input} and discharge power value of pulsed plasma discharges for each pH values have been likewise calculated from equation 18 and equation 19, respectively.

The influence of initial pH of precursor solution on generation of plasma discharges in the reaction media is determined through *I*- and *U*-waveforms on figure 60.

Table 18: Electrical parameters obtained for changes in initial pH value of precursor solution between pH2 and pH11.

Buffer	Initial pH	Ionic strength *I, mol/L*	Voltage *U, kV*	Input energy per pulse E_{input}, *mJ/pulse*	Injected discharge power P_{plasma}, *W*
HNO_3	2	1.002	7.5	31.0	1.6
	4	0.052	8.0	40.4	2.0
No buffer	**5**	**0.002**	**8.0**	**42.5**	**2.1**
NH_4OH	7	0.012	7.5	37.7	1.9
	9	1.002	7.8	40.6	2.0
	11	2.002	7.0	30.8	1.5

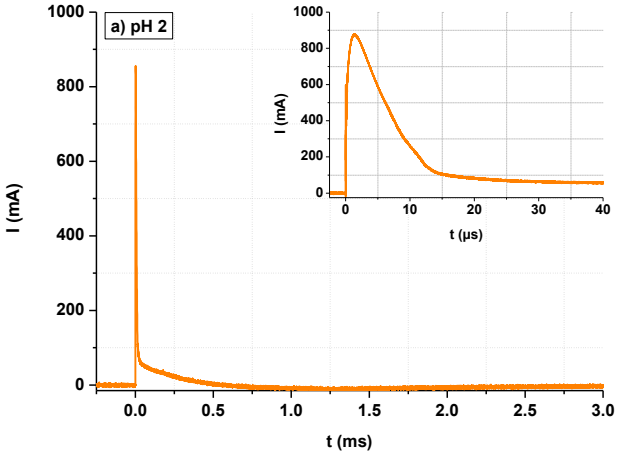

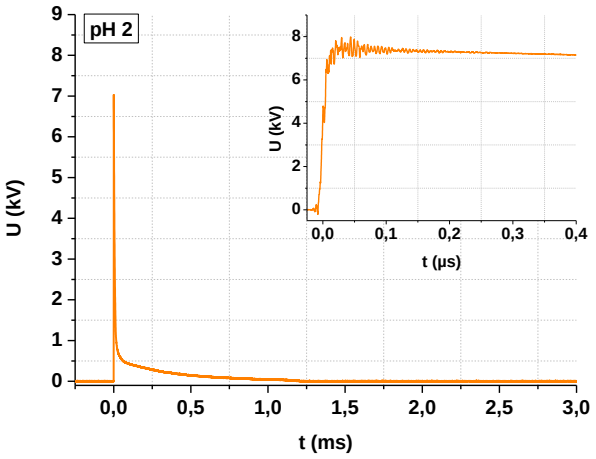

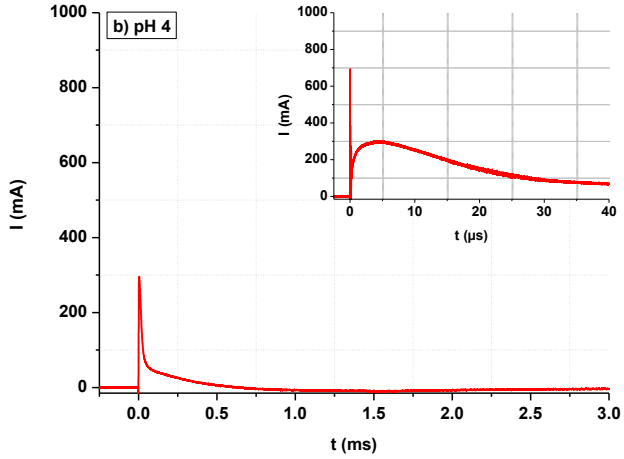

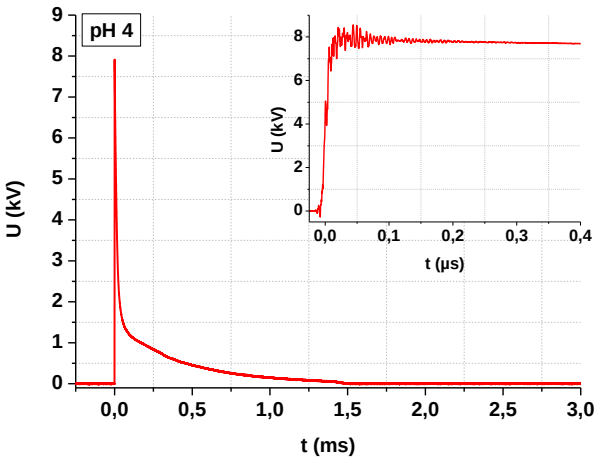

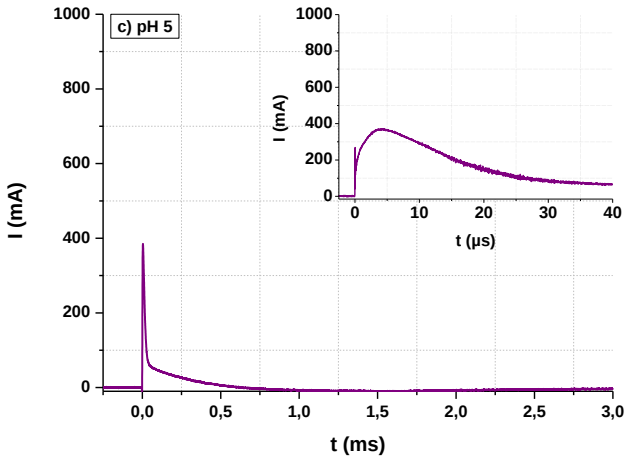
c) pH 5
I (mA)
t (ms)
I (mA)
t (µs)

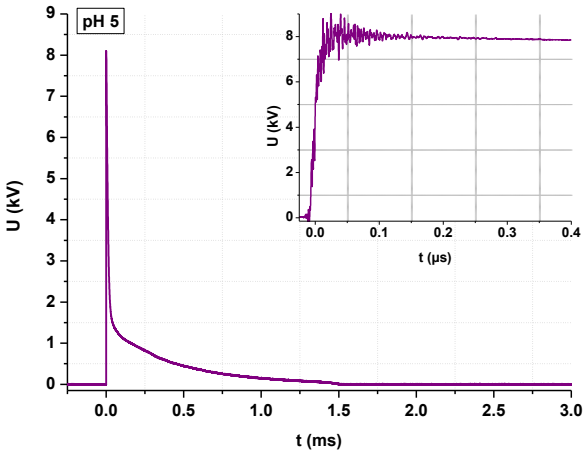
pH 5
U (kV)
t (ms)
U (kV)
t (µs)

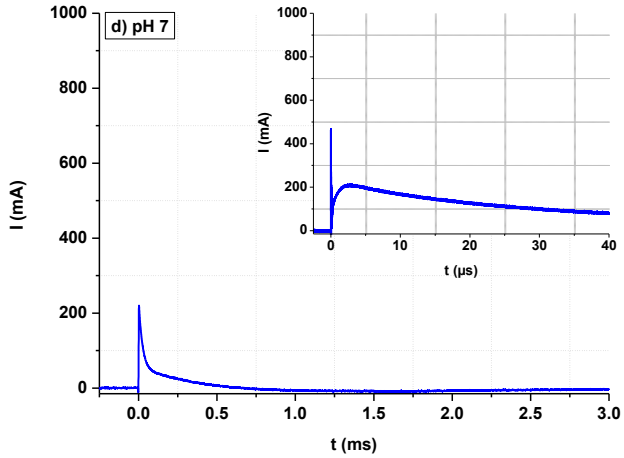
d) pH 7
I (mA)
t (ms)
I (mA)
t (µs)

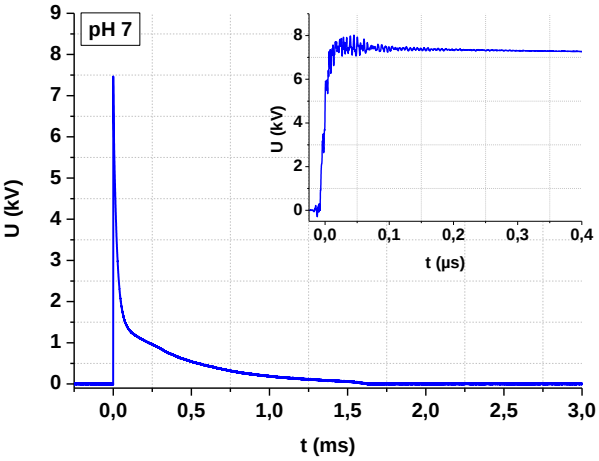
pH 7
U (kV)
t (ms)
U (kV)
t (µs)

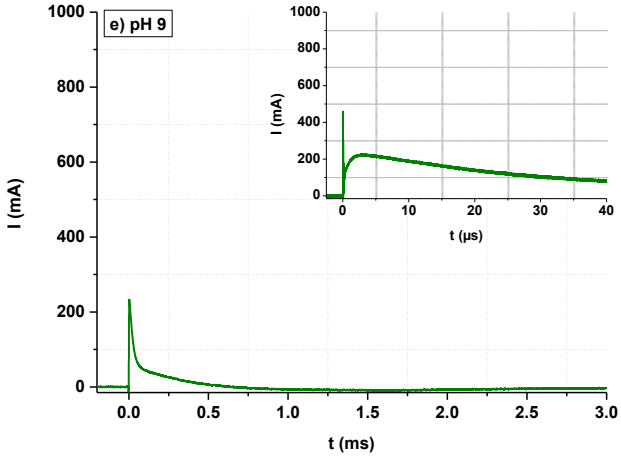
e) pH 9
I (mA)
t (ms)
I (mA)
t (µs)

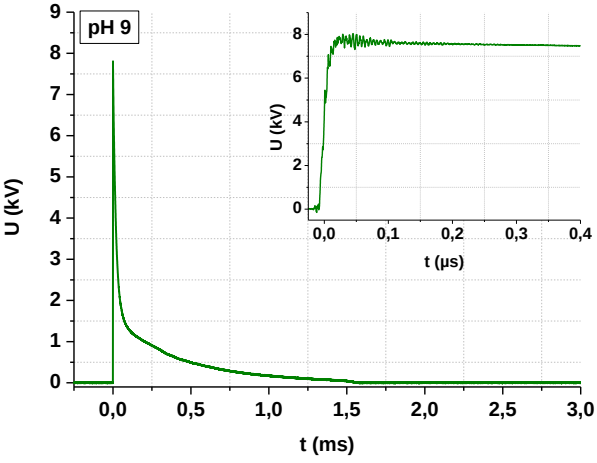
pH 9
U (kV)
t (ms)
U (kV)
t (µs)

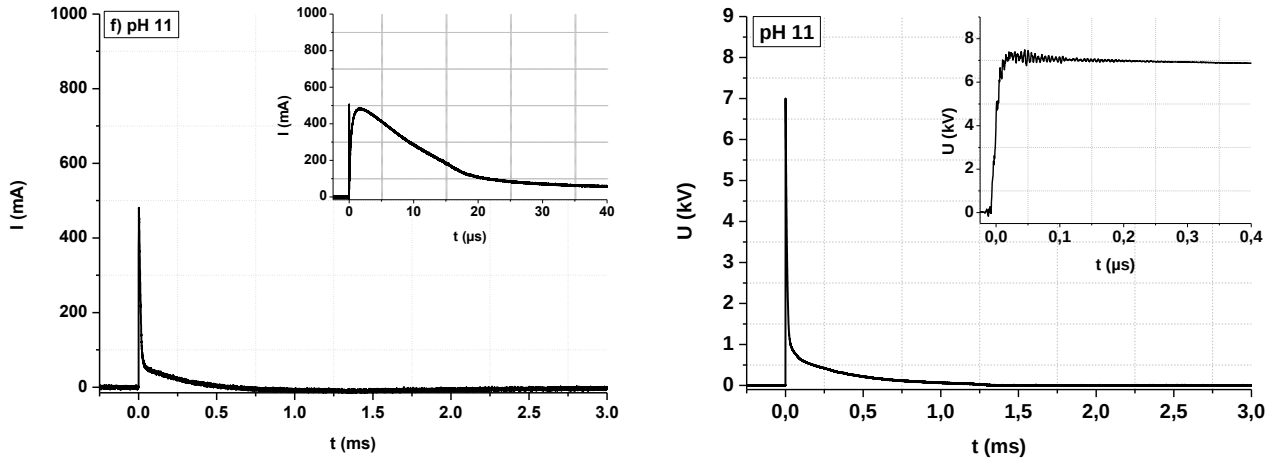

Figure 60: I- and U-waveforms for one pulse (at the end of the process t=20min). Nanoparticle growth environment has been modified by pH-regulation. Waveforms correspond to syntheses for a) pH2, b) pH 4, c) pH 5, d) pH 7, e) pH 9, and f) pH 11

From the *I*- and *U*-waveforms on figure 60 and E_{input} values on table 18, it was determined that the initial pH value of the precursor solution does have an influence on plasma generation in the reaction media. The U-value varies between 7.5kV-8kV towards the end of each synthesis process (t_{plasma}=20min), which is in the measurement range of the MARX pulse generator. However, the U-value for pH 11 has been measured at 7kV. The decrease in the U-value may be due to the influence of the reaction media on pulse generation, or due to experimental uncertainties. From the current waveforms it is shown that the current value and the slope of the decaying current pulses are not similar for each pH value. This occurs since conduction of the electric current is modified by the addition of pH-regulating buffers, which is possibly due to an increase in the number of charge carriers as the concentration of the buffer is increased. Hence, a variation in the E_{input} (per pulse) values occurs. The most significant changes in the E_{input} (per pulse) have been observed for pH2 and pH11, both at around 30mJ/pulse, which is 10mJ/pulse lower than the E_{input} (per pulse) obtained for the syntheses with an initial solution pH between 4 and 9.

Conductivity and pH measurements were performed for each pH value, before and after plasma exposure. As it is shown in table 19, initial pH values have been regulated by the addition of HNO_3 in order to obtain initial pH values of pH2 and pH4, and the addition of NH_4OH to obtain initial pH values of pH7, pH9, and pH11. As the buffer is added to the precursor solution its

initial conductivity changes accordingly, due to an increase in the ion concentration. During the adjustment of the initial pH value of the precursor solution, it is shown that the nanoparticle growth environment is modified in terms of the ionic strength, which is an important factor in the stabilization of silver nanoparticles. The addition of an increased concentration of HNO_3 decreases the initial pH from pH5 to pH2, which results in an increase in the initial solution conductivity and the ionic strength. The addition of NH_4OH increases the initial pH from pH5 to pH11, which results in an increase in the initial solution conductivity and ionic strength, as well. In this case, pH 5 corresponds to the precursor solution without addition of buffers.

Table 19: Physicochemical characteristics of the solution before and after the AgNP synthesis

Buffer	**Initial pH**	**Ionic strength**	**pH**		**ΔpH**	**Solution conductivity σ (μS·cm^{-1})**		**Δ σ (μS·cm^{-1})**
		I, mol/L	*Initial*	*Final*		*Initial*	*Final*	
HNO_3	2	1.002	2.6	3.0	0.4	1278	1285	7
	4	0.052	4.1	3.1	-1.0	318	360	42
No buffer	**5**	**0.002**	**4.5**	**3.7**	**-0.8**	**331**	**373**	**42**
NH_4OH	7	0.012	7.6	3.7	-3.9	298	326	28
	9	1.002	9.0	8.2	-0.8	301	307	6
	11	2.002	11.0	10.7	-0.3	663	697	34

As it is observed on table 19, exposing the precursor solution to 20min of plasma discharge did have an influence on the evolution of its pH, for all the studied initial pH values. The difference in the pH of the reaction solution before and after the discharge is denoted as ΔpH on table 19. From ΔpH it is observed that, apart for the solution having an initial pH of 2, the pH decreases after a 20min of plasma exposure.

As it is shown in figure 61, an evolution in the solution color during the 20min of plasma discharge did not occur for all pH values. Visible color changes did not occur for pH 2 and pH 11, apart from a decrease in terms of solution transparency. Concerning pH 11, the decrease in solution transparency but the absence of the characteristic yellow color might indicate that nanoparticles are agglomerated or exist as large-sized particles in the solution.

A strong yellow color change is an indication for production of small-sized and uniformly distributed silver nanoparticle, which is the case for pH4, pH5 (not shown on figure 61), and pH7. Furthermore, synthesis at pH 9 resulted in a dark colored solution.

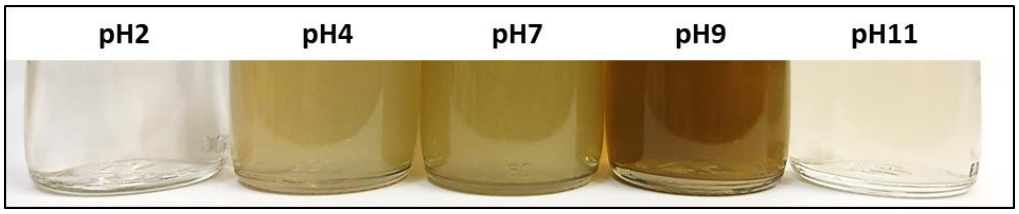

Figure 61: Color change of as-prepared AgNP for each pH values. pH 5 not included, however color change appeared similar to pH 4 and 7.

Changes in the physicochemical solution characteristics through the addition of a buffer compound have a clear effect on the plasma discharge, since the discharge current is transferred by the ions present in the solution. Depending on the precursor solution initial pH, a visible color change of the reaction media is observed.

In order to gather further information on the synthesis of silver nanoparticles, UV-vis absorption spectroscopy and DLS analysis are performed. Sampling of reaction media was done after 20min of plasma exposure for each pH value. These samples are initially analyzed by UV-vis absorption spectroscopy, and the resulting absorption spectra are presented in figure 62, and table 20. The absence of a color change for pH 2 and pH 11 is either due to no particle production or due to the production of highly agglomerated particles. The absorption spectra shown in figure 62, corresponding to the solutions at pH 2 and pH 11 confirm the fact that particle production is limited in these two cases, with absorbance values reaching only 0.205 and 0.126, respectively. The results obtained at pH 4, 5, and 7 are rather similar, not only in the color change, but also in particle concentration, based on the maximum absorbance and λ_{SPR} of silver nanoparticles, as shown in figure 22. From the broadness of the absorption peaks, it is determined that the polydispersity and/or particle agglomeration decreases for an increase in the pH-value. The FWHM value is at the maximum for pH 4, revealing a higher degree of polydispersity among particles. The solution presenting the lowest polydispersity and the higher

particle concentration is obtained at pH 9, as shown by the λ_{max} and FWHM values reported on table 20.

Table 20: Results obtained by UV-vis absorption spectroscopy performed on AgNP solutions obtained from different initial pH values

Initial pH	Absorbance	λ_{max}	FWHM
	a.u.	*nm*	*nm*
2	0.205	390	n/a
4	0.722	391	156
5	0.750	397	137
7	0.733	397	127
9	0.756	404	100
11	0.126	426	n/a

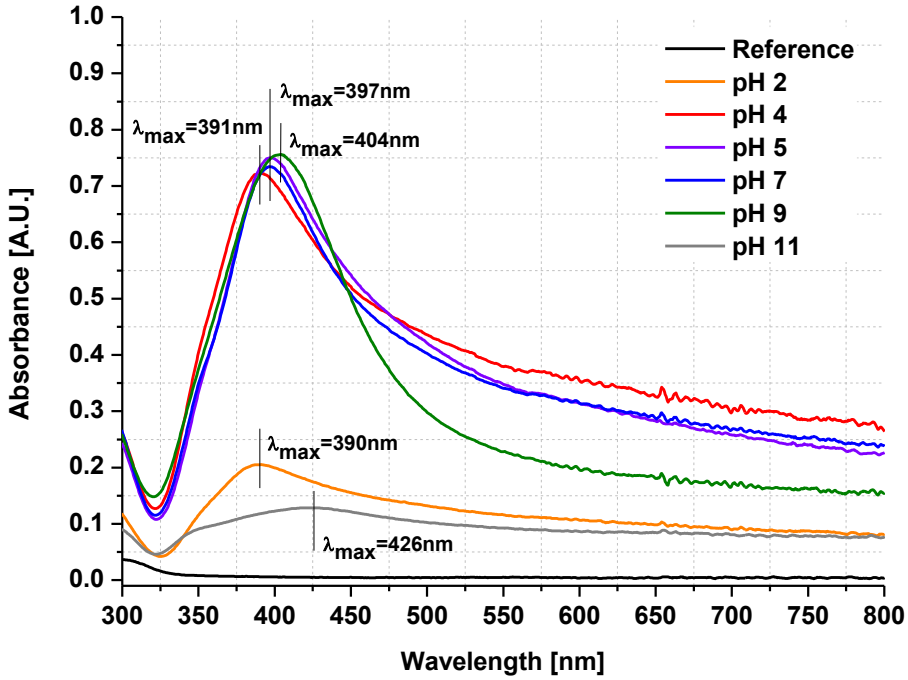

Figure 62: UV-vis absorption spectra of AgNP solutions for 20min of plasma discharge. Initial pH values of precursor solution between pH2 and pH11

DLS analyses are carried out for the same samples, in order to determine the average particle size distribution. The results obtained are presented on table 21, and the corresponding PSD

graphs are presented in both intensity and number based PSD on figure 63a-b.

These results are in agreement with the results obtained by UV-vis spectroscopy. A change in the initial pH of the precursor solution affected the average particle size and particle concentration. In the presence of HNO_3, at pH2 and pH4, similar particle sizes are given by the intensity- and number-based PSD. The only difference is that the particle concentration at pH2 is lower in comparison to the one at pH4. In intensity-based PSD on figure 63a, a bi-modal distribution with size populations at around 20nm and 110nm is obtained for both pH2 and pH4. Without pH regulation, which corresponds to an initial solution pH of 5, a multi-modal PSD occurred, indicating the presence of small-sized and non-agglomerated particles. In intensity-based PSD in figure 63a, the different size populations are detected at around 9nm, 30nm, and 130nm. In terms of number-based PSD in figure 63b, mono-dispersed and small-sized particles for pH 2, 4, and 5 are detected at around 17nm, 14nm, and 8nm, respectively. When NH_4OH is added as a buffer in order to obtain solutions of initial pH of 7, 9, and 11, the intensity-based PSD curves, shown in figure 63c, resulted in bi-modal size distributions of larger sized particle.

Table 21: Results obtained by DLS measurements performed on AgNP solutions obtained at different initial pH values

Initial pH	Peaks	Intensity-based size *%I, nm*	Number-based size *%N, nm*	Count Rate *CR, kcps*
2	1	21	17	5024
	2	113		
4	1	17.5	14	8070
	2	106		
5	1	9	8	7300
	2	31		
	3	132		
7	1	24	18	8900
	2	110		
9	1	21	18	2390
	2	143		
11	1	45.5	30	1877
	2	190		

At pH 7 the particle size populations are at around 24nm and 110nm. The size increased for pH 9, which presents particle populations of sizes at around 20nm and 143nm. Particles populations' size increased further at pH 11, with sizes at around 45nm and 190nm. The same results are obtained from the number-based PSD in figure 63d. Mono-dispersed and small-sized particles are obtained at pH 7, 9, and 11 showing sizes at around 18nm, 18nm, and 30nm, respectively. Furthermore, it was observed that the particle concentration decreased, when increasing the initial pH value of the reaction solution from pH7 to pH11.

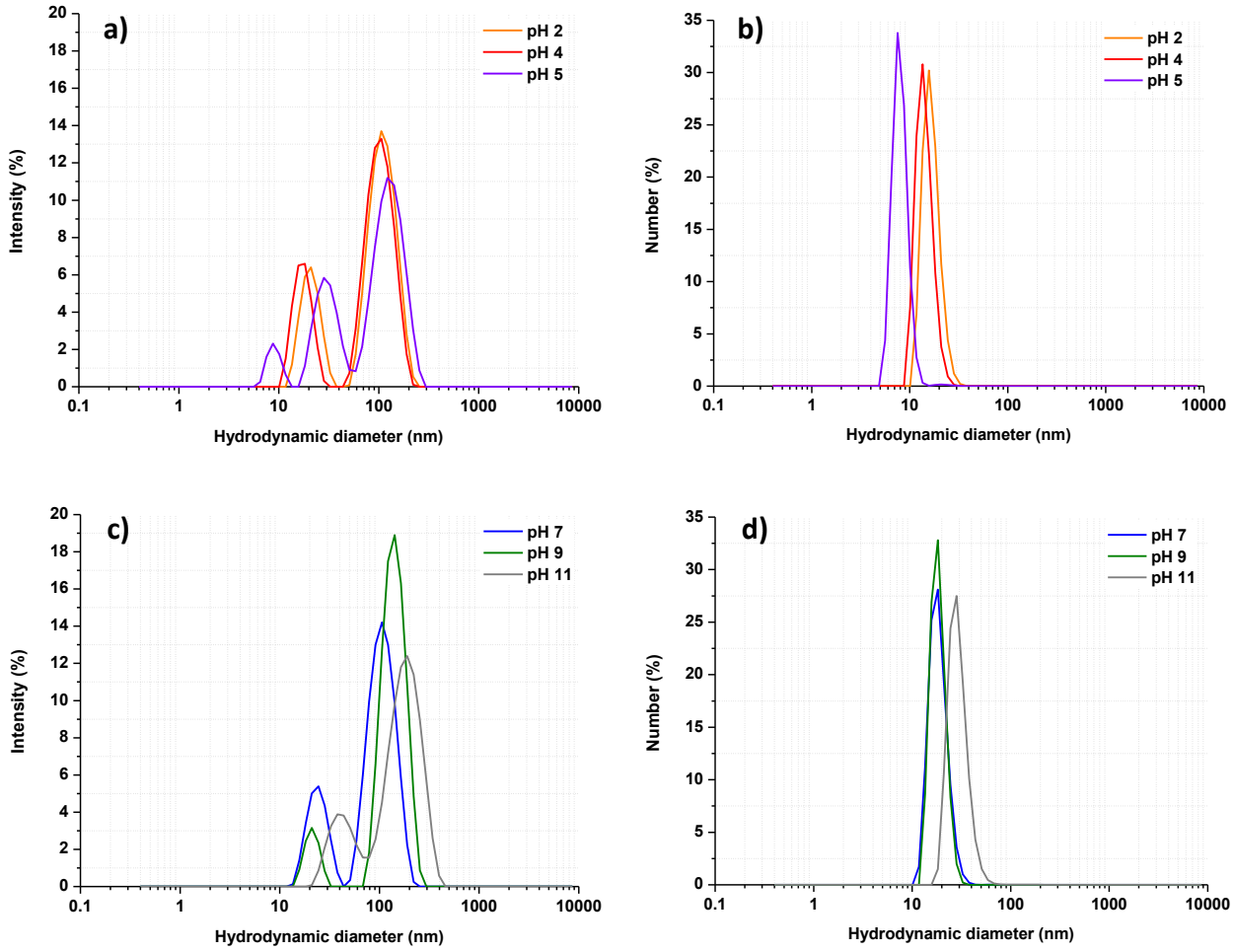

Figure 63: DLS size measurements graphs performed on AgNP for initial pH values between pH 2 and pH 11. Results are presented in intensity (a and c) and number (b and d) based PSD.

The silver nanoparticles obtained are also characterized by TEM. The results are presented in figure 64a-f.

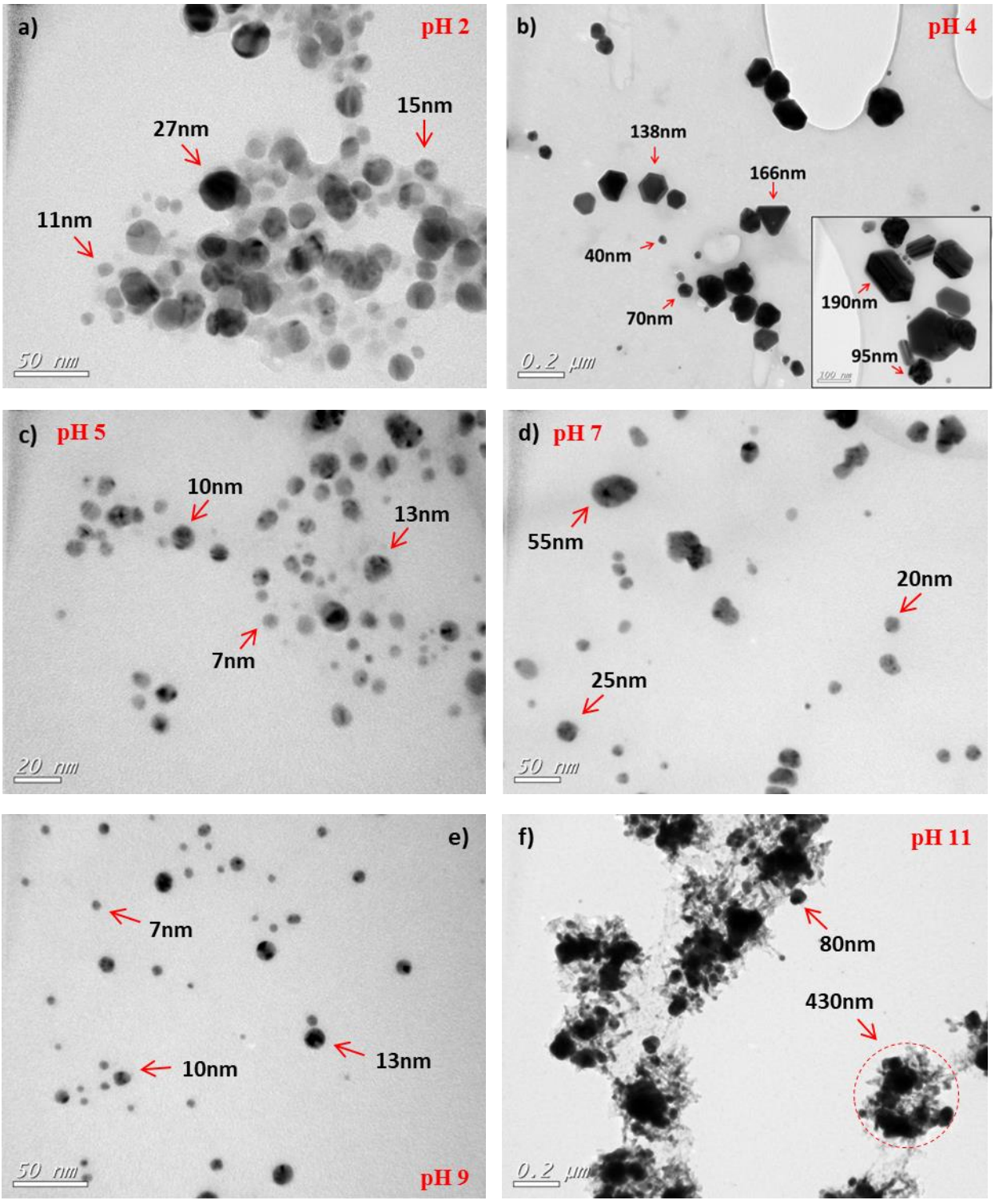

Figure 64: TEM micrographs of AgNPs prepared for different pH values. a) pH 2, b) pH 4, c) pH 5, d) pH 7, e) pH 9, and f) pH 11. Scaling of images are not the same for all.

For an initial solution having a pH2, spherical and non-agglomerated particles of sizes ranging between 10nm and 30nm are obtained. Increasing the initial pH of the precursor solution to pH4 resulted in the production of anisotropic-shaped particles. This includes mainly triangular and hexagonal shaped particles as shown in figure 64b. The size of the particles synthesized at pH 4 ranges approximately between 40nm and 190nm. The only difference between pH2 and pH4 is the ionic strength of the reaction media.

Gold nanoparticles of similar structures were obtained by *(Saito, Hieda, and Takai 2009)*, when producing particles at low pH. Saito *et al*. explained the formation of these shaped particles through the oxidative etching of gold nanoparticles by Cl^- ions during the growth phase.

As a reminder, the pH of the initially prepared precursor solution is around pH5. Thus, a synthesis from a solution at pH5 corresponds to a synthesis without pH regulation by buffer addition. In the TEM micrograph, as shown in figure 64c, silver nanoparticles are non-agglomerated, spherically-shaped and small-sized with particle sizes ranging between 7nm and 13nm. This corresponds well with the results obtained by DLS size measurements. Particles that were synthesized for an initial pH value of the precursor solution at pH7 are less spherical, and larger particles between 20nm and 55nm are present on figure 64d. Despite the same color change in reaction media for pH4, pH5, and pH7, the production of silver nanoparticles of different shapes have been observed, which may be related to the ionic strength of the reaction media. This confirms thus that the environment for nanoparticle synthesis has an important influence on the particle size and morphology.

Particles synthesized for an initial pH value of the precursor solution of pH9 are similar in size and shape as the particles obtained without pH regulation (pH5), as shown on figure 64e. The particles are spherically-shaped, non-agglomerated and small-sized, with sizes between 7nm and 13nm. The only difference between particle synthesis at pH5 and pH9 is the color change at the end of the process, and the ionic strength of the initial solution. In the last nanoparticle synthesis the initial pH value of the precursor solution is adjusted to pH11 by the addition of NH_4OH. The particles obtained in this case are present as particles tangled into groups of knots as shown in figure 64f. The knots were approximately 430nm in size consisting of nanoparticles of 80nm.

The silver nanoparticles produced from a precursor solution at pH 4 are a mixture of spherical and anisotropic shaped particles (triangular and hexagonal). The electrical and optical properties of anisotropic particles are different than those from spherical shaped nanoparticles, and it should be possible to observe the difference in the absorption spectra. In the case of the SPR of the spherical particles, the in-plane quadrupole resonance is observed at around 400nm *(Evanoff and Chumanov 2005).* In the case of the triangular particles, three dominant absorption peaks occur corresponding to the different modes of the plasmon excitation. These are in-plane dipole, in-plane quadrupole, and out-of-plane quadrupole plasmon resonances. As the edge length and particle size increases, in-plane dipole and in-plane quadrupole plasmon resonances red-shifts towards longer wavelengths, while out-of-plane quadrupole plasmon resonance displays a blue-shift *(C. Wu, Zhou, and Wei 2015)*. According to the UV-vis measurements performed on the sample corresponding to pH4, only a single SPR resonance peak is observed. The absence of the SPR resonance peaks characteristic for triangle particles on the absorption spectra may therefore be due to the reaction solution containing anisotropic shaped particles of different size range.

4.4.1 Growth mechanism of silver nanoparticles

In this parametrical study, the influence of reaction media environment has been investigated in terms of initial pH value of the precursor solution. Therefore, it was decided to produce silver nanoparticles by the plasma liquid immersion technique in acidic and alkaline growth conditions. These growth environments were created by the addition of HNO_3 for acidic (pH=2-4) and NH_4OH (pH=7-11) for alkaline conditions to the initial precursor solution (pH=5 for no pH regulation). A large variation in both average size and particle shape has been obtained, and is thus a proof that changes in the growth environment is an important parameter to control particle growth.

Acidic growth conditions (pH = 2 to 4):

As the concentration of H^+ ions increases at pH4 in comparison to pH5, a sudden change in the nanoparticle growth is observed. Under these conditions silver nanoparticles of mainly anisotropic shaped particles (hexagonal and truncated triangles) and isotropic shaped (spherical) particles have been produced. As presented on the TEM micrographs (see figure 64b), it is

observed that these particles may reach up to 200nm in diameter. For face-centered cubic metals (FCC) the thermodynamically favorable shapes are truncated nano-cubes and multiple twinned particles (MTP) *(Sun and Xia 2002)*, *(Washio et al. 2006)*. To reach a minimum surface energy in a FFC crystal structure, the growth direction is weighted on the (100) facet, which is of higher energy than the (111) facet. The truncation of the crystal structure further decreases the surface energy of the total crystal structure *(Capek 2017a)*. Growth directions and crystallographic facets are marked in figure 66b**Erreur ! Source du renvoi introuvable.** on a truncated (incomplete) triangle. The surface energy of a facet can be modified by the adsorption of various additives.

A growth mechanism of anisotropic shaped silver nanoparticles is proposed by *(Saito, Hieda, and Takai 2009)* as shown in figure 65. Saito *et al*. have prepared anisotropic silver nanoparticles through a solution plasma process technique. In the synthesis of silver nanoparticles silver ions were reduced by plasma generated hydrogen radicals into silver atoms. After clustering of silver atoms, silver clusters aggregate and coalesce into large-sized spherical nanoparticles. As a result of dissolution, spherical silver nanoparticles decrease in size and takes form into anisotropic shaped silver particles. This particle growth mechanism does not seem coherent to the results obtained from the particle characterization.

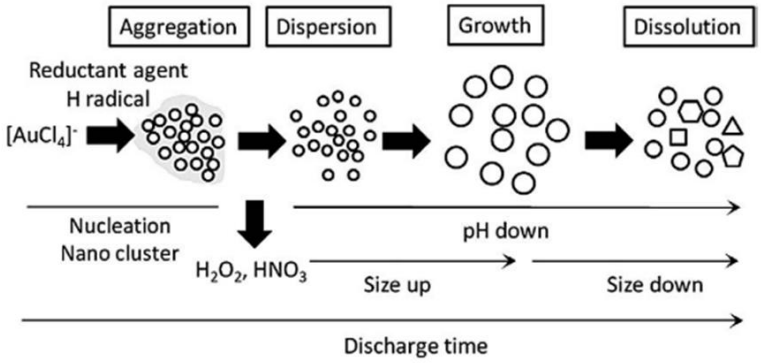

Figure 65: Nanoparticle growth mechanism. Reproduced from *(Saito, Hieda, and Takai 2009)*

Another possible growth mechanism of anisotropic silver nanoparticles is presented in figure 66a. This growth mechanism is proposed by *(P. Yu, Huang, and Tang 2010)*. Silver nanoparticles were prepared by Yu *et al*. by reduction of silver ions ($AgNO_3$ as silver precursor)

with $NaBH_4$ in the presence of PVP as the stabilizing agent. The first three steps are known from the growth mechanism as presented in section 4.2.

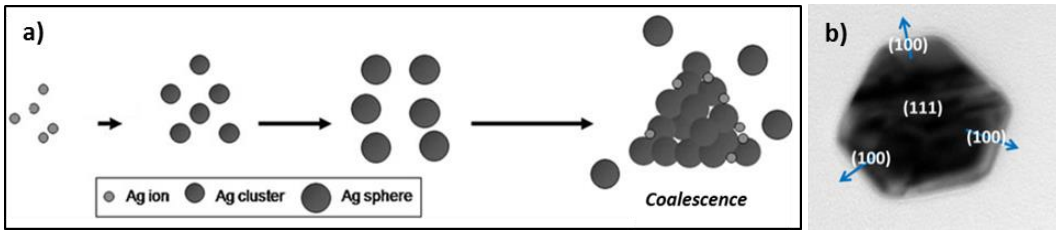

Figure 66: a) Nanoparticle growth mechanism. Modified and reproduced from *(P. Yu, Huang, and Tang 2010).* b) Growth directions of triangular silver nanoparticle. *(This work)*

In the first step, silver ions are reduced by hydrogen radicals into silver atoms, and then silver atoms dimerize and form small clusters. The silver clusters coalesce and forms silver nanoparticles. In the continuation of this growth mechanism, spherical silver nanoparticles are not stable and therefore become thermodynamically stable by coalescing into large-sized triangular particles as shown in figure 66a. this growth mechanism is coherent with results obtained from the particle characterization. As it is shown on figure 66b, growth direction of a triangular plate produced in our study is marked on an incomplete truncated triangular nanoparticle.

Alkaline growth conditions (pH=7-11):

For an initial solution pH of 11, it is observed that particles are no longer as uniformly distributed as it is observed for other solution pH. The particles were tangled into knot-like particle formations. If these particle formations are studied in detail, it is revealed that the knot-like formations consist of non-agglomerated and small-sized silver nanoparticles. They appear to be agglomerated due to encapsulation in the polymeric network, which is also visible on figure 67. As it is observed from the TEM micrographs on figure 64f, when increasing the solution alkalinity, the particles agglomerate through the formation of a polymeric network.

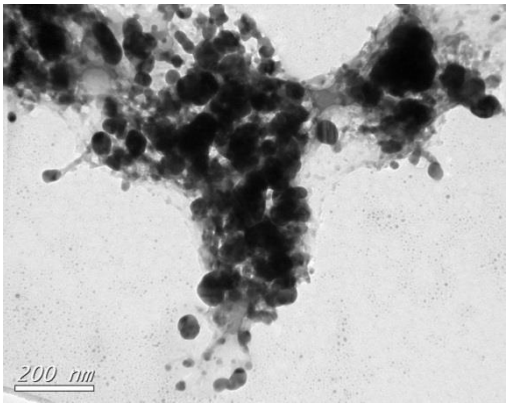

Figure 67: TEM micrograph of silver nanoparticles synthesized in initial solution pH 11. ***(This work)***

In the study performed by *(Chambers et al. 2014)* it is shown that agglomeration of silver nanoparticles increased at a higher ionic strength than at lower ionic strength of the reaction solution. However, *(El Badawy et al. 2010)* showed in their study that the pH and the ionic strength of the electrolyte did not have an impact on PVP-stabilized silver nanoparticles

In this study, modification of the initial solution pH also lead to changes in the ionic strength of the nanoparticle growth environment. And when increasing the ionic strength it is observed that nanoparticle encapsulation in the polymeric network is more likely to occur.

4.4.2 Summary

In this section the nucleation and growth environment during the synthesis of silver nanoparticle is studied with focus on initial pH value of the precursor solution. This study is performed with a 2mM $AgNO_3$ solution, in the presence of 0.02mM PVP. Silver nanoparticles were synthesized by the PLI process in which high voltage DC-pulsed discharges (U=8kV; f=50Hz) are generated between a pair of Pt electrodes. The plasma discharges were generated in the $AgNO_3$ solution during 20min and the resulting nanoparticles were later characterized in terms of particle morphology and size measurements by UV-vis spectroscopy, DLS, and TEM. From this study it was demonstrated that the initial pH value of the precursor solution has an influence on nanoparticle synthesis. The precursor solution was made acidic by the addition of HNO_3. In case of pH4 anisotropic shaped particles were formed, including triangular and hexagonal shapes. The precursor solution was made basic by the addition of NH_4OH. In the case of pH11, the particles were grouped into knots. When no pH regulation was made, which

correspond to pH5, non-agglomerated, small-sized and spherically-shaped silver nanoparticles were produced.

4.5 Conclusion

Silver particles were synthesized using pulsed plasma-in-liquid discharges. The obtained particles were characterized using different techniques such as XRD, SEM-EDS and XPS. It can be concluded that silver particles are in their metallic fcc phase, thus being highly crystalline. In addition, particles are non-oxidized and free from impurities. Indeed, the XRD pattern is in agreement with that of metallic AgNP as stated in ICDD, no. 04-016-6676. This was further confirmed by EDS analysis. Moreover, silver particles are confirmed as not oxidized by XPS, since the BE do not deviate from the theoretical values of metallic silver, located at 374 and 368eV, corresponding to $3d_{3/2}$ and $3d_{5/2}$, respectively.

The influence of different physicochemical parameters of the metal precursor solution on the particles synthesis was studied. The first studied parameter is the $AgNO_3$ concentration. From the results obtained it is shown that using an $AgNO_3$ concentration of 2mM lead to the formation of particles with a lower average particle size. Nevertheless, the resulting particles are rather agglomerated. In order to minimize particle agglomeration, the influence of using a stabilizing agent, in this case PVP, at different concentrations, on the silver nanoparticle morphology and particle size was also studied. Addition of 0.02mM PVP has shown to be the most effective concentration for nanoparticle stabilization. Synthesis of silver nanoparticles in the presence of 0.02mM PVP resulted thus in a uniform distribution of spherically-shaped and small-sized silver nanoparticles. The final parameter which influence was studied is the initial pH of the precursor solution. Under acidic conditions (pH4), large-sized silver particles of anisotropic shapes including triangular and hexagonal were produced. Under basic conditions (pH11), particles were grouped into knots. Silver nanoparticles which resulted in spherical and small-sized particles were synthesized for a pH value of the initial precursor solution of pH5.

Chapter V – Synthesis of silver nanoparticles by pulsed plasma discharges in liquid phase: using a solid state pulse generator

In the previous chapter, silver nanoparticles were produced using a newly-developed PLI process of MARX-pulsed HV plasma discharges. In order to synthesize spherical, small-sized, and non-agglomerated silver nanoparticles, the PLI process has been optimized by performing a parametrical study with focus on the physico-chemical parameters of the solution. In this previous parametrical study, the initial metal precursor concentration, the concentration of the stabilizing agent, and the initial pH were studied. From this parametrical study it was concluded that, in order to synthesize spherical, small-sized, and non-agglomerated silver nanoparticles, the required physico-chemical conditions were an aqueous solution of 2mM precursor concentration ($AgNO_3$) and 0.02mM stabilizing agent concentration (PVP). In these conditions, the as-prepared aqueous silver precursor solution has a pH value of 5 and a conductivity of 300µS/cm. It was further determined that addition of chemicals for the modification of the nanoparticle growth environment was not required. Thus, this set of conditions has been used in the parametrical study presented in this chapter, which focuses on investigating the influence of the physical discharge parameters on the silver nanoparticle synthesis.

In order to easily control and regulate such parameters a high voltage solid-state switch (HTS 161-06-GSM, BEHLKE Electronic GmbH) will be used.

The parametrical study is initiated by the investigation of the influence of the pulse duration on the silver nanoparticle synthesis. Then, the influence of the applied voltage ($U_{applied}$) is considered. Finally, the effect of the inter-electrode distance (l_{Pt}) is studied, while keeping the ratio of $U_{applied}$ /l_{Pt} constant.

The parametrical study proceeds in the same methodology as presented in chapter IV. Silver nanoparticles are synthesized using the PLI process at specific process parameters. Following the synthesis, produced silver nanoparticles were characterized using UV-vis absorption spectroscopy, DLS, SEM, and TEM as main characterization techniques.

5.1 The influence of discharge pulse duration on silver nanoparticle synthesis

The second parametrical study initiates with an investigation of changes in pulse duration of the pulsed partial corona discharges, and how this parameter influences the silver nanoparticle synthesis. This process parameter has been included in this study since the pulse duration of discharges is documented to have an influence on nanoparticle growth. *(H.-J. Kim et al. 2018)* reported that a decrease in the pulse duration of plasma discharges reduces the size of the nanoparticles. In their study, they generate bi-polar pulsed plasma discharges of 3.8kV and 5kHz in pure de-ionized water (80°C), and applied two silver wires as electrodes and silver nanoparticle source. In terms of pulse duration, 20µs, 40µs, and 60µs were applied in their study.

In this study, a high voltage solid-state switch was applied to the PLI process to generate pulsed plasma discharges. For this parametrical study, **pulse duration of plasma discharges generated in liquid phase was applied in the working range between 150µs and 1.5ms.** This range has been determined, due to experimental conditions of the PLI process, which permits generation of pulses for minimum pulse duration of 150µs. Maximum pulse duration of 1.5ms has been determined to be in the same order of magnitude as pulses generated by the MARX pulse generator.

Two Pt wire electrodes (d=200µm) of 3mm inter-electrode distance were horizontally immersed into 100mL of the aqueous silver precursor solution in order to reach a pin-to-pin electrode configuration. Plasma discharges were generated in the precursor solution by applying 9kV high voltage DC-pulsed plasma discharge (f=50Hz) to the high voltage electrode (anode). The applied high voltage was measured on the anode through a high voltage probe, while the current was measured on the ground electrode (cathode) through a current probe. Prior to each synthesis, the applied voltage was regulated on the HV DC power generator, while pulse duration and pulse repetition frequency were regulated on the frequency generator. In the use of a fast solid state high voltage switch, pulsed discharges are generated by charging of a 1nF ceramic capacitor. BEHLKE-generated pulses have a faster voltage rise-time of approx. 2ns, which is 17 times faster than the voltage rise-time of the MARX-generated pulses. Plasma discharges generated under these conditions were in the partial corona discharge regime and did not reach breakdown. PLI process parameters applied in this study are presented in table 22:

Table 22: PLI process parameters with focus on discharge pulse duration

Discharge Physical parameters	Solution Physicochemical parameters
Applied voltage ($U_{applied}$): 9kV	Reaction volume (V): 100mL
Pulse repetition frequency (f): 50Hz	$AgNO_3$ concentration: 2mM
Inter-electrode distance (l_{Pt}): 3mm	PVP concentration: 0.02mM
Discharge time (t_{plasma}): 20min	pH: ≈5
Pulse duration: 150μs – 1.5ms	Conductivity (σ): 300μS/cm

Current (I) and voltage (U) waveforms were recorded towards the end of the synthesis process (t_{plasma}=20min) and are presented on figure 68. In the current waveforms, a complete profile of a single pulse is presented, as well as a detailed profile of current pulses (τ = 40μs) (see insets of current waveforms on figure 68). Voltage waveforms of a single pulse have been presented in a similar approach, but the detailed profile of the pulse is instead up to τ = 0.75μs (see insets of voltage waveforms on figure 68). Discharge parameters were determined as appeared in the waveforms, and they are presented on table 23. The grey field on table 23 corresponds to values obtained for PLI process using the MARX-pulse generator in the generation of 1.5ms pulsed plasma discharges. Oscillations of current and voltage waveform do occur as a result of charge effects from the switching of BEHLKE pulse generator during charging and discharging of the capacitor in the RLC electrical circuit. Comparing the oscillations in the waveforms obtained by using the MARX and BEHLKE generator, it is observed that oscillations are less noisy, when using the BEHLKE generator. Due to charging effects, the measured voltage may be higher than the applied voltage.

Input energy per pulse (E_{input}) was calculated by integrating applied voltage times discharge current over the pulse duration ($t_0 \rightarrow t$), as shown in equation 18. The injected discharge power (P_{plasma}) of pulsed plasma was then calculated by multiplying the input energy per pulse with pulse repetition frequency, as shown in equation 19.

$$E_{input} = \int_{t0}^{t} I \cdot U \, dt \qquad \textit{Equation 20}$$

$$P = E_{input} \cdot f \qquad \textit{Equation 21}$$

E_{input} (per pulse) values are calculated from *I*- and *U*-waveforms of a single pulse and the resulting E_{input} waveform is presented on figure 69.

Table 23: Plasma parameters obtained for an increase in pulse duration using BEHLKE pulse generator. The grey field corresponds to plasma parameters obtained from MARX-generated pulses.

Pulse duration	Voltage	Input energy per pulse	Injected discharge power
µs	*U, kV*	E_{input}, *mJ/pulse*	P_{plasma}, *W*
150	12	38.9	2.0
500	12	52.0	2.6
1500	12	73.1	3.7
1500	8	42.5	2.1

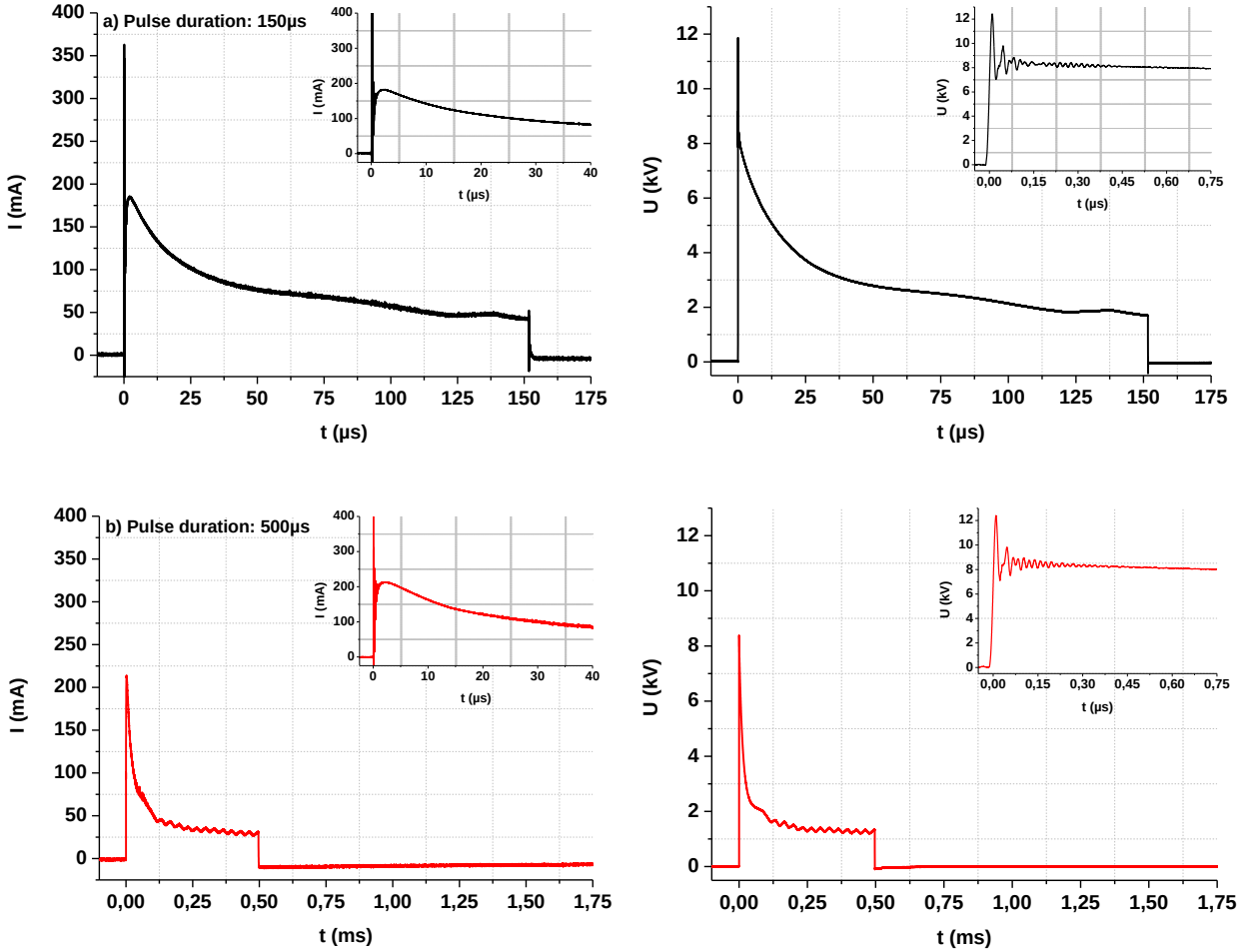

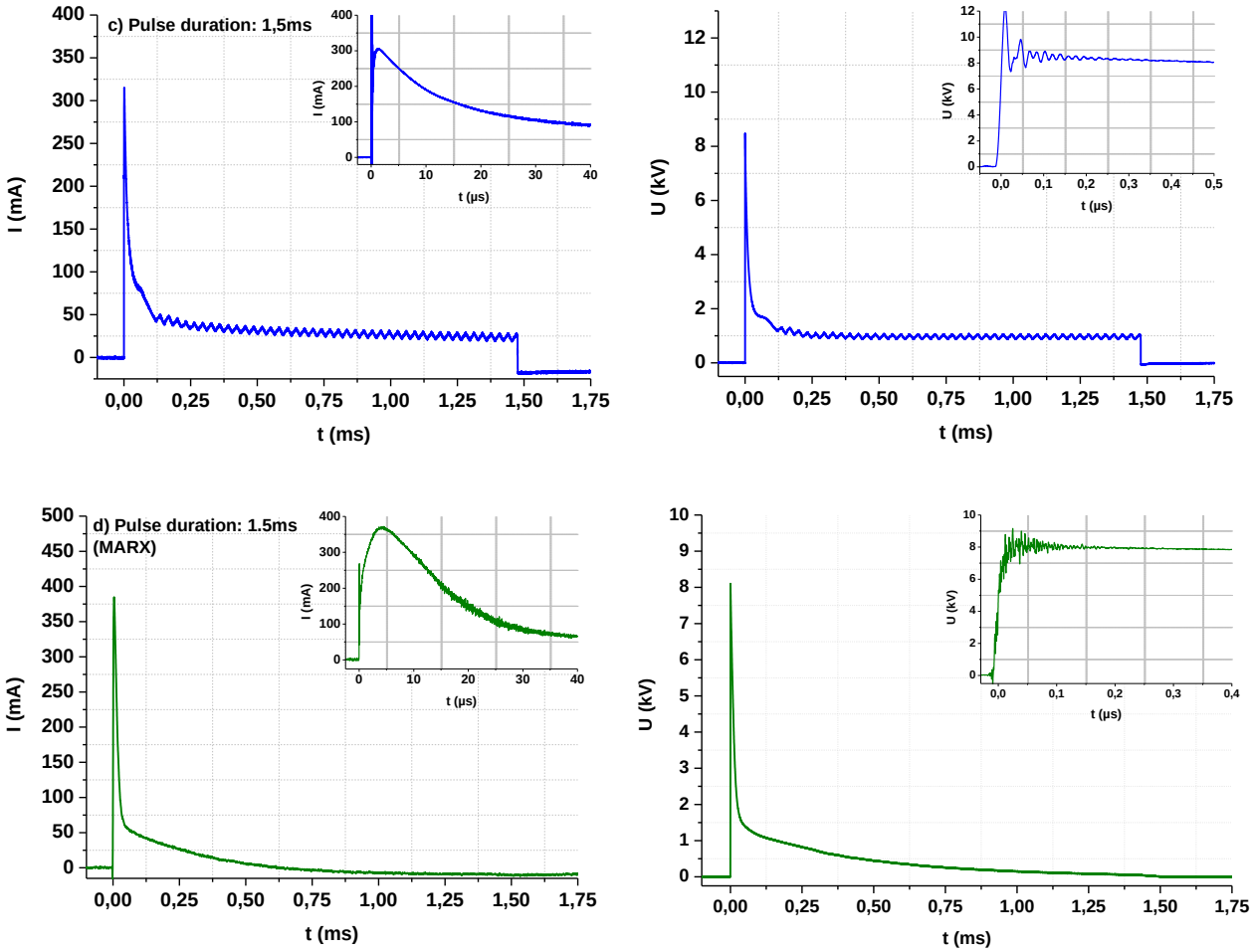

Figure 68: I- and U-waveforms for one pulse (at the end of the process t=20min). Pulse duration applied to plasma discharges are a) 150µs, b) 500µs, c) 1.5ms for BEHLKE-generated pulses, and d) 1.5ms for MARX-generated pulses.

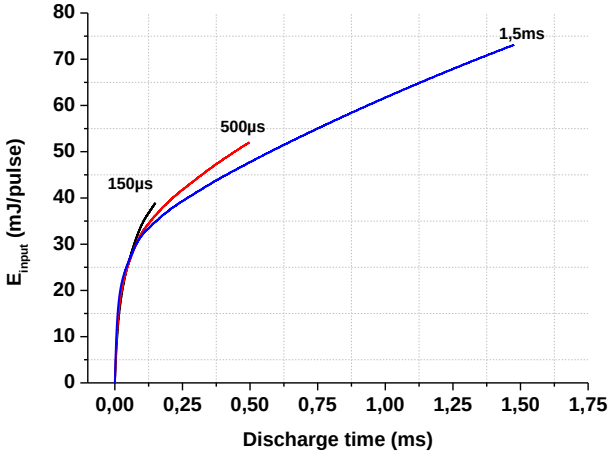

Figure 69: Input energy per pulse of pulsed plasma discharges obtained as a result of 20min silver nanoparticle discharge using the PLI process for different pulse duration of plasma discharges. Pulse duration of plasma discharges used, are 150µs (black), 500µs (red), 1.5ms (blue) for BEHLKE-generated pulses.

From the I- and U-waveforms on figure 68a-c, it is observed that the pulse duration increases from 150 µs to 1.5 ms for a constant $U_{applied}$ value, and that the maximum current value increases. Visual observation of streamer-like discharges generated in the liquid phase at 150µs and 1.5ms, showed that the increase in pulse duration did not influence the streamer-like discharges (e.g. number or length of gaseous channels). However, an increase in pulse duration from 150µs to 1.5µs did result in streamer-like discharge of increased intensity, which may be correlated to the increase in the current value. An increase in pulse duration could thus increase the production of plasma-generated electrons, which results in an increase in the conduction of the electric current, and thus an increase in the E_{input} (per pulse).

From these observations, it is shown that the pulse duration of plasma discharges do have an influence on plasma generation in the liquid media.

The main differences between I- and U-waveforms of pulsed discharges using the MARX and BEHLKE pulse generators is observed on figure 68c-d using 1.5 ms as the pulse duration. Pulses generated using the MARX generator is decreasing exponentially in the discharging of the capacitor until a zero-charge was reached. On the other hand, pulses generated using the BEHLKE pulse generator decreases rapidly up to 150µs and after a slow decay remains constant around 25mA (in terms of current) and 1kV (in terms of voltage). This continues until the specified pulse duration was reached, after which a sudden decrease at zero did occur. Therefore, since the I- and U-values do not reach zero during one pulse, a continuous transfer of energy was put into generation of plasma discharges, as reported on figure 2.

From the values presented on table 23, it is observed that the E_{input} and P_{plasma} values of MARX-generated pulses are lower in comparison to BEHLKE-generated pulses of similar pulse duration (1.5ms). However, similar E_{input} and P_{plasma} values have been obtained for pulse durations of 150µs using BEHLKE and 1.5ms using MARX. These differences may thus occur due to the fact that the measured voltage remains constant at 1kV during the main part of the pulse.

Ex-situ conductivity and pH measurements were conducted for all pulse duration syntheses, before and after 20min of plasma discharge, and these are presented on table 24. As it is shown on table 24, initial pH and solution conductivity remains constant at pH5 and 300µS/cm, respectively. However, changes in the physico-chemical parameters of the reaction media occurs during 20min of plasma discharge. From a general point of view, a decrease in pH indicates

acidification of the solution, and an increase in solution conductivity indicates formation of ions. It was previously in chapter IV discussed, that acidification of the reaction media might be a result of HNO_3 formation. This acidic compound might be produced, when NO_3^- (dissolved $AgNO_3$ salt) reacts with $H^\bullet$ (dissociation of water molecules due to e_{aq}^-).

Table 24: Changes in solution chemistry monitored before and after silver nanoparticle synthesis using BEHLKE pulse generator. Grey field corresponds to values obtained from MARX-generated pulses.

Pulse duration	**pH**		**Solution conductivity** σ, $\mu S.cm^{-1}$	
µs	*Initial*	*Final*	*Initial*	*Final*
150	5	3.5	300	324
500	5	3.3	300	350
1500	5	3.4	300	407
1500	4.5	3.65	331	373

As it is shown on table 24, there is no significant change in the final pH values for an increase in the pulse duration of plasma discharges, and may be due to a constant formation rate of HNO_3. An increase between the initial and final solution conductivity is also observed for all pulse durations. In theory, this increase is due to the fact that the excitation, ionization, and dissociation of water molecules lead to the formation of ionic species. It is also observed, that an increase in the final solution conductivity values, at the end of the 20 min process, occurs for an increase in the pulse duration. Due to the increase in final solution conductivity values, it may occur that the plasma processes rate increases. For an increase in the solution conductivity, an increase of the discharge current and increase in electron density occurs *(Šunka 2001)*. This increase in solution conductivity is associated to an increase in E_{input} values, since an increase in the input energy per pulse does result in an increased production of reactive species. Therefore, for an increase in the pulse duration, an increase in the production rate of reactive species may occur. Hence, it is expected that an increase in pulse duration may influence nanoparticle production.

As-synthesized silver nanoparticle solutions prepared with BEHLKE-generated pulsed plasma discharges of different pulse durations are presented in figure 70. As it is observed, these solutions are, from a qualitative point of view, significantly different, presenting distinct colors.

Since metallic nanoparticles of different sizes and geometries possess different absorption properties as a result of the SPR excitation *(Millstone et al. 2009), (J. Cao, Sun, and Grattan 2014)*, this can explain the differences in the solution color. Another possible reason for this color difference could be related to particle concentration, as an increase in the particle concentration leads to a decrease in solution transparency.

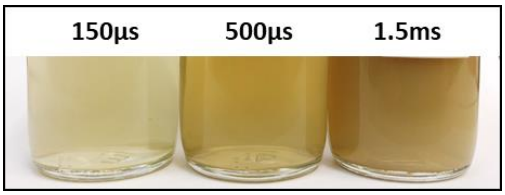

Figure 70: Color changes for 20min nanoparticle synthesis applying 150µs, 500µs, and 1.5ms pulse duration of plasma discharges

An increased particle concentration for an increase in the pulse duration may thus confirm that an increase in plasma processes, and thus an increase in the production rate of reactive species occur. However, the difference in particle size and geometry could also be a possible reason.

In order to determine how the pulse duration influences the silver nanoparticle synthesis by the PLI process, further analyses were performed. After a 20min of process time, as-synthesized silver nanoparticles were analyzed by UV-vis absorption spectroscopy. The results are presented on figure 71 and table 25.

Table 25: Results obtained from UV-vis absorption spectra of silver nanoparticle synthesis applying 150µs, 500µs, and 1.5ms pulse duration of plasma discharges. Marked field corresponds to values obtained from MARX-generated PLI process.

Pulse duration	**Absorbance**	**λ_{max}**	**FWHM**
µs	*a.u.*	*nm*	*nm*
150	0.29	402	138.6
500	0.72	400	161.4
1500	1.69	402	145.0
1500	0.75	397	137.0

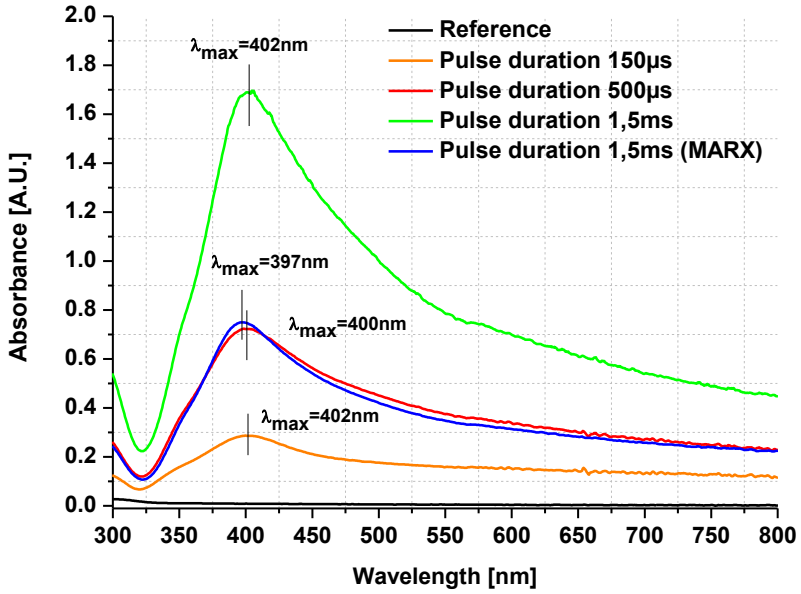

Figure 71: UV-vis absorption spectra of silver nanoparticles synthesized by applying plasma discharge of pulse duration 150µs (orange), 500µs (red), and 1.5ms (green). In addition, 1.5ms pulse duration (blue) of plasma discharges for nanoparticle synthesis using a Marx pulse generator is shown.

From these results, it is determined that the maximum absorption of silver nanoparticles is observed at a wavelength (λ_{max}) around 400nm. This is in agreement with surface plasmon resonance (SPR) of spherical silver nanoparticles absorbing visible light at around 400nm. At λ_{max}, silver nanoparticle light absorption increases with increasing the pulse duration from 0.29 at 150µs to 1.69 at 1.5ms. **These results confirm that an increase in the pulse duration of plasma discharges increases the rate of plasma-chemical processes to result in an increased particle concentration of silver nanoparticles**.

Broad absorption peak and slow decrease in the absorption band of silver nanoparticles produced by BEHLKE-generated pulse discharges have been observed. This could occur due to the polydispersity of nanoparticles and/or the particle agglomeration.

Absorption bands of silver nanoparticles produced by MARX-pulsed PLI process (AgNP-MARX) of 1.5ms in pulse duration are presented as the blue line on figure 71. The absorption band of silver nanoparticles produced by BEHLKE-pulsed PLI process (AgNP-BEHLKE) of 1.5ms is likewise presented as the green line figure 71. By comparing these two absorption bands at λ_{max}, it is shown that the absorbance of AgNP-BEHLKE is more than 2-fold the one of AgNP-

MARX. Differences in the intensity of absorption band indicate that particle concentration of silver nanoparticles is not similar for these two processes. Plasma parameters for these two processes are presented on table 23 (p. 144), and it is shown that for a pulse duration of 1.5ms, E_{input} = 40mJ/pulse for MARX-pulsed PLI process and E_{input} = 73mJ/pulse for BEHLKE-pulsed PLI process. Thus, for a given pulse duration, the BEHLKE-pulsed discharge delivers more energy to the system, leading to the production of a higher amount of particles. **Differences in the maximum absorption band of silver nanoparticles, and hence in nanoparticle concentration, of these two processes are thus explained by the differences in the E_{input}, which is delivered to the process.**

Another comparison can be made from the spectra presented on figure 71. This concerns the absorption band of AgNP-MARX at 1.5ms pulse duration (blue line), and the absorption band of AgNP-BEHLKE at 500µs pulse duration (red line), which are (nearly) superposed. Comparison of these absorption spectra may reveal that similar type of nanoparticles has been produced. Similar absorption bands are also reflected on the color of the colloidal silver nanoparticle solution prepared by BEHLKE-pulsed PLI process (see figure 70), which is similar to the solution color of AgNP-MARX (c.f. figure 52 in chapter IV).

The last absorption band obtained for AgNP-BEHLKE of 150µs pulse duration is represented as the orange line on figure 71. A comparison of this absorption band to absorption band of AgNP-MARX of 1.5ms in pulse duration (blue line) shows that these two absorption band are not similar. The maximum absorption value for AgNP-MARX is 0.75, and maximum absorption value for AgNP-BEHLKE is 0.29. Differences in maximum absorption values for these two processes indicate that particle concentration is different. Besides differences in the absorption band, it is shown on table 23, that E_{input} (per pulse) are similar for BEHLKE- and MARX-pulsed PLI process. The input energy value for both BEHLKE- and MARX-pulsed PLI process is approx. E_{input}= 40mJ/pulse. For E_{input} (per pulse) being similar for BEHLKE- and MARX-pulsed PLI process of different pulse durations, it was demonstrated that the maximum absorption and thus particle concentration are not similar. Similarities in E_{input} and P_{Plasma} (but difference in absorption bands) are reflected on the colloidal silver nanoparticle solution. It is shown that AgNP-BEHLKE appears to contain fewer particles, than AgNP-MARX, which explains thus the low maximum absorption, and hence the difference in colloidal solution.

From this analysis, it is thus shown that an increase in pulse duration (150µs to 1.5ms) does have an influence on the production of reactive species.

Furthermore, it is from this analysis shown that in the use of two different pulse generators, plasma discharges are not generated on a similar basis, which is also reflected on the E_{input} (per pulse) values. On table 26, it is possible to find an overview of parameters, which have been compared in the use of two different pulse generators for silver nanoparticle production.

Pulse duration of Behlke pulsed discharge	**E_{input}**	**max. absorbance**
150µs	Similar	Lower
500µs	Higher	Similar
1.5ms	Higher	Higher

Table 26: Comparison of the results obtained by BEHLKE-pulsed PLI process at different pulse duration with the results obtained using the MARX-pulsed PLI process with 1.5ms pulse duration.

As an example, comparison of the E_{input} (per pulse) value obtained from the BEHLKE-pulsed PLI process at 150µs is performed by comparing AgNP-BEHLKE to AgNP-MARX using the keywords "lower than…", "similar to…", and "higher than…". From this comparison, it is shown that nanoparticle production are not similar for all E_{input} (per pulse) values.

Silver nanoparticles prepared by the BEHLKE-pulsed PLI process at different pulse durations were analyzed by the Dynamic Light Scattering (DLS) technique for determination of particle size distribution (PSD). For the DLS analysis, 1mL of as-synthesized nanoparticles was transferred into a quartz cuvette (1×1cm) and the DLS analysis was carried out. Results obtained from the DLS analysis are presented in table 27, and corresponding PSD graphs are presented in both intensity- and number-weighted PSD, shown on figure 72a-b.

Table 27: Results obtained by DLS analysis of silver nanoparticles produced by BEHLKE-pulsed PLI process. Silver nanoparticles produced for different plasma pulse durations. The last field corresponds to results obtained from MARX-generated PLI process.

Pulse duration	Peaks	Intensity-based size (%I)		Number-based size (%N)		Count Rate
µs		*nm*	*%*	*nm*	*%*	*kcps*
150	1	15.5	3.0	13.7	100	7576
	2	36.1	11.0			
	3	162.4	86.0			
500	1	27	25.7	20.5	100	11120
	2	129	74.3			
1500	1	31.8	23.4	25.5	100	29010
	2	126.3	76.6			
1500 *(MARX)*	1	9.0	6.5	7.99	100	7300
	2	31.40	28.1			
	3	132	65.4			

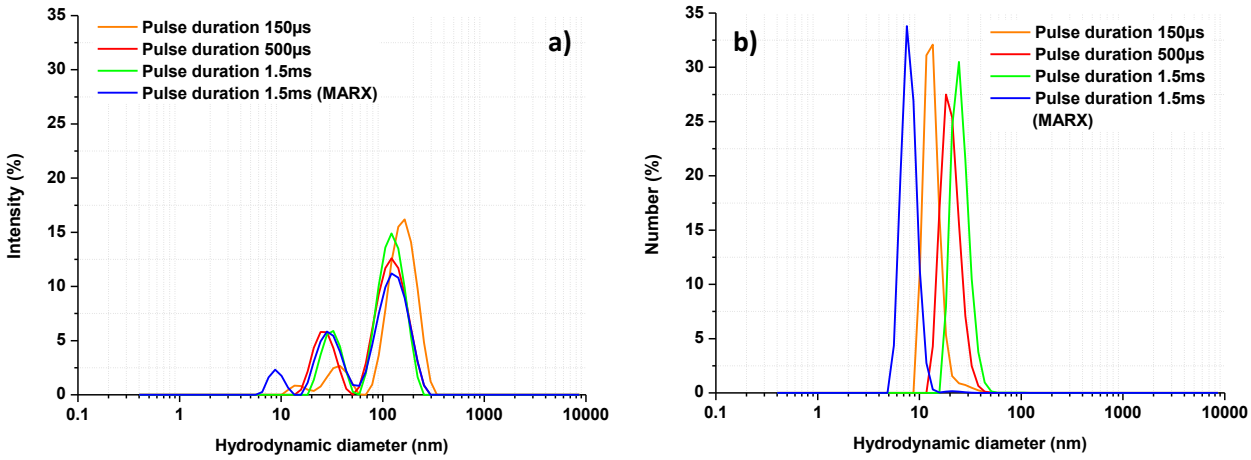

Figure 72: Graphs showing PSD of silver nanoparticles produced by BEHLKE-pulsed PLI process of pulse durations: 150µs (orange), 500µs (red), and 1.5ms (green). Results obtained by the MARX-pulsed PLI process for pulse duration of 1.5ms (blue) are also presented. All results are presented in both a) intensity and b) number based PSD.

Particle size distributions are presented in hydrodynamic diameter (in nanoscale) and scattered light (in percentage) for both intensity- and number-weighted PSD on table 27. The DLS results presented on figure 72 corresponds to AgNP-BEHLKE at 150µs (orange), 500µs (red), and 1.5ms (green). Furthermore, the DLS result of AgNP-MARX at 1.5ms (blue) is also included in this analysis in order to compare MARX- and BEHLKE-pulsed PLI process.

From the DLS results on figure 72a, it is shown that BEHLKE-pulsed PLI process at 150µs in pulse duration results in a multi-modal size distribution (three size populations) of produced silver nanoparticles. The hydrodynamic diameters for these particles are determined to be around 15.5nm (3%), 36nm (11%), and 162nm (86%). An increase in pulse duration to 500µs results in a bi-modal PSD. For a pulse duration at 500µs the hydrodynamic size of particles are approximately 27nm (25.7%) and 129nm (74.3%). Further increase in the pulse duration to 1.5ms resulted in a bi-modal PSD with particle sizes detected to be more or less equal to nanoparticles produced at 500µs in pulse duration. Particle sizes are detected to be around 31.8nm (23.4%) and 126.3nm (74.6%) in hydrodynamic diameter.

From the number-weighted PSD on figure 72b, it is shown that hydrodynamic diameter of nanoparticles increases approximately by 5nm for an increase in plasma pulse duration from 150µs to 1.5ms. The hydrodynamic diameter of nanoparticles produced for plasma pulse durations of 150µs, 500µs, and 1.5ms corresponds thus to 13.7nm, 20.5nm, and 25.5nm, respectively.

From these results, it can be concluded that an increase in plasma pulse duration increases the average nanoparticle size.

Silver nanoparticles produced by the MARX-pulsed PLI process at 1.5ms pulse duration are represented by the blue graph on figure 72a-b. For a pulse duration of 1.5ms, the hydrodynamic size of nanoparticles are approx. 9nm (6.5%), 31.4nm (28.1%), and 132nm (65.4%) in intensity-weighted PSD and 8nm in number-weighted PSD. **Results obtained from DLS analysis show that small-sized silver nanoparticles are produced using the MARX-pulsed PLI process at 1.5ms in plasma pulse duration. Average nanoparticle sizes are reduced in comparison to nanoparticles produced from the BEHLKE-pulsed PLI process**.

The count rate (CR) value represents scattered light (in kcps) by nanoparticles exposing Brownian motion. This value may as well be interpreted as particle concentration present in the dispersing media. In order to avoid measurement bias, such as multi-scattering effects, the colloidal solutions were diluted. The CR values presented in table 27 are thus corrected for any dilution. An increase in the CR has been detected from the DLS analysis. This indicates thus that an increase in particle concentration occurs for an increase in pulse duration of plasma discharges. These results are thus in agreement with an increase in maximum absorbance, which

was obtained from UV-vis absorption spectroscopy, and the decrease in solution transparency.

From this measurement, it was determined that an increase in pulse duration of plasma discharges influences silver nanoparticle production. This is determined, since an increase in pulse duration resulted in an increase of the average particle size. An increase in the average particle size is possible due to the fact that an increase in pulse duration increases the production of reactive species. This results in an increase in the rate of particle synthesis and an increase in particle concentration, which enhances particle-particle interaction. An enhancement in particle-particle interaction may promote particle coalescence and increase the average size of silver nanoparticles.

Polydispersity of nanoparticles is identified through a multi-modal PSD on figure 72a-b. Multi-modality did occur on intensity-weighted PSD, and may thus indicate presence of polydisperse nanoparticles. However, in number-weighted PSD, multi-modal PSD did not occur, and may thus indicate that the smaller particle size population is dominating. Currently, it is from these results difficult to determine whether polydispersity (intensity-weighted PSD) among silver nanoparticles occurs due to particles of different size populations, or due to particle agglomeration. In order to determine the morphology of AgNP-BEHLKE and to determine the presence of agglomerated particles, further characterization of silver nanoparticles are required.

In the following, as-synthesized silver nanoparticles were characterized by Scanning Electron Microscopy (SEM) in order to determine nanoparticle shape, and to reveal any presence of agglomerated nanoparticles. Samples for this characterization technique were prepared by following the same sample preparation procedure as applied in chapter IV. Silver nanoparticles were deposited onto microscopy glass plate for one hour, carefully rinsed with deionized water, and dried in oven overnight at 80°C. Results of SEM characterization are shown in figure 73a-b.

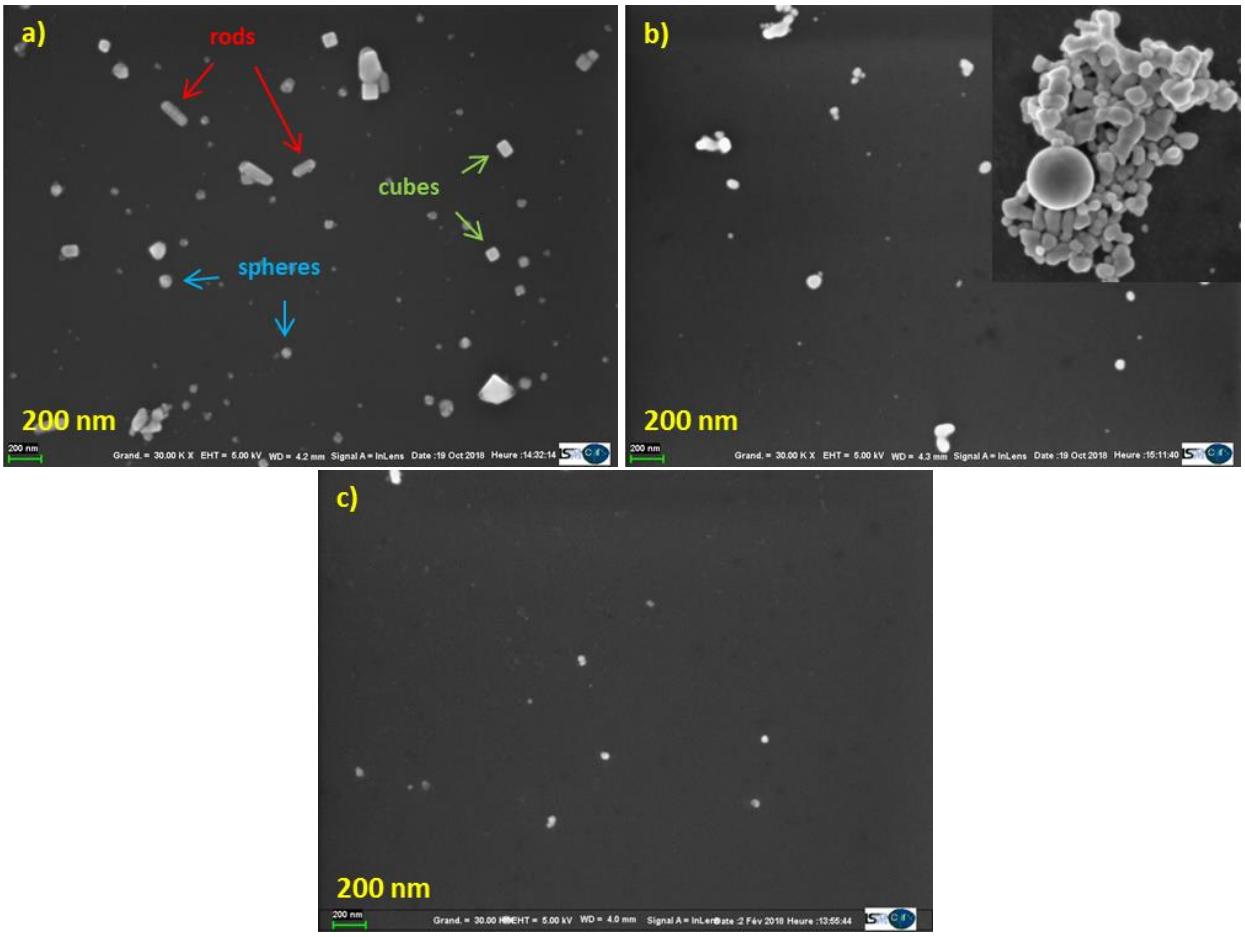

Figure 73: SEM micrographs of silver nanoparticles prepared using the BEHLKE-pulsed PLI process with pulse duration: a) 150µs and b) 1.5ms. (Inset image for 1.5ms are in scale). c) Silver nanoparticles prepared using MARX-pulsed PLI process at 1.5ms pulse duration. (Magnification: 30kX)

Silver nanoparticles presented in figure 73a-b are obtained from the BEHLKE-pulsed PLI process with pulse durations at 150µs and 1.5ms, respectively. Silver nanoparticles presented on figure 73c are obtained from the MARX-pulsed PLI process at 1.5ms pulse duration. Silver nanoparticles obtained by 150µs in pulse duration (see figure 73a) were produced in different sizes and shapes, such as cubes, spheres, and rods. Small-sized spherical nanoparticles between 10nm and 80nm were produced, which corresponds to spherical nanoparticle produced using the MARX-pulsed PLI process. Apart from spherical nanoparticles, silver nano-cubes and silver nano-rod shaped particles were also produced using the BEHLKE-pulsed PLI process. Silver nano-cubes are larger in size, between 75nm and 120nm, and silver nano-rods are between 150nm and 200nm in length and 70nm wide. It appears that nanoparticles produced at different pulse durations are significantly different in morphology.

From these observations, it is therefore determined that pulse duration of plasma discharge is an important parameter in nanoparticle synthesis using PLI processes.

Variation in particle sizes and shapes may explain the broad absorption peak, which was obtained from the UV-vis absorption spectroscopy. It explains furthermore multiple size population in the DLS analysis. Each size population is monodisperse and particles of each shape are of narrow size distribution. From a global point of view, particles produced for 150µs in pulse duration are polydisperse in the presence of various particle geometries and various particle sizes. This indicates thus the production of heterogeneous particles during nanoparticle synthesis using the BEHLKE-pulsed PLI process for 150µs in pulse duration. One explanation to the production of shaped particles may be due to the decreased production rate of reactive species, which occurred for decreased pulse duration of streamer-like discharges. Silver ions are reduced into zero-valent silver atoms in the production of reactive species, and most of their growth phase may occur during the charging of the capacitor. Since this charging time of the capacitor of low pulse durations is higher, than for streamer-like discharges of 1.5ms pulse duration, particles may appear as shaped particles. Further detailed studies on the production of shaped particles in plasma in liquid phase should be performed in order to determine what causes the shaped nanoparticles.

In UV-vis absorption spectroscopy, particle size, shape, and aspect ratio do influence the optical properties of nanoparticles, in which absorption properties of the incident light is changed *(K. L. Kelly et al. 2003)*. Since particle geometries and thus the aspect ratio in the case of 150µs in pulse duration are different, this may therefore affect absorption of light and influence the surface plasmon resonance of metallic silver nanoparticles to result in a broad absorption band.

For an increase in pulse duration to 1.5ms, silver nanoparticles obtained from the BEHLKE-pulsed PLI process are presented in figure 73b. Particles do not exist in different particle geometries as observed in figure 73a, but they exist as irregular-shaped particles. Regular occurrence of particle agglomerates, as shown on the inset image of figure 73b, was observed. Among agglomerates it was highly possible to observe perfectly shaped spherical nanoparticles

at around 400nm in diameter. Agglomeration of silver nanoparticles would explain the broad absorption band in the absorption spectra.

Particle agglomeration has been avoided through particle stabilization in the presence of a minimum PVP concentration of 0.02mM using the MARX pulse generator, as presented on figure 73c (for more information see chapter IV, section 4.3). AgNP-MARX in the presence of 0.02mM PVP appears small-sized and uniformly distributed in the absence of aggregates. However, AgNP-BEHLKE is larger in size and formation of regular agglomeration, in the presence of same amount of PVP stabilizing agent, does occur.

For an increase in pulse duration from 150µs to 1.5µs of plasma discharges it is shown that an increase in particle production occurs. With this increase the amount of PVP becomes insufficient in stabilizing silver nanoparticles, resulting thus in their agglomeration. This occurs since an increase in pulse duration increases the production of reactive species, which increases the synthesis rate of silver nanoparticles to result in an increase in the particle concentration. This means that the stabilizing effect of PVP decreases for a constant PVP concentration, which results in exposed active sites of silver nanoparticles. With an increased particle-particle interaction, silver nanoparticles coalesce and agglomerate. In order to avoid particle agglomeration, it is therefore important to inhibit reactive sites on nanoparticles by increasing the concentration of stabilizing agent for an increase in pulse duration of plasma discharges.

The study performed by *(H.-J. Kim et al. 2018)* shows that an increase in nanoparticle size occurs for an increase in the discharge pulse duration. For short pulse durations (20µs) small-sized and spherical particles were produced (80nm). Increase in the pulse duration (40µs), increased further the size of spherical particles (100nm). As the pulse duration was increased to 60µs, the discharge region was completely covered by gas bubbles. This resulted in the production of triangular silver nano-plates of 8µm. It has thus been concluded that the average nanoparticle size increases for an increase in pulse duration. Without further studies on micro-bubble production, it is not possible to confirm, whether microbubbles has an influence the nanoparticle synthesis, in our case.

5.1.1 Summary

The first parameter that was studied is the pulse duration of the BEHLKE-pulsed plasma discharges. Pulse durations between 150µs and 1.5ms have been selected. 150µs was applied as the minimum applicable pulse duration of the PLI process. Pulse duration of 1.5ms was applied in order to be in the same order of magnitude of plasma pulse duration obtained using the MARX pulse generator. Increasing the streamer pulse duration would increase plasma process rate in the liquid phase, which results in the increased production of reactive species. This is in agreement with the increase in the solution conductivity, as a result of increased production of ionic species. The conduction of the electric current becomes enhanced for this reason and an increase in the E_{input} (per pulse) of streamer-like discharges was obtained.

Increase in pulse duration was first reflected on the solution transparency, as the concentration of produced particles would increase. UV-vis absorption spectroscopy verified production of silver nanoparticles, due to the presence of SPR peak at around 400nm. The average particle size of silver nanoparticles was determined by DLS, and the increase in size for an increase in pulse duration of BEHLKE-pulsed plasma discharges was confirmed. From these measurements, it was further determined that silver nanoparticles were polydisperse. Silver nanoparticles were further characterized by SEM. For 150µs pulse duration different shaped particles including spheres, cubes and rods was formed at different sizes. The streamer-like discharges of low pulse duration (150µs) may generate reactive species at a reduced production rate. Reduction of silver ions into zero-valent silver atoms occurs. The growth of the silver nanoparticles occurs thus during the charging of the capacitor, before another streamer-like discharge is activated in the discharge of the capacitor. Since this charging time of the capacitor is increased than for streamer-like discharges of 1.5ms pulse duration, particles may appear as shaped particles. For 1.5ms pulse duration large-sized and irregular-shaped particles were aggregated. It is a possibility that due to an increased particle concentration that PVP concentration was not sufficient to prevent particles from aggregation.

In order to produce small-sized silver nanoparticles in the use of the BEHLKE-pulsed PLI process, pulse duration of 150µs should be applied. Based on these results, the second parametrical study with focus on $U_{applied}$ will be performed with pulse duration of 150µs.

5.2 The influence of applied voltage on nanoparticle synthesis

The influence of applied voltage on silver nanoparticle synthesis has been investigated. This parameter has been studied, since it was observed by several authors that an increase in applied voltage would decrease nanoparticle size *(Hieda, Saito, and Takai 2008)*, *(Saito, Hieda, and Takai 2009)*.

For this study, $U_{applied}$ was applied in the working range between 1kV and 12kV, with an inter-electrode distance fixed at 3 mm. At the minimum applied voltage (1kV), plasma discharges are not visible. Plasma discharges for the maximum applied voltage (12kV) would change the regime into the sparking discharge regime for the given inter-electrode distance of 3mm.

Silver nanoparticles were synthesized using a BEHLKE-pulsed PLI process with pulse duration at 150µs, as was determined from section 5.1. No modification on the electrical circuit has been performed, and also no modification of the precursor solution has been executed. Silver nanoparticle synthesis did proceed similar to nanoparticle synthesis as reported in the previous section, which are as follows:

The aqueous precursor solution consists of 2mM $AgNO_3$ as the silver source. For nanoparticle stabilization 0.02mM PVP was added into the aqueous precursor solution. In these conditions, the as-prepared aqueous silver precursor solution has pH5 and 300µS/cm in solution conductivity.

Nanoparticle synthesis was carried out by immersing a pair of Pt wire electrode (d: 200µm, L: 0.5mm) in silver nitrate precursor solution. In this study the inter-electrode distance of Pt wires was kept constant at 3mm. High voltage DC-pulsed plasma discharge was generated in the electrode gap by applying high voltage to electrodes in the range between 1kV and 12kV. The pulse repetition frequency of pulsed plasma discharges was 50Hz, and as determined from previous section pulse duration of 150µs has been applied. High voltage pulse discharges were generated using a solid state HV switch. PLI process parameters applied in this study are presented in table 28:

Table 28: PLI process parameters with focus on applied voltage

Discharge Physical parameters	Solution Physicochemical parameters
Applied voltage ($U_{applied}$): **1-12kV**	Reaction volume (V): 100mL
Pulse repetition frequency (f): 50Hz	$AgNO_3$ concentration: 2mM
Inter-electrode distance (l_{Pt}): 3mm	PVP concentration: 0.02mM
Discharge time (t_{plasma}): 20min	pH: ≈5
Pulse duration: 150μs	Conductivity (σ): 300μS/cm

Current (I) and voltage (U) waveforms were recorded towards the end of the synthesis process (t_{plasma}=20min) and are presented on figure 74. In current waveforms, a complete profile of a single pulse is presented, as well as a detailed profile of current pulses (τ = 40μs) (see insets of current waveforms on figure 74). Voltage waveforms of a single pulse have been presented in similar approach, but the detailed profile of the pulse is instead up to τ = 0.75μs (see insets of voltage waveforms on figure 74). Relevant discharge parameters were extracted as appeared in the waveforms, and presented in table 29. The grey field on table 29 corresponds to plasma parameters obtained for PLI process using the MARX-pulse generator in the generation of plasma discharges of 8kV (pulse duration 1.5ms).

The input energy per pulse was then determined from waveforms presented on figure 74 corresponding to each $U_{applied}$ value, and the resulting waveform of input energy was presented in figure 75.

Table 29: Plasma parameters obtained for different applied voltages using BEHLKE pulse generator. Grey field corresponds to values obtained from MARX-generated pulses.

Applied voltage	Input energy per pulse	Injected discharge power
$U_{applied}$, *kV*	E_{input}, *mJ/pulse*	P_{plasma}, *W*
1	1.0	0.05
5	13.5	0.7
8	42.5	2.1
9	38.9	2.0
12	65.1	3.3

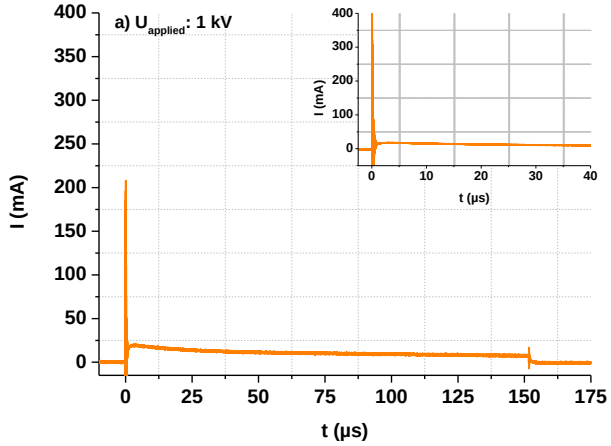
a) U applied: 1 kV
I (mA)
t (µs)

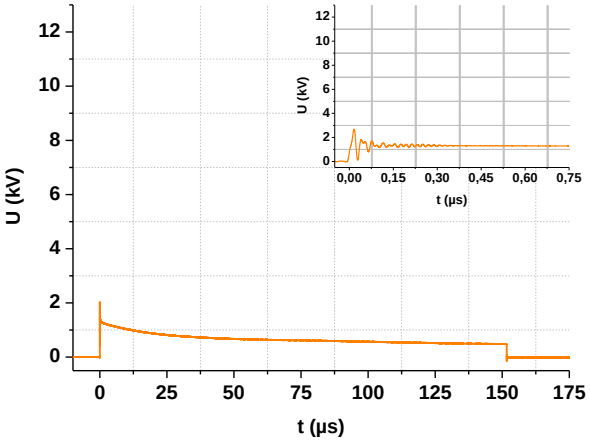
U (kV)
t (µs)

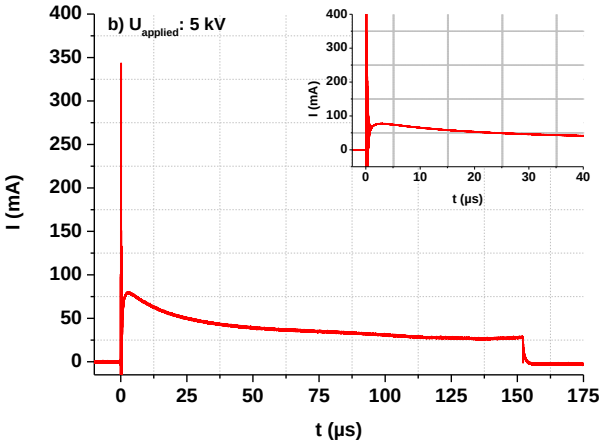
b) U applied: 5 kV
I (mA)
t (µs)

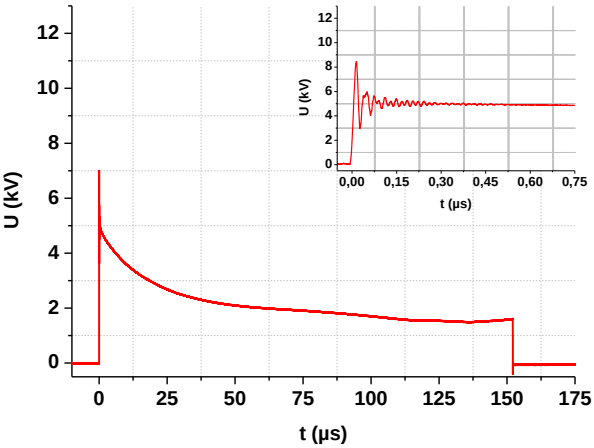
U (kV)
t (µs)

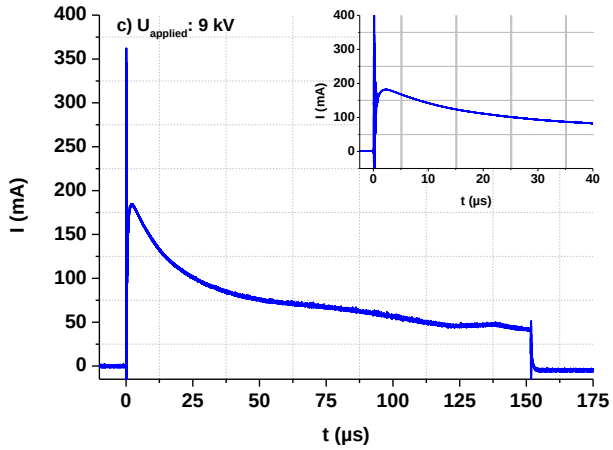
c) U applied: 9 kV
I (mA)
t (µs)

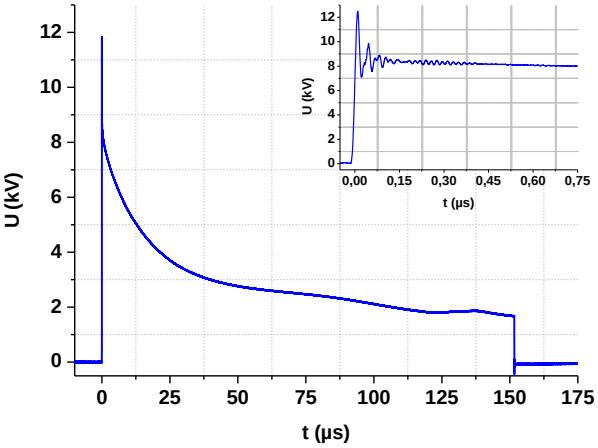
U (kV)
t (µs)

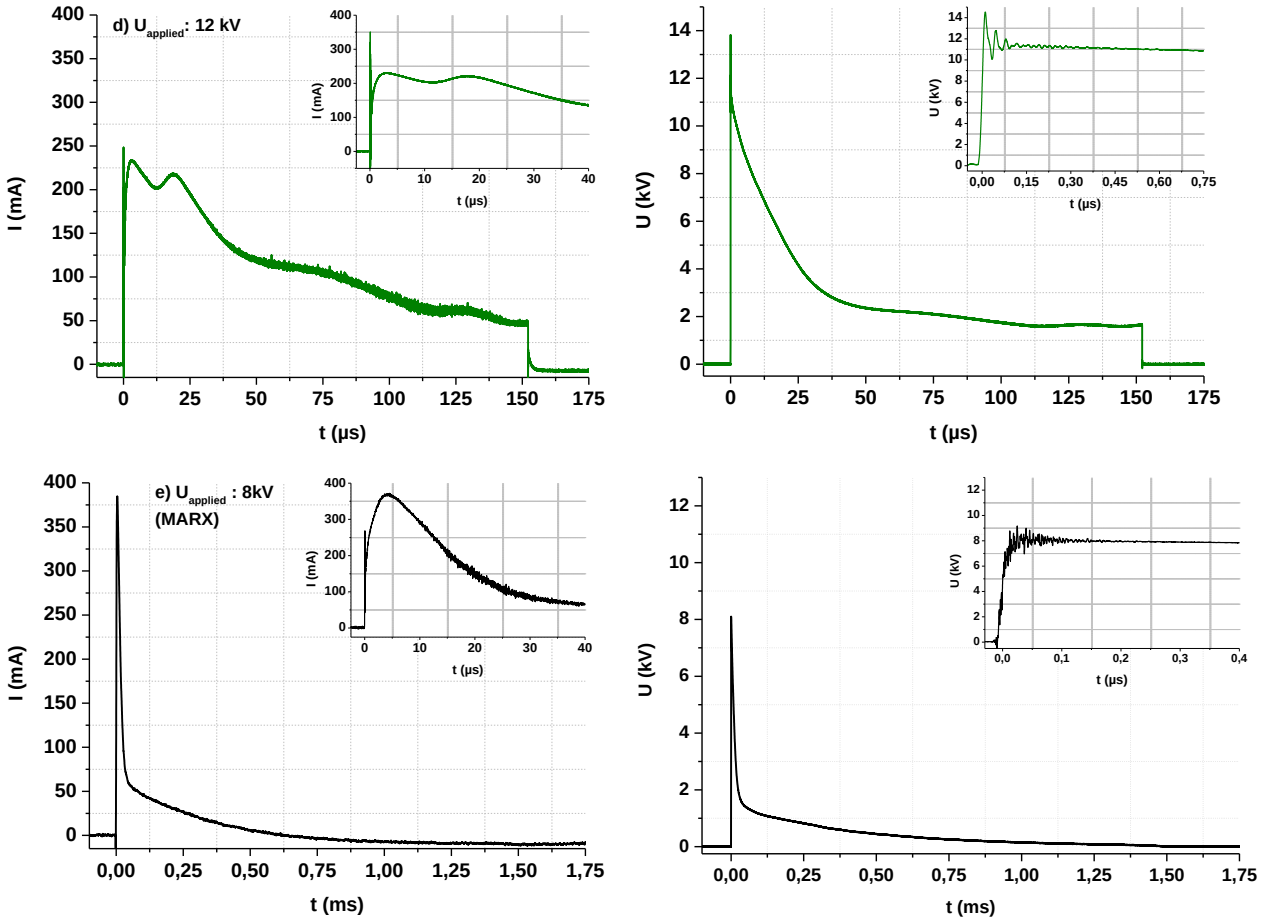

Figure 74: I- and U-waveforms for one pulse (at the end of the process t=20min). Applied voltages of plasma discharges are: a) 1kV, b) 5kV, c) 9kV, and d) 12kV for BEHLKE-generated pulses, and e) 8kV for MARX-generated pulses.

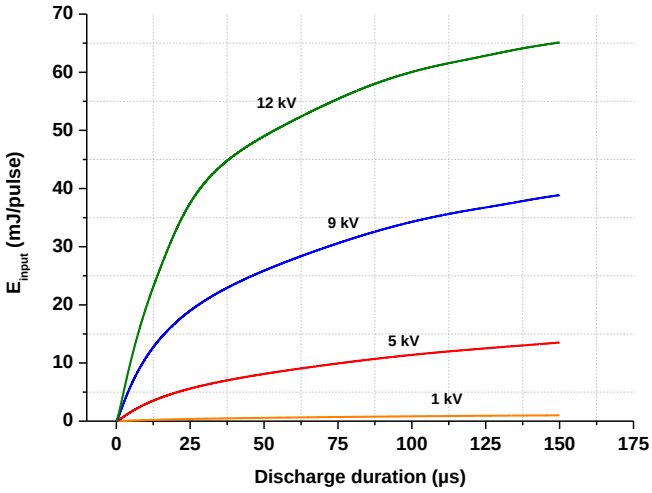

Figure 75: Input energy per pulse of pulsed plasma discharges obtained as a result of 20min silver nanoparticle discharge using the PLI process for increase in the applied voltage. Applied voltages are 1kV (orange), 5kV (red), 9kV (blue), and 12kV (green) for BEHLKE-generated pulses with 150µs in pulse duration.

From the electrical waveforms, presented on figure 74a-e, it is observed that the conduction of electrical current is increased as the applied voltage is increased from 1kV to 12kV. This increment in applied voltage leads thus to an increase in the input energy (per pulse) of BEHLKE-generated plasma discharges from 1mJ/pulse to 65mJ/pulse, respectively (c.f. figure 75). It is also noticed that an increase in the applied voltage from 9kV to 12kV affects the current waveform by the appearance of a second conduction "peak". This may be due to an increase in the electric field around the electrodes. From these observations it is shown that the applied voltage does have an influence on pulsed plasma generation in the liquid phase.

The current- and voltage waveforms, which have been obtained from BEHLKE- and MARX-pulsed PLI process, are compared. It should be noticed that pulse durations for these two processes are different. BEHLKE-pulsed plasma discharges are generated with 150µs in pulse duration, while MARX-pulsed plasma discharges are generated with 1.5ms in pulse duration. However, at τ=1.5µs in the waveforms of MARX-pulsed plasma discharges, it is observed that current and voltage values are close to values obtained from BEHLKE-pulsed plasma discharges. Despite the differences in plasma generation using two different pulse generators, similar E_{input} (per pulse) and P_{plasma} values around 40mJ/pulse and 2W, respectively, have been obtained.

The influence of the applied voltage on pulsed plasma generation in a liquid phase is also visualized through images of plasma discharges as shown on figure 76a-d. From these images, we can observe that the plasma discharge runs into different discharge regimes as the $U_{applied}$ value is increased from 1kV-12kV.

A transition from streamer-to-spark plasma regimes for an increase in $U_{applied}$ and constant inter-electrode gap occurs, due to an increase of the electric field. In terms of plasma discharges generated in liquid phase, two types of plasma regimes occur. These are classified as streamer/corona discharges and spark/arc discharges *(B. R. Locke et al. 2006)*. In our case, no luminous plasma discharge was observed applying a high voltage between 1kV and 5kV to the electrodes. Applying 1kV to the electrodes do not result in generation of visible plasma discharges nor in micro-bubble production (c.f. figure 76a). It may occur that large-sized bubbles are visible near the anode capillary on figure 76a, but it did not occur as a result of plasma discharges. These were present throughout the experimentation.

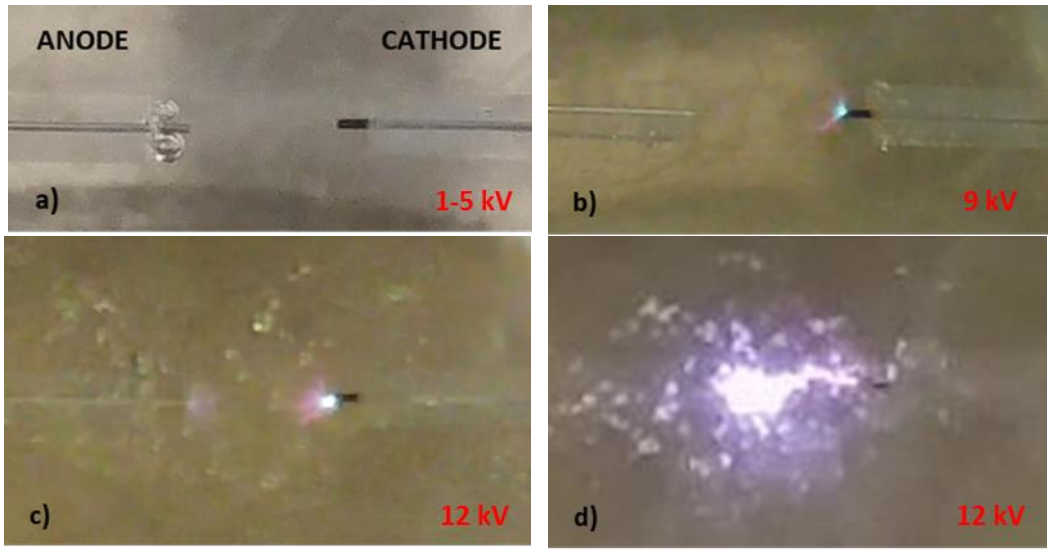

Figure 76: Changes in visible plasma discharge during AgNP synthesis for increase in $U_{applied}$. a) represents discharges applying 1kV and 5kV, b) partial corona discharges observed on cathode when applying 9kV, and c-d) corona discharges on both anode and cathode that frequently connects and results in breakdown when applying 12kV.

At 1kV, the energy that is put into discharges and the injected power is as low as 1mJ/pulse and 0.05W, respectively, which are not sufficient in generation of luminous discharges. Increasing $U_{applied}$ to 5kV results in similar discharge observations (c.f. figure 76a), however the input energy and discharge power increases to 13.5mJ/pulse and 0.7W, respectively. Such an increase does not result in visible plasma generation, but result in generation of micro bubbles. As a result of an increase in applied voltage, production of silver nanoparticles near the Pt cathode surface is initiated. Further increase in $U_{applied}$ to 9kV increased the input energy to 40mJ/pulse and the discharge power to 2W. The input energy was sufficiently high to ionize gaseous species resulting in UV-light emission and to generate partial corona discharges on the cathode Pt wire. For an increase in discharge power strong shockwaves accompanied with excessive micro bubble formation occurs. The intensity of UV-light increases as the applied voltage increases, and thus the input energy per pulse, is increased *(B. R. Locke et al. 2006)*.

According to *(An, Baumung, and Bluhm 2007)* generation of streamers or corona discharges in water are initiated by formation of non-luminous and bush-like **primary streamers**, when the electric field is in the order of $100 MV \cdot m^{-1}$. As the electric field around primary streamer tips becomes high enough, luminous and filamentary **secondary streamers** are formed. The electric field around secondary streamers reaches up to $2 GV \cdot m^{-1}$ *(An, Baumung, and Bluhm 2007)*.

According to *(Hoffer 2014)* channels of secondary streamers are larger in diameter and propagate at a higher speed than primary streamers.

At 12kV, the input energy and discharge power increased to 65mJ and 3.3W, respectively. This increase resulted in an increase of the electric field around Pt electrodes, which is sufficiently high enough to activate a second plasma discharge around the anode Pt wire tip (c.f. figure 76c). Furthermore, streamer-to-spark transitions occurred as streamer-like channels propagated towards the opposite electrode to reach breakdown. This streamer-to-spark transition is illustrated on figure 76c-d.

The streamer-to-spark transition was in a similar study further investigated by *(Rond et al. 2018)*. In this study, pulsed plasma discharges were generated in a NaCl solution. A sufficiently high electric field was created by applying 12 kV to a pair of tungsten electrodes in order to sustain electric discharges to reach breakdown. Generation and the transition of streamer-to-spark pulsed discharges were investigated through Schlieren spectroscopy. Recordings which illustrate two types of spark formations are shown in selected images from the work of Rond *et al*. on table 30.

Table 30: Two breakdown mechanisms of BEHLKE-pulsed plasma discharges generated at 12kV. Modified and reproduced from *(Rond et al. 2018)*.

	Case 1 (12kV)	Case 2 (12kV)	
t=19.25µs		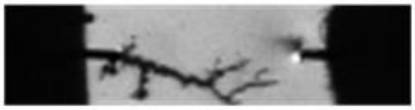	t=3.5µs
t=21µs		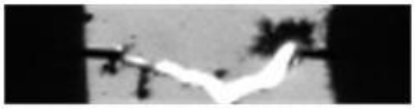	t=5.25µs

In case 1, the streamer-like discharge propagates towards the anode, and the breakdown is controlled from streamer-like propagation mechanism. Whereas in case 2, the streamer-like discharge propagates towards the cathode and each streamer leads to breakdown.

Putting the findings of this study in parallel to our work reveals that by applying 12kV to the PLI process, for an inter-electrode distance of 3mm, the streamer-to-spark transition is generated irregularly. This is controlled by streamer-like discharge initiation mechanism, which for each

pulse either may remain as streamer-like discharge, propagate as in case 1 or propagate as in case 2.

Ex-situ conductivity and pH measurements of the reaction media were conducted before and after nanoparticle synthesis with exposure to 20min of plasma discharges. Results of these measurements are presented in table 31.

Table 31: Changes in solution chemistry of the reaction media, before and after silver nanoparticle synthesis using BEHLKE pulse generator. Grey field corresponds to values obtained from MARX-generated PLI process.

Applied voltage $U_{applied}$, *kV*	**pH**		**Solution conductivity** σ, $\mu S.cm^{-1}$	
	Initial	*Final*	*Initial*	*Final*
1	4.5	4.3	311	312
5	4.5	3.9	304	318
8	4.5	3.7	331	373
9	4.5	3.7	302	325
12	4.5	3.9	307	316

It is observed that initial pH and solution conductivity values of the precursor solution (prior to plasma discharge) are constant at pH4.5 and around 305µS/cm, respectively. However, changes in the solution occur during 20min of plasma discharge. In chapter IV, it was previously discussed that acidification might be due to HNO_3 formation as a result of plasma-generated chemical reactions. If initial pH and σ values are compared to final pH and σ values for nanoparticle synthesis at 1kV, we can conclude that no significant change in the reaction media did occur. This might hence indicate that no particle production occurs for an applied voltage of 1kV.

Significant changes in the physico-chemical parameters of the reaction media occurred for nanoparticle synthesis when applying high voltages at 5kV, 9kV, and 12kV for a decrease in pH between 0.6-0.8 and an increase in solution conductivity between 14-23µS/cm. The increase in solution conductivity for 12kV by 9µS/cm is low in comparison to 5kV and 9kV, which may also have an influence on particle production.

The influence of an increase in the $U_{applied}$ in nanoparticle synthesis was also observed in the color change of the reaction media after 20min of plasma discharge. As shown in figure 77, applying 1kV of pulsed plasma discharges did not result in a color change of the reaction media and confirms thus previous assumptions of no silver nanoparticle production.

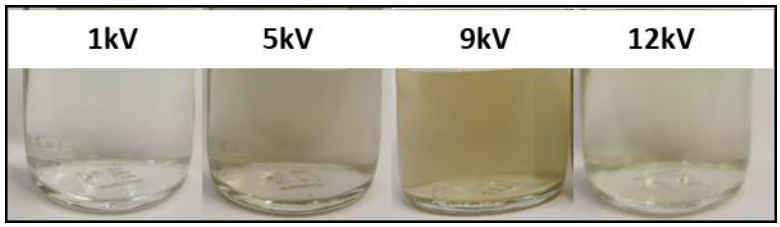

Figure 77: Color changes of reaction media obtained from a 20min nanoparticle synthesis applying 1kV, 5kV, 9kV, and 12kV of DC-pulsed plasma discharge.

An unusual silver nanoparticle production was observed after nanoparticle synthesis in the application of 5kV pulse plasma discharges. The resulting reaction media does have a black shear due to presence of black particles, rather than the traditional yellow color resulting from small-sized spherical silver nanoparticles. The reason to production of black particles may be due to the influence of electrical discharges, which occurred as non-luminous discharges with generation of continuous microbubbles. As a result, it might occur that oxidized silver nanoparticles are produced, however in order to confirm this point of view, further documentation is required. Applying 9kV of plasma discharges to the PLI process during silver nanoparticle synthesis resulted in a yellow color change of the reaction media, which indicates production of small-sized silver nanoparticles. A further increase in applied voltage to 12kV resulted in a different response of color change of the reaction media. During 20min synthesis, the occurrence of spark discharges did appear frequently, and an obvious yellow color did appear. However, after 20min of nanoparticle synthesis with spark discharges, the reaction media became nearly transparent as shown in figure 77. This behavior may be due to the fact that produced silver nanoparticles are not stable, and dissolves into silver ions as reported by *(Saito, Hieda, and Takai 2009)*.

Further investigations of resulting silver nanoparticles were performed. A small volume (2mL) of reaction media containing silver nanoparticles was analyzed by UV-vis absorption

spectroscopy. Absorption spectra of this analysis are shown in figure 78 and information determined from these spectra are listed in table 32.

Table 32: Results obtained from UV-vis absorption spectra of silver nanoparticle synthesis applying 1kV, 5kV, 9kV, and 12kV of pulsed discharges

Applied voltage $U_{applied}$, *kV*	**Absorbance** *a.u.*	**λ_{max}** *nm*	**FWHM** *nm*
1	**n/a**	**n/a**	**n/a**
5	0.13	402	**n/a**
8	0.75	397	137
9	0.29	402	138.6
12	0.09	416	117

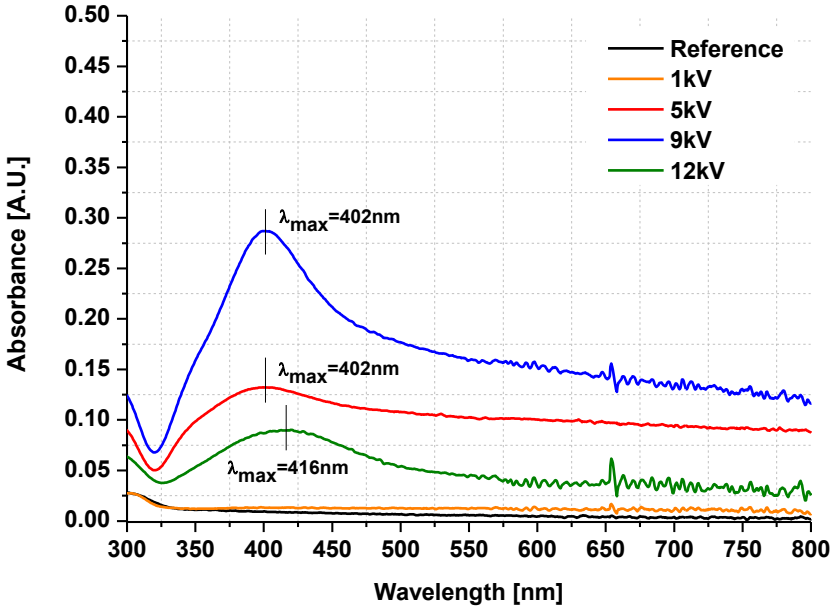

Figure 78: UV-vis absorption spectra of silver nanoparticle synthesis. Nanoparticles synthesized for an increase in applied voltage including 1kV (orange), 5kV (red), 9kV (blue), and 12kV (green).

No absorbance around 400nm is observed from the reaction media, which was exposed to 1kV electric discharges. Absence of the absorption peak around 400nm proves that the reaction media does not contain silver nanoparticles. Based on these results, it is confirmed that no silver nanoparticle production occurred, when 1kV is applied to the BEHLKE-pulsed PLI process in which the E_{input} =1mJ/pulse. Based on solution conductivity measurement, it was also determined

that almost no change in the reaction media did occur for an exposure of discharges during 20min. Applying 5kV discharges to the BEHLKE-pulsed PLI process resulted in production of nanoparticles, which absorb light around 402nm and 0.132 in absorbance. The resulting absorption band is broad and it was therefore not possible to determine the FWHM value. This indicates that particles are either highly polydisperse or agglomerated. Silver nanoparticles produced as a result of applying 9kV to the BEHLKE-pulsed PLI process, resulted in light absorption around 402nm and 0.287 in absorbance. Particles may appear highly polydisperse or agglomerated, since the FWHM value is as high as 138.6. Lastly, silver nanoparticles produced by applying 12kV to the PLI process produced silver nanoparticles, which absorb light around 416nm and 0.09 in absorbance. The absorbance is lower than the ones measured for 5kV and 9kV, and due to a red-shift in λ_{max} of the SPR peak by 14nm, the average particle size may be larger in comparison to nanoparticles produced from 5kV and 9kV. Suggestions to a decrease in the yellow color of the reaction media after plasma exposure at 12kV have been proposed. Based on these results, which presented a low particle concentration and increased particle size may thus guide us towards clearance in particle production in the application of pulsed plasma discharges at 12kV. The first suggestion focused on the dissolution of nanoparticles into silver ions, which might explain the decrease in the yellow color. However, this suggestion is not possible, as a decrease in particle size would be expected. Therefore, the second suggestion is considered to explain this scenario. An increased input energy, and thus increased driving force of nanoparticle crystallization, resulted particles to reach thermodynamic stability. This includes transformation of small-sized spherical particles into large-sized polyhedral-shaped nanoparticles through rapid coalescence, and thereby a decrease in particle concentration *(Tang et al. 2009)*.

Silver nanoparticles were also analyzed by DLS technique in order to determine particle size distribution. A small volume of as-synthesized nanoparticles of as low as 1mL was required for this measurement. Results obtained from the DLS measurements are presented in table 33, and corresponding PSD graphs are both presented in intensity and number weighted PSD as shown in figure 79a-b. DLS measurement of reaction media exposed to pulsed discharges at 1kV was not succeeded, and is therefore not possible to determine particle size. This indicates also that no particle production occurred at these experimental conditions. Applying 5kV to the PLI process resulted in highly polydisperse nanoparticles. From intensity weighted PSD on figure 79a it is shown that particles are polydisperse with size population around 5nm (5%), 57nm (9.7%), and

209nm (85.4%). However, from number weighted PSD on figure 79a particles of 20nm are highly present. Applying discharges of 9kV resulted in a multi-modal size distribution with hydrodynamic diameters at around 15.5nm (3%), 36nm (11%), and 162nm (86%). From the multi-modal particle size distribution it is also shown that nanoparticles are polydisperse. Different results are obtained from applying 12kV of discharges. Particles were partly exposed to spark and corona discharges of 65mJ/pulse in input energy. Intensity weighted PSD showed a bi-modal size distribution with size populations around 35nm (18.3%) and 166nm (79.6%).

We can also observe that particle concentration is lower for 12kV than particle concentration of 5kV and 9kV. For an increase in the average silver nanoparticle size and a decrease in nanoparticle concentration, the suggestion of nanoparticle growth at 12 kV is supported.

Polydispersity of nanoparticles was also detected through particle size measurement. It is from these results difficult to tell whether an increased polydispersity was caused due to various particle sizes or by particle agglomeration.

Table 33: DLS size measurements results of silver nanoparticle synthesis applying pulsed plasma discharges for changes in applied voltage.

Applied voltage	**Peaks**	**Intensity-based size (%I)**		**Number-based size (%N)**		**Count Rate**
$U_{applied}$, *kV*		*nm*	*%*	*nm*	*nm*	*%*
1				**n/a**		
5	1	23.8	4.9	19.89	100	2530
	2	57.05	9.7			
	3	209	85.4			
	1	9.0	6.5	7.99	100	7300
8	2	31.40	28.1			
	3	132	65.4			
9	1	15.5	3.0	13.7	100	7576
	2	36.1	11.0			
	3	162.4	86.0			
12	1	35.18	18.3	26.5	100	792
	2	166.2	79.6			

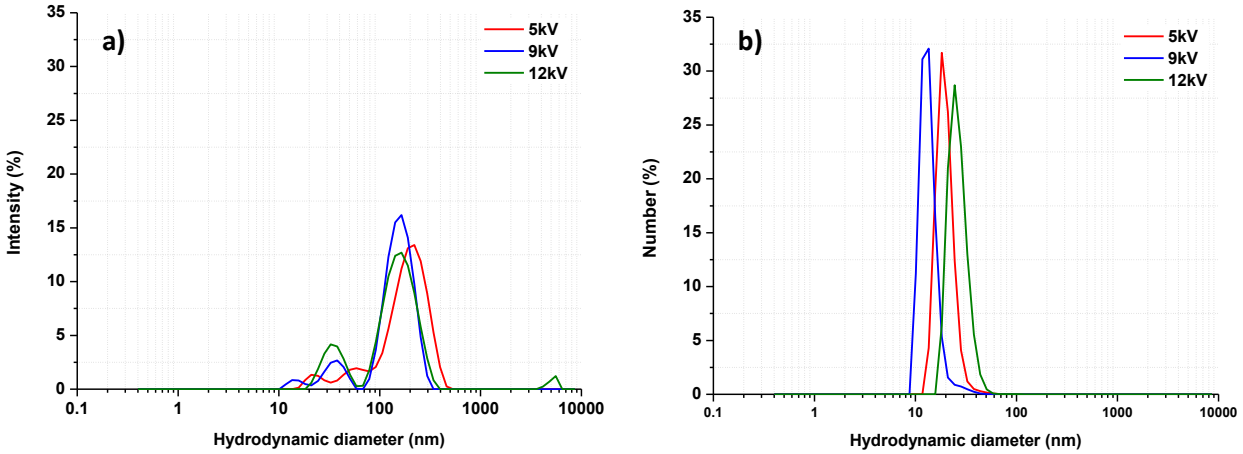

Figure 79: DLS size measurements of silver nanoparticles synthesized for applied voltages 5kV (red), 9kV (blue), and 12kV (green). Results are presented in a) intensity and b) number based PSD as a function

In the following, as-synthesized silver nanoparticles were characterized by Scanning Electron Microscopy (SEM). From this characterization it is possible to find out whether polydispersity is caused by a variety of particle sizes or by particle aggregation. Samples for this particle characterization technique were prepared by applying the same sample preparation procedure as in chapter IV. Silver nanoparticles were deposited onto microscopy glass plate for one hour, carefully rinsed with deionized water, and dried in oven overnight at 80°C. Results of SEM characterization are shown in figure 80a-d. Nanoparticles resulting from 1kV discharge is presented on figure 80a. From this SEM micrograph it is shown that apart from a few particles no silver nanoparticles were formed. Increase in applied voltage to 5kV did not result in the generation of luminous plasma discharges, but generation of continuous micro bubbles did occur. This synthesis resulted in production of dark colored particles.

On figure 80b, particle morphology of the dark colored particles are revealed, and consist of a mixture of spherical and cubic shaped particles of various size distributions. Further increase in the applied voltage and hence input energy generates visible corona discharges on the cathode. Particles resulting from this synthesis are presented on figure 80c, in which the particle morphology is a variation between cubes, spheres, and rod shaped particles of various sizes. The sparking plasma discharges does cause smaller nanoparticles to coalesce rapidly and reach thermodynamic stability to transform into large-sized cubic silver particles *(Tang et al. 2009)*, as shown on figure 80d. From the SEM micrographs it is shown that applying 1kV to 5kV the particle concentration increases.

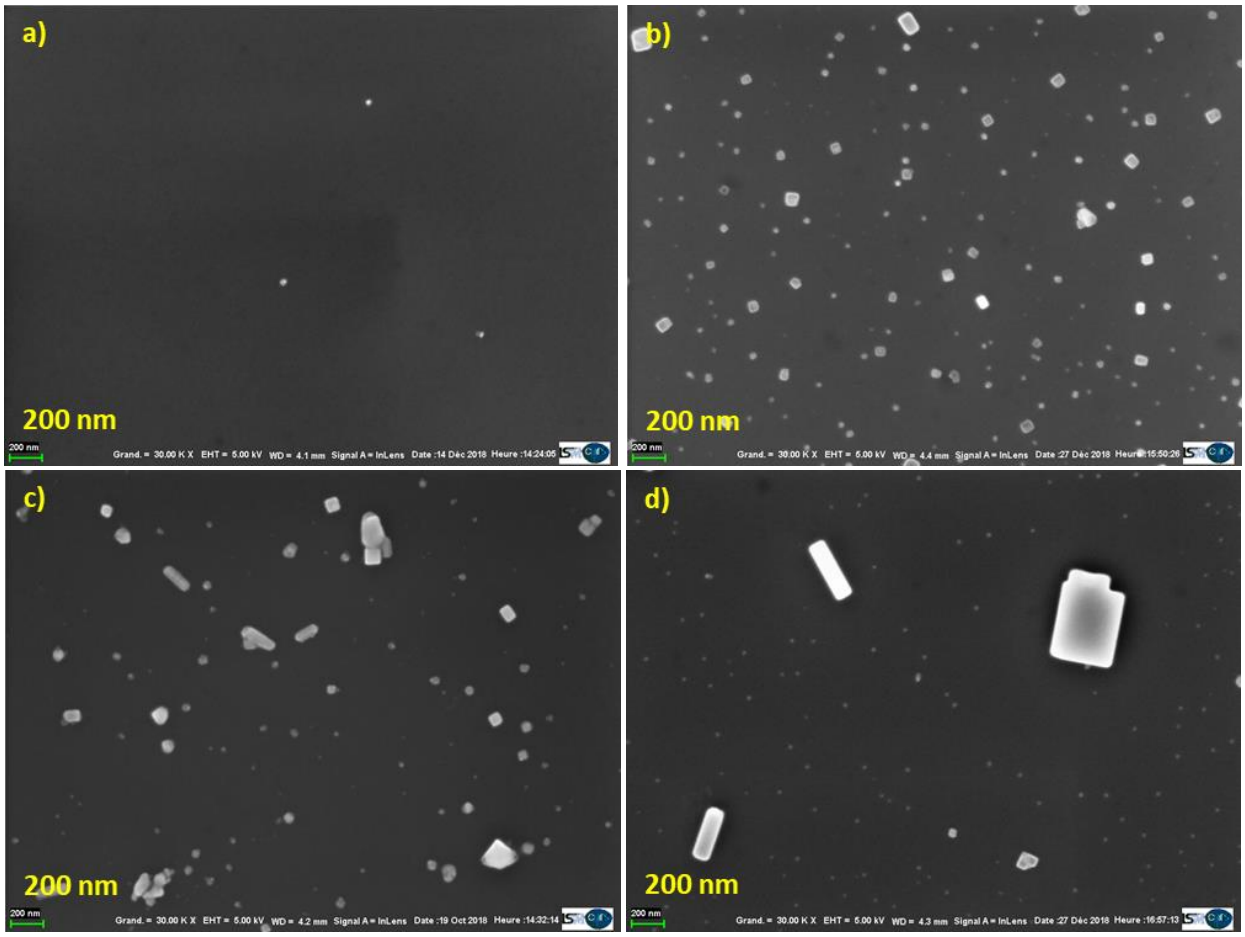

Figure 80: SEM micrographs of AgNP synthesized for 20min of plasma discharge with applied voltage a) 1kV, b) 5kV, c) 9kV, and d) 12kV. Magnification: 30kX

From 5kV to 9kV the average particle size increases in which particles grows into cubic and rod shaped particles. From 9kV to 12kV the particle concentration decreases along with an increase in the average particle size. This modification in particle growth and particle morphology for an increase in the applied voltage of the PLI process may occur, due to a sufficiently high electric field. An increase in the electric field charges nanoparticles, which grows towards thermodynamically favorable particle shapes *(Tang et al. 2009)*. In other words, an increase in electric field enhances the crystallization of nanoparticles, which result in polyhedral shaped nanoparticles, as reported by Tang *et al*. Results obtained from SEM are hence in accordance with results obtained from DLS and UV-vis absorption spectroscopy analysis with respect to the increase in average nanoparticle size and in terms of particle concentration.

In the study performed by *(Saito, Hieda, and Takai 2009)*, gold nanoparticles were produced by DC-pulsed plasma discharges submerged in a $HAuCl_4$ precursor solution. They applied pulsed plasma discharges of 1600V, 2400V, and 3200V to tungsten wire electrodes with an inter-electrode distance of 0.3mm. Pulse plasma discharges were generated for 15kHz in pulse repetition frequency and 2µs in pulse duration. In their study, Saito *et al*. documented that gold nanoparticles would decrease in nanoparticle size for an increase in applied voltage. This occurred as a result of nanoparticle dissolution during nanoparticle synthesis in which the dissolution rate was depending on the applied voltage. Based on our results, dissolution of nanoparticles does not occur during nanoparticle synthesis.

5.2.1 Summary

This section focuses on the influence of applied voltage on nanoparticle synthesis, and how it affects morphology of silver nanoparticle. The pulse duration was fixed at 150µs, based on the results obtained in the previous section. The study was performed with a range of applied voltage values from 1kV up to 12kV and a fixed inter-electrode distance of 3 mm. As a consequence, discharge regime did change as a consequence of increase in input energy per pulse causing breakdown of discharges in liquid phase. Applying 1kV did not result in visible plasma discharges or micro bubble generation, since the input energy was as low as 1mJ/pulse. As a result, no particle formation did occur.

Applying 5kV did not result in visible plasma discharge as well, but continuous bubble generation did occur. Applying 9kV resulted in generation of partial corona discharge on the cathode. Pulse discharges of 40mJ/pulse did result in shockwaves accompanied with bubble generation. Finally, applying 12kV resulted in generation of corona discharges on cathode and anode. This is due to creation of strong electric fields around the electrode tips with input energy of 65mJ/pulse. Under these conditions, corona discharges did frequently develop into spark discharges through vapor channel formation across the inter-electrode distance. Silver nanoparticle generation was observed starting from an applied voltage of 5kV.

As the applied voltage and the input energy increased average size of particles increase as well. Increase in applied voltage does cause smaller nanoparticles to coalesce rapidly and reach thermodynamic stability to transform into large-sized cubic particles. Therefore, synthesis of

small-sized nanoparticles does require a low applied voltage below 9kV and input energy below 40mJ.

5.3 The influence of inter-electrode distance on silver nanoparticle synthesis

The final plasma parameter that is investigated in this parametrical study concerns the inter-electrode distance of Pt wires. In the previous section, it was observed that an increase in the applied voltage of the pulsed discharge did influence the discharges generated in the liquid phase. As the applied voltage was increased, the input energy of discharges per pulse increased, and so did the strength of the electric field, providing thus transition of plasma discharges into different discharge regimes.

As it was presented in the previous section, the discharge regime would change for an increase in the $U_{applied}$, when the inter-electrode distance is kept constant. Therefore, the influence of the inter-electrode distance on silver nanoparticle synthesis was investigated by an increase in the $U_{applied}$ over the inter-electrode values at a constant ratio. This study focuses on how inter-electrode distance in the generation of partial corona discharges affects nanoparticle morphology.

In this study, the inter-electrode distance was applied in the working range between 2mm and 4mm, while the applied voltage was applied in the range between 4kV and 12kV, resulting in a constant ratio between applied voltage and inter-electrode distance.

This working range is chosen in order to generate pulsed plasma discharges in the partial corona discharge regime.

Similar to previous sections in this chapter, silver nanoparticles were synthesized using a BEHLKE-pulsed PLI process for pulse duration of 150µs. Besides above-mentioned, no further modifications in the experimental set-up has been performed in this study. Silver nanoparticle synthesis did proceed similar to nanoparticle synthesis as reported in the previous section, which are as follows:

The aqueous precursor solution consists of 2mM $AgNO_3$ as the silver source. For nanoparticle stabilization 0.02mM PVP was added into the aqueous precursor solution. In these conditions, the as-prepared aqueous silver precursor solution has pH5 and 300µS/cm in solution conductivity.

Silver nanoparticle synthesis was carried out by immersing a pair of Pt wire electrode (d: 200µm, L: 0.5mm) in the silver nitrate precursor solution. The inter-electrode distance of Pt wires was adjusted between 2mm and 4mm by a micrometric screw. DC-pulsed high voltage plasma discharges was generated in the inter-electrode gap by applying high voltage to electrodes in the range between 4kV and 12kV. Indeed, with the aim of studying the influence of the inter-electrode distance on silver nanoparticle synthesis, while keeping the ratio of $U_{applied}$ over the inter-electrode distance constant, the value of the ratio was set at 3. Three different applied voltages were chosen, 6kV, 9kV, and 12kV, corresponding to an inter-electrode distance of 2mm, 3mm, and 4mm, respectively. Nevertheless, due to frequent (visible) spark formations at 6kV/2mm, the applied voltage was reduced to 4kV, while keeping a 2mm gap, ensuring a similar plasma regime for the different tested experimental conditions. The pulse repetition frequency of pulsed plasma discharges was 50Hz, and pulse duration of 150µs has been applied to the PLI process. High voltage pulse discharges were generated using the BEHLKE solid state HV switch. PLI process parameters applied in this study are presented in table 34:

Table 34: PLI process parameters with focus on the inter-electrode distance

Discharge Physical parameters	**Solution Physicochemical parameters**
Applied voltage ($U_{applied}$): 4-12kV	Reaction volume (V): 100mL
Pulse repetition frequency (f): 50Hz	$AgNO_3$ concentration: 2mM
Inter-electrode distance (l_{Pt}): 2-4mm	PVP concentration: 0.02mM
Discharge time (t_{plasma}): 20min	pH: ≈5
Pulse duration: 150µs	Conductivity (σ): 300µS/cm

In our study, the current (I) and voltage (U) waveforms were recorded at the end of the synthesis process (t_{plasma}=20min) and are presented on figure 81. In current waveforms, a complete profile of a single pulse is presented, as well as a detailed profile of current pulses (τ = 40µs) (see insets of current waveforms on figure 81). Voltage waveforms of a single pulse have been presented in similar approach, but the detailed profile of the pulse is instead up to τ = 0.75µs (see insets of voltage waveforms on figure 81). Relevant discharge parameters were

extracted as appeared in the waveforms presented on table 35. The input energy per pulse was determined, and the results are presented in figure 82.

Table 35: Plasma parameters obtained for a constant ratio of applied voltage and inter-electrode distance using BEHLKE pulse generator. Grey field corresponds to values obtained from MARX-generated pulses.

Applied voltage	**Inter-electrode distance**	**Input energy per pulse**	**Injected discharge power**
$U_{applied}$, *kV*	l_{Pt}, *mm*	E_{input}, *mJ/pulse*	P_{plasma}, *W*
4	2	17.2	0.9
8	3	42.5	2.1
9	3	39.0	2.0
12	4	73.5	3.7

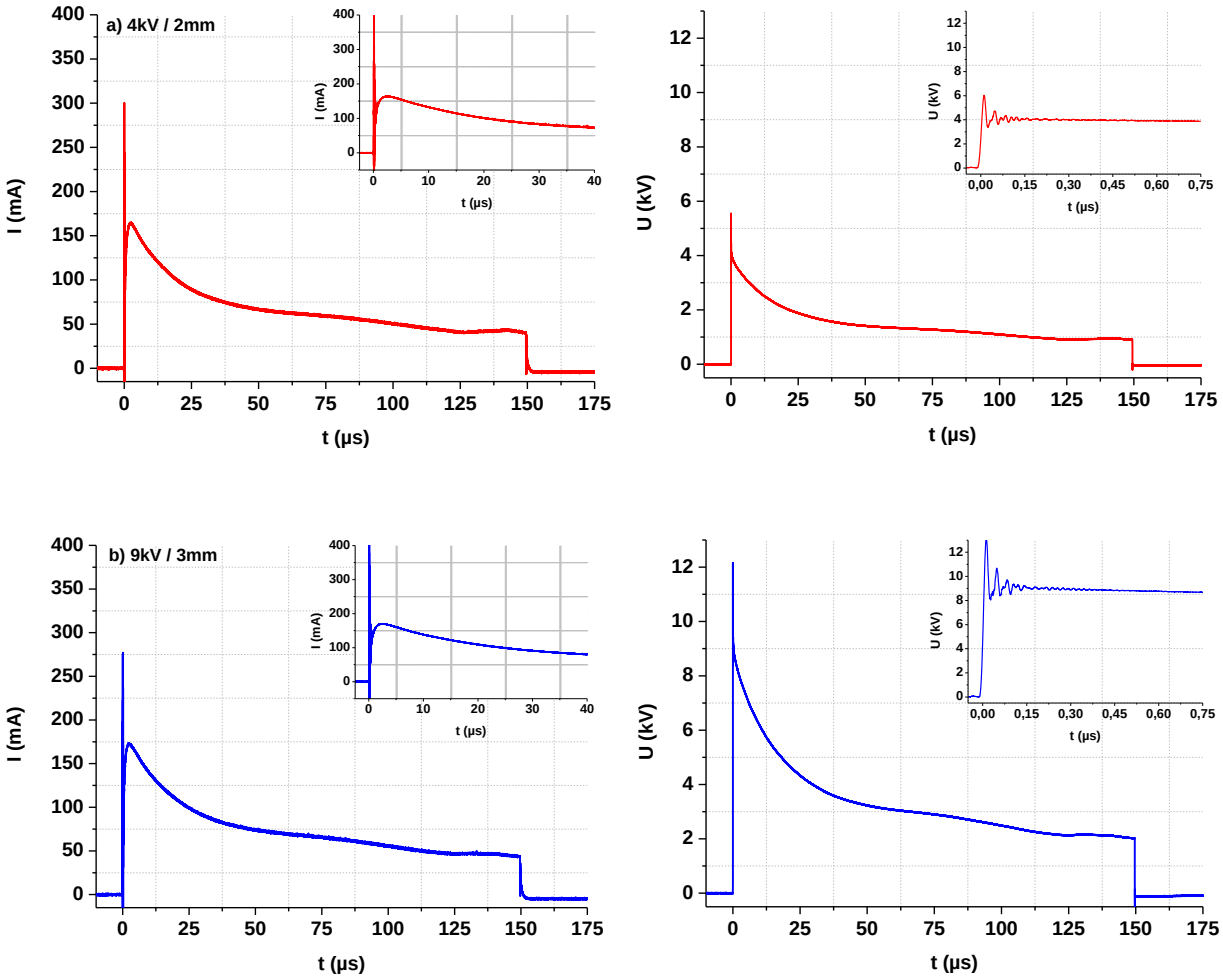

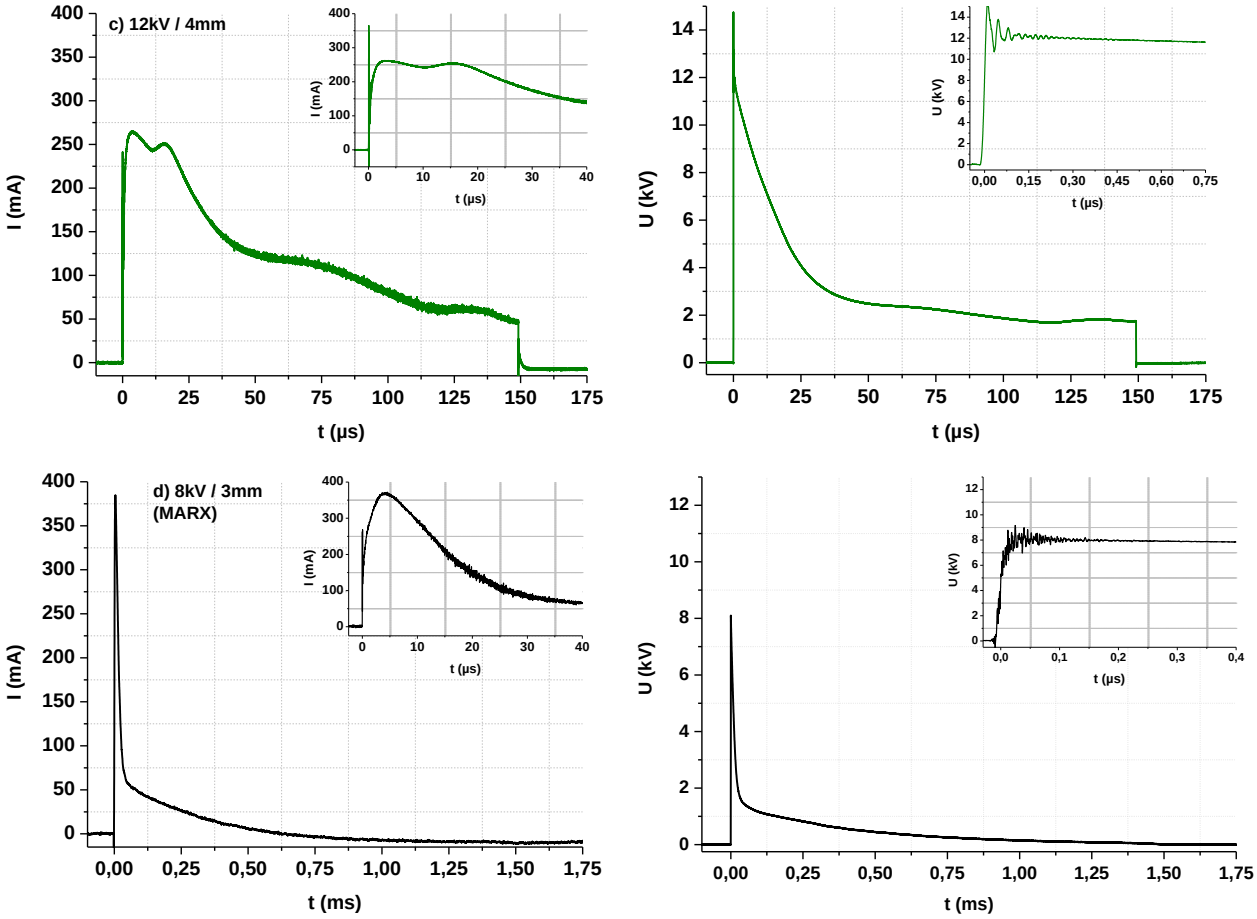

Figure 81: I- and U-waveforms for one pulse (at the end of the process t=20min). Constant ratio of applied voltage and inter-electrode distance used, are: a) 4kV/2mm, b) 9kV/3mm, c) 12kV/4mm for BEHLKE-generated pulses, and d) 8kV/3mm for MARX-generated pulses.

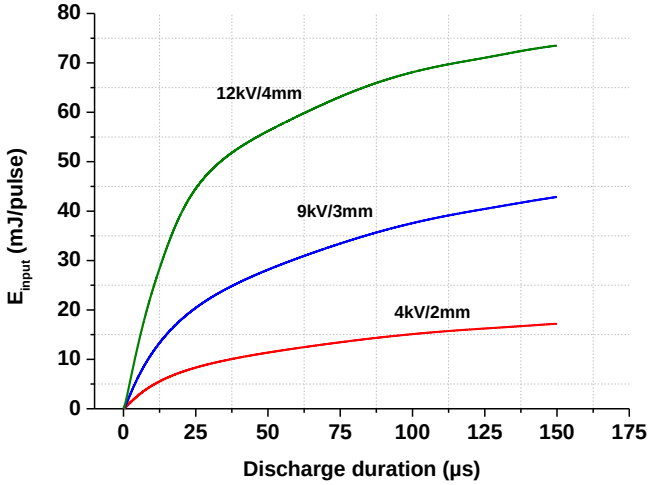

Figure 82: Input energy per pulse of pulsed plasma discharges obtained as a result of 20min silver nanoparticle discharge using the PLI process for a constant ratio of $U_{applied}$ / inter-electrode distance. Applied conditions are: 4kV/2mm (red), 9kV/3mm (blue), and 12kV/4mm (green) for BEHLKE-generated pulses with 150µs in pulse duration.

From the current and voltage waveforms on figure 81 it is observed that for an increase in the $U_{applied}$ over the inter-electrode distance from 4kV/2mm to 9kV/3mm a similar conduction of the electrical current was obtained. However a slight increase in the maximum current does occur from this increase. Besides the discharge current, such increase does increase the E_{input} per pulse value from 17.2mJ/pulse to 39mJ/pulse. Further increase in the $U_{applied}$ over the inter-electrode distance to 12kV/4mm resulted in an unusual trend in the current waveforms on figure 81d. A second conduction peak appeared and may be due to an increase in the electric field around the electrodes with an increase in input energy of 73.5mJ/pulse. A similar trend in the current waveforms was observed as a result of applying 12kV to electrodes in section 5.2. From these observations it is shown that the applied voltage over the inter-electrode distance for a constant ratio does have an influence on plasma generation in the liquid phase. It is likewise on table 35 observed that an increase in the value of this parameter does increase the E_{input} and P_{Plasma}.

Plasma discharges generated under these experimental conditions were mostly in the corona plasma regime and breakdown of plasma discharges were not observed visually during the synthesis process. Visible transition of discharge regimes did not occur from streamer-to-spark discharges, however an increase in inter-electrode distance for an increase in applied voltage does influence number of filamentary vapor channels of corona discharges *(Namihira et al. 2007)*. For an inter-electrode distance at 2mm ($U_{applied}$ = 4kV), channels appear short and only few channels were observed. An increase in the inter-electrode distance to 4mm ($U_{applied}$=12kV) resulted in an increase in the number of channels, as shown in figure 83a-c.

From these observations, it is shown that the applied voltage over the inter-electrode distance (for a constant ratio) does influence the generation of plasma discharges in the liquid phase.

In a study performed by *(Hoonseung Lee, Ueno, and Saito 2015)* the influence of the inter-electrode distance of tungsten wires was investigated on nanoparticle synthesis using a similar electrode configuration. This study was performed with focus on synthesis of carbon nanoparticles. Bi-polar pulsed plasma discharges was applied to tungsten wire electrodes immersed in benzene (solvent), with inter-electrode distances between 0.25mm and 1mm.

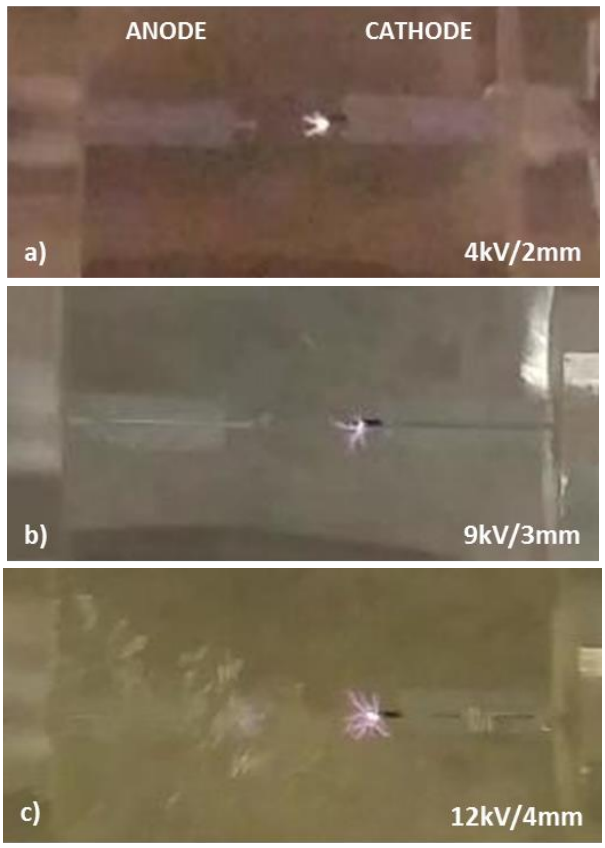

Figure 83: Visible partial corona discharge generated in liquid phase during AgNP synthesis. Plasma discharges generated for a constant $U_{applied}$ and inter-electrode distance ratio, which corresponds to: a) 4kV/2mm, b) 9kV/3mm, and c) 12kV/4mm

Bi-polar pulses were operated between 1kV and 2kV, and with a pulse repetition frequency of 15kHz and 1.2µs duration. Lee *et al.* reported thus that the inter-electrode distance does have an influence on carbon nanoparticle morphology, and that the material properties of the synthesized carbon structures were improved through structural modifications.

Ex-situ conductivity and pH measurements were conducted before and after 20min of plasma discharge. As it is shown on table 36, initial pH and solution conductivity remains stable at pH4.5 and around 304µS/cm, respectively. However, changes in the reaction media occur during 20min of plasma discharge. For inter-electrode distances of 2mm and 3mm an increase in solution conductivity by 21-23µS/cm in the reaction media was observed. Further increase at 4mm and 12kV resulted in a slight change in the physico-chemical solution parameters. The solution conductivity increased by 9µS/cm, which is a similar increase to that observed in section 5.2 for silver nanoparticle synthesis performed in the application of 12kV.

Table 36: Changes in solution chemistry, before and after AgNP synthesis

Inter-electrode distance	pH		Solution conductivity σ ($\mu S/cm$)	
l_{Pt}, *mm*	*Initial*	*Final*	*Initial*	*Final*
2	4.5	3.7	308	329
3	4.5	3.7	302	325
4	4.5	4.0	304	313

From a qualitative point of view, increasing the inter-electrode distance (and $U_{applied}$) has an impact on the aspect of the reaction media, as a color change has been observed. As shown on figure 84, synthesis performed at an inter-electrode distance of 4mm resulted in a less visible color change of the reaction media as compared to 2mm and 3mm.

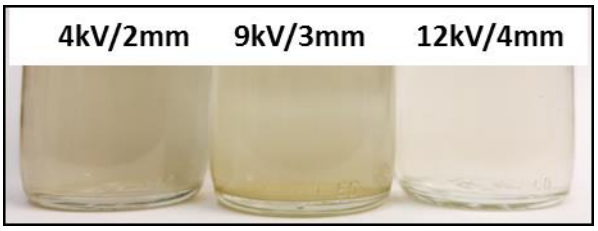

Figure 84: Color changes obtained from 20min nanoparticle synthesis for inter-electrode distance of 2mm, 3mm, and 4mm applying 4kV, 9kV, and 12kV of plasma discharge, respectively.

The results obtained for the synthesis performed at an inter-electrode distance of 4mm remind of the previous results that were obtained for the synthesis performed at 12kV in applied voltage and 3mm in electrode gap.

Further analysis of the resulting particles was performed. After 20min of particle synthesis, 2mL of the reaction media containing the silver nanoparticles were analyzed by UV-vis absorption spectroscopy. Resulting absorption spectra are shown in figure 85 and results determined from the spectra are listed in table 37. Nanoparticles synthesized for an inter-electrode distance of 2mm and 3mm present a maximum absorption wavelength at around λ_{max} = 402nm. Silver nanoparticles synthesized with an inter-electrode distance fixed at 2mm and 4kV present a lower absorption than the ones synthesized with 3mm and 9kV. Concerning the polydispersity, particles produced at an electrode distance of 3mm have a FHWM value of

139nm, which is lower than that of 4kV/2mm particle synthesis, suggesting thus a decrease in poly-dispersion of particles as the $U_{applied}$ over the inter-electrode distance (for a constant ratio) is increased.

Table 37: Results obtained from UV-vis absorption spectra of silver nanoparticle synthesis for 2mm, 3mm, and 4mm of inter-electrode distance.

Applied voltage	**Inter-electrode distance**	**Absorbance**	**λ_{max}**	**FWHM**
$U_{applied}$, kV	*l_{Pt}, mm*	*a.u.*	*nm*	*nm*
4	2	0.21	402	306
9	3	0.29	402	139
12	4	0.09	412	117

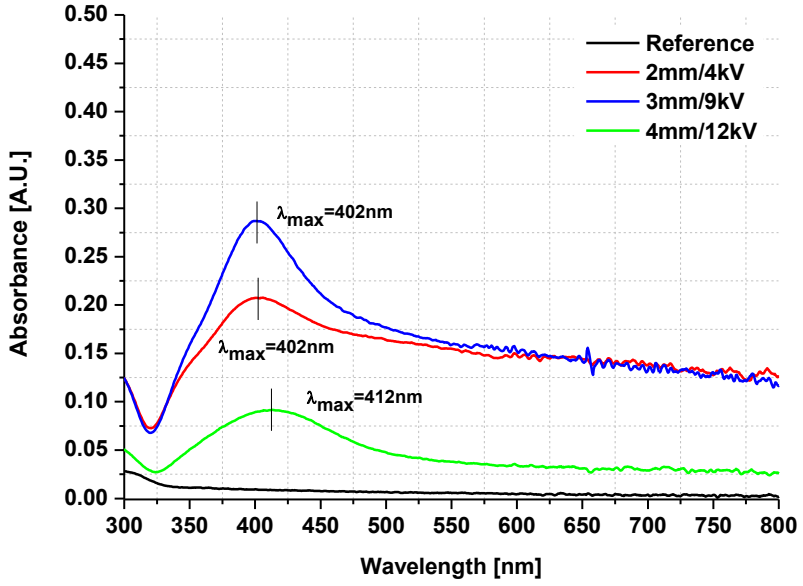

Figure 85: UV-vis absorption spectra of silver nanoparticles synthesized for inter-electrode distance of 2mm (red), 3mm (blue), and 4mm (green) for applied voltage of 4kV, 9kV, and 12kV, respectively.

Nanoparticles synthesized with an inter-electrode distance of 4mm resulted in a lower particle concentration with particles absorbing light at 0.09 in absorbance at around 412nm, and present a lower polydispersity (FHWM=117). Furthermore, a red-shift by 10nm occurs for 12kV/4mm, which indicates an increase in the average nanoparticle size as the $U_{applied}$ over the inter-electrode distance is increased. Results obtained from electrode distance 4mm for 12kV applied voltage are equivalent to results obtained from particle synthesis in section 5.2 with focus on the applied

voltage. The conditions were 12kV in applied voltage for an inter-electrode distance at 3mm. Due to similarities in observation made for nanoparticles produced at 12kV/4mm in this study and nanoparticles produced at 12kV/3mm in section 5.2, similar suggestion on particle growth are proposed. An increase in the $U_{applied}$ over the inter-electrode distance (for a constant ratio) increased the strength of the electrical field around the electrodes. This increases the driving force in particle crystallization, which promotes particles to reach thermodynamic equilibrium. This includes transformation of spherical particles into polyhedron shaped particles through rapid coalescence. This explains the loss in yellow solution color into a nearly transparent solution.

Silver nanoparticles were also analyzed by the DLS technique in order to determine the particle size distribution. A small volume of as-synthesized nanoparticles of as low as 1mL was required for this measurement. Results obtained from the DLS measurements are presented in table 38, and corresponding PSD graphs are presented in both intensity and number weighted PSD, as shown in figure 86a-b. A 2mm inter-electrode distance ($U_{applied}$=4kV) resulted in a bi-modal size distribution with size populations around 32.5nm (14%) and 185.7nm (86%). From intensity weighted PSD on figure 86a it is thus shown that particles are polydisperse. However, from number weighted PSD on figure 86b particles of 26.7nm are highly present. Inter-electrode distance of 3mm ($U_{applied}$=9kV) resulted in a multi-modal size distribution with hydrodynamic diameters around 15.5nm (3%), 36nm (11%), and 162nm (86%). From the multi-modal particle size distribution it is also shown that nanoparticles are polydisperse.

Table 38: Results obtained from DLS size measurements of silver nanoparticle synthesis for 2mm, 3mm, and 4mm inter-electrode distance.

Applied voltage	**Inter-electrode distance**	**Peaks**	**Intensity-based size (%I)**		**Number-based size (%N)**		**Count Rate**
$U_{applied}$, kV	*l_{Pt}, mm*		*nm*	*%*	*nm*	*nm*	*%*
4	2	1	32.5	14	26.7	100	3980
		2	185.7	86			
9	3	1	15.5	3	13.7	100	7576
		2	36.1	11			
		3	162.4	86			
12	4	1	25.3	15	21.2	100	950
		2	154.2	85			

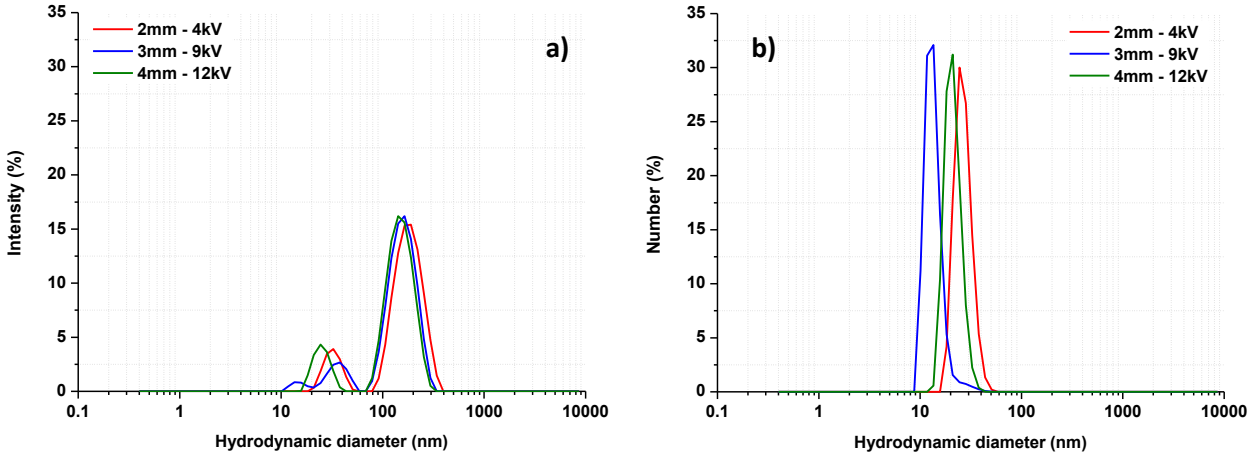

Figure 86: DLS size measurements of silver nanoparticles synthesized for inter-electrode distance of 2mm (red), 3mm (blue), and 4mm (green) for applied voltage of 4kV, 9kV, and 12kV, respectively. Results are presented in a) intensity and b) number based PSD

Inter-electrode distance of 4mm ($U_{applied}$=12kV) resulted in a bi-modal size distribution with size populations around 25.3nm (15%) and 154nm (85%). Bi-modal size distribution is an indication of the presence of large-sized particles in the reaction media. It is also known from the count rate that particle concentration is lower for 4mm ($U_{applied}$=12kV) than particle concentration of 2mm ($U_{applied}$=4kV) and 3mm ($U_{applied}$=9kV).

Based on the results obtained by absorption spectra and DLS analysis of silver nanoparticles, it is concluded that for an increase in the $U_{applied}$ over the inter-electrode distance the particle concentration increases. At a given E_{input} (per pulse) the particle concentration decreases for an increase in the average particle size.

As-synthesized silver nanoparticles were also characterized by SEM. Samples for this particle characterization technique was prepared by applying the same sample preparation procedure as in chapter IV. Silver nanoparticles were deposited onto a microscopy glass plate for one hour, carefully rinsed with deionized water, and dried in oven overnight at 80°C. Results of SEM characterization are shown on figure 87a-c and supports previously made statements of particle synthesis.

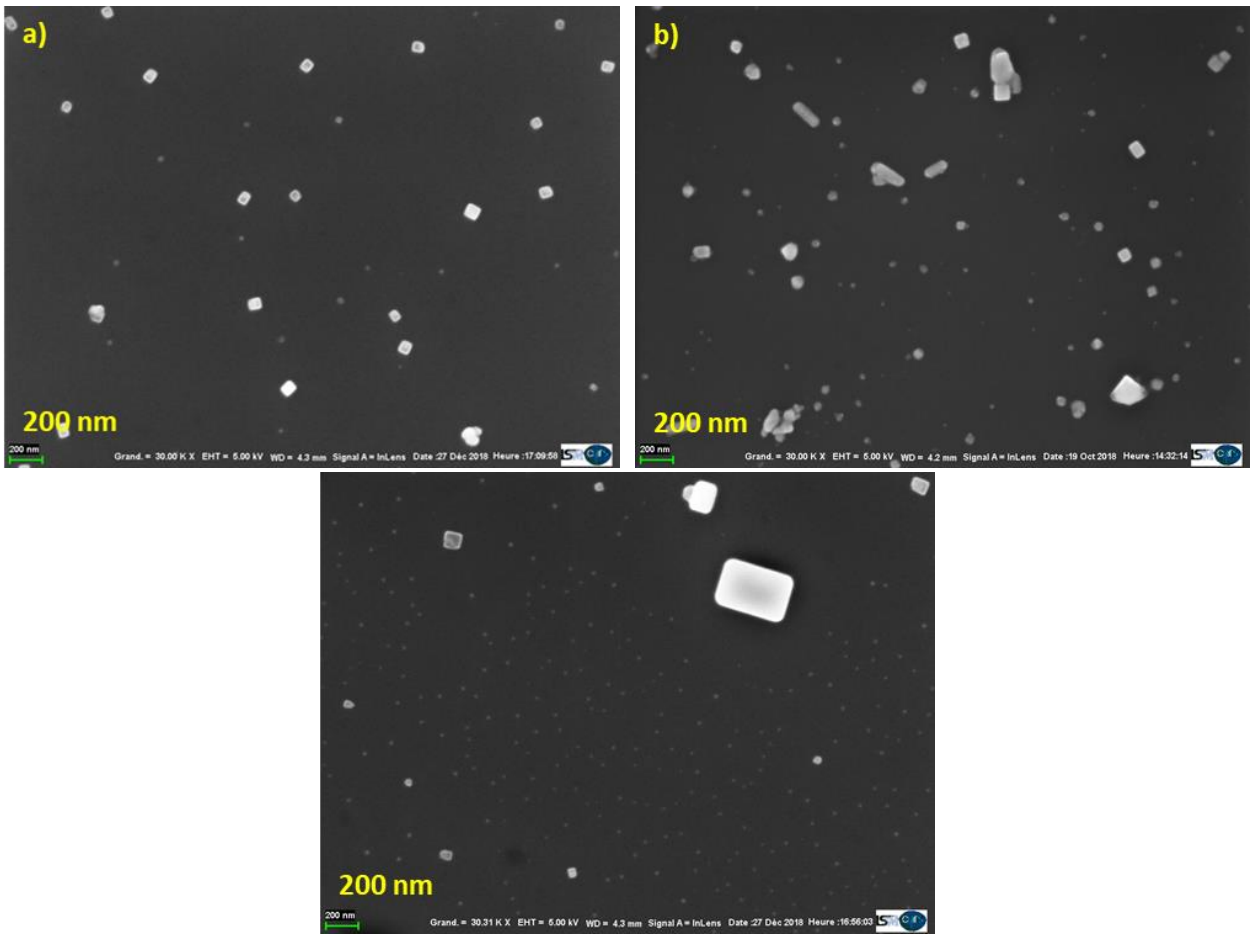

Figure 87: SEM micrographs of AgNP synthesized for 20min of plasma discharge with inter-electrode distance of a) 2mm, b) 3mm, and c) 4mm. Magnification: 30kX

Nanoparticles resulting from 2mm inter-electrode distance applying 4kV pulse discharges is presented on figure 87a. From this SEM micrograph morphology of silver nanoparticles is revealed. Silver nanoparticles are mainly cubic-shaped and spherical silver nanoparticles of various size distributions occur. Further increase in the inter-electrode distance to 3mm and 9kV in applied voltage are shown on figure 87b. The morphology of silver nanoparticles is cubic-, spherical- and rod-shaped particles of various sizes.

As the applied voltage was increased from 4kV to 12kV over an increase in the inter-electrode distance from 2mm to 4mm (for a constant ratio) the input energy per pulse of plasma discharges did increase as well. The highly energized corona pulse discharges does cause smaller nanoparticles to coalesce rapidly and reach thermodynamic stability to transform into large-sized cubic silver particles *(Tang et al. 2009)*, as shown on figure 87c. Results obtained from SEM are

hence in accordance with results obtained from DLS and UV-vis absorption spectroscopy analysis. Comparing silver nanoparticles obtained from current study to nanoparticles obtained from study of applied voltage, it is observed that these two parameters have similar effect on nanoparticle synthesis.

5.3.1 Summary

In this section the inter-electrode distance for a specific plasma regime has been investigated on the influence of nanoparticle synthesis, and how it affects morphology of silver nanoparticle. It was from the previous section determined that an increase in applied voltage and input energy did increase the average particle size as a result of rapid coalescence. The current study was performed as a parallel to the previous study in order to investigate the influence of inter-electrode distance on nanoparticle synthesis by changes in applied voltage. Changing the applied voltage keeps thus the plasma regime stable which is in agreement with the Paschen law. The study was performed with for inter-electrode distance 2mm, 3mm, and 4mm and applied values of 4kV, 9kV, and 12kV, respectively. Applying these values in particle synthesis did not cause breakdown in discharges, however the input energy would increase for an increase in applied voltage. An inter-electrode distance of 2mm ($U_{applied}$=4kV) resulted in partial corona discharges. Branches of plasma were short and only few did appear, since the input energy was as low as 17mJ/pulse. For 3mm ($U_{applied}$=9kV) resulted in an increase in number of plasma filaments, and input energy did increase to 40mJ/pulse. At 4mm ($U_{applied}$=12kV) the amount of plasma branches and the length was increasing as a result of increase in input energy at 74mJ/pulse. Silver nanoparticle appeared cubic, and average particle size was increasing for an increase in input energy. A comparison of nanoparticles obtained from study of applied voltage and inter-electrode distance shows that particle synthesis appears similar for input energies above 17mJ/pulse. And under these conditions the inter-electrode distance does not have an influence on particle morphology and average particle size. Increase in input energy does cause smaller nanoparticles to coalesce rapidly and reach thermodynamic stability to transform into large-sized particles. Therefore, synthesis of small-sized nanoparticles does require a low applied voltage below 9kV and input energy below 40mJ.

5.4 Growth mechanism of silver nanoparticles

In this chapter a parametrical study was performed with focus on physical process parameters and to investigate the influence of these parameters on synthesis of silver nanoparticles.

Throughout the parametrical study, it was realized that the physical parameters investigated in this chapter, such as $U_{applied}$, pulse duration etc. did result in the same result in synthesis of silver nanoparticles.

Common observations made on nanoparticle synthesis under the influence of physical parameters are:

- Increase in average particle size distribution
- Increase in nanoparticle concentration
- Nanoparticle growth towards thermodynamic stability

} For an increase in E_{input}

These observations are valid, when an increase in the pulse duration, the applied voltage, and the applied voltage over the inter-electrode distance (for a constant ratio) results in an increase in the E_{input} (per pulse) of plasma discharges generated in the liquid phase. An increase in E_{input} (per pulse) increases the production of charge carriers, which results in faster particle synthesis process. Therefore, an increase in E_{input} (per pulse) results in an increased particle concentration. As the particle concentration increases for an increase in the E_{input} (per pulse), the average nanoparticle size distribution increases. An increase in size distribution occurs due to a decrease in the particle stabilization. The polymeric compound PVP, which was added as a stabilizing agent in order to stabilize silver nanoparticles does not coat particles completely, which results in active sites on the particles. This promotes particle growth and/or aggregation. As the E_{input} (per pulse) increases, it is further observed that a profound shaping of the particles occurs, which takes form into its thermodynamically favorable shape. In the case of silver particles, which is a FCC element the thermodynamically favorable shape is a cubic.

5.5 Conclusion

Chemical parameters that were optimized from the first parametrical study in chapter IV was applied in the parametrical study with focus on physical process parameters. The aim of this parametrical study was to investigate the influence of parameters on plasma generation in the

PLI process. Furthermore, it was our goal to investigate the influence of these parameters on silver nanoparticle synthesis.

In this parametrical study, physical parameters that have been documented to have an influence of plasma generation was selected and applied in this study. These parameters concern: Pulse duration, applied voltage, and inter-electrode distance.

Prior to the parametrical study, it was necessary to exchange the pulse generator in order to be able to produce clean pulse discharges, which parameters are easily regulated. Therefore, as an alternative to MARX pulse generator, BEHLKE pulse generator was applied instead. As a result of this exchange in pulse generators, modification in the experimental-setup did follow.

The first parameter focused on the influence of pulse duration. From this study it was shown that the pulse duration of plasma discharges does have an influence on the generation of partial streamer-like discharges. This occurs, since an increase in pulse duration from 150µs to 1.5ms does increase in the E_{input} of plasma discharges per pulse. Therefore, as the E_{input} is increased, concentration of produced silver nanoparticle increased, resulting thus in particle aggregation. It was from these observations decided to continue the parametrical study with 150µs in pulse duration in order to produce small-sized and uniformly distributed silver nanoparticles. The second parameter that was investigated is the applied voltage. An increase in the $U_{applied}$ from 1kV to 12kV, for a fixed inter-electrode distance of 3mm, does influence generation of pulse plasma discharges in the liquid phase. The increase in $U_{applied}$ was observed through transition in plasma regimes: non-luminous, partial streamer-like discharges, and spark discharges as this parameter increased. This transition in plasma regime occurred due to an increase in the electric field around the electrodes. In silver nanoparticle synthesis, an increase in $U_{applied}$ resulted in an increase in the concentration of produced silver particle, and also an increase in the average particle size distribution. As an exception in our observations, $U_{applied}$ of 12kV did result in a decrease in produced particle concentration. This may have occurred due to rapid coalescence of smaller sized particles as a result of an increase in the electric field. Therefore, synthesis of small-sized nanoparticles does require a low $U_{applied}$ below 9kV and input energy below 40mJ for this PLI process. As the final parameter, the influence of an increase in $U_{applied}$/inter-electrode distance (for a constant ratio) on plasma generation was determined. Applying 4kV/2mm, 9kV/3mm, and 12kV/4mm to the system would generate partial corona discharges in the liquid

phase. However, an increase in $U_{applied}$/inter-electrode distance was observed on electrical discharges through increase in length and number of filamentary vapor channels of plasma discharges. This occurred as a result of an increase in the electric field around the electrodes. Similar observations were made on production of silver nanoparticles as it was for silver nanoparticle synthesis controlling the $U_{applied}$ parameter. Therefore, in order to produce small-sized silver nanoparticles, parameters below 9kV/3mm (for a constant ratio) and E_{input} below 40mJ was required.

Chapter VI - Conclusion & perspectives

The objective of this thesis is to develop and optimize a plasma liquid immersion (PLI) process with focus on silver nanoparticle synthesis. The goal is to produce small-sized (<20nm) silver nanoparticles using a low-cost PLI process with low power consumption. In particular, among the initial concerns of this work a simple metal precursor ($AgNO_3$ in water) has been used to limit the synthesis steps and to reduce the volume and the number of solvents used.

In the initiation of this work, an experimental set-up of the PLI process has been developed for synthesis of silver nanoparticles. An important part of this work has been to develop, from scratch, the PLI process. First, we used a MARX-type pulsed voltage generator developed in the laboratory. In a second step, we used a high voltage switch (BEHLKE) to produce voltage pulses. Many adaptations have been made for more than a year in particular to ensure the stability of the plasma. As such, numerous tests concerning the electrodes were carried out, in particular to ensure that the shape of the electrodes had only little influence on the stability of the plasma, but also to ensure excellent electrical insulation of the system.

Silver nanoparticles synthesized have been characterized in order to confirm purity and nature of nanoparticle. Based on the results obtained from different characterization techniques, including XRD, SEM-EDS, and XPS, it was determined that **the PLI process would result in the synthesis of pure and metallic silver nanoparticles.**

Following the confirmation of metallic silver nanoparticles, a parametrical study has been performed. The purpose of this parametrical study was to optimize the PLI synthesis process in order to synthesize nanoparticles, which would result in small-sized, spherical and uniformly-distributed silver nanoparticles. In addition to this study, the influence of chemical parameters has been investigated. In the first parametrical study, the pulsed plasma discharge was generated in the use of a low-cost and one-staged MARX pulse generator. This study was mainly focusing on the chemical parameters of the silver nanoparticle synthesis process, and included following parameters: precursor (i.e. $AgNO_3$) concentration, stabilizing agent (i.e. PVP) concentration, and initial pH of precursor solution.

Silver nanoparticles have been synthesized during 20min of pulsed plasma discharges immersed in the precursor solution. Pulsed plasma discharges were generated applying high voltages 8kV to the Pt wire electrodes. From the generated pulsed plasma discharges, the reaction solution would be exposed to discharges of 40mJ/pulse and 2W in the discharge region.

The optimized conditions made it possible to synthesize spherical and uniformly-distributed silver nanoparticles of 10nm (average size in diameter): **The reaction solution comprises an aqueous solution of 2mM $AgNO_3$ in the presence of 0.02mM PVP, and with no further addition of chemical compounds.**

A decrease in the $AgNO_3$ concentration provided synthesis of particles with a decrease in the average particle size. The produced particles were highly aggregated and are composed of large-sized particles of irregular shapes. In order to avoid agglomeration of produced particles, a polymeric stabilizing agent was added into the reaction media. From this investigation, it has been determined that up to 0.01mM in PVP concentration, particles would appear as agglomerated fractions composed of particles of decrease size in average. A complete stabilization of silver nanoparticles has been observed starting from 0.02mM in PVP concentration. **Synthesis of silver nanoparticles in the presence of 0.02mM PVP resulted thus in uniform distribution of spherically-shaped and small-sized silver nanoparticles.** In the continuation of this parametrical study, the influence of the growth environment on silver nanoparticle synthesis has been investigated by varying the initial pH of the precursor solution, through, for example, the addition of HNO_3 resulting in an acidic precursor solution. At pH4, the PLI particle production resulted in formation of large-sized silver particles of anisotropic shapes including triangular and hexagonal shaped particles. Addition of NH_4OH resulted in a basic precursor solution. At pH11 the PLI particle production resulted in formation of particles, which were encapsulated by the polymeric network. **Silver nanoparticles which resulted in spherical and small-sized particles were synthesized for a pH value of initial precursor solution of pH5 and pH9.**

Due to the objectives of this thesis, as in no addition of chemicals, which are hazardous towards environment, it was decided to proceed the silver nanoparticle synthesis without addition of buffer in pH regulation.

The chemical parameters, which have been determined to yield spherical and uniformly-distributed silver nanoparticles in the use of a MARX-pulsed PLI process, have been applied in the second parametrical study. The purpose of this parametrical study was to optimize the PLI synthesis process in order to investigate the influence of the physical process parameters of the PLI process. In the second parametrical study, the pulsed plasma discharge was generated in the use of a higher cost and solid-state BEHLKE switch for generation of HV pulse plasma discharges. This study was mainly focusing on the physical parameters of the silver nanoparticle synthesis process, and included following parameters: Pulse duration, applied voltage, and applied voltage over the inter-electrode distance for a constant ratio.

In this parametrical study, silver nanoparticles have been synthesized in a similar approach to the first parametrical study in the use of the MARX-pulsed PLI process. Silver nanoparticles have thus been synthesized during 20min of pulsed plasma generation immersed in the reaction solution. In the use of a BEHLKE-pulsed PLI process for silver nanoparticle synthesis would result in large-sized polyhedral-shaped nanoparticles, which is different from that obtained from the MARX-pulsed PLI process. This morphology of silver nanoparticles may indicate that silver nanoparticles have reached thermodynamic stability.

At similar input energies per pulse and injected power of pulsed plasma discharges generated in the liquid phase as MARX-pulsed plasma discharges (40mJ/pulse and 2W), silver particles of different aspect ratio with particle sizes ranging from 50nm to 100nm have been produced. Under these experimental conditions, silver nanoparticles were produced by injecting 40mJ energy into pulsed plasma discharges of the PLI process with 2W in power consumption.

From this parametrical study, it was shown that production of a decreased silver particle size is obtained for a low pulse duration (<150µs) in the application of <9kV to Pt electrodes for 3mm in inter-electrode distance.

In the continuation of this project, it is proposed to apply the synthesized silver nanoparticles as nano-catalyst in the decomposition of a simulated air pollutant (e.g. acetaldehyde (CH_3CHO)). Hereby, the catalytic efficiency of nanoparticles produced by the PLI process of low input energy and power consumption would be determined.

However, possible difficulties can occur in the application of these nanoparticles in the two phase plasma/catalysis process during the decomposition of the simulated air pollutant. Difficulties may arise from the following causes in the preparation of the nano-catalysts:

The first reason may be due to weakly bonded silver nanoparticles onto the surface of the SiO_2 pellets (support), which could results in loss of deposited silver nanoparticles during the CH_3CHO degradation. This could occur, if the intermediate phase, the mono-layered TiO_2 coating of the SiO_2 pellets, is excluded.

The second cause may be due to reduced reactivity of silver nanoparticles. This could occur, if the surface of nanoparticles is completely covered by a polymeric stabilizing agent (i.e. PVP), and thus block the reactive sites of the nanoparticles, which thus decreases the reactivity of the nanoparticles. In this case, it is important to ensure that the polymeric network has been removed from the surface of the nanoparticles, once synthesized, through an extensive cleaning process. Another solution is to stabilize nanoparticles using stabilizing agent that provide electrostatic stabilization of nanoparticles (e.g. sodium citrate).

It is also proposed to investigate the presence of various plasma generated species, which are created in the plasma zone during nanoparticle synthesis in the liquid phase. In the identification of some of the reactive species, a colorant (e.g. Methylene blue or Rhodamine) is added into the liquid, which is degraded by the species. Optical techniques (absorption spectroscopy) can be applied in the evaluation of the degradation of the colorant.

References

Aggadi, Najia. (2006). “Etude de La Réactivité de Suies Modèles de N-Hexane Sous Décharge Couronne Pulsée à Pression Atmosphérique.” Université Paris 13.

Agnihotri, Shekhar, Soumyo Mukherji, and Suparna Mukherji. (2014). “Size-Controlled Silver Nanoparticles Synthesized over the Range 5–100 Nm Using the Same Protocol and Their Antibacterial Efficacy.” *RSC Adv.* 4 (8): 3974–83. https://doi.org/10.1039/C3RA44507K.

Ajitha, B, A Divya, GS Harish, and P Sreedhara R. (2013). “The Influence of Silver Precursor Concentration on Size of Silver Nanoparticles Grown by Soft Chemical Route.” *Res. J Physical Sci.* 1 (7): 11–14.

Akolkar, Rohan, and R. Mohan Sankaran. (2013). “Charge Transfer Processes at the Interface between Plasmas and Liquids.” *Journal of Vacuum Science & Technology A: Vacuum, Surfaces, and Films* 31 (5): 050811. https://doi.org/10.1116/1.4810786.

An, Wladimir, Kurt Baumung, and Hansjoachim Bluhm. (2007). “Underwater Streamer Propagation Analyzed from Detailed Measurements of Pressure Release.” *Journal of Applied Physics* 101 (5): 053302. https://doi.org/10.1063/1.2437675.

Ananth, Antony, and Young Sun Mok. (2016). “Dielectric Barrier Discharge (DBD) Plasma Assisted Synthesis of Ag2O Nanomaterials and Ag2O/RuO2 Nanocomposites.” *Nanomaterials* 6 (3): 1–11.

Andrews, R., D. Jacques, A.M. Rao, F. Derbyshire, D. Qian, X. Fan, E.C. Dickey, and J. Chen. (1999). “Continuous Production of Aligned Carbon Nanotubes: A Step Closer to Commercial Realization.” *Chemical Physics Letters* 303 (5–6): 467–74. https://doi.org/10.1016/S0009-2614(99)00282-1.

APS Physics. (2018). “This Month in Physics History.” 2018. https://www.aps.org/publications/apsnews/201108/physicshistory.cfm.

Ashrafi, A. (2011). “Quantum Confinement: An Ultimate Physics of Nanostructures.” In *Encyclopedia of Semiconductor Nanotechnology*, edited by A. Umar, 1–67.

Avantes. (2015). “Avantes - Catalog IX.”

Badawy, Amro M. El, Todd P. Luxton, Rendahandi G. Silva, Kirk G. Scheckel, Makram T. Suidan, and Thabet M. Tolaymat. (2010). “Impact of Environmental Conditions (PH, Ionic Strength, and Electrolyte Type) on the Surface Charge and Aggregation of Silver Nanoparticles Suspensions.” *Environmental Science and Technology* 44 (4): 1260–66. https://doi.org/10.1021/es902240k.

Bagotsky, V. S. (2005). *Fundamentals of Electrochemistry*. Second. John Wiley & Sons.

Bearden, J. A. (1967). “X-Ray Wavelengths.” *Reviews of Modern Physics* 39 (1): 78–124. https://doi.org/10.1103/RevModPhys.39.78.

Behlke Power Electronics GmbH. (2018). “Fast High Voltage Transistor Switches - Technical Data.” 2018. http://www.behlke.com/pdf/301-03-gsm.pdf.

Belloni, J. (2006). “Nucleation, Growth and Properties of Nanoclusters Studied by Radiation Chemistry: Application to Catalysis.” *Catalysis Today* 113 (3–4): 141–56.

Bratescu, Maria Antoaneta, Sung-Pyo Cho, Osamu Takai, and Nagahiro Saito. (2011). “Size-Controlled Gold Nanoparticles Synthesized in Solution Plasma.” *The Journal of Physical Chemistry C* 115 (50): 24569–76. https://doi.org/10.1021/jp207447c.

Brazis, P. W. (2017). “Quantum Dots and Their Potential Impact on Lighting and Display Applications.” https://library.ul.com/wp-content/uploads/sites/40/2017/07/UL-Quantum-Dots-White-Paper.pdf.

Brown, Ashley N., Kathryn Smith, Tova A. Samuels, Jiangrui Lu, Sherine O. Obare, and Maria E. Scott. (2012). “Nanoparticles Functionalized with Ampicillin Destroy Multiple-Antibiotic-Resistant Isolates of Pseudomonas Aeruginosa and Enterobacter Aerogenes and Methicillin-Resistant Staphylococcus Aureus.” *Applied and Environmental Microbiology* 78 (8): 2768–74. https://doi.org/10.1128/AEM.06513-11.

Bruggeman, P J, M J Kushner, B R Locke, J G E Gardeniers, W G Graham, D B Graves, R C H M Hofman-Caris, et al. (2016). “Plasma–liquid Interactions: A Review and Roadmap.” *Plasma Sources Science and Technology* 25 (5): 053002. https://doi.org/10.1088/0963-0252/25/5/053002.

Bruggeman, Peter, and Christophe Leys. (2009). “Non-Thermal Plasmas in and in Contact with Liquids.” *Journal of Physics D: Applied Physics* 42 (5): 053001. https://doi.org/10.1088/0022-3727/42/5/053001.

Bruggeman, Peter, Daan Schram, Manueí A González, Robby Rego, Michael G Kong, and Christophe Leys. (2009). “Characterization of a Direct Dc-Excited Discharge in Water by Optical Emission Spectroscopy.” *Plasma Sources Sci. Technol. Plasma Sources Sci. Technol* 18 (18): 25017–13. https://doi.org/10.1088/0963-0252/18/2/025017.

Brust, Mathias, Merryl Walker, Donald Bethell, David J. Schiffrin, and Robin Whyman. (1994). “Synthesis of Thiol-Derivatised Gold Nanoparticles in a Two-Phase Liquid–Liquid System.” *J. Chem. Soc., Chem. Commun.*, no. 7: 801–2. https://doi.org/10.1039/C39940000801.

Burakov, V .S., E. A. Nevar, M. I. Nedel’ko, and N. V. Tarasenko. (2015). “Synthesis and Modification of Molecular Nanoparticles in Electrical Discharge Plasma in Liquids.” *Russian Journal of General Chemistry* 85 (5): 1222–37. https://doi.org/10.1134/S1070363215050400.

Cao, G. (2004). *Nanostructures and Nanomaterials: Synthesis, Properties, and Applications*.

Cao, Jie, Tong Sun, and Kenneth T.V. Grattan. (2014). “Gold Nanorod-Based Localized Surface Plasmon Resonance Biosensors: A Review.” *Sensors and Actuators B* 195 (2014): 332–51.

Capek, Ignác. (2017a). “Noble Metal Nanoparticles.” In *Noble Metal Nanoparticles:*

Preparation, Composite Nanostructures, Biodecoration and Collective Properties, 125–93.

Capek, Ignác. (2017b). "Stabilizers-Mediated Nanoparticles Syntheses." In *Noble Metal Nanoparticles: Preparation, Composite Nanostructures, Biodecoration and Collective Properties*, 211–16.

Chambers, Bryant A., A. R. M. Nabiul Afrooz, Sungwoo Bae, Nirupam Aich, Lynn Katz, Navid B. Saleh, and Mary Jo Kirisits. (2014). "Effects of Chloride and Ionic Strength on Physical Morphology, Dissolution, and Bacterial Toxicity of Silver Nanoparticles." *Environmental Science & Technology* 48 (1): 761–69. https://doi.org/10.1021/es403969x.

Chen, Qiang, Junshuai Li, and Yongfeng Li. (2015). "A Review of Plasma – Liquid Interactions for Nanomaterial Synthesis." *Journal of Physics D: Applied Physics* 48: 424005. https://doi.org/10.1088/0022-3727/48/42/424005.

Chiang, Wei-Hung, Carolyn Richmonds, and R Mohan Sankaran. (2010). "Continuous-Flow, Atmospheric-Pressure Microplasmas: A Versatile Source for Metal Nanoparticle Synthesis in the Gas or Liquid Phase." *Plasma Sources Sci. Technol. Plasma Sources Sci. Technol* 19 (2010): 1–8. https://doi.org/10.1088/0963-0252/19/3/034011.

Chimentao, Ricardo José, Francesc Medina, Jesús Eduardo Sueiras, José Luís García Fierro, Yolanda Cesteros, and Pilar Salagre. (2007). "Effects of Morphology and Cesium Promotion over Silver Nanoparticles Catalysts in the Styrene Epoxidation." *Journal of Materials Science* 42 (10): 3307–14. https://doi.org/10.1007/s10853-006-0570-1.

Cho, Sung-pyo, Maria Antoaneta Bratescu, Nagahiro Saito, and Osamu Takai. (2011). "Microstructural Characterization of Gold Nanoparticles Synthesized by Solution Plasma Processing." *Nanotechnology* 22 (45): 455701. https://doi.org/10.1088/0957-4484/22/45/455701.

Choi, Kyeong Woo, Do Youb Kim, Seong Ji Ye, and O Ok Park. (2014). "Shape- and Size-Controlled Synthesis of Noble Metal Nanoparticles." *Advances in Materials Research* 3 (4): 199–216. https://doi.org/10.12989/amr.2014.3.4.199.

Choi, Young Chul, Dong Jae Bae, Young Hee Lee, Byung Soo Lee, Gyeong-Su Park, Won Bong Choi, Nae Sung Lee, and Jong Min Kim. (2000). "Growth of Carbon Nanotubes by Microwave Plasma-Enhanced Chemical Vapor Deposition at Low Temperature." *Journal of Vacuum Science & Technology A: Vacuum, Surfaces, and Films* 18 (4): 1864–68. https://doi.org/10.1116/1.582437.

Chrzanowska, Justyna, Jacek Hoffman, Artur Małolepszy, Marta Mazurkiewicz, Tomasz A. Kowalewski, Zygmunt Szymanski, and Leszek Stobinski. (2015). "Synthesis of Carbon Nanotubes by the Laser Ablation Method: Effect of Laser Wavelength." *Physica Status Solidi (B)* 252 (8): 1860–67. https://doi.org/10.1002/pssb.201451614.

Cordeiro, Mílton, Fábio Ferreira Carlos, Pedro Pedrosa, António Lopez, and Pedro Baptista. (2016). "Gold Nanoparticles for Diagnostics: Advances towards Points of Care." *Diagnostics* 6 (4): 43. https://doi.org/10.3390/diagnostics6040043.

Cosgrove, Terence. (2010). *Colloid Science: Principles, Methods and Applications*. Edited by Terence Cosgrove. 2nd ed. John Wiley & Sons, 2010.

Creighton, J Alan, and Desmond G. Eadon. (1991). "Ultraviolet–visible Absorption Spectra of the Colloidal Metallic Elements." *J. Chem. Soc., Faraday Trans.* 87 (24): 3881–91. https://doi.org/10.1039/FT9918703881.

Crist, B. Vincent, and XPS International LLC. (1999). "PDF Handbooks of Monochromatic XPS Spectra - Volume 1: The Elements and Native Oxides." 1999. http://www.xpsdata.com/.

Crist, B. Vincent, and XPS International LLC. (2005). "PDF Handbooks of Monochromatic XPS Spectra - Volume 2: Commercially Pure Binary Oxides." 2005. http://www.xpsdata.com/.

Cuenya, Beatriz Roldan. (2010). "Synthesis and Catalytic Properties of Metal Nanoparticles: Size, Shape, Support, Composition, and Oxidation State Effects." *Thin Solid Films* 518 (12): 3127–50. https://doi.org/10.1016/j.tsf.2010.01.018.

Dahl, Jennifer A., Bettye L. S. Maddux, and James E. Hutchison. (2007). "Toward Greener Nanosynthesis." *Chemical Reviews* 107 (6): 2228–69. https://doi.org/10.1021/cr050943k.

Dankovich, Theresa A., and Derek G. Gray. (2011). "Bactericidal Paper Impregnated with Silver Nanoparticles for Point-of-Use Water Treatment." *Environmental Science & Technology* 45 (5): 1992–98. https://doi.org/10.1021/es103302t.

Das, Rasel, Md. Eaqub Ali, and Sharifah Bee Abd Hamid. (2014). "Current Applications of X-Ray Powder Diffraction - A Review." *Reviews on Advanced Materials Science* 38 (2): 95–109.

Dikonimos Makris, Th., R. Giorgi, N. Lisi, L. Pilloni, E. Salernitano, F. Sarto, and M. Alvisi. (2004). "Carbon Nanotubes Growth by HFCVD: Effect of the Process Parameters and Catalyst Preparation." *Diamond and Related Materials* 13 (2): 305–10. https://doi.org/10.1016/j.diamond.2003.10.013.

Dikovska, A. O., M. T. Alexandrov, G. B. Atanasova, N. T. Tsankov, and P. K. Stefanov. (2013). "Silver Nanoparticles Produced by PLD in Vacuum: Role of the Laser Wavelength Used." *Applied Physics A* 113 (1): 83–88. https://doi.org/10.1007/s00339-013-7834-9.

Dong, Xiao-Yun, Zi-Wei Gao, Ke-Fang Yang, Wei-Qiang Zhang, and Li-Wen Xu. (2015). "Nanosilver as a New Generation of Silver Catalysts in Organic Transformations for Efficient Synthesis of Fine Chemicals." *Catalysis Science & Technology* 5 (5): 2554–74. https://doi.org/10.1039/C5CY00285K.

Dorelon, A, M Lombardi, and J C Maan. (1982). "Electron Temperature Measurement of Cold Plasma in a Strong Magnetic Field." *Journal of Physics D: Applied Physics* 15 (4): 605–14. https://doi.org/10.1088/0022-3727/15/4/012.

Doria, Gonçalo, João Conde, Bruno Veigas, Leticia Giestas, Carina Almeida, Maria Assunção, João Rosa, and Pedro V. Baptista. (2012). "Noble Metal Nanoparticles for Biosensing Applications." *Sensors* 12 (2): 1657–87. https://doi.org/10.3390/s120201657.

Dung Dang, Thi My, Thi Thu Tuyet Le, Eric Fribourg-Blanc, and Mau Chien Dang. (2012). "Influence of Surfactant on the Preparation of Silver Nanoparticles by Polyol Method." *Advances in Natural Sciences: Nanoscience and Nanotechnology* 3 (3): 035004. https://doi.org/10.1088/2043-6262/3/3/035004.

Eatemadi, Ali, Hadis Daraee, Hamzeh Karimkhanloo, Mohammad Kouhi, Nosratollah Zarghami, Abolfazl Akbarzadeh, Mozhgan Abasi, Younes Hanifehpour, and Sang Joo. (2014). "Carbon Nanotubes: Properties, Synthesis, Purification, and Medical Applications." *Nanoscale Research Letters* 9 (1): 393. https://doi.org/10.1186/1556-276X-9-393.

Evanoff, David D., and George Chumanov. (2005). "Synthesis and Optical Properties of Silver Nanoparticles and Arrays." *ChemPhysChem* 6 (7): 1221–31. https://doi.org/10.1002/cphc.200500113.

Fang, Jinghua, Igor Levchenko, Zhao Han, Samuel Yick, and Kostya Ostrikov. (2014). "Carbon Nanotubes on Nanoporous Alumina: From Surface Mats to Conformal Pore Filling." *Nanoscale Research Letters* 9 (1): 390. https://doi.org/10.1186/1556-276X-9-390.

Feng, Xin, Wen Cui, Junbo Zhong, Xiaoying Liu, Fan Dong, and Yuxin Zhang. (2015). "Enhanced Visible Light Photocatalytic Activity of Br-Doped Bismuth Oxide Formate Nanosheets." *Molecules* 20 (10): 19189–202. https://doi.org/10.3390/molecules201019189.

Foster, John E. (2017). "Plasma-Based Water Purification: Challenges and Prospects for the Future." *Physics of Plasmas* 24 (5): 055501. https://doi.org/10.1063/1.4977921.

Fridman, A., A. Gutsol, and Y.I. Cho. (2007). "Non-Thermal Atmospheric Pressure Plasma." In , 1–142. https://doi.org/10.1016/S0065-2717(07)40001-6.

Fridman, A, A Chirokov, and A Gutsol. (2005). "Non-Thermal Atmospheric Pressure Discharges." *Journal of Physics D: Applied Physics* 38 (2): R1–24. https://doi.org/10.1088/0022-3727/38/2/R01.

Fujita, Hidemasa, Seiji Kanazawa, Kiyonobu Ohtani, Atsuki Komiya, Toshiro Kaneko, and Takehiko Sato. (2014). "Initiation Process and Propagation Mechanism of Positive Streamer Discharge in Water." *Journal of Applied Physics* 116 (21): 213301. https://doi.org/10.1063/1.4902862.

Gershman, S., O. Mozgina, A. Belkind, K. Becker, and E. Kunhardt. (2007). "Pulsed Electrical Discharge in Bubbled Water." *Contributions to Plasma Physics* 46 (1–2): 1–7. https://doi.org/10.1002/ctpp.200710004.

Gleiter, H. (2000). "Nanostructured Materials: Basic Concepts and Microstructure." *Acta Materialia* 48 (1): 1–29. https://doi.org/10.1016/S1359-6454(99)00285-2.

Gorbanev, Yury, Deborah O'Connell, and Victor Chechik. (2016). "Non-Thermal Plasma in Contact with Water: The Origin of Species." *Chemistry - A European Journal* 22 (10): 3496–3505. https://doi.org/10.1002/chem.201503771.

Graham, W G, and K R Stalder. (2011). "Plasmas in Liquids and Some of Their Applications in Nanoscience." *Journal of Physics D: Applied Physics* 44 (17): 174037.

https://doi.org/10.1088/0022-3727/44/17/174037.

Gual, Aitor, Cyril Godard, Sergio Castillón, and Carmen Claver. (2010). "Soluble Transition-Metal Nanoparticles-Catalysed Hydrogenation of Arenes." *Dalton Transactions* 39 (48): 11499. https://doi.org/10.1039/c0dt00584c.

Haertel, Beate, Thomas von Woedtke, Klaus-Dieter Weltmann, and Ulrike Lindequist. (2014). "Non-Thermal Atmospheric-Pressure Plasma Possible Application in Wound Healing." *Biomolecules & Therapeutics* 22 (6): 477–90. https://doi.org/10.4062/biomolther.2014.105.

Hafner, Bob. (2006). "Energy Dispersive Spectroscopy on the SEM: A Primer." *Characterization Facility, University of Minnesota*, 7–10. http://scholar.google.com/scholar?hl=en&btnG=Search&q=intitle:Energy+Dispersive+Spectroscopy+on+the+SEM+:#8.

Haruta, Masatake. (2004). "Gold as a Novel Catalyst in the 21st Century: Preparation, Working Mechanism and Applications." *Gold Bulletin* 37 (1–2): 27–36. https://doi.org/10.1007/BF03215514.

Hayashi, Yui, Noriharu Takada, Hideki Kanda, and Motonobu Goto. (2015). "Effect of Fine Bubbles on Electric Discharge in Water." *Plasma Sources Science and Technology* 24: 055023. https://doi.org/10.1088/0963-0252/24/5/055023.

Helmlinger, J., C. Sengstock, C. Groß-Heitfeld, C. Mayer, T. A. Schildhauer, M. Köller, and M. Epple. (2016). "Silver Nanoparticles with Different Size and Shape: Equal Cytotoxicity, but Different Antibacterial Effects." *RSC Advances* 6 (22): 18490–501. https://doi.org/10.1039/C5RA27836H.

Hieda, Junko, Nagahiro Saito, and Osamu Takai. (2008). "Exotic Shapes of Gold Nanoparticles Synthesized Using Plasma in Aqueous Solution." *Journal of Vacuum Science & Technology A: Vacuum, Surfaces, and Films* 26 (4): 854–56. https://doi.org/10.1116/1.2919139.

Hoffer, Ing Petr. (2014). "Shock Waves Generated by Corona - like Discharges in Water Doctoral Thesis," no. June.

Horikoshi, Satoshi, and Nick Serpone. (2013). "Introduction to Nanoparticles." In *Microwaves in Nanoparticle Synthesis*, edited by S. Horikoshi and N. Serpone, 1–24. Weinheim, Germany: Wiley-VCH Verlag GmbH & Co. KGaA. https://doi.org/10.1002/9783527648122.ch1.

Horoz, Sabit, Liyou Lu, Qilin Dai, Jiajun Chen, Baichhabi Yakami, J. M. Pikal, Wenyong Wang, and Jinke Tang. (2012). "CdSe Quantum Dots Synthesized by Laser Ablation in Water and Their Photovoltaic Applications." *Applied Physics Letters* 101 (22): 223902. https://doi.org/10.1063/1.4768706.

Hrabovský, Milan. (2002). "Generation of Thermal Plasmas in Liquid-Stabilized and Hybrid Dc-Arc Torches." *Pure and Applied Chemistry* 74 (3): 429–33. https://doi.org/10.1351/pac200274030429.

Hsu, Steve Lien-Chung, and Rong-Tarng Wu. (2011). "Preparation of Silver Nanoparticle with Different Particle Sizes for Low- Temperature Sintering." In *International Conference on*

Nanotechnology and Biosensors, 2:55–58.

Huang, X Z, X X Zhong, Y Lu, Y S Li, A E Rider, S A Furman, and K Ostrikov. (2013). "Plasmonic Ag Nanoparticles via Environment-Benign Atmospheric Microplasma Electrochemistry." *Nanotechnology* 24 (9): 1–8. https://doi.org/10.1088/0957-4484/24/9/095604.

Huang, Xunzhi, Yongsheng Li, and Xiaoxia Zhong. (2014). "Effect of Experimental Conditions on Size Control of Au Nanoparticles Synthesized by Atmospheric Microplasma Electrochemistry." *Nanoscale Research Letters* 9 (1): 572. https://doi.org/10.1186/1556-276X-9-572.

Hyning, Dirk L. Van, and Charles F. Zukoski. (1998). "Formation Mechanisms and Aggregation Behavior of Borohydride Reduced Silver Particles." *Langmuir* 14 (24): 7034–46. https://doi.org/10.1021/la980325h.

Inkson, B.J. (2016). "Scanning Electron Microscopy (SEM) and Transmission Electron Microscopy (TEM) for Materials Characterization." In *Materials Characterization Using Nondestructive Evaluation (NDE) Methods*, 17–43. Elsevier. https://doi.org/10.1016/B978-0-08-100040-3.00002-X.

Iowa State University. (2018). "Diffraction Basics." 2018. https://www.cif.iastate.edu/acide/xrd-tutorial/xrd.

ISO. (2015a). Nanotechnologies - Vocabulary - Part 1: Core terms. (Standard no. 80004-1:2015), issued 2015. https://www.iso.org/obp/ui/#iso:std:iso:ts:80004:-1:ed-2:v1:en.

ISO. 2015b. Nanotechnologies - Vocabulary - Part 2: Nano-objects. (Standard no. 80004-2:2015), issued 2015. https://www.iso.org/obp/ui/#iso:std:iso:ts:80004:-2:ed-1:v1:en.

Jiang, Zhong-Jie, Chun-Yan Liu, and Lu-Wei Sun. (2005). "Catalytic Properties of Silver Nanoparticles Supported on Silica Spheres." *The Journal of Physical Chemistry B* 109 (5): 1730–35. https://doi.org/10.1021/jp046032g.

Joshi, M., A. Bhattacharyya, and S. Wased Ali. (2008). "Characterization Techniques for Nanotechnology Applications in Textiles." *Indian Journal of Fibre & Textile Research* 33: 304–17.

Joshi, Ravindra P., Juergen F. Kolb, Shu Xiao, and Karl H. Schoenbach. (2009). "Aspects of Plasma in Water: Streamer Physics and Applications." *Plasma Processes and Polymers* 6 (11): 763–77. https://doi.org/10.1002/ppap.200900022.

Kang, Yongyin, Zhicheng Song, Xiaofang Jiang, Xia Yin, Long Fang, Jing Gao, Yehua Su, and Fei Zhao. (2017). "Quantum Dots for Wide Color Gamut Displays from Photoluminescence to Electroluminescence." *Nanoscale Research Letters* 12 (1): 154. https://doi.org/10.1186/s11671-017-1907-1.

Kaspar, Tiffany C., Tim Droubay, Scott A. Chambers, and Paul S. Bagus. (2010). "Spectroscopic Evidence for Ag(III) in Highly Oxidized Silver Films by X-Ray Photoelectron Spectroscopy." *The Journal of Physical Chemistry C* 114 (49): 21562–71.

https://doi.org/10.1021/jp107914e.

Katsuki, Sunao, Keiichi Tanaka, Taisuke Fudamoto, Takao Namihira, Hidenori Akiyama, and Hansjoachim Bluhm. (2006). "Shock Waves Due to Pulsed Streamer Discharges in Water." *Japanese Journal of Applied Physics* 45 (1A): 239–42. https://doi.org/10.1143/JJAP.45.239.

Kelly, J. M., G. Keegan, and M. E. Brennan-Fournet. (2012). "Triangular Silver Nanoparticles Their Preparation, Functionalisation and Properties.Pdf" 122 (2): 337–45. https://doi.org/10.12693/APhysPolA.122.337.

Kelly, K. Lance, Eduardo Coronado, Lin Lin Zhao, and George C. Schatz. (2003). "The Optical Properties of Metal Nanoparticles: The Influence of Size, Shape, and Dielectric Environment." *The Journal of Physical Chemistry B* 107 (3): 668–77. https://doi.org/10.1021/jp026731y.

Khaydarov, Rashid A., Renat R. Khaydarov, Olga Gapurova, Yuri Estrin, and Thomas Scheper. (2009). "Electrochemical Method for the Synthesis of Silver Nanoparticles." *Journal of Nanoparticle Research* 11 (5): 1193–1200. https://doi.org/10.1007/s11051-008-9513-x.

Kim, H. H., Y. Teramoto, T. Hirakawa, N. Negishi, and A. Ogata. (2013). "Microbubble Formation in Underwater Pulsed Streamer Discharge." *International Journal of Plasma Environmental Science and Technology* 7 (2): 109–14.

Kim, Hwan-Gi, Heon Lee, Sun-Jae Kim, Do-Heyoung Kim, Jung-Sik Kim, Sang-Yong Kang, and Sang-Chul Jung. (2013). "Synthesis of Manganese Nanoparticles in the Liquid Phase Plasma." *Journal of Nanoscience and Nanotechnology* 13 (9): 6103–8. https://doi.org/10.1166/jnn.2013.7681.

Kim, Hyun-Jin, Jun-Goo Shin, Choon-Sang Park, Dae Kum, Bhum Shin, Jae Kim, Hyung-Dal Park, Muhan Choi, and Heung-Sik Tae. (2018). "In-Liquid Plasma Process for Size- and Shape-Controlled Synthesis of Silver Nanoparticles by Controlling Gas Bubbles in Water." *Materials* 11 (6): 891. https://doi.org/10.3390/ma11060891.

Kim, Myungjoon, Saho Osone, Taesung Kim, Hidenori Higashi, and Takafumi Seto. (2017). "Synthesis of Nanoparticles by Laser Ablation: A Review." *KONA Powder and Particle Journal* 34: 80–90. https://doi.org/10.14356/kona.2017009.

Klett, Charles. (2011). "Etude de La Dégradation d'un Composé Organique Volatil Modèle, l'acétaldéhyde, Par Des Procédés Diphasiques Utilisant Des Techniques de Décharges Électriques Non-Thermiques à Pression Atmosphérique Couplées à Un Lit Fixe." Université Paris 13.

Koch, C. C. (2003). "Top-down Synthesis of Nanostructured Materials: Mechanical and Thermal Processing Methods." *Rev. Adv. Mater. Sci* 5 (2): 91–99.

Kocik, Marek, Miroslaw Dors, Janusz Podlinski, Jerzy Mizeraczyk, Seiji Kanazawa, Ryuta Ichiki, and Takehiko Sato. (2013). "Characterisation of Pulsed Discharge in Water." *The European Physical Journal Applied Physics* 64 (1): 10801. https://doi.org/10.1051/epjap/2013120426.

Koczkur, Kallum M., Stefanos Mourdikoudis, Lakshminarayana Polavarapu, and Sara E. Skrabalak. (2015). "Polyvinylpyrrolidone (PVP) in Nanoparticle Synthesis." *Dalton Transactions* 44 (41): 17883–905. https://doi.org/10.1039/C5DT02964C.

Kolb, J F, R P Joshi, S Xiao, and K H Schoenbach. (2008). "Streamers in Water and Other Dielectric Liquids." *Journal of Physics D: Applied Physics* 41 (23): 234007. https://doi.org/10.1088/0022-3727/41/23/234007.

Kondeti, V. S. Santosh K., Urvashi Gangal, Shurik Yatom, and Peter J. Bruggeman. (2017). "Ag + Reduction and Silver Nanoparticle Synthesis at the Plasma–liquid Interface by an RF Driven Atmospheric Pressure Plasma Jet: Mechanisms and the Effect of Surfactant." *Journal of Vacuum Science & Technology A: Vacuum, Surfaces, and Films* 35 (6): 061302. https://doi.org/10.1116/1.4995374.

Kora, Aruna Jyothi, R. Manjusha, and J. Arunachalam. (2009). "Superior Bactericidal Activity of SDS Capped Silver Nanoparticles: Synthesis and Characterization." *Materials Science and Engineering: C* 29 (7): 2104–9. https://doi.org/10.1016/j.msec.2009.04.010.

Kozáková, Zdenka. (2011). "Electric Discharges in Water Solutions." Brno University of Technology.

Kujda, M., M. OćWieja, Z. Adamczyk, O. BocheńSka, G. Braś, A. Kozik, E. BielańSka, and J. Barbasz. (2015). "Charge Stabilized Silver Nanoparticles Applied as Antibacterial Agents." *Journal of Nanoscience and Nanotechnology* 15 (5): 3574–83. https://doi.org/10.1166/jnn.2015.9727.

Kundu, Niloy, Devdeep Mukherjee, Tapas Kumar Maiti, and Nilmoni Sarkar. (2017). "Protein-Guided Formation of Silver Nanoclusters and Their Assembly with Graphene Oxide as an Improved Bioimaging Agent with Reduced Toxicity." *The Journal of Physical Chemistry Letters* 8 (10): 2291–97. https://doi.org/10.1021/acs.jpclett.7b00600.

Kupper, Martin. (2012). "Very Sharp Platinum Tips by Electrochemical Etching." Graz University of Technology.

Kvítek, Libor, Aleš Panáček, Jana Soukupová, Milan Kolář, Renata Večeřová, Robert Prucek, Mirka Holecová, and Radek Zbořil. (2008). "Effect of Surfactants and Polymers on Stability and Antibacterial Activity of Silver Nanoparticles (NPs)." *The Journal of Physical Chemistry C* 112 (15): 5825–34. https://doi.org/10.1021/jp711616v.

LaMer, Victor K., and Robert H. Dinegar. (1950). "Theory, Production and Mechanism of Formation of Monodispersed Hydrosols." *Journal of the American Chemical Society* 72 (11): 4847–54. https://doi.org/10.1021/ja01167a001.

Langley, Daniel, Gaël Giusti, Céline Mayousse, Caroline Celle, Daniel Bellet, and Jean-Pierre Simonato. (2013). "Flexible Transparent Conductive Materials Based on Silver Nanowire Networks: A Review." *Nanotechnology* 24 (45): 452001. https://doi.org/10.1088/0957-4484/24/45/452001.

Lee, Heon, Sung Hoon Park, Sang-Chul Jung, Je-Jung Yun, Sun-Jae Kim, and Do-Heyoung

Kim. (2013). “Preparation of Nonaggregated Silver Nanoparticles by the Liquid Phase Plasma Reduction Method.” *Journal of Materials Research* 28 (08): 1105–10. https://doi.org/10.1557/jmr.2013.59.

Lee, Heon, Sung Hoon Park, Sun-Jae Kim, Young-Kwon Park, Kay-Hyeok An, Byung-Joo Kim, and Sang-Chul Jung. (2014). “Liquid Phase Plasma Synthesis of Iron Oxide/Carbon Composite as Dielectric Material for Capacitor” 2014: 1–6. https://doi.org/10.1155/2014/132032.

Lee, Heon, Sung Hoon Park, Seong-Gyu Seo, Sun-Jae Kim, Sang-Chai Kim, Young-Kwon Park, and Sang-Chul Jung. (2014). “Preparation and Characterization of Copper Nanoparticles via the Liquid Phase Plasma Method.” *Current Nanoscience* 10 (1): 7–10. https://doi.org/10.2174/15734137096661311112217 41.

Lee, Hoonseung, Tomonaga Ueno, and Nagahiro Saito. (2015). “The Effect of Electrode Gap Distance on the Synthesis of Carbon Materials by Using Solution Plasma Process.” *JOM* 67 (11): 2550–56. https://doi.org/10.1007/s11837-015-1660-9.

Lee, Jong-Min, Yong-Geun Lee, Dae-Wook Kim, Chul Oh, Sang-Man Koo, and Seong-Geun Oh. (2007). “Facile and Novel Route for Preparation of Silica/Silver Heterogeneous Composite Particles with Hollow Structure.” *Colloids and Surfaces A: Physicochemical and Engineering Aspects* 301 (1–3): 48–54. https://doi.org/10.1016/j.colsurfa.2006.12.020.

Lee, P. C., and D. Meisel. (1982). “Adsorption and Surface-Enhanced Raman of Dyes on Silver and Gold Sols.” *The Journal of Physical Chemistry* 86 (17): 3391–95. https://doi.org/10.1021/j100214a025.

Lehman, John H., Rohit Deshpande, Paul Rice, Bobby To, and Anne C. Dillon. (2006). “Carbon Multi-Walled Nanotubes Grown by HWCVD on a Pyroelectric Detector.” *Infrared Physics & Technology* 47 (3): 246–50. https://doi.org/10.1016/j.infrared.2004.12.004.

Levko, Dmitry, Ashish Sharma, and Laxminarayan L Raja. (2016). “Plasmas Generated in Bubbles Immersed in Liquids: Direct Current Streamers versus Microwave Plasma.” *Journal of Physics D: Applied Physics* 49 (28): 285205. https://doi.org/10.1088/0022-3727/49/28/285205.

Li, O. L., J. Kang, K. Urashima, and N. Saito. (2013). “Solution Plasma Synthesis Process of Carbon Nano Particles in Organic Solutions.” *International Journal of Plasma Environmental Science & Technology* 7 (1): 31–36.

Li, Xuan, and John J. Lenhart. (2012). “Aggregation and Dissolution of Silver Nanoparticles in Natural Surface Water.” *Environmental Science & Technology* 46 (10): 5378–86. https://doi.org/10.1021/es204531y.

Li, Xuechen, Panpan Zhang, Pengying Jia, Jingdi Chu, and Junying Chen. (2017). “Generation of a Planar Direct-Current Glow Discharge in Atmospheric Pressure Air Using Rod Array Electrode.” *Scientific Reports* 7 (1): 2672. https://doi.org/10.1038/s41598-017-03007-1.

Lisitsyn, I.V., H. Nomlyama, S. Katsuki, and H. Akiyama. (1999). “Thermal Processes in a

Streamer Discharge in Water." *IEEE Transactions on Dielectrics and Electrical Insulation* 6 (3): 351–56.

Liu, Chang, Feng Li, Lai-Peng Ma, and Hui-Ming Cheng. (2010). "Advanced Materials for Energy Storage." *Advanced Materials* 22 (8): E28–62. https://doi.org/10.1002/adma.200903328.

Liu, Hongjun, Wei-Peng Goh, Man-Yin Leung, Yuning Li, and Tyler B. Norsten. (2012). "Effect of Nanoparticle Stabilizing Ligands and Ligand-Capped Gold Nanoparticles in Polymer Solar Cells." *Solar Energy Materials and Solar Cells* 96 (January): 302–6. https://doi.org/10.1016/j.solmat.2011.09.056.

Liu, Jia, Lingling Xu, Bo Wei, Wei Lv, Hong Gao, and Xitian Zhang. (2011). "One-Step Hydrothermal Synthesis and Optical Properties of Aluminium Doped ZnO Hexagonal Nanoplates on a Zinc Substrate." *CrystEngComm* 13 (5): 1283–86. https://doi.org/10.1039/C0CE00704H.

Liu, Jun, Changhao Liang, Zhenfei Tian, Shuyuan Zhang, and Guosheng Shao. (2013). "Spontaneous Growth and Chemical Reduction Ability of Ge Nanoparticles." *Scientific Reports* 3 (1): 1741. https://doi.org/10.1038/srep01741.

Liu, Peisheng, Zhigang Li, Weiping Cai, Ming Fang, and Xiangdong Luo. (2011). "Fabrication of Cuprous Oxide Nanoparticles by Laser Ablation in PVP Aqueous Solution." *RSC Advances* 1 (5): 847. https://doi.org/10.1039/c1ra00261a.

Locke, B. R., M. Sato, P. Sunka, M. R. Hoffmann, and J.-S. Chang. (2006). "Electrohydraulic Discharge and Nonthermal Plasma for Water Treatment." *Industrial & Engineering Chemistry Research* 45 (3): 882–905. https://doi.org/10.1021/ie050981u.

Locke, Bruce R. (2012). "Environmental Applications of Electrical Discharge Plasma with Liquid Water - A Mini Review." *International Journal of Plasma Environmental Science & Technology* 6 (3): 194–203.

LPP. (2018). "Classification of Natural and Laboratory Plasmas." 2018. https://www.lpp.polytechnique.fr/Our-research-in-a-few-words?lang=en.

Lu, Haijiao, Jingkang Wang, Marco Stoller, Ting Wang, Ying Bao, and Hongxun Hao. (2016). "An Overview of Nanomaterials for Water and Wastewater Treatment." *Advances in Materials Science and Engineering* 2016: 1–10. https://doi.org/10.1155/2016/4964828.

Lukes, Petr. (2001). "Water Treatment by Pulsed Streamer Corona Discharge." Institute of Plasma Physics.

Lukes, Petr, Martin Clupek, Vaclav Babicky, and Pavel Sunka. (2008). "Ultraviolet Radiation from the Pulsed Corona Discharge in Water." *Plasma Sources Science and Technology* 17 (2): 024012. https://doi.org/10.1088/0963-0252/17/2/024012.

Lutterotti, Luca. (2010). "Total Pattern Fitting for the Combined Size–strain–stress–texture Determination in Thin Film Diffraction." *Nuclear Instruments and Methods in Physics Research Section B: Beam Interactions with Materials and Atoms* 268 (3–4): 334–40.

https://doi.org/10.1016/j.nimb.2009.09.053.

Mailer, Alastair G, Paul S Clegg, and Peter N Pusey. (2015). "Particle Sizing by Dynamic Light Scattering: Non-Linear Cumulant Analysis." *Journal of Physics. Condensed Matter : An Institute of Physics Journal* 27 (14): 145102. https://doi.org/10.1088/0953-8984/27/14/145102.

Malina, Dagmara, Agnieszka Sobczak-Kupiec, Zbigniew Wzorek, and Zygmunt Kowalski. (2012). "Silver Nanoparticles Synthesis With Different Concentrations of Polyvinylpyrrolidone." *Digest Journal of Nanomaterials and Biostructures* 7 (4): 1527–34.

Malvern. (2014). "Dynamic Light Scattering: An Introduction in 30 Min." https://warwick.ac.uk/fac/cross_fac/sciencecity/programmes/internal/themes/am2/booking/particlesize/intro_to_dls.pdf.

Malvern Instruments Ltd. (2018). "Zetasizer NANO Series: Performance, Simplicity, Versatility."

Manawi, Yehia, Ihsanullah, Ayman Samara, Tareq Al-Ansari, and Muataz Atieh. (2018). "A Review of Carbon Nanomaterials' Synthesis via the Chemical Vapor Deposition (CVD) Method." *Materials* 11 (5): 822. https://doi.org/10.3390/ma11050822.

Maretti, Luca, Paul S. Billone, Yun Liu, and Juan C. Scaiano. (2009). "Facile Photochemical Synthesis and Characterization of Highly Fluorescent Silver Nanoparticles." *Journal of the American Chemical Society* 131 (39): 13972–80. https://doi.org/10.1021/ja900201k.

Marinov, I, O Guaitella, A Rousseau, and S M Starikovskaia. (2013). "Modes of Underwater Discharge Propagation in a Series of Nanosecond Successive Pulses." *Journal of Physics D: Applied Physics* 46 (46): 464013. https://doi.org/10.1088/0022-3727/46/46/464013.

Mariotti, Davide, A.C. Bose, and K. Ostrikov. (2009). "Atmospheric-Microplasma-Assisted Nanofabrication: Metal and Metal–Oxide Nanostructures and Nanoarchitectures." *IEEE Transactions on Plasma Science* 37 (6): 1027–33. https://doi.org/10.1109/TPS.2009.2014067.

Mariotti, Davide, Jenis Patel, Vladimir Švrček, and Paul Maguire. (2012). "Plasma-Liquid Interactions at Atmospheric Pressure for Nanomaterials Synthesis and Surface Engineering." *Plasma Processes and Polymers* 9 (11–12): 1074–85. https://doi.org/10.1002/ppap.201200007.

Medix. (2016). "Solutions Colloïdales : Toute Solution Liquide'' N'est Pas Forcément Colloïdale''." 2016. https://medix.fr/solutions-colloidales/.

Meireles, M., F. Bourgeois, M. Tourbin, P. Guiraud, and C. Frances. (2010). "Review: Removal of Oversize Recovery of Particles from Suspensions in the Nano Size Range." *HAL*. https://hal.archives-ouvertes.fr/hal-01186033.

Miller, R. B. (1982). *An Introduction to the Physics of Intense Charged Particle Beams*.

Millstone, Jill E., Sarah J. Hurst, Gabriella S. Métraux, Joshua I. Cutler, and Chad A. Mirkin.

(2009). “Colloidal Gold and Silver Triangular Nanoprisms.” *Small* 5 (6): 646–64.

Mizuno, Tadahiko, Tadayoshi Ohmori, Tadashi Akimoto, and Akito Takahashi. (2000). “Production of Heat during Plasma Electrolysis in Liquid.” *Japanese Journal of Applied Physics, Part 1: Regular Papers and Short Notes and Review Papers* 39 (10): 6055–61. https://doi.org/10.1143/JJAP.39.6055.

Mørup, Steen, Cathrine Frandsen, and Mikkel F. Hansen. (2017). “Magnetic Properties of Nanoparticles.” In *Oxford Handbook of Nanoscience and Technology*, edited by A.V. Narlikar and Y.Y. Fu, 2:713–44. Oxford University Press. https://doi.org/10.1093/oxfordhb/9780199533053.013.20.

Moulder, John F., William F. Stickle, Peter E. Sobol, and Kenneth D. Bomben. (1992). *Handbook of X-Ray Spectroscopy*. Edited by Jill Chastain. Perkin-Elmer Corporation.

Mun, Mu Kyeom, Won Oh Lee, Jin Woo Park, Doo San Kim, Geun Young Yeom, and Dong Woo Kim. (2017). “Nanoparticles Synthesis and Modification Using Solution Plasma Process.” *Applied Science and Convergence Technology* 26 (6): 164–73. https://doi.org/10.5757/ASCT.2017.26.6.164.

Namihira, T., T. Yamaguchi, K. Yamamoto, J. Choi, T. Kiyan, T. Sakugawa, S. Katsuki, and H. Akiyama. (2007). “Characteristics of Pulsed Discharge Plasma in Water.” *Digest of Technical Papers-IEEE International Pulsed Power Conference*, no. JULY: 1013–16. https://doi.org/10.1109/PPC.2005.300473.

nanoComposix. (2018). “Gold Colloid.” 2018. https://nanocomposix.com/pages/gold-colloid.

Nijdam, Sander, Eddie van Veldhuizen, Peter Bruggeman, Ute Ebert, Eddie Van Veldhuizen, Peter Bruggeman, and Ute Ebert. (2012). “An Introduction to Nonequilibrium Plasmas at Atmospheric Pressure.” In *Plasma Chemistry and Catalysis in Gases and Liquids*, edited by Vasile I. Parvulescu, Monica Magureanu, and Petr Lukes, 1–44. Weinheim, Germany: Wiley-VCH Verlag GmbH & Co. KGaA. https://doi.org/10.1002/9783527649525.ch1.

Nikov, Rumen G, Anna Og Dikovska, Nikolay N Nedyalkov, Georgi V Avdeev, and Petar A Atanasov. (2017). “Au Nanostructure Fabrication by Pulsed Laser Deposition in Open Air: Influence of the Deposition Geometry.” *Beilstein Journal of Nanotechnology* 8 (November): 2438–45. https://doi.org/10.3762/bjnano.8.242.

NIST. (2019a). “Solution Kinetics Database Resources.” 2019. https://kinetics.nist.gov/solution/Detail?id=1965BAX/FIE207-216B:1.

NIST. (2019b). “Solution Kinetics Database Resources.” 2019. https://kinetics.nist.gov/solution/Detail?id=1988BUX/GRE513-886:54.

Odularu, Ayodele Temidayo. (2018). “Metal Nanoparticles: Thermal Decomposition, Biomedicinal Applications to Cancer Treatment, and Future Perspectives.” *Bioinorganic Chemistry and Applications* 2018: 1–6. https://doi.org/10.1155/2018/9354708.

Oost, G Van. (2017). “Plasma for Environment.” *Journal of Physics: Conference Series* 941 (December). https://doi.org/10.1088/1742-6596/941/1/012014.

Pacioni, N. L., C. D. Borsarelli, V. Rey, and A. V. Veglia. (2015). "Synthetic Routes for the Preparation of Silver Nanoparticles." In *Silver Nanoparticle Applications*, edited by E. I. Alarcon, M. Griffith, and K. I. Udekwu, 13–46. https://doi.org/10.1007/978-3-319-11262-6_2.

Paliwal, Rishi, R. Jayachandra Babu, and Srinath Palakurthi. (2014). "Nanomedicine Scale-up Technologies: Feasibilities and Challenges." *AAPS PharmSciTech* 15 (6): 1527–34. https://doi.org/10.1208/s12249-014-0177-9.

Park, Keum Hwan, Sang Hyuk Im, and O Ok Park. (2011). "The Size Control of Silver Nanocrystals with Different Polyols and Its Application to Low-Reflection Coating Materials." *Nanotechnology* 22 (4): 045602. https://doi.org/10.1088/0957-4484/22/4/045602.

Patel, J, L Němcová, P Maguire, W G Graham, and D Mariotti. (2013). "Synthesis of Surfactant-Free Electrostatically Stabilized Gold Nanoparticles by Plasma-Induced Liquid Chemistry." *Nanotechnology* 24 (24): 245604. https://doi.org/10.1088/0957-4484/24/24/245604.

Peiris, Sunari, John McMurtrie, and Huai-Yong Zhu. (2016). "Metal Nanoparticle Photocatalysts: Emerging Processes for Green Organic Synthesis." *Catalysis Science & Technology* 6 (2): 320–38. https://doi.org/10.1039/C5CY02048D.

Pokropivny, V.V., and V.V. Skorokhod. (2007). "Classification of Nanostructures by Dimensionality and Concept of Surface Forms Engineering in Nanomaterial Science." *Materials Science and Engineering: C* 27 (5–8): 990–93. https://doi.org/10.1016/j.msec.2006.09.023.

Polte, J., X. Tuaev, M. Wuithschick, A. Fischer, A.F. Thuenemann, K. Rademann, R. Kraehnert, and F. Emmerling. (2012). "Formation Mechanism of Colloidal Silver Nanoparticles: Analogies and Differences to the Growth of Gold Nanoparticles." *ACS Nano* 7 (7): 5791–5802. https://doi.org/10.1021/nn301724z.

Polte, Jörg. (2015). "Fundamental Growth Principles of Colloidal Metal Nanoparticles – a New Perspective." *Cryst Eng Comm* 17 (36): 6809–30. https://doi.org/10.1039/C5CE01014D.

Pootawang, Panuphong. (2011). "Solution Plasma Synthesis and Characteristic for Mesoporous Silica and Metal Nanoparticles System."

Pootawang, Panuphong, Nagahiro Saito, and Sang Yul Lee. (2013). "Discharge Time Dependence of a Solution Plasma Process for Colloidal Copper Nanoparticle Synthesis and Particle Characteristics." *Nanotechnology* 24 (5): 055604. https://doi.org/10.1088/0957-4484/24/5/055604.

Prasad, Karthika, Chaturanga Bandara, Shailesh Kumar, Gurinder Singh, Bastian Brockhoff, Kateryna Bazaka, and Kostya Ostrikov. (2017). "Effect of Precursor on Antifouling Efficacy of Vertically-Oriented Graphene Nanosheets." *Nanomaterials* 7 (7): 170. https://doi.org/10.3390/nano7070170.

Pulit-Prociak, Jolanta, and Marcin Banach. (2016). "Silver Nanoparticles – a Material of the

Future…?" *Open Chemistry*, no. 14 (January): 76–91. https://doi.org/10.1515/chem-2016-0005.

Radoń, Adrian, Dariusz Łukowiec, Marek Kremzer, Jarosław Mikuła, and Patryk Włodarczyk. (2018). "Electrical Conduction Mechanism and Dielectric Properties of Spherical Shaped Fe3O4 Nanoparticles Synthesized by Co-Precipitation Method." *Materials* 11 (5): 1–12. https://doi.org/10.3390/ma11050735.

Ravi, M., S. Bhavani, K. Kiran Kumar, and V.V.R. Narasimaha Rao. (2013). "Investigations on Electrical Properties of PVP:KIO4 Polymer Electrolyte Films." *Solid State Sciences* 19 (May): 85–93. https://doi.org/10.1016/j.solidstatesciences.2013.02.006.

Redolfi, Michaël. (2007). "Etude de l' Oxydation de Différents Types d'hydrocarbures Par Des Procédés Utilisant Des Techniques de Déharges Électriques Non- Thermiques à Pression Atmosphérique: Application à La Problématique Du Démarrage à Froid." Université Paris 13.

Reiss, Howard. (1951). "The Growth of Uniform Colloidal Dispersions." *The Journal of Chemical Physics* 19 (4): 482–87. https://doi.org/10.1063/1.1748251.

Richmonds, Carolyn, and R. Mohan Sankaran. (2008). "Plasma-Liquid Electrochemistry: Rapid Synthesis of Colloidal Metal Nanoparticles by Microplasma Reduction of Aqueous Cations." *Applied Physics Letters* 93 (13): 131501. https://doi.org/10.1063/1.2988283.

Rivera, V.A.G., F.A. Ferri, and E. Marega. (2012). "Localized Surface Plasmon Resonances: Noble Metal Nanoparticle Interaction with Rare-Earth Ions." In *Plasmonics - Principles and Applications*, 283–312. InTech. https://doi.org/10.5772/50753.

Robertson, James D., Loris Rizzello, Milagros Avila-Olias, Jens Gaitzsch, Claudia Contini, Monika S. MagoÅ, Stephen A. Renshaw, and Giuseppe Battaglia. (2016). "Purification of Nanoparticles by Size and Shape." *Scientific Reports* 6: 1–9. https://doi.org/10.1038/srep27494.

Rodríguez-Sánchez, L., M. C. Blanco, and M. A. López-Quintela. (2000). "Electrochemical Synthesis of Silver Nanoparticles." *The Journal of Physical Chemistry B* 104 (41): 9683–88. https://doi.org/10.1021/jp001761r.

Roduner, Emil. (2006). "Size Matters: Why Nanomaterials Are Different." *Chemical Society Reviews* 35 (7): 583. https://doi.org/10.1039/b502142c.

Roldán, M. Virginia, Nora Pellegri, and Oscar de Sanctis. (2013). "Electrochemical Method for Ag-PEG Nanoparticles Synthesis." *Journal of Nanoparticles* 2013: 1–7. https://doi.org/10.1155/2013/524150.

Rond, C., J. M. Desse, N. Fagnon, X. Aubert, M. Er, A. Vega, and X. Duten. (2018). "Time-Resolved Diagnostics of a Pin-to-Pin Pulsed Discharge in Water: Pre-Breakdown and Breakdown Analysis." *Journal of Physics D: Applied Physics* 51 (33): 1–9. https://doi.org/10.1088/1361-6463/aad175.

Ruma, P Lukes, N Aoki, E Spetlikova, S H R Hosseini, T Sakugawa, and H Akiyama. (2013).

"Effects of Pulse Frequency of Input Power on the Physical and Chemical Properties of Pulsed Streamer Discharge Plasmas in Water." *Journal of Physics D: Applied Physics* 46 (12): 125202. https://doi.org/10.1088/0022-3727/46/12/125202.

Rumbach, Paul, Megan Witzke, R. Mohan Sankaran, and David B. Go. (2013). "Decoupling Interfacial Reactions between Plasmas and Liquids: Charge Transfer vs Plasma Neutral Reactions." *Journal of the American Chemical Society* 135 (44): 16264–67. https://doi.org/10.1021/ja407149y.

Saito, Nagahiro, Junko Hieda, and Osamu Takai. (2009). "Synthesis Process of Gold Nanoparticles in Solution Plasma." *Thin Solid Films* 518 (3): 912–17. https://doi.org/10.1016/j.tsf.2009.07.156.

Sakiyama, Yukinori, David B Graves, Hung-Wen Chang, Tetsuji Shimizu, and Gregor E Morfill. (2012). "Plasma Chemistry Model of Surface Microdischarge in Humid Air and Dynamics of Reactive Neutral Species." *Journal of Physics D: Applied Physics* 45 (42): 425201. https://doi.org/10.1088/0022-3727/45/42/425201.

Saleh, Tawfik Abdo, and Vinod Kumar Gupta. (2016). "Synthesis, Classification, and Properties of Nanomaterials." In *Nanomaterial and Polymer Membranes*, 83–133. Elsevier. https://doi.org/10.1016/B978-0-12-804703-3.00004-8.

Serway, Raymond A., and John W. Jewett. (2003). "Linear Momentum and Collisions." In *Physics for Scientists and Engineers*, 6th ed., 251–91. Thomson Brooks/Cole.

Shabbeer, Hafiza, Asad Khan, Afzal Shah, Zia Ur Rehman, Syed Mujtaba Shah, Athar Khan, and Syed Sakhawat Shah. (2012). "Effect of Acidic and Basic Conditions on the Plasmon Band of Colloidal Silver." *Walailak Journal of Science and Technology* 9 (3): 229–37.

Shi, Jingyu. (2002). "Steric Stabilization."

Shin, Hyeon Suk, Hyun Jung Yang, Seung Bin Kim, and Mu Sang Lee. (2004). "Mechanism of Growth of Colloidal Silver Nanoparticles Stabilized by Polyvinyl Pyrrolidone in γ-Irradiated Silver Nitrate Solution." *Journal of Colloid and Interface Science* 274 (1): 89–94. https://doi.org/10.1016/j.jcis.2004.02.084.

Shrivastava, Siddhartha, Tanmay Bera, Arnab Roy, Gajendra Singh, P Ramachandrarao, and Debabrata Dash. (2007). "Characterization of Enhanced Antibacterial Effects of Novel Silver Nanoparticles." *Nanotechnology* 18 (22): 225103. https://doi.org/10.1088/0957-4484/18/22/225103.

Sigma-Aldrich. (2018). "Quantum Dots." 2018. https://www.sigmaaldrich.com/technical-documents/articles/materials-science/nanomaterials/quantum-dots.html.

Singh, Ashok K. (2016). "Introduction to Nanoparticles and Nanotoxicology." In *Engineered Nanoparticles*, 1–18. Elsevier. https://doi.org/10.1016/B978-0-12-801406-6.00001-7.

Skiba, Margarita, Alexander Pivovarov, Anna Makarova, Oleksandr Pasenko, Aleksey Khlopytskyi, and Viktoria Vorobyova. (2017). "Plasma-Chemical Formation of Silver Nanodispersion in Water Solutions." *Eastern-European Journal of Enterprise Technologies*

6 (6 (90)): 59–65. https://doi.org/10.15587/1729-4061.2017.118914.

Skiba, Margarita, Alexander Pivovarov, Anna Makarova, and Viktoria Vorobyova. (2018). "Plasmochemical Preparation of Silver Nanoparticles: Thermodynamics and Kinetics Analysis of the Process." *Eastern-European Journal of Enterprise Technologies* 2 (6 (92)): 4–9. https://doi.org/10.15587/1729-4061.2018.127103.

Sommers, B S, and J E Foster. (2014). "Plasma Formation in Underwater Gas Bubbles." *Plasma Sources Science and Technology* 23 (1): 015020. https://doi.org/10.1088/0963-0252/23/1/015020.

Soroushian, Behrouz, Isabelle Lampre, Jacqueline Belloni, and Mehran Mostafavi. (2005). "Radiolysis of Silver Ion Solutions in Ethylene Glycol: Solvated Electron and Radical Scavenging Yields." *Radiation Physics and Chemistry* 72 (2–3): 111–18. https://doi.org/10.1016/j.radphyschem.2004.02.009.

Su, Shei Sia, and Isaac Chang. (2018). "Review of Production Routes of Nanomaterials." In *Commercialization of Nanotechnologies–A Case Study Approach*, 15–29. Cham: Springer International Publishing. https://doi.org/10.1007/978-3-319-56979-6_2.

Subba Reddy, Ch.V., Xia Han, Quan-Yao Zhu, Li-Qiang Mai, and Wen Chen. (2006). "Dielectric Spectroscopy Studies on (PVP+PVA) Polyblend Film." *Microelectronic Engineering* 83 (2): 281–85. https://doi.org/10.1016/j.mee.2005.08.010.

Sugimoto, Tadao. (1987). "Preparation of Monodispersed Colloidal Particles." *Advances in Colloid and Interface Science* 28: 65–108. https://doi.org/10.1016/0001-8686(87)80009-X.

Sun, Yugang, and Younan Xia. (2002). "Shape-Controlled Synthesis of Gold and Silver Nanoparticles." *Science* 298 (5601): 2176–79.

Sunka, P, V Babický, M Clupek, P Lukes, M Simek, J Schmidt, and M Cernák. (1999). "Generation of Chemically Active Species by Electrical Discharges in Water." *Plasma Sources Science and Technology* 8 (2): 258–65. https://doi.org/10.1088/0963-0252/8/2/006.

Šunka, Pavel. (2001). "Pulse Electrical Discharges in Water and Their Applications." *Physics of Plasmas* 8 (5): 2587–94. https://doi.org/10.1063/1.1356742.

Surudzic, Rade, Zeljka Jovanovic, Natasa Bibic, Branislav Nikolic, and Vesna Miskovic-Stankovic. (2013). "Electrochemical Synthesis of Silver Nanoparticles in Poly(Vinyl Alcohol) Solution." *Journal of the Serbian Chemical Society* 78 (12): 2087–98. https://doi.org/10.2298/JSC131017124S.

Takai, Osamu. (2008). "Solution Plasma Processing (SPP)." *Pure and Applied Chemistry* 80 (9): 2003–11. https://doi.org/10.1351/pac200880092003.

Takai, Osamu. (2014). "Fundamentals and Applications of Solution Plasma." *Journal of Photopolymer Science and Technology* 27 (3): 379–84. https://doi.org/10.2494/photopolymer.27.379.

Takamatsu, Toshihiro, Kodai Uehara, Yota Sasaki, Hidekazu Miyahara, Yuriko Matsumura,

Atsuo Iwasawa, Norihiko Ito, Takeshi Azuma, Masahiro Kohno, and Akitoshi Okino. (2014). "Investigation of Reactive Species Using Various Gas Plasmas." *RSC Adv.* 4 (75): 39901–5. https://doi.org/10.1039/C4RA05936K.

Tang, Shaochun, Xiangkang Meng, Hongbin Lu, and Shaopeng Zhu. (2009). "PVP-Assisted Sonoelectrochemical Growth of Silver Nanostructures with Various Shapes." *Materials Chemistry and Physics* 116 (2–3): 464–68. https://doi.org/10.1016/j.matchemphys.2009.04.004.

Teng, Fei, Li Wang, and Yongfa Zhu. (2008). "Porous Nanoballs Formed through an in Situ Generated 'Framework' Template." *Colloids and Surfaces A: Physicochemical and Engineering Aspects* 312 (1): 39–46. https://doi.org/10.1016/j.colsurfa.2007.06.021.

Terashima, Chiaki, Yujiro Iwai, Sung Pyo Cho, Tomonaga Ueno, Nobuyuki Zettsu, Nagahiro Saito, and Osamu Takai. (2013). "Solution Plasma Sputtering Processes for the Synthesis of PtAu/C Catalysts for Li-Air Batteries." *International Journal of Electrochemical Science* 8 (4): 5407–20.

Thanh, Nguyen T. K., N. Maclean, and S. Mahiddine. (2014). "Mechanisms of Nucleation and Growth of Nanoparticles in Solution." *Chemical Reviews* 114 (15): 7610–30. https://doi.org/10.1021/cr400544s.

Thermo Scientific. (2018). "Learn XPS - Analysis of Surfaces and Thin Films." 2018. https://xpssimplified.com/whatisxps.php.

Tien, Der-Chi, Liang-Chia Chen, Nguyen Van Thai, and Sana Ashraf. (2010). "Study of Ag and Au Nanoparticles Synthesized by Arc Discharge in Deionized Water." *Journal of Nanomaterials* 2010: 1–9. https://doi.org/10.1155/2010/634757.

Tiwari, Jitendra N., Rajanish N. Tiwari, and Kwang S. Kim. (2012). "Zero-Dimensional, One-Dimensional, Two-Dimensional and Three-Dimensional Nanostructured Materials for Advanced Electrochemical Energy Devices." *Progress in Materials Science* 57 (4): 724–803. https://doi.org/10.1016/j.pmatsci.2011.08.003.

Tomaszewska, Emilia, Katarzyna Soliwoda, Kinga Kadziola, Beata Tkacz-Szczesna, Grzegorz Celichowski, Michal Cichomski, Witold Szmaja, and Jaroslaw Grobelny. (2013). "Detection Limits of DLS and UV-Vis Spectroscopy in Characterization of Polydisperse Nanoparticles Colloids." *Journal of Nanomaterials* 2013: 1–10. https://doi.org/10.1155/2013/313081.

Trinh, Dung Chinh, Thi My Dung Dang, Kim Khanh Huynh, Eric Fribourg-Blanc, and Mau Chien Dang. (2015). "Synthesis of Cu Core Ag Shell Nanoparticles Using Chemical Reduction Method." *Advances in Natural Sciences: Nanoscience and Nanotechnology* 6 (2): 025018. https://doi.org/10.1088/2043-6262/6/2/025018.

Tsuzuki, Takuya. (2009). "Commercial Scale Production of Inorganic Nanoparticles." *International Journal of Nanotechnology* 6 (5/6): 567–78. https://doi.org/10.1504/IJNT.2009.024647.

Turkevich, John, Peter Cooper Stevenson, and James Hillier. (1951). "A Study of the Nucleation and Growth Processes in the Synthesis of Colloidal Gold." *Discussions of the Faraday Society* 11: 55. https://doi.org/10.1039/df9511100055.

Veldhuizen, E. M. Vvn, and W. R. Rutgers. (2001). "Corona Discharges: Fundamentals and Diagnostics." In *Frontiers in Low Temperature Plasma Diagnostics IV*, 40–49. http://www.researchgate.net/publication/242454280_Corona_discharges_fundamentals_and_diagnostics/file/5046352cfd3c1cabdc.pdf.

Venugopal, Gunasekaran, and Sang-Jae Kim. (2013). "Nanolithography." In *Advances in Micro/Nano Electromechanical Systems and Fabrication Technologies*. InTech. https://doi.org/10.5772/55527.

Verwey, E. J. W. (1947). "Theory of the Stability of Lyophobic Colloids." *The Journal of Physical and Colloid Chemistry* 51 (3): 631–36. https://doi.org/10.1021/j150453a001.

Wang, Hongshui, Xueliang Qiao, Jianguo Chen, Xiaojian Wang, and Shiyuan Ding. (2005). "Mechanisms of PVP in the Preparation of Silver Nanoparticles." *Materials Chemistry and Physics* 94 (2–3): 449–53. https://doi.org/10.1016/j.matchemphys.2005.05.005.

Wang, Lina, Junyi Yang, Haobo Ma, Zeyuan Wang, Kabir Olanrewaju, and Kamel Kerrouche. (2018). "Analysis and Suppression of Unwanted Turn-On and Parasitic Oscillation in SiC JFET-Based Bi-Directional Switches." *Electronics* 7 (8): 126. https://doi.org/10.3390/electronics7080126.

Wang, Ruixue, Shasha Zuo, Dong Wu, Jue Zhang, Weidong Zhu, Kurt H. Becker, and Jing Fang. (2015). "Microplasma-Assisted Synthesis of Colloidal Gold Nanoparticles and Their Use in the Detection of Cardiac Troponin I (CTn-I)." *Plasma Processes and Polymers* 12 (4): 380–91. https://doi.org/10.1002/ppap.201400127.

Washio, Isao, Yujie Xiong, Yadong Yin, and Younan Xia. (2006). "Reduction by the End Groups of Poly(Vinyl Pyrrolidone): A New and Versatile Route to the Kinetically Controlled Synthesis of Ag Triangular Nanoplates." *Advanced Materials* 18 (13): 1745–49. https://doi.org/10.1002/adma.200600675.

Weiss, Joseph. (1935). "The Catalytic Decomposition of Hydrogen Peroxide on Different Metals." *Transactions of the Faraday Society* 31: 1547–57. https://doi.org/10.1039/tf9353101547.

Wiley, Benjamin J., Sang Hyuk Im, Zhi-Yuan Li, Joeseph McLellan, Andrew Siekkinen, and Younan Xia. (2006). "Maneuvering the Surface Plasmon Resonance of Silver Nanostructures through Shape-Controlled Synthesis." *The Journal of Physical Chemistry B* 110 (32): 15666–75. https://doi.org/10.1021/jp0608628.

Woedtke, Th. von, S. Reuter, K. Masur, and K.-D. Weltmann. (2013). "Plasmas for Medicine." *Physics Reports* 530 (4): 291–320. https://doi.org/10.1016/j.physrep.2013.05.005.

Wu, Chunfang, Xue Zhou, and Jie Wei. (2015). "Localized Surface Plasmon Resonance of Silver Nanotriangles Synthesized by a Versatile Solution Reaction." *Nanoscale Research Letters*

10 (1): 354. https://doi.org/10.1186/s11671-015-1058-1.

Wu, Jing-Yuan, Meng-Na Lin, Long-De Wang, and Tong Zhang. (2014). "Photoluminescence of MoS 2 Prepared by Effective Grinding-Assisted Sonication Exfoliation." *Journal of Nanomaterials* 2014: 1–7. https://doi.org/10.1155/2014/852735.

Wu, Zhi-Cheng, Lei-Lei Guan, Hui Li, Jia-Da Wu, Jian Sun, and Ning Xu. (2017). "Growth of Single-Crystalline Silicon Nanocone Arrays by Plasma Sputtering Reaction Deposition." *Chinese Physics Letters* 34 (2): 025202. https://doi.org/10.1088/0256-307X/34/2/025202.

Wu, Zhuo-Fu, Zhi Wang, Ye Zhang, Ya-Li Ma, Cheng-Yan He, Heng Li, Lei Chen, Qi-Sheng Huo, Lei Wang, and Zheng-Qiang Li. (2016). "Amino Acids-Incorporated Nanoflowers with an Intrinsic Peroxidase-like Activity." *Scientific Reports* 6 (1): 22412. https://doi.org/10.1038/srep22412.

Wuithschick, Maria, Benjamin Paul, Ralf Bienert, Adnan Sarfraz, Ulla Vainio, Michael Sztucki, Ralph Kraehnert, et al. (2013). "Size-Controlled Synthesis of Colloidal Silver Nanoparticles Based on Mechanistic Understanding." *Chemistry of Materials* 25 (23): 4679–89. https://doi.org/10.1021/cm401851g.

Xia, Younan, Yujie Xiong, Byungkwon Lim, and Sara E. Skrabalak. (2009). "Shape-Controlled Synthesis of Metal Nanocrystals: Simple Chemistry Meets Complex Physics?" *Angewandte Chemie International Edition* 48 (1): 60–103. https://doi.org/10.1002/anie.200802248.

Xiong, Huayu, Huiling Zheng, Wei Wang, Jichao Liang, Wei Wen, Xiuhua Zhang, and Shengfu Wang. (2016). "A Convenient Purification Method for Silver Nanoclusters and Its Applications in Fluorescent PH Sensors for Bacterial Monitoring." *Biosensors and Bioelectronics* 86 (December): 164–68. https://doi.org/10.1016/j.bios.2016.06.038.

Yamada, Risa, Kosuke Nozaki, Naohiro Horiuchi, Kimihiro Yamashita, Reina Nemoto, Hiroyuki Miura, and Akiko Nagai. (2017). "Ag Nanoparticle–coated Zirconia for Antibacterial Prosthesis." *Materials Science and Engineering: C* 78 (September): 1054–60. https://doi.org/10.1016/j.msec.2017.04.149.

Yang, Xuegeng, Shenhao Chen, Shiyong Zhao, Degang Li, and Houyi Ma. (2003). "Synthesis of Copper Nanorods Using Electrochemical Methods." *Journal of the Serbian Chemical Society* 68 (11): 843–47. https://doi.org/10.2298/JSC0311843Y.

Yu, Ser-Sing Chang, Chien-Liang Lee, and C. R. Chris Wang. (1997). "Gold Nanorods: Electrochemical Synthesis and Optical Properties." *The Journal of Physical Chemistry B* 101 (34): 6661–64. https://doi.org/10.1021/jp971656q.

Yu, Fan, Yingying Chen, Xingbo Liang, Jiale Xu, Chiahsun Lee, Qi Liang, Peng Tao, and Tao Deng. (2017). "Dispersion Stability of Thermal Nanofluids." *Progress in Natural Science: Materials International* 27 (5): 531–42. https://doi.org/10.1016/j.pnsc.2017.08.010.

Yu, Pyng, Jane Huang, and Jau Tang. (2010). "Observation of Coalescence Process of Silver Nanospheres During Shape Transformation to Nanoprisms." *Nanoscale Research Letters*, September. https://doi.org/10.1007/s11671-010-9808-6.

Zhang, Hua, Douglas Yee, and Chun Wang. (2008). "Quantum Dots for Cancer Diagnosis and Therapy: Biological and Clinical Perspectives." *Nanomedicine* 3 (1): 83–91. https://doi.org/10.2217/17435889.3.1.83.

Zhang, Jian, Yi Fu, Dong Liang, Richard Y. Zhao, and Joseph R. Lakowicz. (2008). "Enhanced Fluorescence Images for Labeled Cells on Silver Island Films." *Langmuir* 24 (21): 12452–57. https://doi.org/10.1021/la801749f.

Zhang, Jing, Feng Huang, and Zhang Lin. (2010). "Progress of Nanocrystalline Growth Kinetics Based on Oriented Attachment." *Nanoscale* 2 (1): 18–34. https://doi.org/10.1039/B9NR00047J.

Zhang, Qingbo, Jianping Xie, Yue Yu, and Jim Yang Lee. (2010). "Monodispersity Control in the Synthesis of Monometallic and Bimetallic Quasi-Spherical Gold and Silver Nanoparticles." *Nanoscale* 2 (10): 1962. https://doi.org/10.1039/c0nr00155d.

Zhang, Xi-Feng, Zhi-Guo Liu, Wei Shen, and Sangiliyandi Gurunathan. (2016). "Silver Nanoparticles: Synthesis, Characterization, Properties, Applications, and Therapeutic Approaches." *International Journal of Molecular Sciences* 17 (9): 1534. https://doi.org/10.3390/ijms17091534.

Zhang, Zongtao, Bin Zhao, and Liming Hu. (1996). "PVP Protective Mechanism of Ultrafine Silver Powder Synthesized by Chemical Reduction Processes." *Journal of Solid State Chemistry* 121 (1): 105–10. https://doi.org/10.1006/jssc.1996.0015.

Zhu, Jun-Jie, Xue-Hong Liao, Xiao-Ning Zhao, and Hong-Yuan Chen. (2001). "Preparation of Silver Nanorods by Electrochemical Methods." *Materials Letters* 49 (2): 91–95. https://doi.org/10.1016/S0167-577X(00)00349-9.

Zhu, Liping, Jiesheng Li, Zhizhen Ye, Haiping He, Xiaojun Chen, and Binghui Zhao. (2008). "Photoluminescence of Ga-Doped ZnO Nanorods Prepared by Chemical Vapor Deposition." *Optical Materials* 31 (2): 237–40. https://doi.org/10.1016/j.optmat.2008.03.015.

Zielińska, Anna, Ewa Skwarek, Adriana Zaleska, Maria Gazda, and Jan Hupka. (2009). "Preparation of Silver Nanoparticles with Controlled Particle Size." *Procedia Chemistry* 1 (2): 1560–66. https://doi.org/10.1016/j.proche.2009.11.004.